Thermal-mechanical behaviour of the hierarchical structure of human dental tissue

Submitted by

Tan SUI

Supervisor: Prof. Alexander M. Korsunsky

St Cross College

Department of Engineering Science

University of Oxford

A thesis submitted for the degree of

Doctor of Philosophy

Trinity Term 2014

Abstract

Human dental tissues are fascinating nano-structured hierarchical materials that combine organic and mineral phases in an intricate and ingenious way to obtain remarkable combinations of mechanical strength, thermal endurance, wear resistance and chemical stability. Attempts to imitate and emulate this performance have been made since time immemorial, in order to provide replacement (e.g. in dental prosthodontics) or to develop artificial materials with similar characteristics (e.g. light armour). The key objectives of the present project are to understand the structure-property relationships that underlie the integrity of natural materials, human dental tissues in particular, and the multi-scale architecture of mineralized tissues and its evolution under thermal treatment and mechanical loading. The final objective is to derive ideas for designing and manufacturing novel artificial materials serving biomimetic purposes.

The objectives are achieved using the combination of a range of characterization techniques, with particular attention paid to the synchrotron X-ray scattering (Small- and Wide-Angle X-ray Scattering, SAXS and WAXS) and imaging techniques (Micro Computed Tomography), as well as microscopy techniques such as Environmental Scanning Electron Microscopy (ESEM), Transmission Electron Microscopy (TEM) and Atomic Force Microscopy (AFM). Mechanical properties were characterized by nanoindentation and photoelasticity; and thermal analysis was carried out via thermogravimetric analysis (TGA). Experimental observations were critically examined and matched by advanced numerical simulation of the tissue under thermal-mechanical loading.

SAXS and WAXS provided the initial basis for elucidating the structure-property relationships in human dentine and enamel through *in situ* experimentation. Four principal types of experiment were used to examine the thermal and mechanical behaviour of the hierarchical structure of human dental tissue and contributed to the Chapters of this thesis: (i) *In situ* elastic strain evolution under loading within the hydroxyapatite (HAp) in both dentine and enamel. An improved multi-scale Eshelby inclusion model was proposed taking into account the two-level hierarchical structure, and was validated against the experimental strain evaluation data. The achieved agreement indicates that the multi-scale model accurately reflects the structural arrangement of human dental tissue and its response to applied forces. (ii) The morphology of the dentine-enamel junction (DEJ) was examined by a range of techniques, including X-ray imaging and diffraction. The transition of mechanical properties across the DEJ was evaluated by the high resolution mapping and *in situ* compression measurement, followed by a brief description of the thermal behaviour of DEJ. The results show that DEJ is a narrow band of material with graded structure and mechanical properties, rather than a discrete interface. (iii) Further investigation regarding the thermo-mechanical structure-property relationships in human dental tissues was carried out by nanoindentation mapping of the nano-mechanical properties in *ex situ* thermally treated dental tissues. (iv) In order to understand the details of the thermal behaviour, *in situ* heat treatment was carried out on both human dental tissues and synthetic HAp crystallites. For the first time the *in situ* ultrastructural alteration of natural and synthetic HAp crystallites was captured in these experiments. The results presented in this thesis contribute to the fundamental understanding of the structure-property integrity mechanisms of natural materials, human dental tissues in particular. These results were reported in several first author publications in peer-reviewed journals, conference proceedings, and a book chapter.

Acknowledgement

A few lines are too short to make a complete account of my deep appreciation for my supervisor Prof. Alexander M. Korsunsky. His curiosity, dedication and passion for research impressed and influenced me deeply. It was his unwavering trust and constant encouragement that have been essential for my success through the last three years. I would like to thank him for his steady support in the most difficult times. His trust and honesty, his efforts in understanding a student's personality and tailoring his approach accordingly translated for me into, although away from home, a very pleasurable 3.5-year stay in the UK.

This episode of acknowledgement would not be complete without the mention of my family. I wish to thank my parents for their love and patience both mentally and financially during the past 3.5 years. Also, I need to show my special sincere thanks to my husband Jianan Hu, who helped with many useful advices in understanding the fundamental mechanical theory. The encouragement from my daughter was invaluable as well. Any words are weak here to express my gratitude to my family. I wish to dedicate this thesis to them, and thank them with all my heart for their love, care and patience.

I am grateful to my collaborators Prof. Gabriel Landini, Michael Sandholzer (University of Birmingham, U.K.), Prof. Eric Le Bourhis (University of Poitiers, France), A.P. Kaiyang Zeng, Dr. Li Tao (National University of Singapore, Singapore), Prof. Angus Kirkland, Chen Huang (Department of Materials, University of Oxford) for their assistance. It was an unforgettable experience to work with them.

I would like to thank my colleagues in Solid Mechanics and Materials group of Department of Engineering Science, including Dr. Kalin Dragnevski, Dr. Igor N. Dyson, Dr. Xu Song, Dr. Felix Hofmann, Mengyin Xie, Nikolaos Baimpas, Alexander Lunt, Taehoon Kim, Siqi Ying. Thanks go to them for valuable technical advice on the research and the experiments as well as warm friendship.

I would very much like to thank Dr. Mark S. Thompson and Dr. Jonathan D. Almer for taking time to read my thesis so thoroughly and for sparking very interesting and helpful discussions in the viva.

I gratefully acknowledge the Department of Engineering Science at the University of Oxford, and St Cross College for awarding me a grant under the “Travel and Research Fund”.

Contents

Chapter 1. Introduction

Chapter 2. Literature Review

Chapter 3. Methodology

Chapter 4. Multi-scale modelling and diffraction based characterization of elastic behaviours of human dentine

Chapter 5. Hierarchical modelling of *in situ* elastic deformation of human enamel based on photoelastic and X-ray scattering analysis of stresses and strains

Chapter 6. Structural-property characterization of the dentine-enamel junction (DEJ)

Chapter 7. Nano-scale structure-mechanical property relations as a function of temperature of thermal exposure

Chapter 8. X-ray scattering evaluation of ultrastructural changes of natural and synthetic hydroxyapatite under *in situ* thermal treatment

Chapter 9. Conclusions and Future work

List of Tables

List of Figures

Publications

Journal Publications:

1. **Tan Sui**, Michael Sandholzer, Alexander Lunt, Nikolaos Baimpas, Andrew Smith, Gabriel Landini, Alexander M. Korsunsky, *In situ* X-ray scattering evaluation of ultrastructural changes of natural and artificial hydroxyapatite under thermal treatment, *Journal of the Royal Society - Interface*, Vol. 11, 2014.
2. Michael Sandholzer, **Tan Sui**, Alexander M. Korsunsky, A. Damien Walmsley, Philip J. Lumley, Gabriel Landini, X-ray scattering evaluation of ultrastructural changes of human dental tissues with thermal treatment, *Journal of Forensic Science*, Vol. 59 (3), pp. 769-774, 2014.
3. **Tan Sui**, Michael Sandholzer, Alexander Lunt, Nikolaos Baimpas, Jianan Hu, Igor P. Dolbnya, Gabriel Landini, Alexander M. Korsunsky, Hierarchical modelling of in situ elastic deformation of human enamel based on photoelastic and diffraction analysis of stresses and strains, *Acta Biomaterialia*, Vol. 10 (1), pp. 343-354, 2014.
4. **Tan Sui**, Michael Sandholzer, Eric Le Bourhis, Nikolaos Baimpas, Gabriel Landini, Alexander M. Korsunsky, Structure-mechanical function relations at nano-scale in heat-affected human dental tissue, *Journal of the Mechanical Behavior of Biomedical Materials*, Vol. 32, pp.113-124, 2014.
5. **Tan Sui**, Michael Sandholzer, Nikolaos Baimpas, Igor P. Dolbnya, Gabriel Landini, Alexander M. Korsunsky, Hierarchical modelling of elastic behaviour of human enamel based on synchrotron diffraction characterization, *Journal of Structural Biology*, Vol. 184 (2), pp. 136-146, 2013.
6. **Tan Sui**, Michael Sandholzer, Nikolaos Baimpas,Igor P. Dolbnya, Anthony Walmsley, Philip J. Lumley, Gabriel Landini, Alexander M. Korsunsky, Multi-scale modelling and diffraction-based characterization of elastic behaviour of human dentine, *Acta Biomaterialia*, Vol. 9 (8), pp. 7937-7947, 2013.
7. **Tan Sui**, Gabriel Landini, and Alexander M. Korsunsky, Investigation of the structure of human dental tissue at multiple length scales using high energy synchrotron X-ray SAXS/WAXS, *AIP Conf. Proc.* 1394, pp. 113-124, 2010.

Book Chapter:

1. **Tan Sui,** Alexander M. Korsunsky, Hierarchical modelling of elastic behaviour of human dental tissue based on synchrotron diffraction characterization: Chapter **7** in *Advanced Healthcare Materials*, A. Tiwari, Ed., Advanced Materials Series, WILEY-Scrivener Publishing LLC, USA, 2013.

Conference Contributions:

1. **Tan Sui**, Michael Sandholzer, Nikolaos Baimpas, Alexander J.G. Lunt, Igor P. Dolbnya, Jianan Hu, Anthony D. Walmsley, Philip J. Lumley, Gabriel Landini, and Alexander M. Korsunsky, Hierarchical modelling and X-ray analysis of human dentine and enamel, *IMECS proceedings*, 2014. **Certificate of Merit.**
2. **Tan Sui**, Michael Sandholzer, Eric Le Bourhis, Nikolaos Baimpas, Gabriel Landini, Alexander M. Korsunsky, Nano-scale thermo-mechanical structure-property relationships in human dental tissues studied by nanoindentation and synchrotron X-ray scattering, *ICBME proceedings*, 2013.
3. **Tan Sui**, Michael Sandholzer, Nikolaos Baimpas, Gabriel Landini, A. Damien Walmsley, Philip J. Lumley and Alexander M. Korsunsky, Ultrastructural changes in burnt dental tissue revealed by synchrotron X-ray scattering, *IMECS proceedings*, 2013.
4. **Tan Sui**, Michael Sandholzer, Nikolaos Baimpas, Gabriel Landini, Alexander M. Korsunsky, Multi-scale modelling and diffraction-based characterization of elastic behaviour of human enamel, *ICF 13 (Intl Conference on Fracture) Proceedings*, 2013. **Best paper award.**
5. **Tan Sui**, Kalin Dragnevski, Tee Neo, Alexander Korsunsky, Mechanisms of failure in porcelain-veneered sintered zirconia restorations, *ICF 13 (Intl Conference on Fracture) Proceedings*, 2013
6. **Tan Sui**, Ultrastructural changes in burnt dental tissues revealed by synchrotron small angle X-ray scattering, S4SAXS workshop, Sheffield, U.K., 30-min oral presentation 2013.
7. **Tan Sui**, Felix Hofmann, Tao Li, Kaiyang Zeng, Sophie Eve, Alexander M. Korsunsky, Local orientation analysis of abalone nacre by micro-beam Laue diffraction, *Mechanics of Nano, Micro and Macro Composite Structures*, 2012.
8. **Tan Sui**, Felix Hofmann, Xu Song, Tao Li, Kaiyang Zeng and Alexander M. Korsunsky, Bio-materials Characterization Across Multiple Scales at Oxford HEX-lab, *WCE proceedings*, 2012.
9. **Tan Sui**, Alexander M. Korsunsky, T.K. Neo, Interfacial strength and mechanisms of failure in porcelain veneer-zirconia core dental restorations, EMC, Poster, 2012.

10. **Tan Sui**, Michael Sandholzer, Gabriel Landini, Alexander M. Korsunsky, SAXS evaluation of ultrastructural changes of human dental tissues with thermal treatment, 20-min oral presentation, CMA-UK, 2012.

Chapter 1

Introduction

1.1. General background

Biological hard tissues, for example, bones, dental tissues and varieties of shell structures, are of considerable interest for biomimetic applications due to the evident success of nature's intricate hierarchical (macro-/micro-/ultra-structural) design: guided assembly and organic bonding of nano-crystallites of common mineral substances such as calcite and calcium phosphate to produce hard yet tough structures that display thermal and chemical stability under the relevant conditions of their use. Imitating and emulating natural design is a long term objective of biomimetic studies that is likely to require extended research effort. In the short to medium-term time scale, the use of artificial materials, e.g. for dental restorations, continues to present a major challenge in terms of achieving satisfactory performance and structural integrity.

The investigation of remarkable properties of natural and novel artificial hard tissues has the potential to give insight into biomimetic material design and novel functional materials development [1-7]. The overall objective of the present project is to undertake multi-scale characterization and modelling of the structure as well as the mechanical and thermal properties of natural and artificial hard tissue, in particular human dental tissue, to provide improved solutions for biomedical and structural engineering applications.

X-ray diffraction and imaging provides an arsenal of characterization tools for the study of the internal structure of materials, from macro- to nano- and the atomic scale. More specifically, Small Angle X-ray Scattering (SAXS) and Wide Angle X-ray Scattering (WAXS) methods are introduced here as tools for the analysis of human dental tissue. Analysis of SAXS patterns provides insight into the mean dimension and orientation of particles, while that of WAXS (or X-ray Powder Diffraction, XRD) patterns allows the determination of the crystallographic unit cell parameters, statistical crystal orientation (texture) and lattice strain when subjected to the external or residual loading of the inorganic phase. Complementary structural characterization methods are helpful in investigating the hierarchical structure of dental tissues at the macro-scale by Micro Computed Tomography (Micro-CT), micro-scale by Environmental Scanning Electron Microscopy (ESEM), and at the ultra-structural scale by Atomic Force Microscopy (AFM) and Transmission Electron Microscopy (TEM). Furthermore, nanoindentation, Photoelasticity and thermogravimetric analysis (TGA) techniques are able to reveal the mechanical and thermal behaviour.

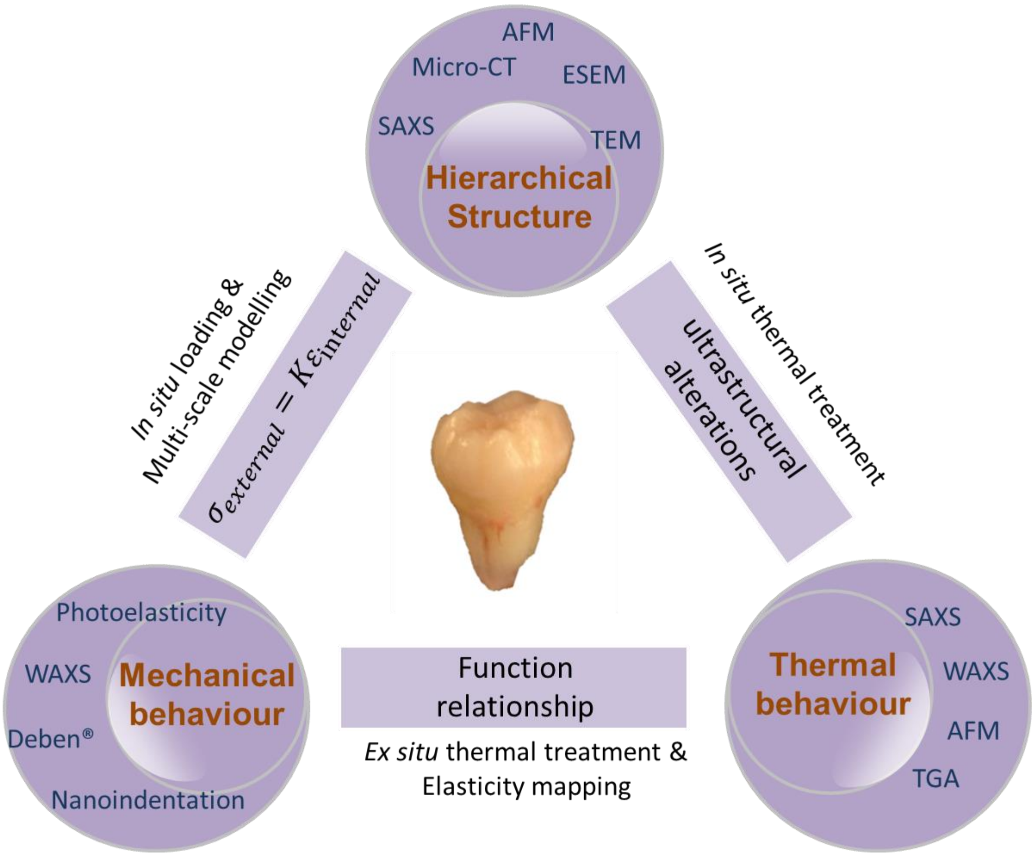

Fig. 1.1 Overview of the work reported in this thesis

A schematic overview of the work undertaken and reported in this thesis is shown in Figure 1.1. The visualization and understanding of the internal architecture of human dental tissue is essential for the further study of thermo-mechanical behaviour. Therefore, firstly, the hierarchical structure of human dental tissues was investigated by advanced synchrotron scattering techniques and several other characterization methods. The remarkable mechanical performance of human dentine and enamel subjected to *in situ* uniaxial compressive loading was then studied by collecting multi-scale structural information and deformation data by applying SAXS/WAXS techniques simultaneously. The achieved agreement between structurally informed multi-scale Eshelby inclusion modelling with the experimental strain evaluation data indicates that the structural arrangement, especially the nano-scale structure, has an influential effect on the mechanical properties of hierarchical biomaterials. The microstructure of DEJ and its response to external loading were examined by SAXS/WAXS, as well as the X-ray imaging method. The ultrastructural features and the correlation with elasticity mapping at high spatial resolution show that DEJ is a band with graded mechanical properties rather than a discrete interface. Furthermore, the correlation study regarding the thermo-mechanical structure-property relationships in human dental tissues was also undertaken by *ex situ* measurement, and the relationship between the changes in ultrastructure and mechanical behaviour with increasing temperature indicated that the structural alteration has a strong effect on the mechanical properties. In order to investigate in more detail the thermal response of hydroxyapatite (HAp) crystallites, especially in view of the importance of this insight in the forensic and archaeological context, ultrastructural alterations of both natural and synthetic HAp polycrystals exposed to *in situ* thermal treatment were analysed. The information about the internal architecture (the variation of HAp crystalline size and the nano-particle orientation) of dental tissues and synthetic HAp polycrystals was collected, providing a basis for estimating the exposure temperature of forensic and archaeological dental samples. This is also useful for further improvement in the clinical practice on laser-assisted caries prevention.

1.2. Aims and scope of the current research

The key objectives of this thesis are:

- To develop and demonstrate the capabilities of X-ray characterization techniques for elucidating the remarkable natural microstructure and architecture of biological hard tissues. In particular, the focus is placed on the study of the size, orientation and spatial distribution of HAp crystalline particles and the determination of crystallographic unit cell parameters of this phase in human dental tissues.

- To improve the understanding of the nano-scale structure variation of the hierarchical two-level structure of human dental tissues (enamel and dentine) and its influence on the materials, mechanical response both experimentally and theoretically.
- To investigate the (dentine-enamel junction) DEJ, by microstructural observation and the study of its load and thermal treatment characteristics, in order to obtain critical insight into how the microstructure of DEJ correlates with its function.
- To study the thermal-mechanical relationships at the nano-scale in the human dental tissues for the purpose of understanding and predicting the effects of microstructural alterations that may occur due to disease or treatment on the performance of dental tissues and their artificial replacements.
- To investigate the ultrastructural alteration of human skeletal hard tissues subjected to high temperatures in the context of forensic investigations and archaeological analysis, as well as the application of laser-assisted caries prevention.

1.3. Thesis structure

The general review on the natural biological mineralized tissue is given at the beginning of **Chapter 2**. Then, the review moves forward to the human dental tissues, in particular by introducing their hierarchical structure, initially with several typical microscopy images. Furthermore, the relevant literature on the mechanical function and thermal behaviour of human dental tissues is reviewed.

Chapter 3 summarizes the most relevant and useful characterization methods and the theoretical modeling basis that are used in the subsequent chapters. The Chapter starts with the summary of the relevant literature on the fundamentals of X-ray diffraction techniques. Focusing on the data interpretation, SAXS and WAXS are introduced in detail as advanced techniques to characterize the mineralized materials at the nano- and sub-nano scales. A multi-scale model is established and illustrated in this part, which allows the assessment of internal strain of hydroxyapatite crystallites subjected to external loading. At the end, some other complementary characterization methods are also shortly described.

Chapter 4 and **Chapter 5** present the results pertaining to *in situ* elastic strain response of HAp crystallites within dentine and enamel respectively when these are subjected to external uniaxial compressive loading. Furthermore, the quantitative evaluation of the stress distribution within samples of human dental enamel embedded in the birefringent mounting epoxy is performed using photoelastic techniques. Finite element simulation in conjunction with improved multi-scale Eshelby inclusion modelling are proposed as a combination that takes into account the two-level hierarchical structure, and is validated with multi-directional experimental lattice strain results. The agreement between the simulation and measurement indicates that the multi-scale hierarchical model established here accurately reflects the structural arrangement and mechanical response of human dentine and enamel.

Chapter 6 presents the microstructure of the DEJ examined by X-ray imaging and scattering techniques. The consistent observation of the size of DEJ is obtained from micro- and nano- scale evaluation. Furthermore, high resolution elastic modulus mapping across this transition region of DEJ is presented. *In situ* measurements further confirm that the loading transition is correlated with the nano-particle distribution. Finally, some interesting aspects of the thermal response of DEJ are briefly introduced.

The following **Chapter 7** describes the structural-mechanical property alteration of human dentine, enamel and DEJ coupled with the effect of temperature by *ex situ* measurement using X-ray techniques and nanoindentation. The results enable an improved understanding of the mechanical property correlation in hierarchical biological materials, and human dental tissues in particular.

In **Chapter 8**, the information on the ultrastructural alterations in the natural and synthetic HAp crystallites exposed to thermal treatment is collected by *in situ* X-ray scattering measurement. Careful analysis of the results provides a reliable basis for deducing the heating history for the dental tissues in the forensic and archaeological context and will allow further design and optimization of biomimetic materials.

Chapter 9 provides the summary and conclusions drawn from the research results obtained so far, and presents the discussion of the directions for future work.

Chapter 2

Literature Review

2.1. Brief overview of natural hard tissues

Natural hard tissues, primarily mineralized, are biological tissues that incorporate minerals into soft matrices. These tissues often form a protective shield (exoskeleton) or internal structural support (endoskeleton) [8]. Bone, tooth, and seashell are some typical mineralized tissues of significant research interest. Although the present overview focuses on the dental tissues, a quick scan of some other biological tissues is likely to be relevant for understanding the micro- and nano-scopic origins of the macroscopic properties achieved by Nature’s ingenuous design.

2.1.1. Bone

As with many biological tissues, bone has a hierarchical structure that has two major structural constituents, soft collagen protein matrix and much stiffer apatite mineral reinforcement and water is the third constituent. At the nano-scale, the interactions between collagen fibrils and the mineral hydroxyapatite (HAp) are known to play a significant role in providing strength and toughness to the bone [9]. Dentine is similar to bone in several aspects, in terms of composition (similar content of organic and inorganic phases) and the nano-scale dimensionality (the size of apatite mineral particles and gaps between them). Therefore, studies on bone tissues can be helpful for the investigation of dental tissues, especially **dentine** [10].

2.1.2. Abalone shell

Abalone is a gastropod mollusk whose shell is a biocomposite consisting of organic macromolecules and inorganic components ($CaCO_3$) [11]. There are two distinct mineralized regions in the abalone shell, namely, the outer prismatic layer containing calcite, and the inner nacre layer containing aragonite, as illustrated schematically in Figure 2.1 a. The calcite *prismatic layer* contains a small quantity of organic components with calcite crystallites at the micro-scale preferentially oriented with respect to the interface, conferring high hardness to the exterior of the shell [12, 13], making its function similar to that of dental **enamel**. Underneath the prismatic layer lies the mother-of-pearl, or *nacre layer*, which is one of the best known examples of bottom-up self-assembled natural nano-composite materials. This nacre layer exhibits high strength and toughness, despite the brittle nature of its constituents. This is achieved by having tablet-shaped single crystals of aragonite with their internal crystal structure oriented so that the *c*-axis is aligned normally to their faces [14, 15]. Understanding the structure of abalone shell is desirable as it can provide guidance for creating new materials with strong mechanical strength and toughness [16].

The interpretation of the micro-beam Laue diffraction patterns from the nacreous layer shows that the overall alignment of the *c*-axis of aragonite tablet is such that the [001] direction is almost coincident with the surface normal, as expected. However, not only the shell itself is curved, but even within a small region of nacreaous surface small misorientation exists compared to pure [001] [17]. This is illustrated in Figure 2.1 b and c, which may reflect how the adjustment of crystal orientation occurs. The *z*-axis in Figure 2.1 b is aligned with the average [001] orientation within the crystal, and each 3D vector represents the actual direction of the *c*-axis in the nacreous layer for each scanned point. Four distinct arrow colours were ascribed based on the tablets (grains) distribution, and used to distinguish between adjacent regions. The length of the projection arrow (Figure 2.1 c) indicates the vector deviation from *z*-axis: if alignment is perfect, the projection appears as a point. The longer the vector, the greater the misorientation is at the indicated position. The direction of the vector in the *x*-*y* plane indicates the direction of the rotation of the tablet plane around *x*-axis and/or *y*-axis. The existing misorientation is likely to have influence on the mechanical properties via intricate strengthening mechanisms [18], which is essential for improving our understanding of the intricate link between crystallography and mechanical properties of these fascinating systems.

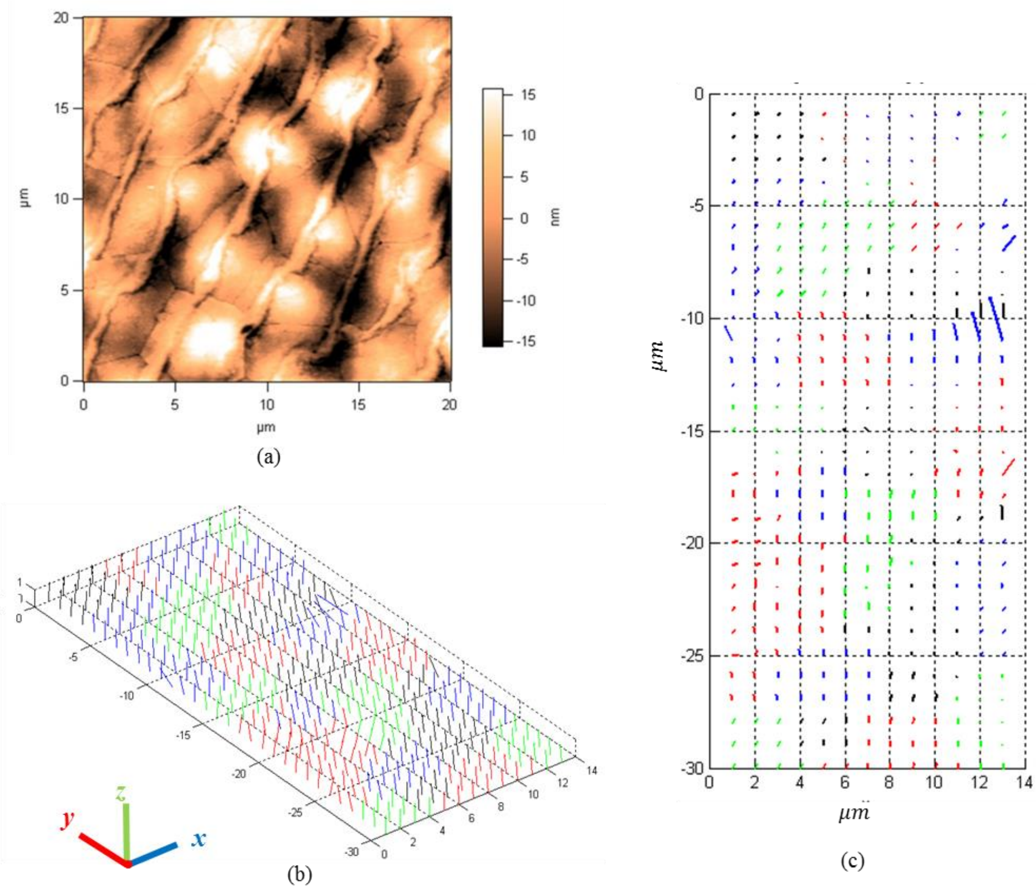

(a)

(b)

(c)

Fig. 2.1 (a) AFM observation of aragonite layer of abalone shell on *x*-*y* plane; (b) 3-D *c*-axis orientation mapping of aragonite tablets; (c) projection of mapping on *x*-*y* plane [17].

2.2. Human dental tissue

Teeth, the human masticatory apparatus play a largely biomechanical role in the preparation of food for the final absorption by the alimentary tract. The human dentition is replaced once in a lifetime, but during this lifetime, the permanent teeth undergo cyclical load frequently (mastication force about 300N [19], one will chew 500~600 times each meal). During mastication the teeth are subjected to intermittent pressure. The amount of the load, both under normal masticating force and maximum biting effort, varies in different human. Much of the load on the teeth is being transmitted from the occlusal surface through a rather thin outer cylinder of enamel which is more resistant to compression than the inner dental tissues to the dentine composed of a large number of tubules filled with living connective tissue and cells (odontoblast) and dentinal fluid. The dental pulp contains large nerve trunks and blood vessels. The vitality of the dentin-pulp complex, both during health and after injury, depends on pulp cell activity and the signaling processes that regulate the cell's behaviour [20]. Incisor, canine, premolar and molar are primary types of teeth with different structures functions. This study focuses on the molar teeth, which are widely used in the synchrotron X-ray experiments [21], due to the large size of the enamel. Such size guarantees the preparation of cubic samples for the in situ loading measurement and several samples can be prepared at the same time out of the same area to keep the experiment constantly.

2.2.1. Hierarchical structure

Human dental tissues are fascinating nano-structured and hierarchical materials that combine organic and mineral phases in an intricate and ingenious way to obtain remarkable combinations of mechanical strength, thermal endurance, wear resistance and chemical stability. The knowledge of the microstructural features of human dental tissues (mainly enamel, dentine and their junction, the DEJ, as shown in Figure 2.2 a) is important in order to understand the natural properties of human teeth, and also the mechanism of these load-bearing tissues' contribution to the life-long success of human teeth during mastication, as well as the prediction of the factors that affect the performance of dental tissues, such as disease, treatment, environmental or thermal exposure. Meanwhile, it is also beneficial to the development of biomimetic materials and their artificial replacements, e.g. teeth restorations. Among the all-porcelain crown materials, yttrium-stabilised polycrystalline zirconia is one of the most promising restorative structural materials that offer an alternative to metallic alloys, due to its biocompatibility, aesthetic appearance and favourable mechanical properties. However, veneering porcelain chipping and breakage remain the major concerns in the clinical environment. Although long-term data on survival of these restorations is not sufficient, dentists have voiced concerns. Thus, improving the durability and fracture resistance of all ceramic dental restorations remains an outstanding challenge.

2.2.1.1. Dentine

Dentin is a tough and flexible material containing ~50% of mineral hydroxyapatite (HAp) with the formula $\mathrm{Ca_{10}(PO_4)_6OH_2}$, ~30% of organic material (mostly Type I collagen) and ~20% of water by volume [22]. From Figure 2.2 d, it is observed that at the microscopic level of the hierarchical structure, it has a typical well-oriented microstructure with an arrangement of dentinal tubules with the area density within (19-45)×1000/mm^2 (the mean diameter is around 0.8-2.5 μm), where they extend throughout the entire dentine thickness, from the dentine-enamel junction, DEJ (also sometimes referred to as the amelo-dentinal junction, ADJ) to the pulp [23-25]. At the finer nano-scale level, dentine is a composite of plate-like hydroxyapatite (HAp) crystallites that have the shape of elongated pancakes (approximately 2-4 nm of thickness, 30 nm in width and up to 100 nm in length) randomly embedded in a fibrous collagen matrix [26, 27]. The crystal *c*-axis (corresponding to the (002) peak) of the HAp crystallites is thought to be parallel to the long dimension of the platelet [28, 29].

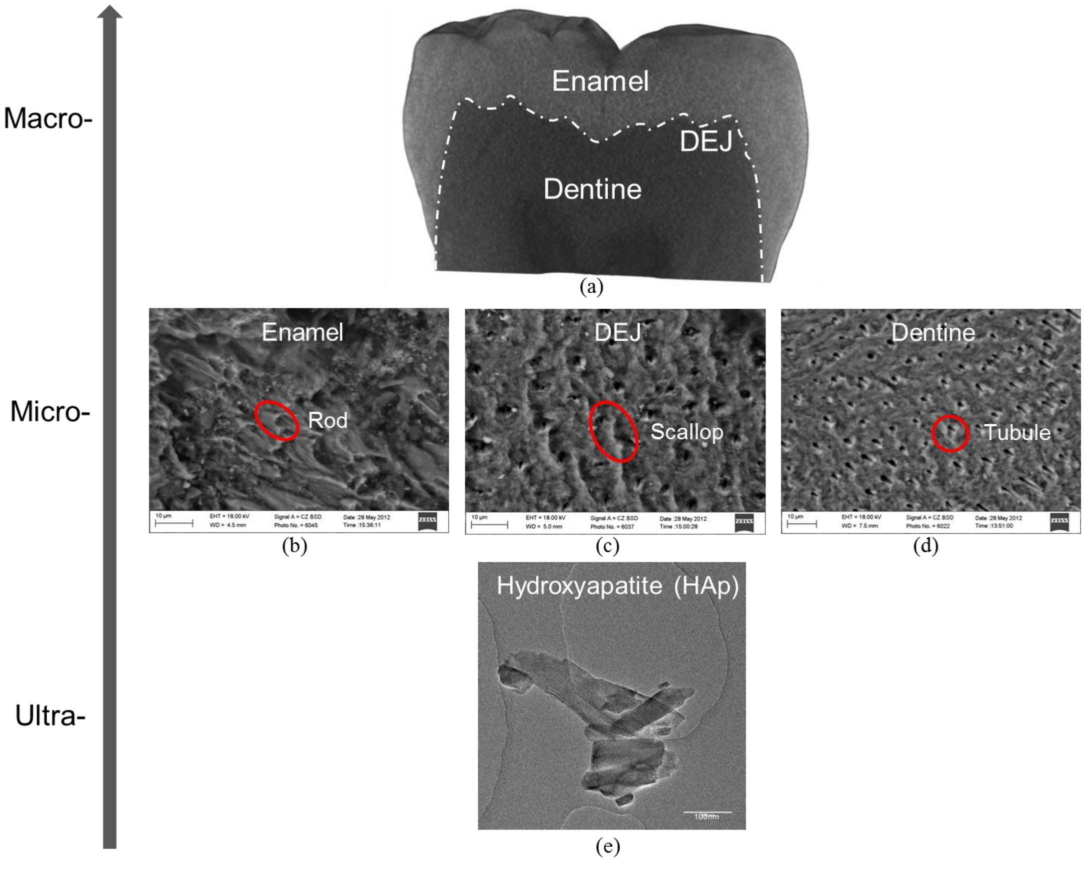

(a)

(b) (c) (d)

(e)

Fig. 2.2 Hierarchical structure of human dental tissue from macro-scale by Micro-CT, micro-scale by ESEM and nano-scale by TEM (author's unpublished work). (a) the macroscale structure of human dental tissue; (b)-(d) the microscale features of rod, scallop and tubule for enamel, DEJ and dentine respectively; (e) the ultrastructural hydroxyapatite (HAp) crystallites.

2.2.1.2. Enamel

In comparison to dentine, enamel is a harder and more brittle outer layer that covers the crown portion of the tooth serving as an important stiff, hard and wear-resistant outer shell of the tooth exposed to mastication contact loading and grinding action. It is characterised by the high content of inorganic mineral hydroxyapatite, approximately 87% by volume, and relatively low organic content of collagen Type I [30]. At the microstructural level the notable features present in the enamel are, the long aligned prisms (or rods, see Figure 2.2 b) with a cross-section that looks like a keyhole with ~5 μm diameter arranged to fill the space from the interface with dentine to the outer enamel surface, with the top oriented towards the crown of the tooth [31]. At the nano-scale, each rod is thought to be a composite with needle-like HAp crystalline particles (approximately 25-30 nm in diameter, and length is thought to be more than 1000 nm [32] that may even span through the entire enamel layer [23]) held together by an organic collagenous matrix [33-35].

2.2.1.3. Dentine-enamel-junction (DEJ)

The dentine-enamel junction (DEJ) is an important biological interface between the highly mineralized hard outer layer (enamel) and the comparatively softer tooth core (dentine). DEJ is a life-long success story: unless diseased, this interface never fails (e.g. by de-cohesion or cracking), despite the thermo-mechanical loading in the oral cavity. 5 ℃ and 55 ℃ are normally used to simulate the thermal changes occurring in the oral environment to represent the cold or hot conditions. This remarkable performance provides the motivation for numerous investigations into the detail of the micro- and nano-structure of enamel, dentine and DEJ.

It has been surmised that the complex scalloped microstructure of DEJ (shown in Figure 2.2 c) acts as a crack-stopping, stress-distributing mechanism [36]. It has a three-level structure, 25-100 μm scallops with their convexities towards dentine and concavities towards enamel; 2-5 μm micro-scallops; and a finer nano-level structure within each micro-scallop [37-40]. The sizes of DEJ scallops vary depending on the tooth type and function. The average scallop size in incisors is 29.4±5.5 μm, and 42.3±8.5 μm in molars [41]. In the DEJ region, dentine and enamel tissues form an interpenetrating transition band, rather than a sharp interface. Collagen fibrils (100 nm in diameter) actually penetrate the DEJ, providing a stitching connection between dentine and enamel [42, 43]. It is reasonable to conclude [44] that Nature's design of the composite structure and functionally graded interface confers crack propagation resistance on the tooth, resulting in excellent toughness. DEJ constitutes a superb lesson from nature on how to achieve strong, durable bond in a structure containing joints between dissimilar materials.

2.2.1.4. Hydroxyapatite (HAp) in dental tissues

By way of introduction to the study of the nano-structure influence on the macroscopic mechanical and thermal properties, the morphology of the composites formed by organic bonding of hydroxyapatite (HAp) crystallites and the structure, mechanical properties and thermal behaviour of HAp crystallites are summarized below.

Hydroxyapatite (HAp) is a naturally occurring mineral form of calcium apatite with the formula $\mathrm{Ca_{10}(PO_4)_6OH_2}$. HAp is the key inorganic component in dentine and enamel at the nano-scale level (Figure 2.2 e). Its crystallograpic space symmetry group is $P6_3/m$ and the reference lattice parameters found in published literature are a=9.441(2) Å and c=6.878(1) Å [45-47]. Since these values were acquired from powdered teeth, they represent highly averaged information that cannot be related to the spatial variation between positions in a sample.

The initial mineralization occurs in small nuclei near the DEJ within the supramolecular aggregates of amelogenins and enamelins. Soon thereafter, these HAp crystallites become confluent with the smaller hydroxyapatite crystallites in the neighboring dentine[48]. In the dentine and enamel specifically, the HAp crystallites have different shapes and distinct distributions as shown in Figure 2.3. In dentine, the shape of the HAp crystallites is platelet-like (Figure 2.3 a), The *c*-axis of the HAp crystallites (corresponding to the (002) plane normal) is thought to be parallel to the long dimension of the platelet-like single crystals. In contrast with dentine, in the enamel the HAp crystallites are said to have needle shape or cylindrical fibre shape (Figure 2.3 b) with the *c*-axis parallel to the long axis of the cylinder [49].

The HAp crystallites in dentine decorate the fibrils in a “necklace” arrangement, forming a net-like structure of fibrils around tubules. As a consequence, HAp crystallites in dentine have a rather low degree of alignment. In the enamel, by contrast, although the HAp crystallites are still partially (incompletely) aligned within each rod (particularly due to the continuous orientation change within the sampling volume), the degree of alignment is rather high compared to dentine.

The comprehensive investigation of the structural features of HAp crystallites needs to be based on properly justified geometric assumptions used to build multi-scale models. Specifically, in dentine the HAp crystallites can be assumed to be penny-shape inclusions with almost random distribution, whereas in the enamel, cylinder-shape inclusions in a highly aligned distribution seem to offer a suitable picture.

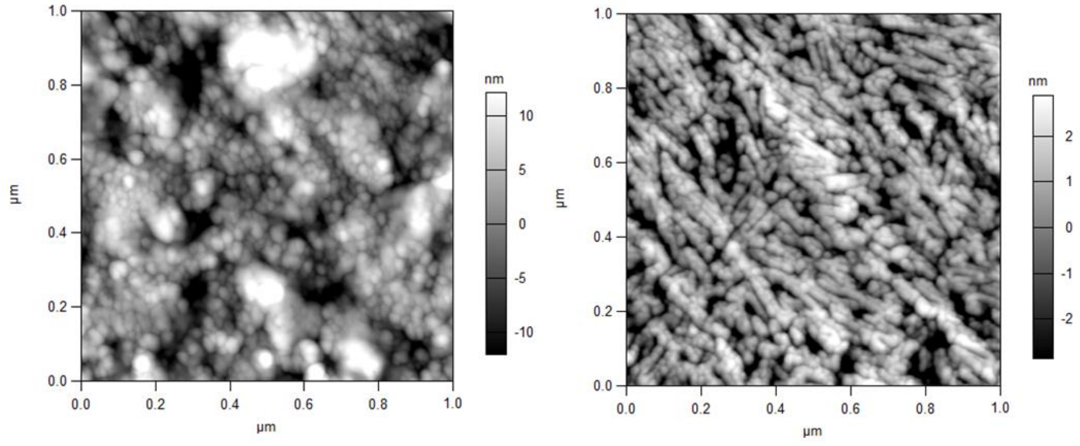

(a) (b)

Fig. 2.3 AFM investigation of the morphology of HAp crystallites: (a) HAp crystallites in enamel (needle-like shape); (b) HAp crystallites in dentine (platelet-like shape). Generally the size of HAp crystallites in the enamel is larger than that of HAp crystallites in dentine.

2.2.2. Mechanical behaviour

Mechanical properties like elastic modulus, hardness, toughness are important physical material properties, associated with elastic or plastic deformation. A thorough knowledge and in-depth investigation of these mechanical properties is essential of understanding the materials. The review below focuses on the elastic modulus, which is mostly investigated in the current study.

2.2.2.1. Elastic modulus

Hooke's law states that within the linear elastic range, the deformation induced by loading is directly proportional to the applied stress. *Elastic modulus* is defined as the ratio of stress to strain below the proportional limit. It is therefore the macroscopic manifestation of the interatomic stretching and compression of interatomic bonds within the material when tensile or compressive forces are applied within the elastic range. It is also an indication of the amount of reversible deformation that can occur in a structure when reversed loading is applied.

Elastic modulus is a basic parameter that describes material stiffness, i.e. the ratio of certain measures of stress and strain. Of particular interest often is the ratio between the macroscopic remotely applied stress and microscopic strain in one of the constituents, e.g. in the reinforcing phase that performs the load-bearing function. This ratio can be called the apparent modulus [50] that is often used for experimental and modeling evaluation of the mechanical response of composite structures.

The mechanical tests to determine the elastic modulus and hardness of dentine and enamel have advanced in several stages over the last several decades, from macro-scale progressively down to the micro- and nano-scale. With the development of the low load, continuously recording indentation techniques and increasing access to the appropriate experimental facilities, micro-indentation and nano-indentation have been widely employed in the investigation of mechanical properties of human dentine and enamel. The reported results are shown in Table 2.1 and Table 2.2 respectively.

2.2.2.2. Mechanical properties of dentine

Human dentine, one of the principal tissues of human teeth, provides soft, flexible, energy absorbing support for the hard, wear-resistant enamel during mastication. The mechanical properties of dentine are critical to the performance of teeth. The selected data is shown in Table 2.1. The elastic modulus varies over a wide range due to the test techniques and the location within the tooth of the specimen.

Tab. 2.1 Elastic modulus of sound dentine from different measurements

	Method	**Position**	**Elastic modulus (GPa)**	**Reference**
Macro-scale tests	Compression		13.8	Stanford et al. [51]
	Tension		19.3	Bowen et al. [52]
Micro- and Nano- scale tests	Micro indentation	Buccal aspect	19.89±1.92	Mahoney et al. [53]
		Faciolingual cervical	6.18~16.52	Kishen et al. [54]
			11.6~17	Angker et al. [55]
	AFM	Across DEJ	18.6~20.7	Marshall et al.[56]
	Nanoindentation	Buccal lingual	15~25	Hosoya [57]
		Near DEJ	18¬22	Ziskind et al. [58]

2.2.2.3. Mechanical properties of enamel

Enamel is the hardest substance in the human body (harder than bone and significantly harder than cartilage) and also exhibits a high value of elastic modulus. These superior mechanical properties make it ideally suited for the physiological function of mastication (crushing and chewing). Mechanical property data for enamel is summarized in Table 2.2. The hierarchical microstructure leads to an anisotropic elastic behaviour in enamel, of which the property depends on the rod orientation. Studies have shown that enamel is anisotropic geometrically and in terms of its mechanical properties (as illustrated in Table 2.2) may be dependent on the type and direction of the stress applied, with respect to the prismatic orientation [59-61].

2.2.2.4. Mechanical properties of the DEJ

Nanoindentation and AFM techniques are widely used to estimate the mechanical properties of DEJ by averaging the measured results of dentine and enamel. As illustrated in [37] and [56], the reported values of hardness are 4.79±0.21 GPa or 3.5 GPa in enamel and 0.79±0.04 GPa or 0.7 GPa in dentine, and for the average elastic modulus the values are 98.3±5.9 GPa or 65 GPa in enamel and 24.8±1.4 GPa or 20 GPa in dentine. There is a consistent trend decreasing hardness and modulus across the DEJ from enamel to dentine. Rather than to be represented by a step function, this decrease is gradual and continuous across the DEJ.

The method of the elasticity mapping using arrays of low load indentations has also been applied to determine the functional width of the DEJ. Large variation has been reported between different techniques, with a width of 100 to 200 μm being suggested [37, 67] based on the results of the micro-hardness method, while nanoindentation measurements revealed a width of 12 to 20 μm [59, 68]. Micro-beam X-ray can determine the range of the region by using very highly focused beams of only a few micrometres cross-section.

Tab. 2.2 Elastic modulus of sound enamel from different measurements

	Method	**Position**	**Elastic modulus (GPa)**	**Reference**
Macro-scale tests	Compression	Perpendicular to rods	84.1 ±6	Craig et al. [62]
		Parallel to rods	77.39 ±4.8	
	Four-point bending	/	131 ±16	Tyldeslsy [63]
Micro- and Nano- scale tests	Micro indentation	Perpendicular to rods	94 ±5	Xu et al. [64]
		Parallel to rods	80 ±4	
		Perpendicular to rods	60.90 ±3.51~ 89.91 ±7.67	Mahoney et al. [53]
		Perpendicular to rods	125~120	Braly et al. [65]
	AFM	Across DEJ	62.1~65.0	Marshall et al.[56]
	Nanoindentation	Perpendicular to rods	90.6 ±6.1	Willems et al. [66]
		Parallel to rods	87.5 ±2.2	Habelitz et al. [38]
		Perpendicular to rods	72.2 ±4.5	

2.2.2.5. Mechanical properties of HAp crystallites

HAp crystallizes into hexagonal closely packed lattice structure, that is transversely isotropic with respect to the *c*-axis (Figure 2.4 a). Due to this symmetry, the stiffness matrix C_{ij} of HAp crystallites can be expressed in terms of five independent components (assuming *c*-axis is along the 3 direction) [69].

$$\begin{bmatrix} \sigma_{xx} \\ \sigma_{yy} \\ \sigma_{zz} \\ \sigma_{yz} \\ \sigma_{yx} \\ \sigma_{xy} \end{bmatrix} = \begin{bmatrix} C_{11} & C_{12} & C_{13} & 0 & 0 & 0 \\ C_{12} & C_{11} & C_{13} & 0 & 0 & 0 \\ C_{13} & C_{13} & C_{33} & 0 & 0 & 0 \\ 0 & 0 & 0 & C_{44} & 0 & 0 \\ 0 & 0 & 0 & 0 & C_{44} & 0 \\ 0 & 0 & 0 & 0 & 0 & (C_{11}-C_{12})/2 \end{bmatrix} \begin{bmatrix} \varepsilon_{xx} \\ \varepsilon_{yy} \\ \varepsilon_{zz} \\ 2\varepsilon_{yz} \\ 2\varepsilon_{zx} \\ 2\varepsilon_{xy} \end{bmatrix} \qquad \text{Eq. 2.1}$$

The same elastic properties can be expressed equivalently in terms of the matrix of compliance coefficients S_{ij}. The compliance matrix S_{ij} is the inverse of the C_{ij} matrix, i.e. $S_{ij} = C_{ij}^{-1}$. The elastic moduli values E_{ij} can be readily extracted from Eq. 2.2.

$$\begin{bmatrix} \varepsilon_{xx} \\ \varepsilon_{yy} \\ \varepsilon_{zz} \\ 2\varepsilon_{yz} \\ 2\varepsilon_{zx} \\ 2\varepsilon_{xy} \end{bmatrix} = \begin{bmatrix} \frac{1}{E_x} & -\frac{\nu_{yx}}{E_y} & -\frac{\nu_{yx}}{E_y} & 0 & 0 & 0 \\ -\frac{\nu_{xy}}{E_x} & \frac{1}{E_y} & -\frac{\nu_{yz}}{E_y} & 0 & 0 & 0 \\ -\frac{\nu_{xy}}{E_x} & -\frac{\nu_{yz}}{E_y} & \frac{1}{E_y} & 0 & 0 & 0 \\ 0 & 0 & 0 & \frac{2(1+\nu_{yz})}{E_y} & 0 & 0 \\ 0 & 0 & 0 & 0 & \frac{1}{G_{xy}} & 0 \\ 0 & 0 & 0 & 0 & 0 & \frac{1}{G_{xy}} \end{bmatrix} \begin{bmatrix} \sigma_{xx} \\ \sigma_{yy} \\ \sigma_{zz} \\ \sigma_{yz} \\ \sigma_{yx} \\ \sigma_{xy} \end{bmatrix} \qquad \text{Eq. 2.2}$$

Within the hexagonal crystallites, the stiffest direction is associated with the crystalline *c*-axis, as can be seen from the 3-D directional modulus diagram of HAp crystal shown in Figure 2.4 b, computed based on Eq. 2.1,.

Experimentally, Katz and Ukraincik (1971) [70] performed an extended experimental analysis to derive a set of pseudo single crystal stiffness constants for HAp crystallites. Remarkably, those values constitute the only experimentally-derived stiffness constants available today for HAp crystallites [70]. Recently, Tofail et al. (2009) [71] have measured the elastic constants of a textured polycrystalline sample of HAp crystallites that has transverse isotropy. There has been recent computational effort devoted to the determination of mechanical properties on HAp crystallites that is included in Table 2.3. The methodological differences generally lead to marginal discrepancies.

Tab. 2.3 HAp crystallites elastic constants (in GPa)

Methods	C_{11}	C_{12}	C_{13}	C_{33}	C_{44}	**References**
Experiment	137	42.5	54.9	172	39.6	Katz, et al. [70]
	137.2	53	55	123.2	42.2	Tofail, et al. [71]
Theory	145.2	47.8	73.6	191.4	37.6	Menendez-Proupin et al. [72]
	140.0	42.4	58.3	174.8	47.5	Ching, et al. [73]
	117.1	26.2	55.6	231.8	56.4	Snyders, et al. [74]
	134.4	48.9	68.5	184.7	51.4	De Leeuw et al. [75]

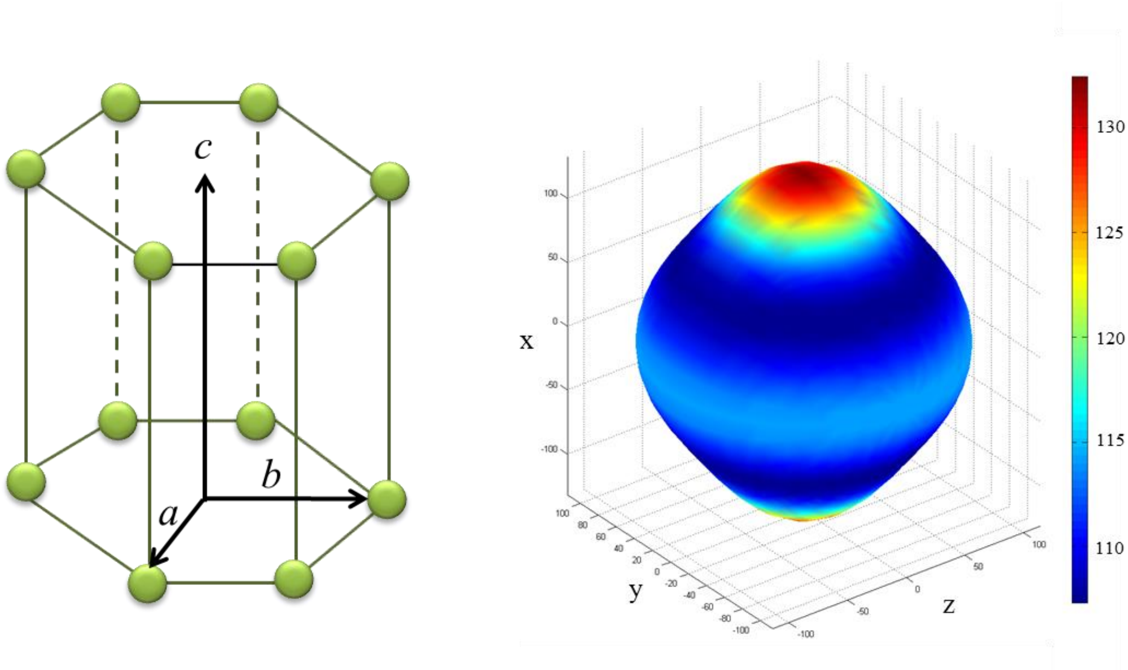

(a) (b)

Fig. 2.4 (a) Illustration of the hexagonal lattice cell and (b) 3D representation of the directional dependency of the elastic modulus of HAp crystal (GPa)

2.2.2.6. Brief discussion

Several factors may cause the variation of the measured elastic properties of human dental tissues, e.g. changes in the testing environment, e.g. temperature, storage conditions, e.g. in deionized water, calcium chloride buffered saline solution, etc., caries, etc. Apart from the elastic constants, fracture properties and inelastic behaviour are also important aspects that affect the performance of human dental tissues. The present thesis focuses on the elastic constants of dentine, enamel, and the DEJ. Published work reviewed in this section serves to provide a firm basis for the experimental approaches and results presented in Chapters 4-8.

The majority of research in this area has concentrated on the mechanical properties of dentine and enamel at the macro- and micro-scale. However, few studies have focused on the nano-scale, where the mechanical alterations can be considered to be a function of the shape and orientation of the mineral phase. During elastic loading, stresses are expected to be transferred to the much stiffer HAp crystallites from the surrounding collagen matrix [76]. To investigate this, it is required to use techniques that allow *in situ* quantification of the mechanical response of nano-scale HAp phases to external loading as illustrated in Chapters 4-6.

2.2.2.7. Mechanical analytical model

The complex hierarchical structures of dentine and enamel have elicited a number of attempts to model them. Here, several widely accepted models are summarized as an introduction to the work presented in this thesis.

Various analytical models of composites have been proposed to describe the interaction of different phases and model the elastic properties of hard tissues. As the first stage it is logical to consider the traditional composite models, notably such as the Voigt (Eq. 2.3) and Reuss (Eq. 2.4) bounds described below (*f* indicates the volume fraction and *E* represents the elastic modulus for each phase), as well as the Jones [77], Bar-on and Wagner (BW) models (staggered microstructural model) [78] and the shear-lag model [79]. Without considering the microstructure of the biological composite, significant overestimation or underestimation of the elastic modulus represent the key shortcoming of these mechanical models.

$$E_{com}(Voigt) = f_{org}E_{org} + f_{HAp}E_{HAp} + f_{water}E_{water} \qquad \text{(Eq. 2.3)}$$

$$E_{com}(Reuss) = \frac{E_{org}E_{HAp}E_{water}}{f_{org}E_{HAp}E_{water} + f_{HAp}E_{org}E_{water} + f_{water}E_{org}E_{HAp}} \qquad \text{(Eq. 2.4)}$$

Another widely accepted model is the Eshelby inclusion model [80, 81] that can be used to simulate hierarchical structures. It has the strong physical significance in that it captures the detailed interaction between two different phases (represented by the inhomogeneous inclusion and the surrounding matrix). This compares favourably with the simple models, such as Voigt and Reuss. The interface in the Eshelby model is assumed to be fully coherent, in line with the prevailing view in the literature. Recently, the Eshelby model has been applied in dental research in conjunction with nanoindentation and finite element model data [82-85] to explain and predict the elastic response of dentine at the microscopic level. However, the models used in these simulations had serious limitations, e.g. no consideration was given to the nano-scale structure, leading to discrepancies between the predictions and experimental results [76]. Therefore, a modelling approach needs to be established and applied to the evaluation of the mechanical response of hierarchical structured human dentine and enamel tissues by capturing the relationship between the nano-scale structure and macroscopic loading. This is the key challenge addressed by the new two-level Eshelby model that sought deeper understanding of the relationship between the nano-scale structure and mechanical behaviour.

For the correct evaluation of the apparent modulus of HAp crystallites, i.e. the coefficient of proportionality between the external macroscopic stress and the lattice strain in the HAp nano-crystallites, the composite effect cannot be ignored. The particular influence of the woven structure is the so-called self-locking effect [86]. It is noted here that it is expected to be effective only under tensile loading and is significant particularly in connection with the fracture resistance of enamel. However, since elastic deformation under compressive loading is the focus of the present study, multi-scale Eshelby model is appropriate in this case.

2.2.3. The heat-induced alteration of skeletal hard tissue

2.2.3.1. Background of the thermal behaviour

Advanced high-energy techniques are finding increasing use in modern dentistry. In the early 1970s, Kantola et al. [87] showed that laser treatment of dental tissues can be used to increase the mineral content and crystallinity of dentine by preferential removal of the inherent water and protein. With the advent of a variety of new laser systems spanning by a range of energy densities and pulse durations, clinical treatments such as laser-assisted caries protection were proposed and developed (Figure 2.5). During short pulse laser treatment, the energy absorbed by the illuminated surface of dentine or enamel leads to a local heating to temperatures between several hundred ℃ to over 1000 ℃. This effect is confined to depths of less than 10 μm (at the fluence of 2 J/cm^2). Heat conduction into the body of the tooth means that the increase in its overall temperature does not exceed 0.5 ℃, so that no painful sensation is produced, and the alteration of dental tissue remains highly localised. The treatment has been shown to prevent further progression of caries, whilst leaving the remaining tissues intact [88, 89]. Improved caries prevention is surmised to be associated with increased mineralisation and sintering of HAp crystallites that leads to the sealing of dentinal tubules. However, the confirmation of this by direct microscopic characterization of the very thin surface layer affected by laser therapies is an extremely challenging experimental task.

Any change in the local environment of HAp crystallites, e.g. through laser illumination or direct heating, is bound to affect the mineral ultrastructure. In the context of archaeological and forensic investigations, the macroscopic alterations (e.g. surface colour) can be used to deduce an approximate temperature range, while the investigation of the micro- and ultrastructural alterations of skeletal hard tissues exposed to high temperatures turned out to be an excellent means of obtaining reliable estimates of the temperatures of exposure [90-92]. Burned human remains as a result of ritual cremations, natural disasters, accidents or crime are frequently recovered from archaeological sites and forensic settings (Figure 2.5) [91, 93, 94]. Careful analysis of the remains sheds light on the attendant circumstances, e.g. the presence and nature of combustible agent used, etc. Dental tissues, being the most highly mineralised part of the human body, can withstand longer thermal exposure and survive higher temperatures, thus offering the possibility of extending the range of applicability of this technique [95].

The above considerations provide a strong motivation for a detailed study into the effect of thermal exposure on the nano-structure (HAp crystallites and protein bonding) of human dental tissue as well as the role played by the organic phase. The investigation of the micro- and ultrastructural alterations of burned skeletal hard tissues exposed to high temperatures has proven to be crucial for archaeological and forensic sciences to obtain reliable estimations of the temperature to which they were exposed [94, 96-98]. Although human remains including dental tissues are frequently recovered from archaeological sites, interpretation in terms of thermal exposure history is hardly possible due to the very limited data available on effect of heat on the compositional and structural alterations [90, 99].


Dental surgery

Forensic & Archaeological study

Fig. 2.5 Background of the heat-induced alteration of dental tissues in dental surgery, forensic and archaeology

2.2.3.2. Multi-scale thermal behaviour

In terms of the study of heat-induced changes that occur in the human dental tissues, the only data available concerns the changes occur at the level of entire tooth. The ultrastructural differences between dentine and enamel have so far not been taken into account [90], let alone the spatial variation of these changes within individual teeth. In general, skeletal hard tissues undergo macroscopic and microscopic alterations [91, 100], and a variety of factors during cremation determine the extent of those alterations, such as duration of exposure, temperature profile and oxygen availability [101]. The investigation of the micro- and ultrastructural alterations of skeletal hard tissue exposed to high temperatures has proven to be crucial to get a reliable estimation of the maximum exposure temperature [90, 91, 102].

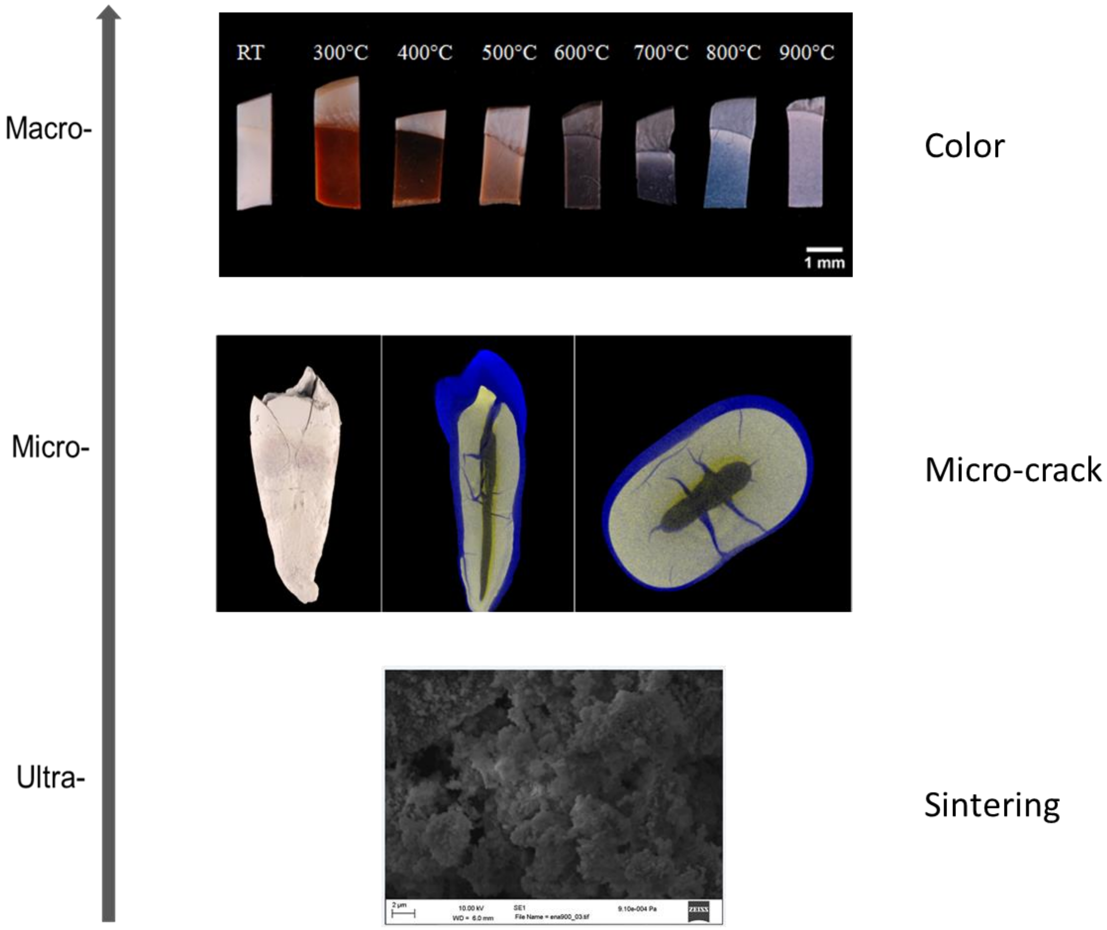

Fig. 2.6 A multi-scale schematic view of the heat-induced alterations of dental tissue. At the macro-scale, the colour may change depending on the temperatures of exposure. At the micro-scale, the micro-crack initiation can be observed before it is visible macroscopically. Ultrastructural sintering of nano-crystallites occurs at very high temperatures.

The macroscopic level alterations (e.g. colour changes shown in Figure 2.6) can be used to deduce the approximate exposure temperature range. A shift from the natural tooth colour to light yellow, brown, grayish blue, white and finally pink is often reported in literature [103-107]. Specific research on heat-induced changes of teeth colour is rare [108-111], although general observation is that teeth react to thermal exposure in a manner that is quite similar to that of bones.

Thermal stressing is also likely to result in microscopic cracking of human dental tissues. The volume density of cracks can provide a rough indication of the temperature of exposure.

Ultrastructural changes of burned bones and teeth of human and animal were often examined using classical histology techniques [106, 110, 112, 113]. The alteration may be quantified in terms of the mean changes in HAp crystalline size and morphology. Based on the experience of bone analysis, there is a general trend towards the formation of HAp crystallites with higher levels of perfection at high temperatures, as well as the emergence of different mineral phases. Apart from this, increases in the thickness and the alterations of crystalline morphology with heat that are observed may be associated with sintering processes (Figure 2.6) leading to the emergence of HAp crystallites of particular shape and size following the heating regimens.

2.2.3.3. Multiple techniques for the characterization of thermal behaviour

Multiple techniques have been used to study the microstructural and ultrastructural heat-induced alterations of skeletal hard tissues (Figure 2.7). Most widely applied techniques are based on the absorption spectra for infrared radiation (Fourier transform infrared spectroscopy, FTIR), or lab-based X-ray powder diffraction (XRD) [90, 94, 114-116]. However, there have been ongoing debates on the general limitations and validity of the results quantified by FTIR [90, 114, 115]. WAXS (XRD) has been proved capable of showing the distinct differences of response between HAp crystallites in animal and human bones upon heating [90, 115, 117].

However, in most cases the preparation of samples for lab-based XRD usually involves the mechanical destruction of a sample (grinding) and subsequent examination that produces volume-weighted average results. Local fine-scale changes of ultrastructure [118] are not revealed or taken into account, although non-uniform response to the thermal treatment may be expected due to the ultrastructural differences between dentine and enamel [119].

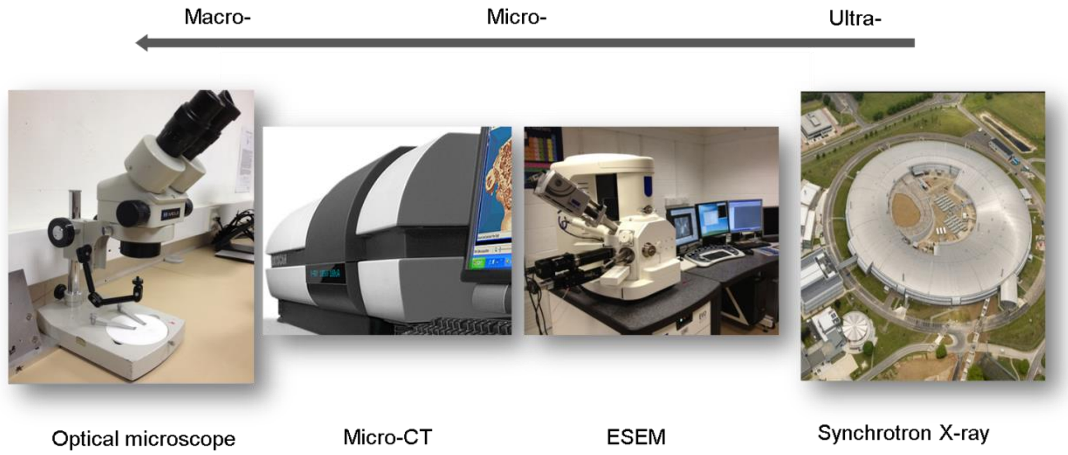

Fig. 2.7 Multiple techniques for the study of heat-induced alteration of skeletal hard tissues, ranging from optical microscopy, Micro-CT, ESEM and Synchrotron X-ray facilities.

Compared with conventional high-magnification microscopic methods, e.g. SEM observation of heat-induced changes of ultrastructure of bone and teeth [94], SAXS allows a far higher throughput of samples due to shorter data collection time. The non-destructive identification of local structural alterations at the nano-scale is the remarkable advantage of SAXS and of the combined SAXS/WAXS characterization methods. This is particularly crucial when the destruction of samples is not acceptable, e.g. in the case of archaeological excavation material or evidence from forensic cases. However, the systematic investigation of thermally treated mineralized tissues using SAXS technique has remained lacking until very recently. It is worth noting that lab-based SAXS has been successfully used to characterize the heat-induced structural changes in *human bone* for forensic and archaeological purposes [118, 120], but, once again, the corresponding SAXS data analysis on *human dental tissue* remains absent. The ultrastructural changes of human bone and teeth described in the previously published research reports showed that crystallites derived from bone and dental tissues react differently to heat, indicating that these tissues have to be investigated separately and specifically when precise temperature estimation is desired [94].

Chapter 3

Methodology

3.1. Synchrotron X-ray diffraction techniques

3.1.1. Particle beams used for materials characterization

Diffraction techniques can be classified depending on different kinds of radiation employed: lab-based X-ray beams, synchrotron X-ray beams, neutron beams, infra-red beams, visible light, etc. The characteristics of these beams and their experimental implementation differ in various aspects. One particular special source of bright radiation that has become widely used since the last decades of the 20th century is the synchrotron [121]. Discussion below focuses on this type of source, as lab-based X-ray beams and neutron beams lie beyond the scope of the current study. A brief overview is given of the applications of the synchrotron X-ray technique.

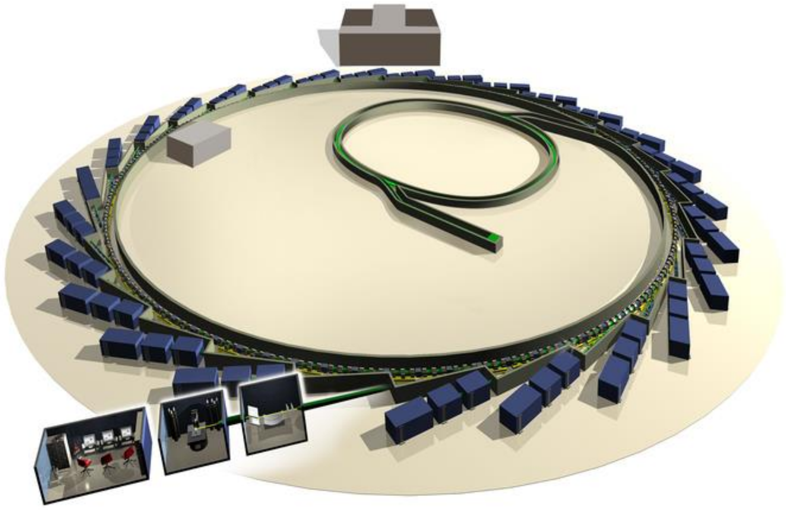

Fig. 3.1. Schematic diagram of a synchrotron facility [122]

In a synchrotron process, electrons produced by an electron gun are accelerated in a vacuum by an electric field to a large energy of a few GeV. The electrons are subsequently injected into a storage ring, and their circulation is maintained almost at the speed of light. High magnetic fields force electrons to deflect and continue to circulate following a polygonal closed path. The concomitant energy loss (undesired from the viewpoint of accelerator operation) results in the emission of X-rays of a wide spectrum. Additional acceleration is applied to the electrons so that the energy of the stored beam is kept constant. The X-rays emitted at bending magnets or insertion devices are guided through individual beamline front ends (seen as branch-outs of the storage ring in the schematic diagram of the synchrotron facility shown in Figure 3.1).

Synchrotron X-rays are an ideal tool for the investigation of material properties from the macro- to the nano-scale. Compared to the traditional techniques such as optical microscopy, SEM, AFM and other methods that are limited to the sample surface, or TEM measurements limited to very thin sections, X-ray measurements have the ability to analyse the behaviour of material in the bulk. The major common methods employed at synchrotron facilities are X-ray imaging (including tomography and coherent diffraction imaging), X-ray scattering (including diffraction), X-ray spectroscopy, and combined techniques, e.g. X-ray spectro-tomography or diffraction strain tomography. [123]. The content below focuses principally on two diffraction techniques: small angle X-ray scattering (SAXS) and wide angle X-ray scattering (WAXS).

3.1.2. SAXS/WAXS techniques

As illustrated in Figure 3.2, the incident beam with the wave vector $\overrightarrow{k_0}$ is transmitted through the sample and scattered. The scattered beam with the wave vector is $\vec{k}$ that is deflected from $\overrightarrow{k_0}$ by the scattering angle 2θ. The scattering vector $\vec{q}$ is defined as

$$\vec{q} = \vec{k} - \overrightarrow{k_0} \qquad \text{(Eq.3.1)}$$

i.e. $\vec{q}$ is the difference of the wave vector of the scattered beam and the incident beam. Thus the length $|\vec{q}|$ is:

$$|\vec{q}| = \frac{4\pi}{\lambda}\sin\theta \qquad \text{(Eq.3.2)}$$

where λ is the radiation wavelength, and 2θ is the scattering angle [124].

In accordance with Bragg's law (to be introduced in more detail below), $|\vec{q}|$ can be expressed as $|\vec{q}| = 2\pi/d$. Here d denotes the real space dimension (length) that governs the X-ray scattering. As a consequence, larger real space dimensions correspond to features observed at smaller scattering angles, and vice versa. Experimentally, the difference between the two scattering modes is only expressed in terms of the angle at which the scattered signal is recorded. In practice, this usually requires a change in the distance between the sample and the detector with WAXS demanding larger scattering angle and hence shorter sample-detector distances (see Table 3.1).

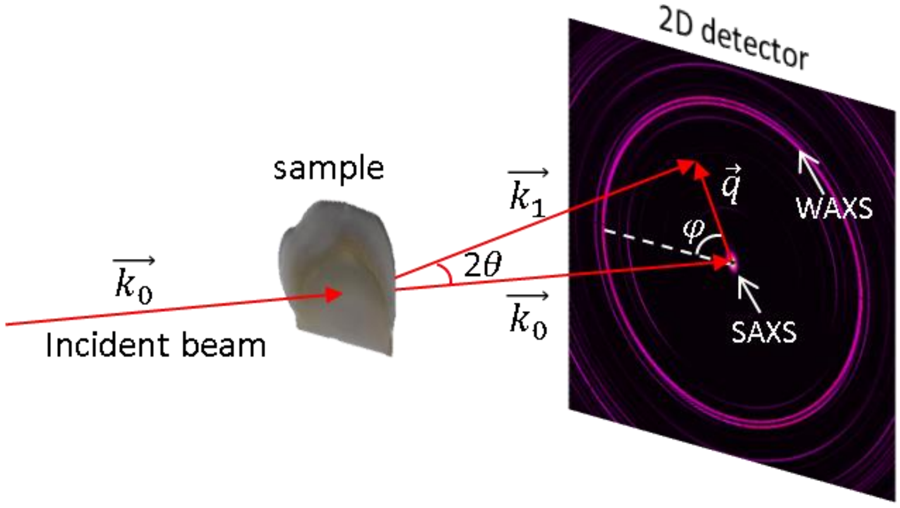

Fig. 3.2 Schematic illustration of the elastic X-ray scattering setup.

Tab. 3.1 SAXS/WAXS techniques

Techniques	**Scattering vector**	**Dimension in real space**	**Approximate characterization region**
Small angle X-ray scattering	small q	large d	1-1000 nm
Wide angle X- ray scattering	large q	small d	0.1 A-1 nm

3.1.2.1. Small angle X-ray scattering (SAXS)

Small-angle scattering (SAS) occurs in the angular range of a few degrees around the original beam. It is a coherent scattering phenomenon in which the scattering effect is due to the fluctuation of electron density with X-rays (or neutron scattering length with neutron) at the length scale of (several nm to several hundred nm) within materials [124, 125].

In terms of different types of incident radiation, small angle scattering can be divided into small angle X-ray scattering (SAXS), small angle neutron scattering (SANS), small angle lighting scattering (SALS), etc. Each one has its specific characteristics. This thesis focuses on the discussion of SAXS. When a highly parallel incident X-ray beam (typically of wavelength of ~1Å) irradiates the sample, small angle scattering occurs within the angular range of 0-5^o around the incident X-ray beam, with the intensity decreasing with the scattering angle [126].

Diffuse scattering is dominant in the small angle region, although both diffuse scattering and discrete diffraction peaks may appear. The discrete diffraction peaks observed in the small angle regime are associated with the presence of distinct underlying structural order (periodicity), as e.g. in collagen fibres [127]. Diffuse elastic scattering of the primary beam is due to the coherent scattering from electrons, i.e. mutual interferences occur among electromagnetic waves scattered from different positions within the gauge volume. The principle can be explained by considering the X-ray beam impinging on the samples containing nano-particles, i.e. electron density fluctuations on the nanometre scale. The measured scattering intensity $I(q)$ is related to the squared modulus of the Fourier transform of the electron density distribution $\rho(r)$ as follows:

$$I(q) = K\frac{d\Sigma}{d\Omega}(q) = \frac{K}{V}\left|\int_V \rho(r)\exp(iqr)d^3r\right|^2 \qquad \text{(Eq.3.3)}$$

where V is the sample volume, K is an instrumental constant, and $\frac{d\Sigma}{d\Omega}(q)$ corresponds to the macroscopic differential scattering cross-section of the sample. In the case of two phases A and B with constant compositions, the scattered intensity can be written as:

$$I(q) = \frac{K}{V}(\rho_A - \rho_B)^2\left|\int_V \exp(iqr)d^3r\right|^2 \qquad \text{(Eq.3.4)}$$

Thus the scattering intensity is proportional to the squared difference of the two densities, $(\rho_A - \rho_B)^2$. Nano-voids correspond to another condition that produces scattering in the SAXS regime. Since electron density within voids is zero ($\rho_B = 0$), sharp difference in electron density exists between the voids and the material of density $\rho_A$making small angle scattering possible with scattered intensity proportional to ${\rho_A}^2$ (let particles have electron density ρ and the surrounding media densityρ_0). In more general cases, even in the absence of abrupt density jumps, electron density fluctuations also lead to the phenomenon of SAXS [128].

In order to visualize how SAXS could be used to interpret the structural arrangement in real space, a schematic diagram is shown in Figure 3.3. In SAXS, the width of the scattering signal in the reciprocal space is inversely proportional to the dimension of the scattering object in real space, as dictated by the Fourier transform. If the scattering object in a 1-D case has width $2a$ (Figure 3.3 a), the scattering vector $|\vec{q}| \propto \pi/a$ and the transformed scattered image is shown in Figure 3.3 b. This relationship can be generalised to 2-D cases. In the case of real human dentine and enamel, the electron density distribution of the crystalline structure or the scattering object is expressed by the grey scale density in real space microscopy. An example of AFM image is illustrated in Figure 3.3 c. As an example of more detailed consideration, HAp crystallites in dentine are more isotropic but in the enamel they have a preferred orientation. This is reflected in the corresponding simulated SAXS pattern (derived as the square of Fourier transform of the real space microscopic image) shown in Figure 3.3 d. It is worth noting the degree of similarity between the simulated pattern and the data collected in the SAXS experiment (Figure 3.7). The generated patterns contain statistical information about the internal particle arrangement within the material studied.

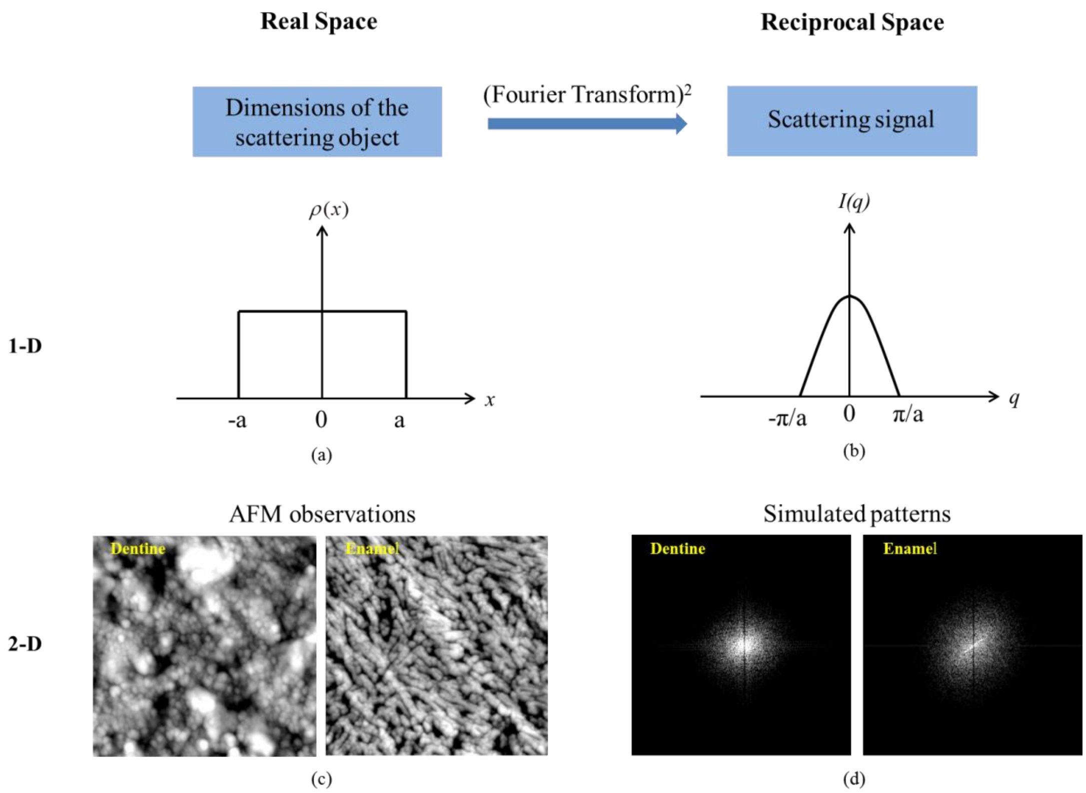

Fig. 3.3 Classical diagram of SAXS pattern formation based on Fourier transform of the electron density fluctuation distribution. (a) A one-dimensional example of a scattering object with width 2a; (b) The Fourier transformed image of (a); (c) The real two-dimensional case of nanoscale structure in dentine and enamel; (d) The corresponding Fourier transform of the structures shown in (c)

3.1.2.2. Wide angle X-ray scattering (WAXS)

WAXS is an X-ray diffraction technique allowing rapid non-destructive analysis of the crystal lattice structure and strain without extensive sample preparation. It is widely employed to determine the material structure. In terms of the scattering process and setup, the technique has some commonalities with SAXS. However, unlike SAXS, WAXS patterns are collected at larger angles, thus shorter detector-to-sample distance is required; and for polycrystals the patterns consist of sharp peaks (or arcs, if 2-D detectors are used). The analysis of peaks scattered by large angles is usually performed with the help of Bragg’s law (see Figure 3.4). The analysis of wavelengths and scattering angles demonstrates that Bragg peaks arise from sub-nanometre-sized structures [129]. Bragg's Law is written as:

$$n\lambda = 2d_0^{hkl}\sin\theta \qquad \text{(Eq. 3.5)}$$

where λ is the wavelength; d_0^{hkl} is the strain-free interplanar spacing between planes with Miller indices (*hkl*), θ is one half of the scattering angle, and n is the order of the reflection. The classic diagrammatic illustration of Bragg diffraction analysis is shown in Figure 3.4. Bragg's law establishes the relationship between the spacing of atomic planes in the crystal and the scattering angle at which these planes produce intense reflections. The characteristics of diffraction peak (position, amplitude, and width) are closely related to the crystal structure. Each peak corresponds to a certain family of lattice planes within a certain crystallographic phase. Therefore, diffraction pattern analysis can be used to identify and quantify crystallographic phases and crystal structure parameters.

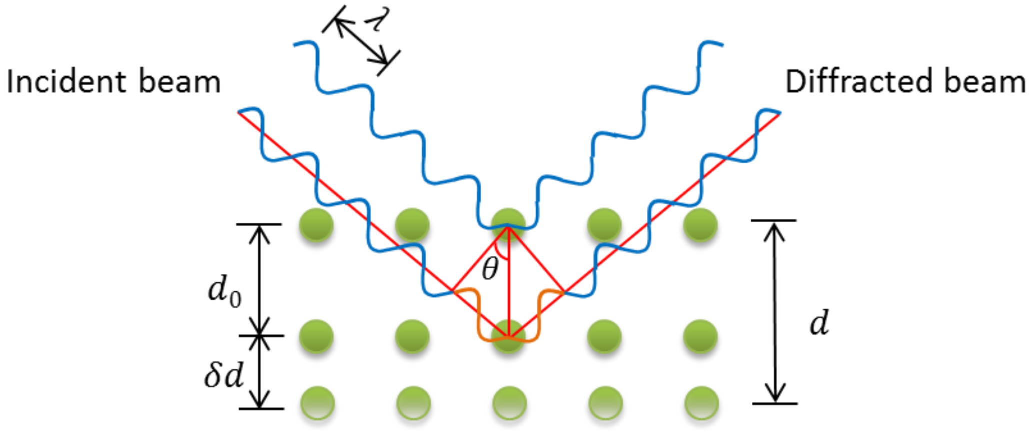

Fig. 3.4 Classical diagram of Bragg diffraction based on the atom plane model. d_0 is the strain-free *d*-spacing, while *d* is the *d*-spacing after the deformation. δd is the difference between d_0 and *d*

3.1.2.3. Combined SAXS/WAXS analysis

SAXS has a broad range of application, and can be used to analyse many kinds of material samples. The scattering signal contains information [128, 130] relating to the long-periodic structure (i.e. at the nanometre length scale, as opposed to Angstrom scale for crystal lattice) of electron density fluctuation or discontinuities due to particles or voids. Such structural information is sometimes referred to as “large-scale”, compared with the crystal lattice structure information obtained from WAXS. SAXS patterns can be interpreted to extract micro- and nano-structural information about the sample, such as the number density of scattering centres, their average size and size distribution, thickness of interface layers, the fractal dimension, the surface area per unit volume, the mass of scattering bodies, their orientation and aspect ratio, etc. [125]. Figure 3.5 provides a comparison of the resolution range of SAXS/WAXS with other techniques.

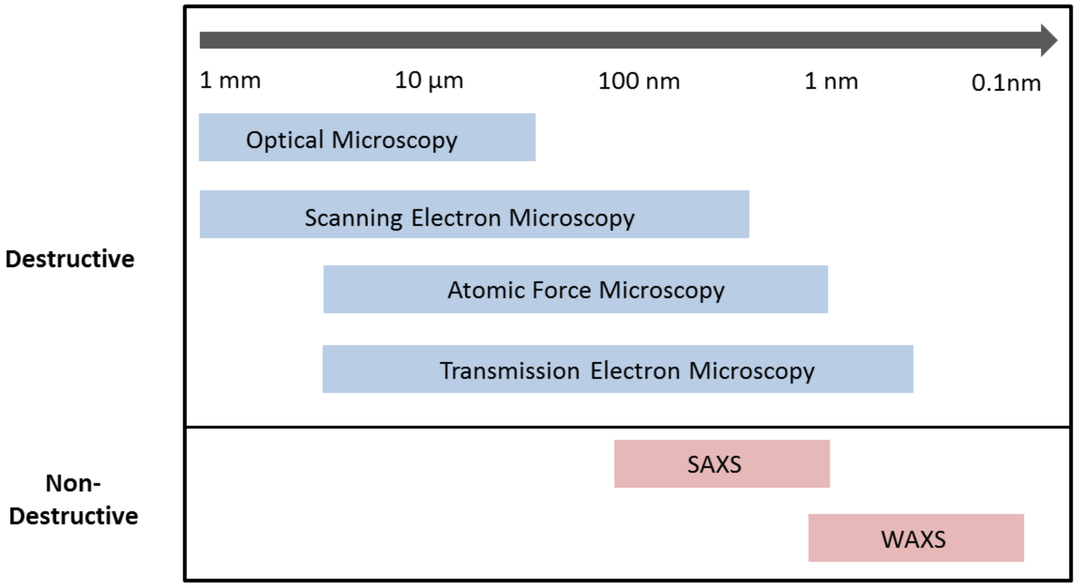

Fig. 3.5 Resolution range coverage of SAXS and WAXS in comparison with other techniques.

The combined SAXS/WAXS methods typically use monochromatic X-rays, i.e. are restricted to beams of narrow band width ($\Delta E / E \sim 10^{-2} - 10^{-4}$, E is the energy) around a single wavelength [131]. Performing SAXS and WAXS simultaneously opens up a new realm of possible diffraction experiments. SAXS provides information on the mineral nano-structure, i.e. the size and distribution of crystalline particles. WAXS allows the determination of crystallographic features for different phases, as well as crystal lattice preferred orientation (texture). WAXS provides reciprocal space information about the sub-nm structure of the atomic lattice, including orientation, size and shape of the unit cell, defect structure (e.g. dislocations and voids), etc. SAXS-derived information covers the range 1-100nm, also via the interpretation of reciprocal space data. Finally, with the high brilliance of synchrotrons providing useful flux in beam spot sizes on the ~100 nm level and below, line scanning and mapping leads to real space characterization down to these resolutions. This provides unprecedented multi-scaling coverage needed for all-round characterization of hierarchical structures.

3.1.3. SAXS/WAXS techniques for biological hard tissues

Due to the hierarchical structure of biological hard tissues (e.g. bone and dental tissues), analysing this material requires appropriate methods to derive information on different length scales at the same time. SAXS/WAXS is a powerful approach for multi-scale characterization of dental tissues spanning the range of length scales from nanometers (SAXS) down to the sub-nanometer crystal structure obtainable from the WAXS pattern. In combination with scanning of sub-micron focused beams this provides continuous length scale coverage from macroscopic through microscopic and down to ultra-structural (sub-nm) length scales.

SAXS/WAXS has been applied only recently to the study of mineralized biological composites, such as bones and bovine teeth [76, 132-134]. Deymier-Black et al. [76] determined the longitudinal apparent modulus of hydroxyapatite (HAp) in bovine dentine using synchrotron based WAXS, while strain distribution across the DEJ in bovine teeth was investigated by Almer and Stock [132]. However, very few studies devoted to enamel have been published [135], and early studies did not take into account the nanoparticle shape, size and orientation distribution [136]. Therefore, a deep understanding of the relationship between the nano-scale structure and the macroscopic mechanical behaviour of enamel is still lacking. In addition, all these studies were carried out on non-human samples, in which different particularities of the tubule structure and morphology are expected to result in differences in the mechanical properties [137, 138].

The spatial distribution of basic crystallographic parameters of HAp phase within mineralized tissues is determined by WAXS [47, 139]. Texture (preferred orientation) variation mapping can be accomplished by tracking the (002) plane of HAp crystallites, since the (002) reflection gives the information on the orientation of the hexagonal *c*-axis, which in turn allows the determination of the fibril orientation as they are orientated parallel to each other [28, 29]. Furthermore, WAXS has already been used to quantify the internal strains of the mineralised biological composites such as bone [133, 134, 140, 141] and teeth [76, 132, 142] on non-human samples.

In a two-phase system based on mineralized tissue, the difference in the average electron density between the mineral HAp crystalline particles and the surrounding protein matrix leads to the X-ray scattering in the typical range of scattering vector q for the nano-scale information to be derived from SAXS on the mean nanocrystal size, predominant crystal orientation, and typical shape of mineral crystallites in bone and teeth [143]. Although the method is indirect (e.g. in comparison with the real space imaging, i.e. microscopy), it provides statistical quantitative information about the average values (crystal size, shape, orientation and arrangement) of the parameters identified as critical for the mechanical strength and stability of mineralized tissue [86].

3.1.4. X-ray scattering data interpretation

3.1.4.1. WAXS

Quantitative interpretation of WAXS patterns provides insight into the lattice strain, preferred orientation and the particle length of HAp crystallites. The data analysis procedure involves converting the 2-D diffraction images (Figure 3.6 a) into 1-D intensity profiles and pre-processing e.g. using Fit2D software package [144]. Figure 3.6 b&c illustrate the azimuthal integration given by $\hat{I}(q) = \int I(q,\varphi)\,\mathrm{d}\varphi$, and radial integration given by $\tilde{I}(\varphi) = \int I(q,\varphi)\,\mathrm{d}q$.

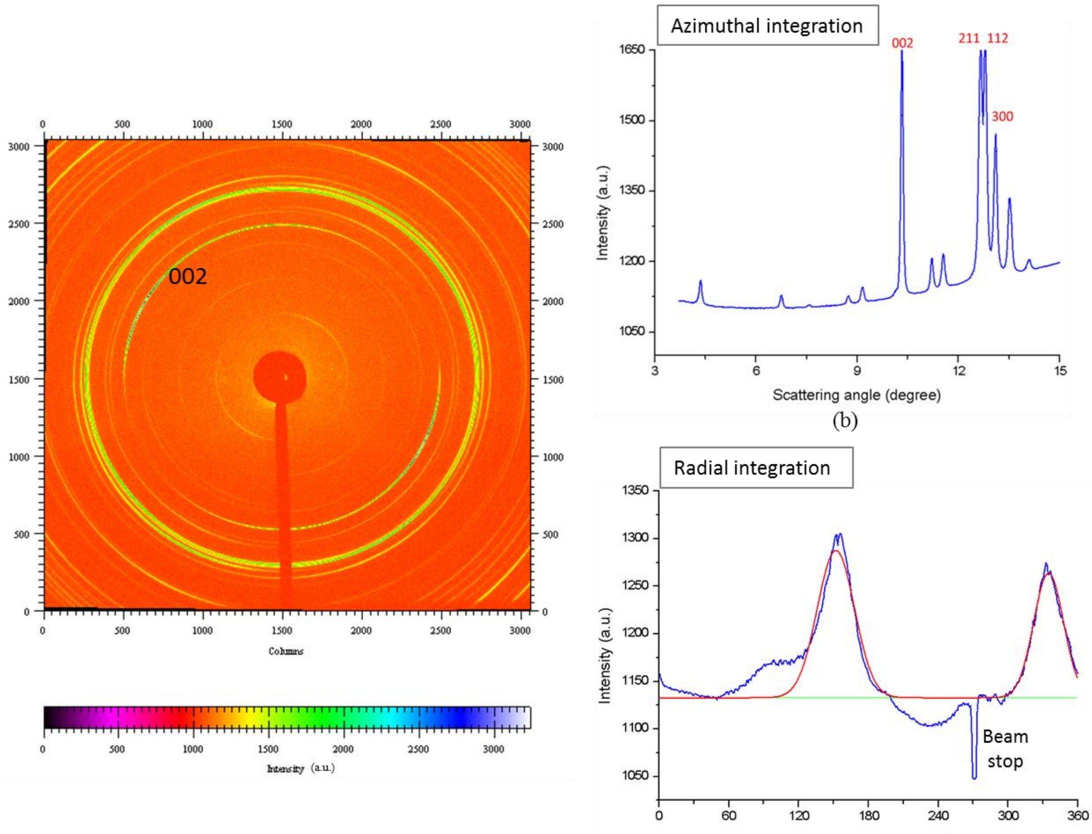

(a) (b) (c)

Fig. 3.6 WAXS data interpretation from (a) 2-D pattern to 1-D profile by (b) azimuthal and (c) radial integration (Gaussian fit indicated in red, background shown in green)

a). Lattice strain

WAXS data can be interpreted in terms of the shift of the diffraction peak obtained from a cluster of HAp crystallites, so that the average micro-strain (lattice strain) in the crystals can be deduced [145-147]. The lattice strain might be produced by the substitution of ions, .e.g. carbonate apatite, fluoride apatite. Changes in the *d*-spacing between the lattice planes in the mineral HAp phase were used to determine the elastic lattice strain [148]. The apparent elastic lattice strain ε was computed from the definition:

$$\varepsilon = \frac{d_{002} - d_{002}^{0}}{d_{002}^{0}} \qquad \text{(Eq. 3.6)}$$

where according to Figure 3.4, (*hkl*) is (002) in this case and d_{002} is the *d*-spacing after deformation and d_{002}^{0} is the reference strain-free value of the initial *d*-spacing.

To determine the strain from the mineral HAp phase, 2-D diffraction images were pre-processed into 1-D intensity plot using Fit2D [144] by integrating azimuthally. In order to determine the specific peaks and the strain components along different directions, “caking” is applied to each pattern, with a step of 10° -20° in the angular range of interest (0°-360°). “Caking” is a term that refers to the following procedure. A sector is selected in the radial-azimuthal coordinates of each pattern. The intensity data contained in this sector is then reduced to 1-D radial line profiles by averaging (“binning”) the intensity across the angular width of the sector within each pre-defined range (“bin”) of radial coordinates. The determination of the 1-D peak centre position in each “cake slice” (sector) allows finding the normal strain component along the centre direction of this “cake slice”. The result is taken to represent the strain distribution in the corresponding orientation. Subsequently, the 1-D intensity plot of each “cake slice” (covering 10° -20°) can be obtained by appropriately weighted integration with respect to the azimuthal angle of the converted 2-D images. Afterwards, the 1-D profiles of each individual peak can be fitted with e.g. Gaussian curves to determine the peak centre position after the subtraction of the fitted background. To calculate the HAp lattice strain, the WAXS pattern of the unloaded condition is used as a nominally strain-free reference point. The validity of this assumption is discussed in each specific case.

b). Preferred orientation

In addition, the preferred orientation angle can also be determined by azimuthal-radial “caking” of the peak of interest, and fitting using appropriate function(s). The azimuthal centre position of the pronounced peaks in the $I_{WAXS}(\varphi) \sim \varphi_{\_WAXS}$ plot are then used to define the preferred orientation direction [139].

c). Particle length

The width of the peaks in the 1-D radial diffraction pattern is related to the average size of the mineral HAp crystallites. It is important to note that peak broadening is caused by the finite sub-micron size of mineral particles, the inherent instrumental broadening and also non-uniform microstrain. The non-uniform microstrain contributions to the peak broadening could be excluded, according to the calculation reported for dental tissues [[149]. Scherrer first observed that small crystallite size could give rise to line broadening. The evaluation is carried out based on the *Scherrer Equation*, widely used in the analysis of heat-treated bones and teeth [99, 150].

$$L = \frac{k\lambda}{B\cos\theta} \qquad \text{(Eq. 3.7)}$$

where k is a constant close to unity that varies somewhat depending on the crystallite shape, while λ and θ have their usual meanings in *Bragg's law*. L is the particle size in the direction defined by the scattering vector, and B is the full-width at half maximum (FWHM) of (002) peaks selected for analysis. Due to the alignment of the *c*-axis in HAp crystallites within enamel and dentine, L reveals a parameter that is referred to as the length (i.e. the longest dimension) of HAp crystallites. By monitoring the variation of FWHM during different heat treatment procedures, the variation of the length of HAp crystallites can be derived.

3.1.4.2. SAXS

Quantitative interpretation of SAXS patterns provides insight into the mean thickness (a conventional parameter used to describe the particle size) and degree of alignment (i.e. the percentage of the aligned particles) of HAp crystallites. 2-D diffraction images (Figure 3.7 a) need to be initially converted into 1-D intensity profiles (Figure 3.7 b and c) and pre-processed using e.g. Fit2D software package [144].

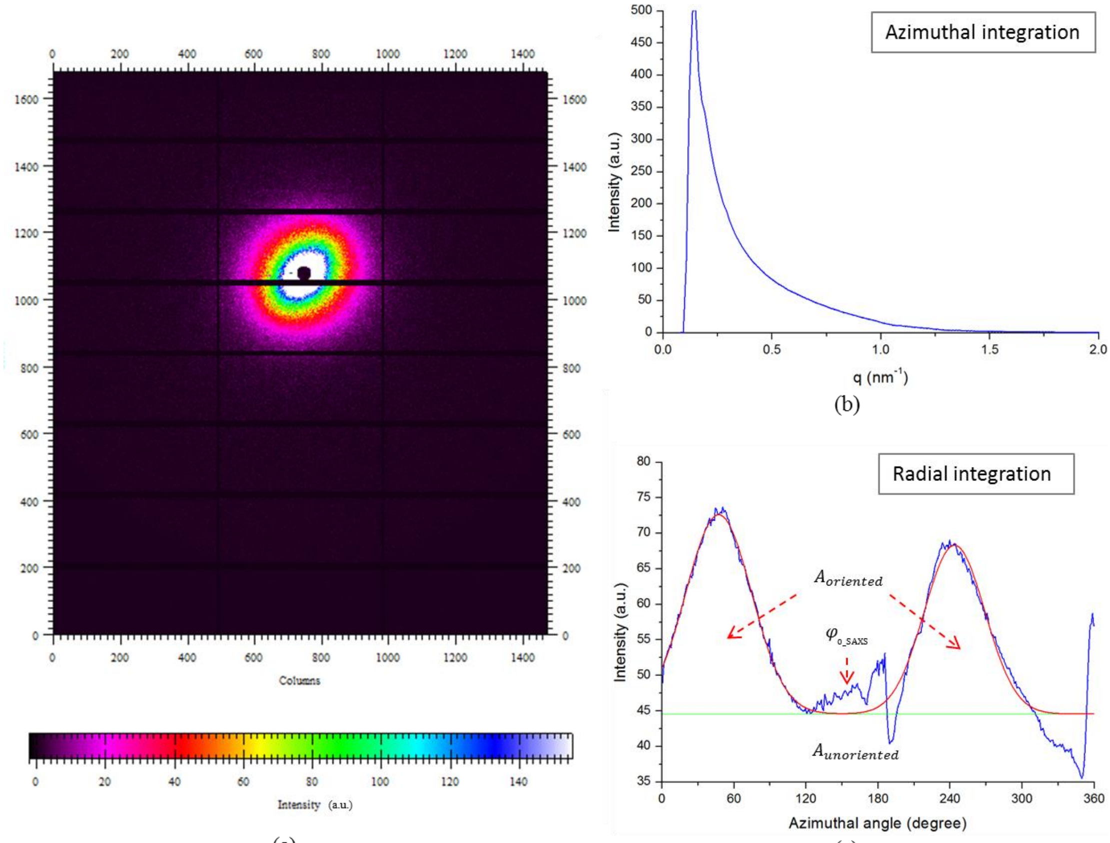

(a)

(b)

(c)

Fig. 3.7 SAXS data interpretation in the form of (a) 2-D pattern converted to 1-D profiles by (b) azimuthal and (c) radial integration (Gaussian fit indicated in red, scattering intensity from unoriented particles shown in green). The predominant orientation φ_{0_SAXS} is the average position of the two peaks. The ratio $A_{oriented} / (A_{oriented} + A_{unoriented})$ gives the degree of alignment.

a). Mean thickness

In order to determine the mean crystal thickness, the scattering intensity $I(q,\varphi)$ can be integrated over the entire range of the azimuthal angle φ to obtain a function of $\hat{I}(q)$, where q represents the length of the scattering vector $\vec{q}$ on the detector in the following calculation. The crystalline mean thickness T is defined as the *Porod* chord length based on *Porod's law* valid in a two-phase system, which represents the total surface area of the particles per unit volume, i.e. the average thickness:

$$T = \frac{4}{\pi}\frac{Q}{P} \qquad \text{(Eq. 3.8)}$$

where P is the *Porod* constant given by

$$\hat{I}(q) = \frac{P}{q^4} + B \quad \text{(\textit{Porod's law} in the large } q \text{ range),} \qquad \text{(Eq. 3.9)}$$

where P and the constant background B can be determined from the so-called Porod-plot ($\hat{I}(q)\cdot q^4$ vs. q^4), and Q is the integrated area of the $\hat{I}(q)\cdot q^2$ vs. q plot. Porod's law is valid for a two-phase system with sharp interface and the scattering intensity of this system decreases with q^4. Note that the definition of T is used without any assumption of the particle shape. However, for specific cases of needle or platelet shape, T can be interpreted as an average measurement of the smallest dimension of crystallites. The actual mean crystalline thickness can be further calculated based on T and other factors like the volume fraction [151].

In detail, the length of the strongly scattering phase ($\overline{l_1}$) and the second phase ($\overline{l_2}$) in a two-phase system is defined as [124]

$$\bar{l}_1 = \frac{T}{(1-f_1)} \qquad \text{and} \qquad \bar{l}_2 = \frac{T}{f_1} \qquad \text{(Eq. 3.10)}$$

where f_1 is the volume fraction of the scattering phase. Eq. 3.10 indicates that T can be interpreted as an average measure of the thickness and is close to the smaller dimension of the two phases. $\bar{l}_1$ and $\bar{l}_2$ are not independent but are related to T with the volume fraction of the scattering object. Therefore, if f_1 is a constant, T can be used to characterize the average thickness of the scattering objects ($\bar{l}_1$). Otherwise, $\bar{l}_1$ or $\bar{l}_2$ will be used as the guideline values for the mean thickness of crystallites.

b). Orientation and the degree of alignment

In dentine, the degree of alignment (ρ) of HAp crystalline particles is used to measure the fraction of aligned particles. It should be noted that in the enamel, due to the dense distribution of crystals, it is the electron density change occurring in the gaps between crystalline particles that gives rise to the scattering signal [152]. It is also understood that the orientation of the gaps between rods roughly coincides with the orientation of the crystals within each rod [152]. Thus, the information from gap scattering can be used to deduce the orientation and degree of alignment (percentage of aligned particles) of HAp crystallites.

In order to quantify the orientation and degree of alignment, the 2-D SAXS patterns can be processed by integrating over the entire relevant range of the scattering vector q, resulting in a function $\tilde{I}_{SAXS}(\varphi)$ of the azimuthal angle $\varphi_{\_SAXS}$ (Figure 3.7 c) [153, 154]. The predominant orientation φ_{0_SAXS} of the mineral crystals is determined by the position of the two peaks in the plot of $\tilde{I}_{SAXS}(\varphi)$ (e.g. φ_{0_SAXS} in

Figure 3.7 c). If all the crystallites are oriented in the φ_{0_SAXS} direction parallel to their long dimension in the real space, q would be the smallest in the elliptical pattern of the SAXS in the reciprocal space. Thus the direction of the short axis of the elliptical pattern indicates the predominant orientation of the crystals. Further, the degree of alignment ρ with respect to the predominant orientation of HAp crystallites can be calculated by the ratio of the two areas under the curve of $I_{SAXS}(\varphi)$:

$$\rho = \frac{A_{oriented}}{A_{oriented} + A_{unoriented}} \qquad \text{(Eq. 3.11)}$$

where $A_{umoriented}$ is the area of the constant background level accounting for the scattering from unoriented particles, and $A_{oriented}$ corresponds to the total area below the curve of $I_{SAXS}(\varphi) \sim \varphi_{SAXS}$ left after subtracting $A_{umoriented}$. The value of ρ ranges from 0 to 1, with $\rho = 0$ indicating no predominant orientation within the plane of the section, while $\rho = 1$ indicates strongest alignment of the crystals [153, 154].

c). Scattering object analysis

The scattering contrast in SAXS arises mainly due to the fluctuation of electron density. The integral intensity of SAXS signal $\overline{I}$ is proportional to the square of the difference of electron density between the scattering object(s) and the background, as well as the volume fraction of the scattering object(s) [124]

$$I \propto \overline{\eta} = (\rho_1 - \rho_2)^2 \varphi_1 (1 - \varphi_1) \qquad \text{(Eq. 3.12)}$$

where $\overline{\eta}$ is the mean square fluctuation of electron density, ρ_1 and ρ_2 are the electron densities of the two scattering phases, and φ_1 is the volume fraction of the scattering object(s) as defined in Eq. 3.10. According to the Babinet principle [124], in terms of scattering a system with a relatively low volume fraction of particles is equivalent to a dense system filled with particles but having the same volume fraction and arrangement of voids (i.e. the low density phase). In the former system, the particles act as scattering objects, whereas in the latter it is the voids.

3.2. Multi-scale Eshelby model

3.2.1. Eshelby general theory [155]

A short overview of the Eshelby inclusion theory is given, leading to the derivation of the constitutive law for a non-dilute population of inhomogeneities (HAp crystallites) embedded in a finite organic matrix.

3.2.1.1. Dilute system

The general geometric structure for a dilute system is an ellipsoidal inclusion embedded in an infinite matrix, as illustrated in Figure 3.8. “Dilute” means that the volume fraction of the inclusion is so low that it can be neglected. Without any external stress, the internal stress equilibrium requires that

$$(1-f)\sigma_M + f\sigma_I = 0 \qquad \text{(Eq. 3.14)}$$

where f is the volume fraction of the inclusion, and σ_M and σ_I are the stresses in the matrix and inclusion respectively. For a dilute system, $f \to 0$ and it can be regarded as a composite under remote load, thus Eq. 3.14 is automatically satisfied.

The original Eshelby model determined the elastic field of the inclusion when there is a strain mismatch between the inclusion and the matrix, i.e. a uniform misfit or transformation strain, or the so-called eigenstrain ε^{t*} in the inclusion [156]. Eshelby model shows that the total strain in the inclusion ε^{i} is uniform and related to ε^{t*} by an Eshelby tensor S that depends only on the inclusion shape and isotropic Poisson's ratio of the matrix:

$$\varepsilon^{i} = S\varepsilon^{t*} \qquad \text{(Eq. 3.15)}$$

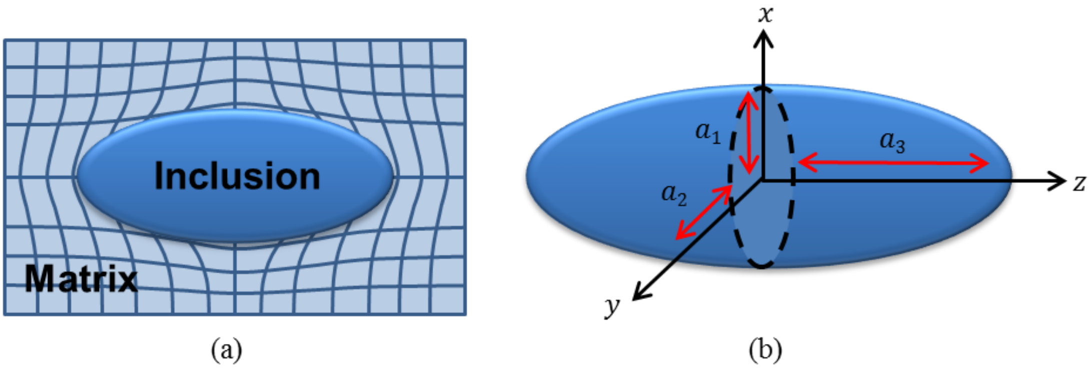

Fig. 3.8 Eshelby model of an ellipsoidal inclusion embedded in an infinite matrix. The ellipsoid has principal half-axes a_1, a_2 and a_3.

Consequently, Hooke's law can be used to calculate the inclusion stress σ_I in terms of the elastic strain and the stiffness tensor C_M (the same as the surrounding matrix) of the inclusion (I is the unity matrix)

$$\sigma_I = C_M(\varepsilon^{i} - \varepsilon^{t*}) = C_M(S - I)\varepsilon^{t*} \qquad \text{(Eq. 3.16)}$$

If an inhomogeneity with a different stiffness tensor C_I is present instead of a homogeneous inclusion, the elastic field of the inhomogeneity can be calculated using the equivalent inclusion method. This formulation regards the inhomogeneity as equivalent to an inclusion with an appropriate (*a priori* unknown) virtual misfit strain ε^{t} which needs to be determined. The function of the virtual misfit strain is to satisfy the equivalence where the elastic field of the inhomogeneity is identical to that of the equivalent inclusion (Eq. 3.17). In this way the classical Eshelby theory can be used to determine the elastic field of any kind of inhomogeneity. This formulation has greater generality and includes the case of HAp crystallites embedded in the isotropic protein matrix.

$$\sigma_I = C_I(\varepsilon^i - \varepsilon^{t*}) = C_M(\varepsilon^i - \varepsilon^t) = C_M(S - I)\varepsilon^t \qquad \text{(Eq. 3.17)}$$

If the material is subjected to an external stress σ^A that results in the overall composite strain ε^A, then the stress of the inhomogeneity can be modified based on Eq. 3.17

$$\sigma_I + \sigma^A = C_I(\varepsilon^i - \varepsilon^{t*} + \varepsilon^A) = C_M(\varepsilon^i - \varepsilon^t + \varepsilon^A) \qquad \text{(Eq. 3.18)}$$

where σ_I here is the stress caused by the elastic property mismatch between the inhomogeneity and the matrix.

3.2.1.2. Non-dilute system

The above section has been based on a single inclusion embedded within an infinite matrix. The results are therefore applicable only to “dilute” systems. If the matrix is not infinite, or multiple oversized inhomogeneities are embedded in the matrix, the composite is considered to be a non-dilute system in which the volume fraction of the inhomogeneities is not negligible. For this system, the stress equilibrium Eq. 3.14 is not satisfied due to the considerable volume fraction *f*. In fact, to maintain the balance of stress, there is a non-zero average matrix stress opposing the inclusion stress. One way of incorporating this into the model is to think of it occurring by the superposition of an average background stress or image stress $\langle\sigma\rangle_M$ within each individual phase as if it were externally applied. The balance of stress described by Eq. 3.14 becomes

$$(1-f)\langle\sigma\rangle_M + f\left(\sigma_I + \langle\sigma\rangle_M\right) = 0 \qquad \text{(Eq. 3.19)}$$

The image stress modifies Eq. 3.16. The inhomogeneities or the equivalent inclusions are now stressed by $\sigma_I + \langle\sigma\rangle_M$ and have a constrained shape of $\langle\varepsilon\rangle^i + \langle\varepsilon\rangle_M$, where $\langle\varepsilon\rangle_M$ is the mean image strain, $\langle\sigma\rangle_M = C_M \langle\varepsilon\rangle_M$. Consequently, the equivalence relation Eq. 3.18 becomes:

$$\langle C\rangle_I (\langle\varepsilon\rangle^i + \langle\varepsilon\rangle_M + \varepsilon^A - \langle\varepsilon\rangle^{t*}) = C_M (\langle\varepsilon\rangle^i + \langle\varepsilon\rangle_M + \varepsilon^A - \langle\varepsilon\rangle^t) \qquad \text{(Eq. 3.20)}$$

where $\langle\cdot\rangle$ signifies the mean value and $\langle C\rangle_I$ is the average stiffness of the multiple inhomogeneities.

3.2.2. Multi-scale model of dental tissues

In human dental tissues, both dentine and enamel have a two-level structure, which is explained in Figure 3.9. The first-level model regards the whole dentine sample as composed of aligned tubules within matrix that consists of HAp crystallites and organic phase, while in the enamel the first-level structure can be seen as aligned key-hole shaped rods within a composite matrix also consisting of HAp crystallite and organic phase. The second-level model considers the matrix of the first-level dentine or the rod of the first-level enamel as a composite in detail. Despite the differences at the first level, dentine and enamel have a similar structure in the second level that consists of partially aligned HAp crystallites embedded in the isotropic organic matrix. The second−level structures of the two tissues differ only in terms of overall stiffness, volume fraction and the geometry and orientation of HAp crystallites.

In terms of the hierarchical structure of dentine and enamel, a two-level Eshelby inclusion model for a non-dilute system described in section 3.2.1 can be used to determine how the ultrastructural HAp crystallites respond to external macroscopic loading in these two-level composites. In this section, we only focus on elastic deformation, where the real average misfit strain $\langle \varepsilon \rangle^{t*}$ in Eq. 3.20 is zero.

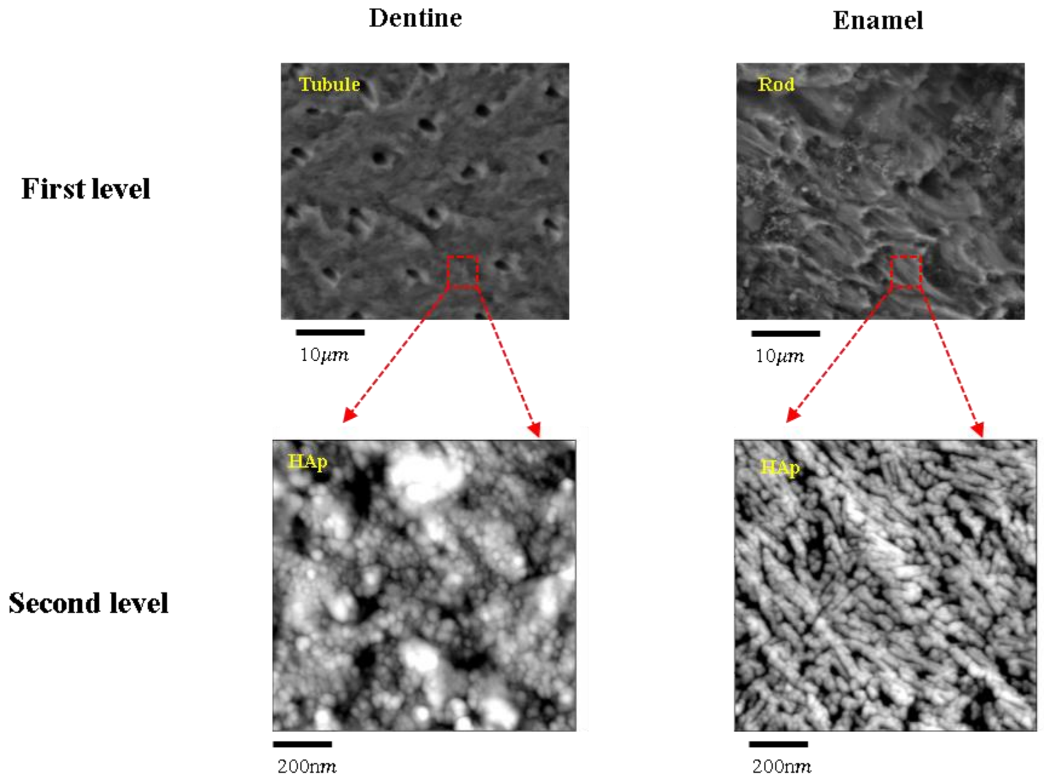

Fig. 3.9 Two-level structure of human dental tissues (dentine and enamel)

3.2.2.1. First-level model of dentine

The first-level structure of human dentine is considered to be a composite consisting of almost perfectly aligned tubules (inhomogeneities) within a finite collagen matrix. The HAp crystallites are contained in the collagen matrix and the first-level model of dentine is to determine the matrix stress. According to Eq. 3.20, the equivalence relation for the first-level human dentine is

$$\langle C \rangle_{tubule}\left(\langle \varepsilon \rangle^{i}+\langle \varepsilon \rangle_{M1}+\varepsilon^{A}-\langle \varepsilon \rangle^{t*}\right)=C_{M1}\left(\langle \varepsilon \rangle^{i}+\langle \varepsilon \rangle_{M1}+\varepsilon^{A}-\langle \varepsilon \rangle^{t}\right) \qquad \text{(Eq. 3.21)}$$

where "$M1$" refers to the first-level matrix model, $\langle\varepsilon\rangle_{M1}$ is the mean image strain in both tubules and matrix at the first level, $\langle\varepsilon\rangle^{i}$ is the averaged total strain in multiple tubules, $\langle\varepsilon\rangle^{A}$ is the external strain caused by the applied stress, $\langle\varepsilon\rangle^{t*}$ is the real average misfit strain for tubules in the first-level matrix, $\langle\varepsilon\rangle^{t}$ is the average misfit strain for the equivalent inclusions to be determined, $\langle C\rangle_{tubule}$ is the average stiffness of the tubules, and C_{M1} is the isotropic stiffness of the collagen matrix and also the equivalent inclusion. Since the tubules are just voids ($\langle C\rangle_{tubule}=0$) and $\langle\varepsilon\rangle^{i}=\langle S\rangle_{tubule}\langle\varepsilon\rangle^{t}$, where $\langle S\rangle_{tubule}$ is the average Eshelby tensor for the multiple tubules, Eq. 3.21 gives a simple expression for $\langle\varepsilon\rangle^{t}$

$$\langle\varepsilon\rangle^{t}=\left(I-\langle S\rangle_{tubule}\right)^{-1}\left(\varepsilon^{A}+\langle\varepsilon\rangle_{M1}\right) \qquad \text{(Eq. 3.22)}$$

In a non-dilute system, in terms of Eq. 3.19 and Eq. 2.20, with the absence of the external stress, the mean image stress is related to the misfit strain $\langle\varepsilon\rangle^{t}$ in the equivalent inclusion by [155]

$$\langle\sigma\rangle_{M1}=-f_{1d}C_{M1}\left(\langle S\rangle_{tubule}-I\right)\langle\varepsilon\rangle^{t} \qquad \text{(Eq. 3.23)}$$

where f_{1d} is the volume fraction of tubules with respect to the whole dentine. Combined with Eq. 3.22, considering that $\langle\sigma\rangle_{M1}=C_{M1}\langle\varepsilon\rangle_{M1}$,

$$\langle\varepsilon\rangle_{M1}=\frac{f_{1d}}{1-f_{1d}}\varepsilon^{A} \qquad \text{(Eq. 3.24)}$$

Therefore, the stress in the matrix is the sum of the applied stress and the image stress

$$\sigma_{M1}=\sigma^{A}+\langle\sigma\rangle_{M1}=\frac{1}{1-f_{1d}}\sigma^{A} \qquad \text{(Eq. 3.25)}$$

Eq. 3.25 indicates that the stress in the first-level collagen matrix is independent on the direction and detailed shape (Eshelby tensor) of the tubules, but depends on the tubule volume fraction alone, which is a consequence of the model assumptions

3.2.2.2. First-level model of enamel

The first-level structure of enamel is also a non-dilute system containing protein matrix and multiple cylindrical rods as the inhomogeneities. It is assumed that all cylindrical rods are nearly parallel to each other. Different from dentine, HAp crystallites are contained in the rods, thus the aim of the first-level model of enamel is to determine the stress field within rods at that lengthscale. The equivalence relation is the same as Eq. 3.21, but $\langle C\rangle_{tubule}$ is replaced by the average stiffness of the rods $\langle C\rangle_{rod}$, which is not zero, in contrast with that of the tubules in dentine. Since Eq. 3.23 still holds for the mean image stress in this case (with $\langle S\rangle_{tubule}$ replaced by $\langle S\rangle_{rod}$, the average Eshelby tensor for cylindrical rods, and f_{1d} replaced by f_{1e}, the volume fraction of the rods), according to Eq. 3.19 and Eq. 3.23. In the absence of the external stress, the mean stress in the rods (or equivalent inclusion) $\langle\sigma\rangle_I$ can be expressed as

$$\langle\sigma\rangle_I = (1-f_{1e})C_{M1}\left(\langle S\rangle_{rod} - I\right)\langle\varepsilon\rangle^t \qquad \text{(Eq. 3.26)}$$

Further, when the external stress is imposed, based on Eq. 3.20 and Eq. 3.23, $\langle\varepsilon\rangle^t$ can be obtained as a function of the externally applied stress

$$\langle\varepsilon\rangle^t = -\left\{\left(C_{M1}-\langle C\rangle_{rod}\right)\left[\langle S\rangle_{rod} - f_{1e}\left(\langle S\rangle_{rod}-I\right)\right]-C_{M1}\right\}^{-1}\left(C_{M1}-\langle C\rangle_{rod}\right)C_{M1}^{-1}\sigma^A$$

(Eq. 3.27)

Therefore, in the first-level model of enamel, with Eq. 3.26 and Eq. 3.27, the total stress in the rods can be obtained as the sum of $\langle\sigma\rangle_I$ and σ^A.

$$\begin{aligned}\langle\sigma\rangle_{rod} &= \langle\sigma\rangle_{I} + \sigma^{A} \\ &= \left\{I - (1 - f_{1e})C_{M1}\left(\langle S\rangle_{rod} - I\right)\left\{\left(C_{M1} - \langle C\rangle_{rod}\right)\left[\langle S\rangle_{rod} - f_{1e}\left(\langle S\rangle_{rod} - I\right)\right] - C_{M1}\right\}^{-1}\left(C_{M1} - \langle C\rangle_{rod}\right)C_{M1}^{-1}\right\}\sigma^{A}\end{aligned}$$

(Eq. 3.28)

It should be noted that the average stiffness of the rods $\langle C\rangle_{rod}$ is initially unknown and needs to be determined in the second-level model.

3.2.2.3. Second-level model

In contrast with the first-level model, the second-level models in dentine and enamel are similar, both considered as a composite consisting of partially aligned HAp crystallites and an organic matrix. Besides the different values of parameters like volume fraction, the average Eshelby tensor and the average stiffness of HAp crystallites, the other difference is that the external stress in the second level of dentine is the stress of matrix in the first level, while that in the second level of enamel it is the stress in the rods. Due to the more complex orientation distribution of inhomogeneities (HAp crystallites) in the second-level structure of dentine and enamel than that of inhomogeneities (tubules or rods) in the first-level structure, the relationship between a single HAp crystallite and the external stress is obtained first. A volume average method is then introduced to obtain the relationship between the local averaged total strain in multiple HAp crystallites and the overall externally applied stress.

For a single HAp crystallite under elastic deformation, the total strain is expressed as $\varepsilon^{i} + \varepsilon_{M} + T^{-T}\varepsilon^{A1}$ (viewed from HAp crystallite local coordinate), where ε^{A1} is the external strain caused by the stress determined from the first-level model and T is the orientation matrix that depends on the three Euler angles (θ,ϕ,ψ), describing the difference between the local HAp crystallite coordinate and the global coordinate. According to Eq. 3.23, in this case ε_M is related to ε^t by

$$\varepsilon_M = -f_2\left(S_{HAp} - I\right)\varepsilon^t \qquad \text{(Eq. 3.29)}$$

where f_2 is the volume fraction of HAp crystallites with respect to the second-level composite and S_{HAp} is the Eshelby tensor for a single HAp crystallite. Further, ε^t in Eq. 3.27 for this case becomes

$$\varepsilon^t = -\left\{\left(C_{M2} - C_{HAp}\right)\left[S_{HAp} - f_2\left(S_{HAp} - I\right)\right] - C_{M2}\right\}^{-1}\left(C_{M2} - C_{HAp}\right)T^{-T}C_{M2}^{-1}\sigma^{A1} \qquad \text{(Eq. 3.30)}$$

where “*M*2” means the second-level organic matrix, and $C_{M2} = C_{M1}$. σ^{A1} is the external stress obtained from the first-level model and C_{HAp} is the stiffness matrix for a single HAp crystallite. Finally, the relationship between the strain in a single HAp crystallite and the external stress (matrix stress in dentine or rod stress in enamel) can be established (transformed into the global coordinate)

$$\varepsilon_{HAp}^{single} = T^T\left\{\left\{\left(I - C_{M2}{}^{-1}C_{HAp}\right)^{-1}\left[S_{HAp} - f_2(S_{HAp} - I)\right]^{-1} - I\right\}^{-1}T^{-T} + T^{-T}\right\}C_{M2}{}^{-1}\sigma^{A1} = K\sigma^{A1}$$

$$\text{(Eq. 3.31)}$$

In reality, the HAp crystallites in the second-level structure of dentine and enamel are partially aligned, but the partial alignment can be represented as a superposition of perfect alignment and random distribution. For a group of perfectly aligned HAp crystallites of a certain orientation, the relationship between the average strain in the group of crystallites and the external stress is the same as Eq. 3.31, where the averaged stiffness and the Eshelby tensor are the same as the values for a single crystal $\langle C\rangle_{HAp} = C_{HAp}$, $\langle S\rangle_{HAp} = S_{HAp}$. As for a group of randomly distributed HAp crystallites, the strain of the group can be determined by a volume average method, which is introduced here.

The purpose of using the volume average method is to avoid the complex calculation of the average Eshelby tensor and average stiffness of the randomly distributed HAp crystallites. In a random distribution, each crystallite follows the relationship of Eq. 3.31 with each individual orientation matrix T_k. Randomly distributed crystallites can have any possible orientation in the space, thus the volume averaging method is to calculate the strain value for each single crystallite and average the results of all the crystallites in the second level over all possible orientations.

$$\left\langle \varepsilon_{HAp}^{single} \right\rangle = \frac{1}{V}\int_V \varepsilon_{HAp}^{single} \mathrm{d}V = \left\langle K \right\rangle \sigma^{A1} \qquad \text{(Eq. 3.32)}$$

The second-level models of dentine and enamel are similar, as is indicated in the schematic flow diagram of the two-level Eshelby model in Figure 3.10. The expressions derived above can be used to determine the unknown stiffness matrix $\left\langle C \right\rangle_{rod}$. The detailed determination has been provided by [155] and is not shown here.

$$\left\langle C \right\rangle_{rod} = \left\{ C_{M2}{}^{-1} - f_2 \left\{ \left(C_{HAp} - C_{M2} \right) \left[S_{HAp} - f_2 \left(S_{HAp} - I \right) \right] + C_{M2} \right\}^{-1} \left(C_{HAp} - C_{M2} \right) C_{M2}{}^{-1} \right\}^{-1}$$

(Eq. 3.33)

Finally, with the two levels combined, a comprehensive model linking the average HAp crystalline lattice strain and the overall externally applied load can be established, which can be used to determine the apparent modulus of HAp crystallites in both dentine and enamel.

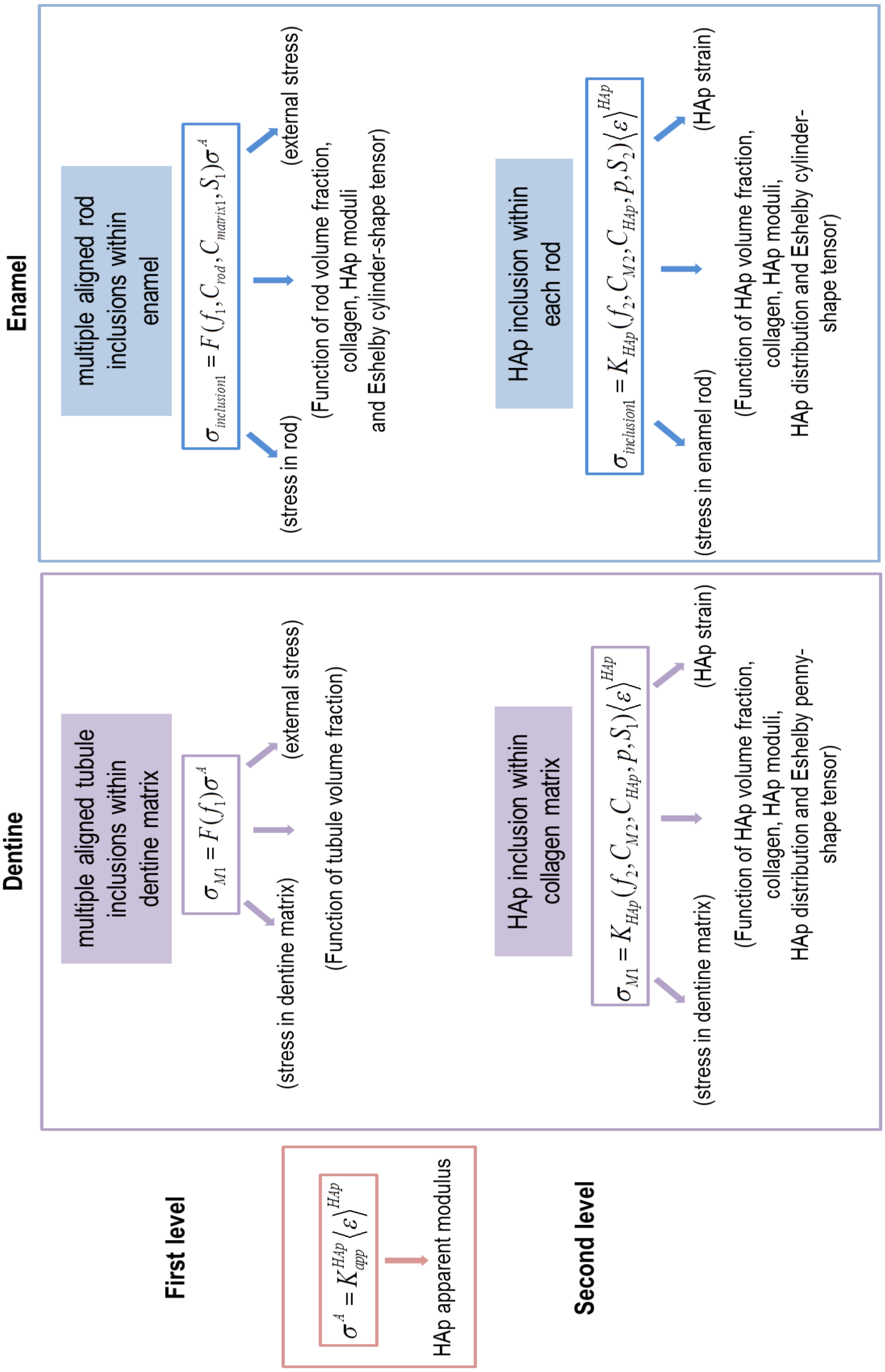

Fig. 3.10 Summary of the two-level Eshelby model in dental tissues

3.2.2.4. Eshelby tensor of multi-scale model

Eshelby introduced a tensor S (see Eq. 3.34) that only depends on the inclusion shape (a_1, a_2 and a_3) and Poisson's ratio of the matrix (υ). The ellipsoid has principal half-axes a_1, a_2 and a_3 as illustrated in Figure 3.8. The rest of the nonzero terms can be found by cyclic permutation of the above formulas. The I_k and I_{kl} terms below are defined in terms of standard elliptic integrals [156].

$$S = \begin{bmatrix} S_{1111} & S_{1122} & S_{1133} & 0 & 0 & 0 \\ S_{2211} & S_{2222} & S_{2233} & 0 & 0 & 0 \\ S_{3311} & S_{3322} & S_{3333} & 0 & 0 & 0 \\ 0 & 0 & 0 & S_{2323} & 0 & 0 \\ 0 & 0 & 0 & 0 & S_{3131} & 0 \\ 0 & 0 & 0 & 0 & 0 & S_{1212} \end{bmatrix}$$

$$\begin{aligned} S_{1111} &= \frac{3}{8\pi(1-\upsilon)} a_1^{\,2} I_{11} + \frac{1-2\upsilon}{8\pi(1-\upsilon)} I_1 \\ S_{1122} &= \frac{1}{8\pi(1-\upsilon)} a_2^{\,2} I_{12} + \frac{1-2\upsilon}{8\pi(1-\upsilon)} I_1 \\ S_{1133} &= \frac{1}{8\pi(1-\upsilon)} a_3^{\,2} I_{13} + \frac{1-2\upsilon}{8\pi(1-\upsilon)} I_1 \\ S_{1212} &= \frac{a^2+b^2}{16\pi(1-\upsilon)} I_{12} + \frac{1-2\upsilon}{16\pi(1-\upsilon)} \left(I_1 + I_2\right) \end{aligned} \tag{3.34}$$

In dentine, the shape of the HAp crystalline platelets in dentine is thought to correspond to elongated flagstone. In classical Eshelby modelling, a very good approximation is to use a penny-shape inclusion to simulate an individual platelet, as the integrals can be readily written. The Eshelby penny-shape tensor has two parameters, where a_1 is the radius while a_3 is half of the thickness of the penny-shape inclusion (see Figure 3.8 b) [168]. The crystal *c*-axis (corresponding to the (002) peak) of the HAp crystallites is thought to be parallel to the long dimension of the platelet [28, 29].

In enamel, both structural levels are considered as non-dilute systems consisting of a number of inhomogeneous inclusions (rods at the first level and HAp crystallites at the second level). For simplicity, both rods and HAp crystallites are assumed to be of cylindrical shape. Therefore, the classical solution for inclusion in the form of a cylinder is used to simulate both the needle-shaped rods and the individual HAp crystallites. In the Eshelby approach, the cylinder is approximated by a prolate spheroid described by the three dimensions, a_1, a_2 and a_3, where $a_1 = a_2 << a_3$, i.e. the cross-section of the ellipsoid perpendicular to its longest axis is a circle [156] (see Figure 3.8 b). The crystal *c*-axis (corresponding to the (002) peak) of the needle-shaped HAp crystallites is normal to this cross section of the cylinder, i.e. is aligned with the a_3 axis [49]. In the next section a detailed derivation and discussion of the model formulation and implementation is introduced.

3.3. Other characterization techniques

3.3.1. Nanoindentation

Nanoindentation has recently emerged as a powerful tool for measuring the nano-scale mechanical properties in biomaterials [157]. Nanoindentation has been applied to the mineralized tissues fairly extensively and has been reviewed by Kinney et al. [158] and Haques et al. [159]. In teeth, the primary focus has been to map the mechanical properties across healthy dental tissue to understand the role of local properties and hierarchical structure, and has also been coupled with the chemical mapping [56, 160, 161]. However, to date, no studies have been reported on the investigation of the variation of mechanical properties in thermally treated dental tissues. Tesch et al. [154] successfully applied SAXS and nanoindentation to characterise non-treated dentine and observed correlated variations of mechanical and structural properties, but the resolution is low. In the present investigation of heat-induced alterations of hard dental tissues with high resolution, a SAXS mapping setup was combined with nanoindentation mapping. The results obtained here are likely to help in a better understanding of the internal architecture alterations and hierarchical properties changes due to heat exposure. In addition, the effect of exposure of human skeletal hard tissues to high temperatures is an important topic of study in the context of forensic investigations and archaeological analysis [90, 94, 96-98].

Nanoindentation tests are widely used to determine local material properties. Continuously recording nano-indentation (CRIT) involves loading and unloading the sample by a sharp hard tip, and the indentation load-depth data registered in the process [162]. A schematic diagram of the nanoindentation process is shown in Figure 3.11, where the indentation depth h is the summation of h_s (displacement due to elastic deformation) and h_c (contact depth). S is the contact stiffness at maximum penetration and is the initial slope of the unloading curve. Using the compliance method, the hardness H and reduced modulus E_r can be determined directly from the analysis of load-displacement data [157]. The hardness of the sample can be obtained by dividing the load by the projected area of indentation

$$H = \frac{F_m}{A_c} \qquad \text{(Eq. 3.35)}$$

where A_c ($A_c = 24.5h_c^2$ for a perfect three-sided pyramid Berkovich tip) is the contact area, F_m is the force at maximum load. The composite modulus E^* (sample and diamond) is extracted from

$$\frac{1}{E^*} = \frac{2\beta}{S}\sqrt{\frac{A_c}{\pi}} \tag{Eq. 3.36}$$

where β is a correction factor depending on the tip geometry ($\beta = 1.034$ for the Berkovich tip). The relation between apparent modulus, the stiffness of diamond and the sample properties is given by

$$\frac{1}{E^*} = \frac{1-\nu_D^2}{E_D} + \frac{1-\nu_S^2}{E_S} \tag{Eq. 3.37}$$

where E and ν are Young's modulus and Poisson's ratio, and subscripts D and S are for diamond and sample respectively (E_D =1141 GPa, ν_D =0.07). The reduced modulus is referred to as:

$$\frac{1}{E_r} = \frac{1-\nu_s^2}{E_s} \tag{Eq. 3.38}$$

which is reported in [163-165].

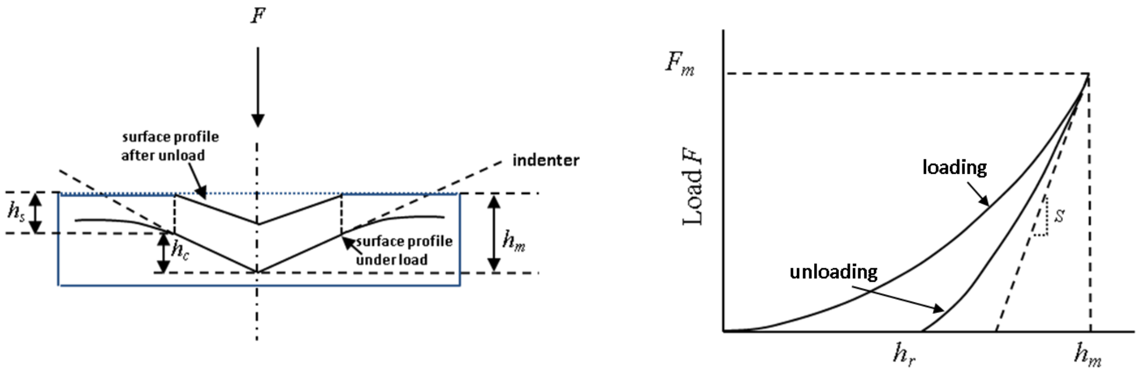

(a) (b)

Fig. 3.11 (a) A schematic diagram of nanoindentation process; (b) Nanoindentation profile showing the quantities used in the analysis.

3.3.2. Photoelasticity

Photoelasticity is a non-destructive, whole-field method widely applied in stress distribution analysis. The fringe pattern arises when the sample is viewed between crossed polarising plates, with the colour or brightness of the fringe being related to the difference between the principal stresses, which is in turn proportional to the maximum shear stress, or Tresca stress, in the material [166].

The use of a diametrically loaded disk is a standard calibration technique which can be used either to obtain the photoelastic properties of the birefringent material, or to determine the calibration constants if these properties are known. The fringe constant of the material is defined as:

$$f = \frac{8}{\pi D}\frac{P}{N_1} \qquad \text{(Eq. 3.39)}$$

where D is the diameter of the epoxy disk (12 mm), N_1 is the number of fringes for the calibration sample and P is the applied load (N). In order to obtain an estimate for the average value of f, a series of known loads can be applied to a monolithic epoxy disk, and the corresponding fringe numbers are recorded.

The stress distribution in the disk is characterised in terms of the difference between the principal stresses (or Tresca shear stress) using the following expression:

$$\sigma_2 - \sigma_1 = N_2 \frac{f}{h} \qquad \text{(Eq. 3.40)}$$

where h is the thickness of epoxy, and N_2 is the number of fringes for the sample of interest. Tresca shear stress is expressed as the maximum difference between any two principal stresses. The deformation state of the plate-shaped epoxy corresponds closely to the plane stress state approximation in two-dimensional photoelasticity.

Both white and monochromatic light photoelastic fringes are shown in Figure 3.12. The coloured image is striking but is difficult to analyse due to the colour interference. Instead, monochromatic light is often used to make it easier to count the fringes.

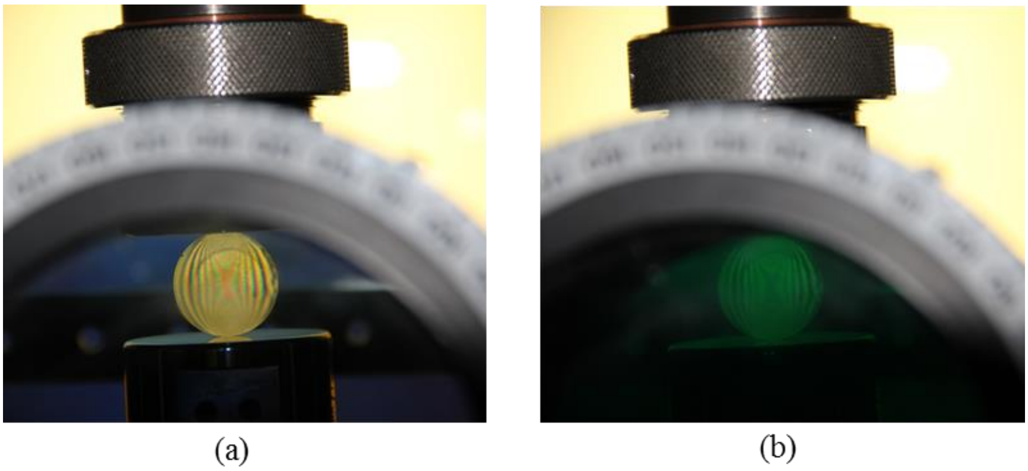
(a) (b)

Fig. 3.12 Illustration of photoelastic fringes of (a) white and (b) monochromatic light filtered by green glass.

3.3.3. Microscopy

Ever since its invention, the microscope has been a valuable tool of scientific discovery. It is widely used to create an enlarged view of an object to observe details otherwise indistinguishable with the human eye. The direct and critical insight into the hierarchical structure of dental tissues needs a range of various microscopy methods. In this section, three microscopy techniques are briefly introduced insofar as they are used to characterise the dental tissue structure in this thesis.

3.3.3.1. Environmental Scanning Electron Microscopy (ESEM)

Environmental scanning electron microscopy (ESEM) is a type of reflection scanning electron microscopy that allows the presence of a gaseous environment in the sample chamber, instead of vacuum in the standard SEM. This confers several advantages, one in particular being that it enables the investigation of electrically non-conductive specimens without coating with gold or carbon [167]. This is of importance for this study by means of allowing avoidance of the need for coating that may interfere with X-ray diffraction experiments if the same sample is used.

In the ESEM the primary electron beam is scanned over the sample and the electrons of the beam interact with the sample surface, thereby producing several signals that are collected with appropriate detectors. One possible detector in the ESEM is the secondary electron (SE) detector, which reveals information of the surface topography. In addition it is possible to detect backscattered electrons (BSE) using a backscattered electron detector (BSD). Backscattered electrons are electrons that are scattered back from the primary electron beam in a region close to the surface of the sample. To investigate dental samples (illustrated in Figure 2.2 b) with the ESEM Evo LS15 (CARL ZEISS, U.K.), the sample blocks were placed in low vacuum and BSE mode used at the working distance of 4.5 mm. The electron beam energy was set to 18 kV. A BSD was used to collect the BSE signals at the sample surface.

3.3.3.2. Transmission Electron Microscopy (TEM)

Transmission electron microscopy (TEM) is capable of imaging at a significantly higher resolution. In the experiment a tightly focused beam of electrons is transmitted through an ultra-thin specimen, interacting with the specimen as it passes through [168]. In order to investigate the HAp crystallites directly at the nano-structural level, TEM imaging technique was applied. Powdered dentine and enamel samples were prepared by grinding down under liquid nitrogen and then thoroughly dispersed by vibrating in an ultrasound bath for 5 minutes. The reason for using liquid nitrogen is to make the powder particles' smaller and thinner without introducing any chemical effects, so that very few crystallites or even a single crystal could be captured by TEM. Afterwards the samples were placed on the TEM copper grid coated with carbon film. Ultrastructure of HAp crystallites in the enamel is shown as an example in Figure 2.2 c collected using JEOL JEM-2200MCO TEM instrument.

3.3.3.3. Scanning Probe Microscopy (SPM)

Scanning Probe Microscopy (SPM) is a set of experimental methods used in imaging of surface structures at subatomic resolution. One of the flavours of SPM is Atomic Force Microscopy (AFM), which is based on mapping of the force field at the surface of the sample using a very sharp probe with ~20nm tip radius [169]. In order to obtain high resolution topographical images of enamel and dentine surface, a commercial SPM (MFP-3-D, Asylum Research, USA) was used. The surface of the dental slice samples was prepared by a series of grinding processes with 1200#, 2400# and 4000# sand papers, and then polished by 0.3μm and 0.05μm alumina powders with fine polishing cloth. Finally, samples were cleaned by sonication in deionized water and blow-dried in air. As is shown in Figure 2.3, the ultrastructure of dentine and enamel layers shows the topographical images of HAp crystallites. CR-FM (contact resonance module) is a general name of the dynamic-approach AFM method, perhaps the most promising method for quantitative measurements of elastic stiffness for relatively stiff materials [170]. The mode was also used to detect the elastic property distribution across the DEJ at high resolution, as shown in Chapter 6.

3.3.4. Micro Computed Tomography (Micro-CT)

The micro computed tomography (micro-CT) is a miniature version of cone-beam CT widely used in medical diagnostics. In the last few years micro-CT scanning technology based on X-ray transmission imaging has become more commonly and widely used in the fields of biology and medicine. Micro-CT provides nondestructive, three-dimensional reconstructions of small objects at very high spatial resolution that may be below 1 micron. For data collection the specimens are placed between source and detector on a rotating disk controlled by a stepper motor inside a lead-shielded chamber [171, 172].

For the purpose of planning and preparation of X-ray measuring positions used in synchrotron experiments, a commercial micro-CT system was used to scan the samples. SkyScan 1172 scanner (SkyScan, Kontich, Belgium) was used at 1.9 µm isotropic resolution using 40kV voltage, 120uA current and a 0.5mm Aluminium filter. The resulting images were used for reconstruction using SkyScan NRECON package. Subsequent 3-D planning models were created with Fiji imaging software [173]. A 3-D reconstruction of human dental tissue is illustrated in Figure 2.2 a.

Chapter 4

Multi-scale modelling and diffraction based characterization of elastic behaviours of human dentine

This chapter is based on the following published manuscripts:

- Tan Sui, Michael Sandholzer, Nikolaos Baimpas, Igor P. Dolbnya, Anthony Damien Walmsley, Philip J. Lumley, Gabriel Landini, Alexander M. Korsunsky, Multi-scale modelling and diffraction-based characterization of elastic behaviour of human dentine, Acta Biomaterialia, Vol.9 (8), pp. 7937-7947, 2013
- Tan Sui, Alexander M. Korsunsky, Hierarchical modelling of elastic behaviour of human dental tissue based on synchrotron diffraction characterization: Chapter **7** in *Advanced Healthcare Materials*, A. Tiwari, Ed., Advanced Materials Series, WILEY-Scrivener Publishing LLC, USA, 2013.

4.1. Brief introduction

Human dentine, as described in Chapter 2 as a hierarchical mineralized tissue with a two-level composite structure, contains tubules as the prominent structural feature at micro-level, and collagen fibres decorated with HAp crystallite platelets at nano-scale.

Previously, most research in this area has concentrated on the mechanical properties of dentine at the macro- and micro-scale, i.e. Young's modulus, Poisson's ratio, hardness and fracture properties, using a variety of measurement methods [158].

Few studies have focused on this two-level structure of human dentine, where the response to mechanical loading is thought to be affected not only by the tubule volume fraction at micro-scale, but also by the shape and orientation distribution of mineral crystallites and their nano-scale spatial arrangement and alignment.

Synchrotron-based X-ray diffraction, SAXS and WAXS have been recently used to study the mechanical behaviour in mineralized biological composites such as bone [133, 134, 140, 141] and teeth [82, 83, 132]. However, the earlier studies did not take into account the nanoparticle distribution [82] and [132], which can be derived from SAXS data. In addition, all these studies were carried on non-human samples, in which different particularities of the tubule structure and morphology are expected to result in differences in the mechanical properties [138]. In addition, various analytical models of composite [174-176] fail to capture the nano-scale structure effect on the apparent modulus, and this led to the discrepancies of overestimation between the modelling predictions and experimental results.

In order to improve the understanding of the influence of the nano-scale structure variation of the two-level composite of human dentine on its mechanical response, in this Chapter, *in situ* elastic strain evolution within HAp crystallites in dentine subjected to uniaxial compressive loading along both the longitudinal and transverse directions was characterised simultaneously by two synchrotron X-ray scattering techniques: WAXS and SAXS. WAXS allows the evaluation of the apparent modulus linking the external load to the internal HAp crystallite strain, while the nano-scale HAp crystallites distribution and arrangement can be quantified by SAXS. An improved multi-scale Eshelby inclusion model was proposed that takes into account the two-level hierarchical structure, and was validated via multi-directional experimental non-destructive strain evaluation. The agreement between the simulation and measurement indicates that the multi-scale hierarchical model developed here accurately reflects the structural arrangement and mechanical response of human dentine. This study benefits the comprehensive understanding of the mechanical behaviour of hierarchical biomaterials. The knowledge of the mechanical properties related to the hierarchical structure is essential for understanding and predicting the effects of structural alterations that may occur due to disease or treatment on the performance of dental tissues and their artificial replacements.

4.2. Materials and methods

4.2.1. Sample preparation

Two freshly extracted sound human third molars (ethical approval obtained from the National Research Ethics Committee; NHS-REC reference 09. H0405.33/ Consortium R&D No. 1465) were washed and cleaned in distilled water to eliminate residues and kept in a -20°C freezer for a maximum of 14 days before the experiment. The samples were rehydrated using distilled water and 2mm thick dentine disks were cut just below the enamel-cement line using a low speed diamond saw (Isomet Buehler Ltd., Lake Bluff, Illinois, USA). The disks were further cut into smaller bars and a series of polishing papers were used to produce the final $2\times2\times2$ mm^3 cubes of dentine (Figure 4.1 b). The samples were kept for a maximum of 7 days in distilled water in a commercial fridge at 4°C until the experiment was performed.

4.2.2. *In situ* scattering measurements

4.2.2.1. Mechanical loading setup

Uniaxial compressive loading was carried out on two dentine samples in the form of small 2×2 mm^2 cubes. The samples were designated HD2, for which the loading was applied in the transverse direction, and HD3, for which the loading was applied in the longitudinal direction with respect to the tubules respectively. Loading was carried out using a remotely operated and monitored compression rig (Deben, Suffolk, UK), with a 5 kN calibrated load cell. The rig was equipped with custom-made jaws, allowing a high-energy transmission X-ray setup to be used, as illustrated in Figure 4.1 a. The samples were deformed at a displacement rate of 0.2 mm/min up to 400N (corresponding to about 100 MPa for the samples) along *x*-axis. The boundary between the sample and the loading platen was regarded as frictionless. After each constant loading increment (HD2 50 N, HD3 100 N), the load was maintained and the WAXS and SAXS patterns were collected. For the purpose of planning the measuring positions and determination of the precise loading cross-sectional area of the dentine cubes, a commercial micro-CT system was used to scan the samples as illustrated in Figure 4.1 b.

4.2.2.2. Beamline diffraction setup

The experiment was carried out on B16 experimental beamline at Diamond Light Source, Oxford Harwell Campus, Didcot, UK. A monochromatic X-ray beam was used to illuminate the sample as illustrated schematically in Figure 4.1 a. The incident beam was monochromated to the photon energy of 17.99 keV, and collimated to the spot size of 0.5×0.5 mm^2 on the sample. The use of this beam size ensures that the irradiated volume is small enough to lie approximately in the centre of the sample and experience a deformation state that is only very weakly dependent on the boundary conditions, yet large enough compared to the principal structural features of dentine, i.e. tubules and intertubular distances, to be representative of the overall material response. WAXS and SAXS patterns were alternately collected at three locations across the sample. A silicon powder was used for the WAXS data calibration and dry chicken collagen was used for the SAXS data calibration [177].

WAXS diffraction patterns were recorded using a Photonic Science Image Star 9000 detector (3056×3056 pixels, $31\times31\,\mu m^2$ pixel size, Photonic Science Ltd., UK) placed at a sample-to-camera distance of 128.72mm (Figure 4.1 a). Further downstream of the beam a Pilatus 300K detector (487×619 pixels, $172\times172\ \mu m^2$ pixel size, Dectris, Baden, Switzerland) was positioned at a distance of 4358.47mm to collect the SAXS patterns (Figure 4.1 a). In order to record both the WAXS and SAXS patterns at each scanning location, the WAXS detector was translated laterally to expose the SAXS detector after each WAXS collection.

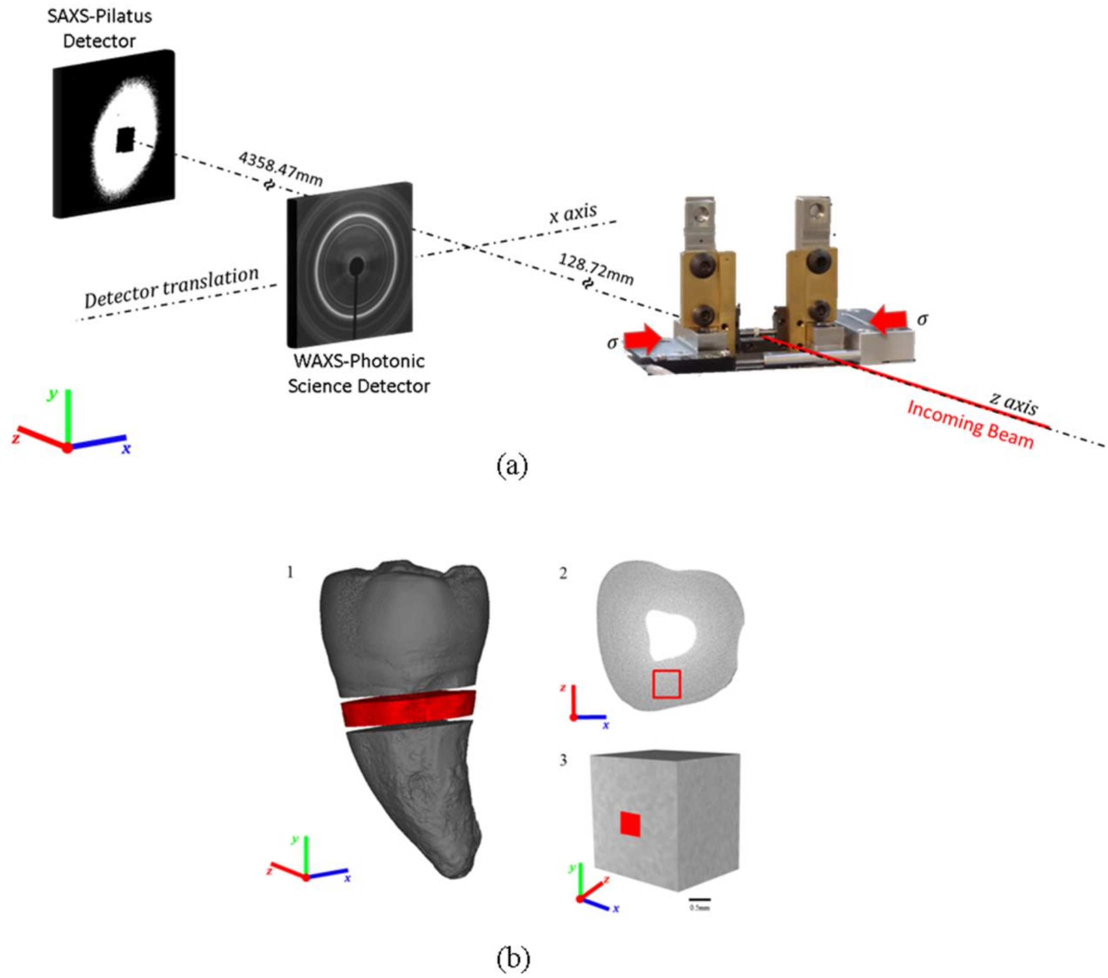

(a)

(b)

Fig. 4.1 Schematic diagram of *in situ* uniaxial loading experimental setup and cubic dentine sample preparation; (a) The sample was under uniaxial compressive loading on the compression stage. The monochromatic X-ray beam was directed perpendicular to the sample surface and the loading direction. WAXS and SAXS diffraction patterns were recorded at each loading step at three locations on the sample. The WAXS detector was translated laterally out of the beam to expose the SAXS detector after each collection of WAXS. (b) Micro-CT based models of the three preparation stages. (1) 2mm thick dentine disk (coloured red) cut below the enamel-cement line and (2) further cut and polished to produce (3) the final $2\times2\times2$ mm^3 cubes of dentine. The red square indicates the central position of the x-ray beam.

4.2.3. Data interpretation

4.2.3.1. WAXS data analysis

To determine the strain from the mineral HAp phase, 2-D diffraction images were pre-processed into 1-D intensity plot using Fit2D [144] by “caking” each pattern with a step of 20° in the range of 0°-360° of the (002) peak under laboratory coordinate

(Figure 4.2 a, only 0°-90 ° is shown). The normal strain component along the centre direction of each cake represents the strain distribution at the corresponding orientation. Subsequently, the 1-D intensity plot of each cake (covering 20°) was obtained by the integration, with respect to the azimuthal angle, of the converted 2-D images. Afterwards, the 1-D profiles of each individual (002) peak were fitted with Gaussian curves to determine the centre position after the subtraction of the linearly fitted background. To calculate the HAp crystalline lattice strain, the WAXS pattern of the unloaded condition was used as a strain-free reference point. The centre position of the scattering patterns were used to ensure that a consistent sample position was interrogated throughout the data analysis, and the relatively small beam compared to the sample dimension guarantee that boundary conditions have negligible influence on the interrogated volume.

4.2.3.2. SAXS data analysis

For the SAXS data analysis, a reference pattern representing the strain-free sample was used to determine the orientation and degree of alignment (ρ) of HAp crystalline particles, which describes the percentage of aligned particles. Figure 4.2 b is an example reference SAXS pattern of HD2. In order to quantify the orientation and degree of alignment, the SAXS patterns were integrated along all the possible scattering vectors q to account for the main scattering effect (with the range selected from the outline of beamstop to the outline of the pattern as marked with red dashes in Figure 4.2 b), which results in a function $I(\varphi)$ with the azimuthal angle φ (Figure 4.2 c). The predominant orientation is determined by the average position of two peaks in the plot of $I(\varphi)$ (e.g. φ_0 in Figure 4.2 c), while the degree of alignment with respect to the predominant orientation of HAp crystallites is defined as the ratio of peak area and the overall area under the curve of $I(\varphi)$.

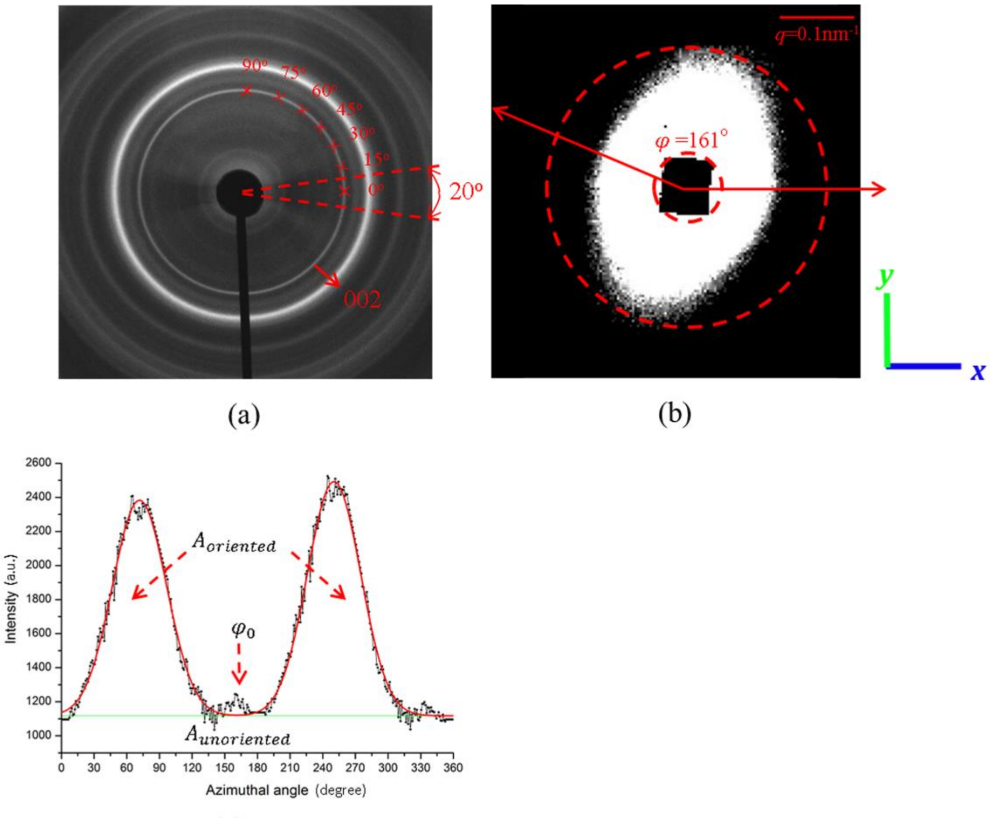

(a)

(b)

(c)

Fig. 4.2 (a) A representative dentine WAXS pattern of Debye-Scherrer rings with different intensities. The dark region in the centre is the beam stop. The (002) peak is marked with a red arrow. Peak shifts at different positions on the (002) ring represent the average strains of (002) along different directions. Multiple angles with respect to the *x*-axis were caked in order to examine the strain variation (seven angles are shown as an example 0^{o}, 15^{o}, 30^{o}, 45^{o}, 60^{o}, 75^{o}, 90^{o}). Each cake was with a 20^{o} range. (b) A representative dentine SAXS pattern of HD2 sample. The *q* scale in the SAXS pattern in the reciprocal space is inversely proportional to the dimension (*d*) in the real space, as dictated by the Fourier transform. The relation is $q=2\pi/d$. If all the HAp crystalline platelets are oriented at φ direction parallel to their long dimension in the real space, *q* would be the smallest in the elliptical pattern of SAXS. Thus the direction of the short axis of the ellipse pattern indicates the predominant orientation of the crystals. (c) A plot of $I(\varphi)$ of HD2 sample without any external load (black points) from SAXS. The Gauss fit is also shown in the figure (red line). The predominant orientation $\varphi_0 = 161^{o}$ is the average position of the two peaks. The ratio $A_{oriented}/(A_{oriented}+A_{unoriented})$ gives the degree of alignment.

.

4.3. Model formulation

4.3.1. Geometrical assumptions

Human dentine has a hierarchical two-level composite structure, where the first level is represented by the dentinal tubules and the second level by the HAp crystallites within a fibrous collagen matrix. Figure 4.3 a, c and d are images of the first-level dentine structure, where Figure 4.3 a is obtained by SEM and Figure 4.3 c-d show the random distribution of collagen fibril viewed respectively along longitudinal and transverse direction of tubules as proposed by Bozec [178]. Figure 4.3 b shows the “woven” structure in dentine based on scanning transmission electron microscopy (STEM) observation. Figure 4.3 e-f are images of the second-level dentine structure, where a randomly distributed structure of HAp crystallites shown in Figure 4.3 e is to be combined with a fully aligned structure to determine the real structure of partial alignment (Figure 4.3 f for HD2), given the detailed information of the degree of alignment by SAXS interpretation.

The thickness of the penny-shape HAp crystalline platelets in dentine is taken to be equal to the thickness of the dentine crystal platelet (2-4nm). The diameter of the penny-shape is the average of the length (100nm) and width (30nm) of HAp crystallites to guarantee the identical cross-sectional area. The size of crystal platelet and the parameters of penny-shape tensor are listed in Table 4.1. The crystal *c*-axis lies on the diametric directions within the penny and is in x-y plane shown in Figure 4.3 f.

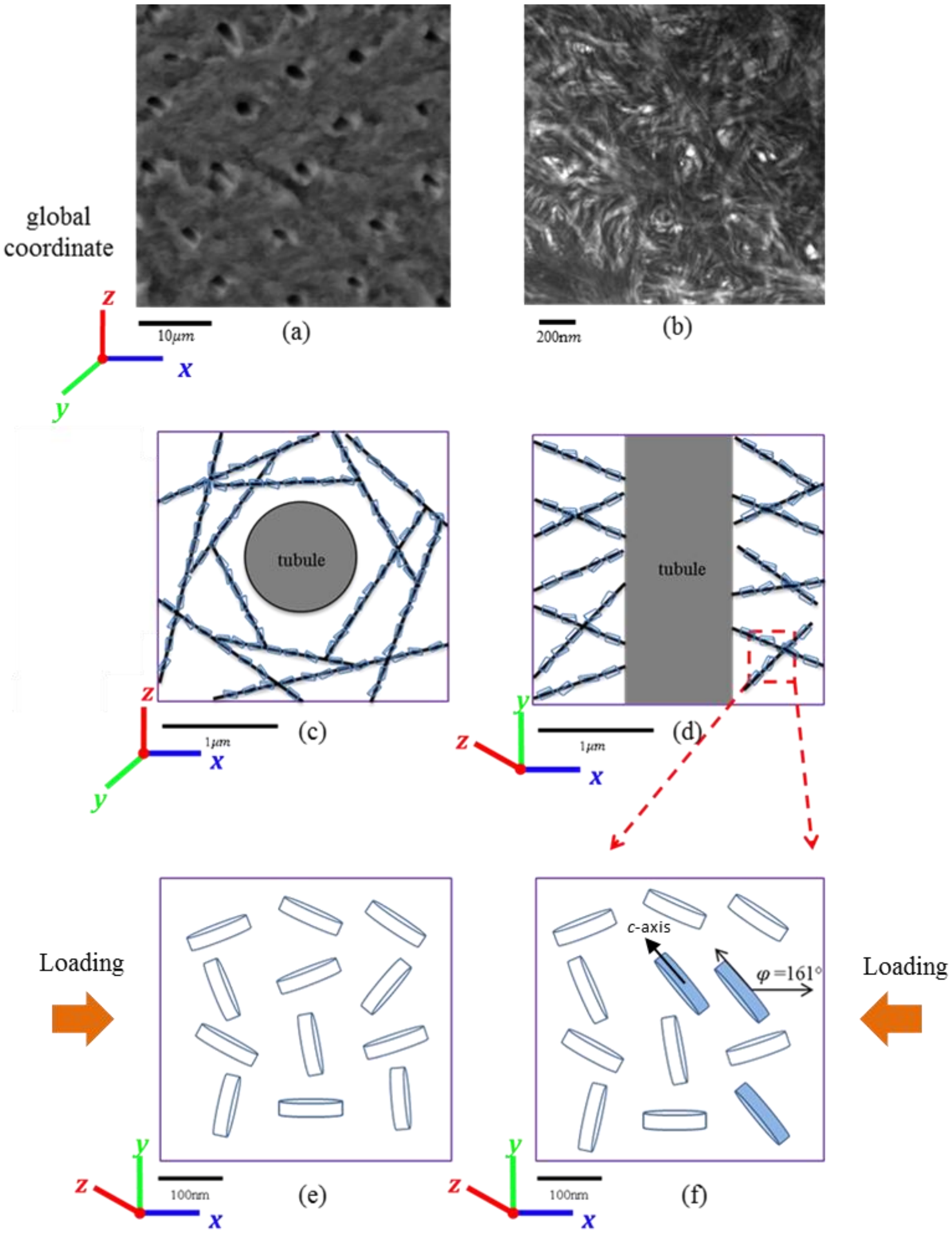

Fig. 4.3 Schematic diagram of the two-level structure of human dentine. (a) SEM observation of the first level tubule structure of human dentine; (b) STEM observation of the “woven” structure in dentine; (c) A schematic structure of the random distribution of collagen fibrils (black lines) besides the tubules, viewed along the longitudinal direction of tubules; (d) Same as (c), viewed along the transverse direction of tubules; (e) The structure of random distribution of HAp crystallites viewed from the cross section parallel to the tubule direction; (f) The real structure of partial alignment, where the pennies are with the alignment angle 161 ^{o} (showing the example of HD2) with respect to the global *X*-axis are shown in blue.

4.3.2. First-level model: multiple aligned tubule inclusions within dentine matrix

The purpose of the first-level model for human dentine is to establish the relationship between the external stress σ^A and the dentine matrix stress σ_{M1}, which will serve as the external stress in the second level. Without any misfit strain in tubules, the Eshelby model for a non-dilute system (Eq. 3.21 [80, 155] indicates that the elastic mechanical response of the tubules can be related to that of an equivalent inclusion with the same property as the matrix.

$$\langle C\rangle_{tubule}(\langle\varepsilon\rangle^i+\langle\varepsilon\rangle_{M1}+\varepsilon^A)=C_{M1}(\langle\varepsilon\rangle^i+\langle\varepsilon\rangle_{M1}+\varepsilon^A-\langle\varepsilon\rangle^t) \qquad \text{(Eq. 4.1)}$$

Considering that the average stiffness of tubules is null $\langle C\rangle_{tubule}=0$, the average stress in the dentine first-level matrix can be expressed merely in terms of the volume fraction of tubules (for details see Eq. 3.21- Eq. 3.25, [80, 155])

$$\sigma_{M1}=\frac{1}{1-f_1}\sigma^A \qquad \text{(Eq. 4.2)}$$

4.3.3. Second-level model: HAp inclusion of collagen matrix

The dispersion of multiple HAp crystallites within the matrix of collagen forms the second hierarchical level model for dentine. The purpose of the second-level model is to establish a relationship between the first-level dentine matrix stress and the average lattice strain in the HAp crystallites $\langle\varepsilon\rangle^{HAp}$, thus to determine the apparent modulus [50] between the global external load and local HAp crystallites strain.

4.3.3.1. Multiple perfectly aligned HAp crystallites

If all HAp crystallites are perfectly aligned described by an orientation matrix *T*, the relationship between the average HAp crystallites strain and the external load (here the first-level dentine matrix stress) can be expressed as [155] (Eq. 3.31).

$$\langle\varepsilon\rangle_{aligned}^{HAp} = T^{T}\left\{\left\{\left(I - C_{M2}{}^{-1}\langle C\rangle_{HAp}\right)^{-1}\left[\langle S\rangle - f_2(\langle S\rangle - I)\right]^{-1} - I\right\}^{-1} T^{-T} + T^{-T}\right\} C_{M2}{}^{-1}\sigma_{M1}$$

or, expressed more simply $\sigma_{M1} = K_{aligned}\langle\varepsilon\rangle_{aligned}^{HAp}$ (Eq. 4.3)

where $\langle C\rangle_{HAp}$ and $\langle S\rangle$ are the average stiffness and Eshelby tensor of HAp crystallites in the gauge volume [179], C_{M2} is the collagen stiffness, and f_2 is the volume fraction of HAp crystallites with respect to the whole second-level structure. For perfectly aligned crystals, $\langle C\rangle_{HAp} = C_{HAp}, \langle S\rangle = S$. Note that different orientations (different orientation matrices) may result in different results of $\langle\varepsilon\rangle_{aligned}^{HAp}$. $K_{aligned}$ is the apparent stiffness matrix of perfectly aligned crystallites. The variation of $K_{aligned}$ with different alignment angles of particles with respect to the loading direction can be calculated by changing the orientation matrix in Eq. 4.3.

4.3.3.2. Multiple randomly distributed HAp crystallites

If HAp crystallites have a random distribution, this group of crystallites will have an isotropic stiffness, as well as an isotropic Eshelby tensor, thus the relationship between the average local HAp crystallites strain and external load is independent on the orientation matrix in Eq. 4.3.

$$\langle\varepsilon\rangle_{random}^{HAp} = \left\{\left\{\left(I - C_{M2}{}^{-1}\langle C\rangle_{HAp}\right)^{-1}\left[\langle S\rangle - f_2(\langle S\rangle - I)\right]^{-1} - I\right\}^{-1} + I\right\} C_{M2}{}^{-1}\sigma_{M1}$$

or, expressed more simply $\sigma_{M1} = K_{random} \langle \varepsilon \rangle_{random}^{HAp}$ (Eq. 4.4)

where K_{random} is the apparent stiffness matrix for randomly distributed crystallites. In contrast to perfectly aligned crystallites, $\langle S \rangle$ and $\langle C \rangle_{HAp}$ were not those of the single crystallite, but were obtained from the volume average of all the randomly distributed crystallites (see Eq. 3.32, averaging the results obtained from each single crystallite relationship as Eq. 4.3 over all possible orientations).

4.3.3.3. Multiple HAp inclusions with partial alignment

In reality, HAp crystallites are partially aligned, thus $K_{partial\_aligned}^{HAp}$ is expected to be between K_{random} and $K_{aligned}$.

$$K_{partial\_aligned}^{HAp} = (1 - f_{aligned})K_{random} + f_{aligned}K_{aligned} \qquad \text{(Eq. 4.5)}$$

where $f_{aligned}$ is the volume fraction of aligned crystallites with respect to all HAp crystallites, i.e. the degree of alignment of crystallites which could be revealed by SAXS measurements.

4.4. Experimental results and model evaluation

4.4.1. Nano-scale HAp crystallites distribution and mechanical response of dentine

The loading areas of the two cubic samples were accurately determined by micro-CT measurement. The loading areas were 4.466 mm^2 (HD2) and 4.413 mm^2 (HD3), respectively. Figure 4.2 a shows a WAXS pattern of dentine consisting of a system of

Debye-Scherrer rings (peaks). The apparent radial shifts of the (002) peak in the WAXS pattern were measured under uniaxial compressive loading applied on both longitudinal and transverse directions with respect to the preferential tubule direction. Values of the shifts along *x*-axis were used to obtain the elastic lattice strain variation along the loading direction. Figure 4.4 a-b show the experimental results of the applied stress vs. HAp crystallites lattice strain of samples HD2 and HD3, indicating a linear increasing tendency as expected. The maximum load used in the model of the two samples was limited to ~100 MPa in the elastic region. The ratio of the uniaxial stress and the average HAp crystallites lattice strain gives the apparent modulus, which is listed in Table 4.1. From Figure 4.4, it is observed that the dentine sample loaded along the longitudinal axis (HD3) has a slightly higher apparent modulus than the one loaded transversally (HD2). The residual (initial) strains were found to be quite small, namely, 205 $\mu\varepsilon$ (HD2) and -578.6 $\mu\varepsilon$ (HD3).

The (002) peak shifts along other directions were also measured by caking each pattern with a step of 20° (in the range of 0°-360°, Figure 4.2 a) to determine the normal strain component variation. The result is shown in polar coordinate as an azimuthal plot in Figure 4.5 a-b for HD2 and HD3 respectively, where 0° or 180° represents the loading direction and 90° or 360° represents that perpendicular to the loading direction. As symmetrical, the results in the typical range of 0°-90° display a positive normal strain from 60°-90° and a negative normal strain from 0°-60°.

Figure 4.2 b is one of the SAXS patterns of HD2 sample. The preferential orientation of HAp crystallites is shown in the figure to be roughly along the short axis of the elliptical pattern. Figure 4.2 c is the plot of $I(\varphi)$ of HD2 sample without any external load. The Gauss fit is also shown in the figure (red line). The detailed values of the orientation and degree of alignment were obtained by examining the plot of $I(\varphi)$ obtained from SAXS data, and interpreted in terms of Eq.3.11. The results are also listed in Table 4.1. The degree of alignment values for both samples are relatively small, indicating that, as expected, the distribution of HAp crystallites in human dentine is close to random, but nevertheless not entirely random.

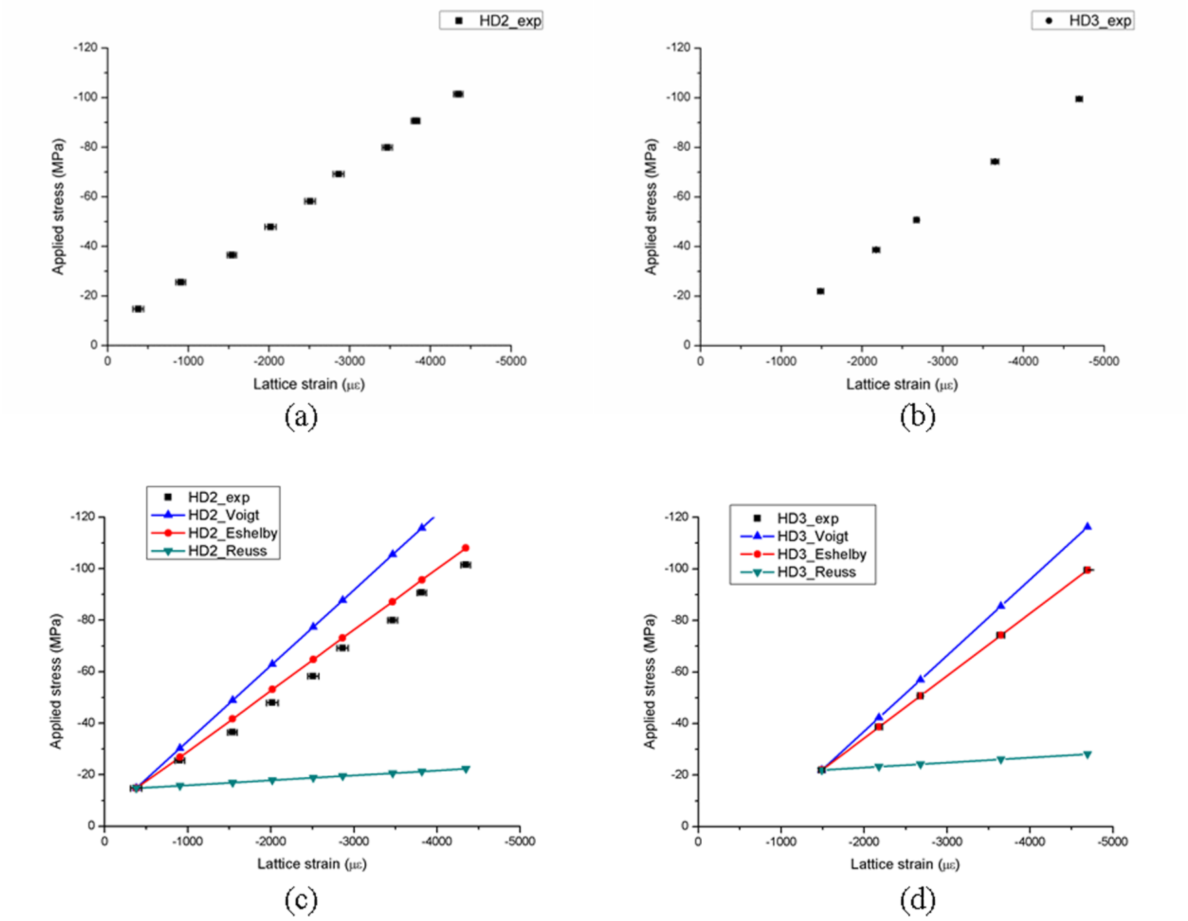

(a) (b) (c) (d)

Fig. 4.4 Comparison of experimental data (filled markers) and modelling results (solid lines) of applied compressive stress vs. elastic lattice strain for HAp crystallites. (a) HD2 experimental data (error bar: 1 SD); (b) HD3 experimental data (error bar: 1 SD); (c) HD2 data (filler markers) and modelling results (red line: multi-scale Eshelby model; blue line: Voigt bound; dark grey: Reuss bound) with the compressive stress along transverse direction with respect to the tubules; (d) HD3 data (black points) and modelling results (red line: multiscale Eshelby model; blue line: Voigt bound; dark grey: Reuss bound) with the compressive stress along longitudinal direction with respect to the tubules. The compressive stresses of HD2 and HD3 were uniformly selected under 100 MPa.

4.4.2. Evaluation and validation of the multi-scale Eshelby model

In the model, the material properties and other parameters were derived from literature and were refined by fitting with the experimental data. It is noted that a precise determination of the volume fraction of tubules in the first level is not available with the commercial micro-CT systems, due to the polychromatic nature of the X-ray source and the limited resolution. Thus, the reported volume fraction of tubules between 3.6 and 10.2% was used [180]. The average mineral concentration (HAp crystallites volume fraction) has been reported to be between 30.5% and 44.4% in human third molars, with a decreasing gradient towards the pulp [181]. In general, a Young’s modulus of 1GPa and Poisson’s ratio of 0.30 for collagen were given in literature, without taking into account the viscoelasticity and viscoplasticity for human dentine [82, 83]. Polycrystalline hydroxyapatite has a high Young’s modulus (40-117GPa), whereas the Poisson’s ratio is 0.27 [21]. However, these values of the Young’s modulus were all from a single perfect crystal. In biological mineralized composites like dentine, imperfectly shaped crystals are likely to exist, thus the high Young’s modulus may induce an error by overestimation [76]. In accordance with Qin and Swain, 40GPa was chosen here as a combination of the intertubular modulus (35.8GPa) and peritubular modulus (66.76GPa) in the respective volume fractions [82]. For the penny-shaped Eshelby tensor, only the ratio of radius and thickness (a_1/a_3) of the penny is needed [26, 27]. All the parameters refined to obtain a best fitting are listed in Table 4.1, also with the reported values from the literature.

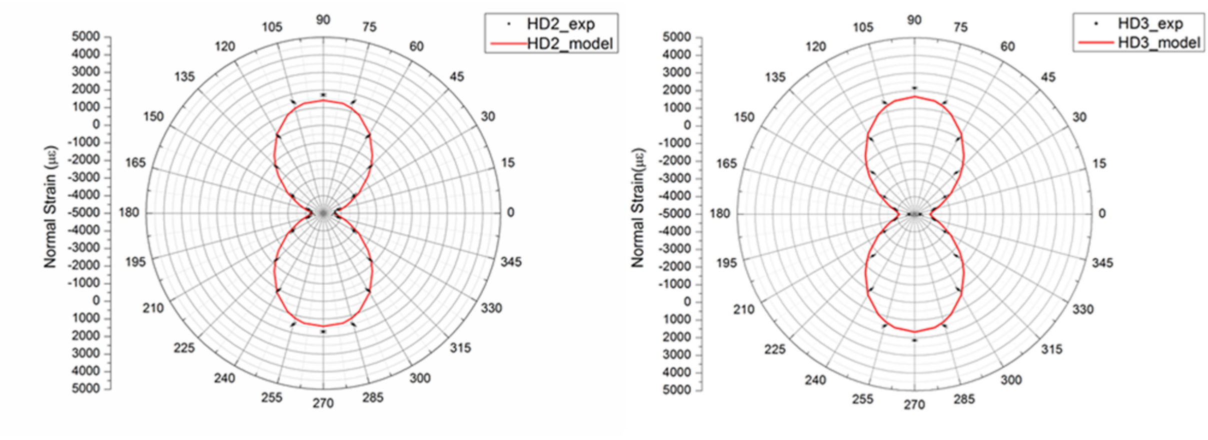

(a) (b)

Fig. 4.5 Comparison of experimental data and modelling results of normal strain component variation with orientation distribution (0 ° -360 °) under polar coordinates. (a) HD2 data (black points) and model fitting (red curve), with the compressive stress along transverse direction with respect to the tubules; (b) HD3 data (black points) and model fitting (red curve), with the compressive stress along longitudinal direction with respect to the tubules..

4.4.2.1. First-level model

The dentine matrix stress for the first level is only dependent on the volume fraction of tubules (see Eq. 4.2). The same volume fraction of tubules was used for both samples, thus they have the same value of matrix stress, $\sigma_{M1} = 1.09\sigma^A$.

4.4.2.2. Second-level model

Based on the SAXS measurement of degree of alignment (Table 4.1), the apparent modulus for each sample can be obtained from Eq. 4.5 with the values listed in Table 4.1. A comparison of the stress/strain curve along the loading direction between the experiment and model evaluation is shown in Figure 4.4 c-d, where the Voigt and Reuss bound predictions are also given. It is found that the Eshelby model prediction lies between the two bound results and is closer to the experimental data, which also reflects the overestimation of the apparent modulus in previous investigation using

Voigt bound [76]. Furthermore, both the Voigt and Reuss bounds predict a composite elastic modulus rather than the relation between the external load and internal HAp crystalline strain. Thus they could not directly reflect the experimental results optained from Synchrotron X-ray techniques. Meanwhile, the comparison of normal strain variation in the azimuthal plot is presented in Figure 4.5 a-b. Good agreement was also observed.

Tab. 4.1 Experimental results from SAXS/WAXS and refined parameters in the Eshelby model of the two dentine samples

Parameters	**HD2_value**	**HD3_value**	**Reference values**
Orientation (degree)	161	78	
Degree of alignment	0.289	0.168	
K_exp. (GPa)	22.129	24.156	
f_1	10%	10%	3.6 ~10.2% [45]
f_2	40%	38%	30.5% , 44.4% [46]
$C_{M1} = C_{M2}$	E_m=1.1GPa, v_m=0.3	E_m=0.8GPa, v_m=0.27	$E_{collagen}$=1GPa, $v_{collagen}$=0.30 [27]
C_{HAp}	E_{HAp}=90GPa, v_{HAp}=0.32	E_{HAp}=90GPa, v_{HAp}=0.32	E_{HAp}=40-117GPa, v_{HAp}=0.27 [47]
a_1 / a_3	31	31	(2-4)×30×100 nm^3[4,5]
K_model (GPa)	22.870	24.189	

4.5. Discussion

This is the first time that the combined SAXS/WAXS technique is used to capture the nano-scale structure and its influence on the macroscopic mechanical behaviour of human dentine. Moreover, it is important to emphasise that the study was conducted using penetrating radiation (synchrotron X-rays), i.e. a probe for bulk structure and strain analysis. Unlike the vast majority of studies that rely on surface characterization (SEM, AFM, nanoindentation, Raman, etc.), this ensures that the effects of sample preparation (e.g. cutting and storage) are minimal, since they typically affect depths not exceeding ~0.05mm out of the total sample thickness of 2mm. It is well-known that differences exist between dentine samples in the dry and wet conditions in terms of the mechanical properties. The hydrated dentine exhibited slight hexagonal anisotropy and almost disappeared when the specimens are dried, which was used in the present work [182]. Since the use of dry sample is more convenient for experimental set-up with *in situ* loading, this option was used throughout the present study,.

4.5.1. Refined parameters derived from the Eshelby model

The parameters refined by the multi-scale Eshelby model, listed in Table 4.1, lie within the range of the reported values in literature. This indicates that the model can be used to predict the nano-scale parameters which are hard obtain by other experimental methods. Of the five refined parameters, initially the sensitivity of those parameters to the result was tested , only to find the three key parameters, i.e. two volume fractions and Young’s modulus of the HAp crystallites. Among these three, Young’s modulus exerts the most significant influence on the result. In the optimization process, the two volume fractions were first fixed at approximate values, and Young's modulus was refined within the range reported in the literature. These three parameters showed by far the strongest influence on the match that could be achieved between the model prediction and measurements. In order to quantify the disagreement between model and experiment, a sum-of-squares measure of misfit between the experimental data and the modelling prediction was calculated. The search for the minimum proceeded as follows. Since HAp Young's modulus showed the strongest influence on the apparent modulus, this parameter was refined first. It is worth noting that a degree of noise is always present in the experimental data. As a consequence, implementing an automatic numerical algorithm was not thought to be appropriate. Instead, a series of trial calculations for different values of HAp Young's modulus were carried out, with decreasing increments, until a good value was found to within a small error margin of a few GPa. The value was then fixed, and the two volume fractions were refined. It is believed that this approach offers a reasonable route to assessing the key parameters, in the context of significant uncertainties remaining due to sample-to-sample variation, biological differences, effect of sample preparation and storage conditions, etc. The samples of dental tissue in this case were taken from the same young patients' teeth, and thus their structural and mechanical properties can be assumed to the similar as the volume fraction of tubules is expected to be high, and was assumed to be 10% for both samples. For the same reason, HAp crystallites were assumed to have a low volume fraction (~40%). Other reasons for the small volume fraction of HAp crystallites may include that the cubes were cut from a position near the pulp chamber where the volume fraction is relatively small [181], and the possible superficial demineralization effect of water storage [183]. Based on the above assumption about the two volume fractions, the refined Young's modulus of HAp crystallites was found to be approximately 90 GPa. At this stage, other parameters were refined as well, although it was found that they only had a minor effect on the apparent modulus result. The influence of the thickness variation on the apparent modulus was found to be small. For the crystal thickness 2 nm, K_model is respectively 22.87 GPa (HD2) and 24.189 GPa (HD3), while the K_model is 23.15 GPa (HD2) and 24.62 GPa (HD3) if the thickness is 4 nm. In order to get best fitting both along loading direction and for normal strain variation, 2 nm is the best refined parameter. This optimization process demonstrates the feasibility of simulating diseased or unhealthy tooth by just changing the three key parameters.

4.5.2. Residual strain

Indeed, a thin layer of initial residual strain may be induced at sample surface during cutting using a low speed diamond saw. However, as clarified above, the effect of this step on the overall measurement will not exceed 5% overall. Initial strain may also be associated with the natural growth process of the tooth. In any case, as shown in the result section 4.1, the initial existing residual strain is quite small. The unstrained reference measurement could introduce errors in determining the elastic strain evaluation, since the lattice parameters reported from the literature are mostly from the powdered samples, of which large volume of averaging the lattice parameters will over- or under- estimate the strain value in the structured sample. In addition, in this experiment, the X-ray beam illuminates on the same area of the sample, which largely reflect the lattice parameters evaluation due to the external loading. Furthermore, our experiment only considered the elastic response. This is reflected in the linearity of the experimental stress-strain curve, and is an underlying assumption for the Eshelby model. The presence of initial strain amounts to an offset that does not affect such parameters as the apparent modulus. In conclusion, the low level residual strain can be ignored in the present analysis, as it does not influence the elastic mechanical behaviour of the crystals. X-ray irradiation might cause a decrease in the residual strain, which suggests the presence of the interfacial damage of HAp-collagen. The dose has been calculated as 63.35 Gv, due to the relatively low flux in the bending magnets beamline. Therefore, the irradiation effect could be neglected. Furthermore, the apparent modulus does not change with the irradiation as discussed in [184], the irradiation damage is not discussed in this section.

4.5.3. Normal strain components variation

To characterize and validate the model of the strain components in different directions, the normal strain variation of the HAp crystallites with respect to different azimuthal angles (0°~90°) is shown in Figure 4.5. The ratio of the normal strain component at 90° to that at 0° (absolute value) for each sample is almost the Poisson’s ratio of the HAp crystallites, which is reasonable. Meanwhile, it should be noted that HAp crystallites oriented at around 60° azimuthal angle has no normal strain, i.e. no peak shift, which demonstrates that the HAp crystallites at this corresponding position are subjected to pure shear stress. From the model, since the first-level dentine matrix stresses are the same for the two samples, the difference in the modulus as well as the normal strain component variation may result from different orientations and degrees of alignment of HAp crystallites (observed and measured by SAXS).

4.5.4. HAp crystallites distribution effects

The extended multi-scale Eshelby model established in the present analysis is able to capture the relationship between the function of human dentine and its multi-scale structure. Moreover, it is also capable of evaluating the effect of the nano-scale structure (e.g. HAp crystallites distribution) on the macroscopic mechanical response, which was not included in earlier studies [76, 132]. To demonstrate the detailed effect of crystal distribution on the apparent modulus, a schematic diagram of a 3-D model of perfectly aligned crystals is selected (Figure 4.6 a) with only one angle freedom φ around *Z*-axis. All aligned HAp crystallites are initially oriented with 90° angle to the platelet surface along the global *Y*-axis, which represents the position of $\varphi = 0^o$. The variation of $K_{aligned}$ along the loading direction was calculated and visualized in Figure 4.6 b (only the result of HD2 is shown since both samples have similar results). The larger the value of $K_{aligned}$ is, the smaller the average lattice strain of HAp crystallites will be under a certain value of external load, i.e. the stiffer the HAp crystallites will be. It is found that the value of $K_{aligned}$ along the loading direction is strongly dependent on the crystal orientation direction. The orientations of HD2 and HD3 in our *in situ* loading experiments were 161° and 78°, respectively. Hence, from Figure 4.6 b, $K_{aligned\_HD3} > K_{aligned\_HD2}$. However, sample HD3 had a lower degree of alignment overall, so that overall the $K^{HAp}_{partial\_aligned\_HD3}$ value lies closer to K_{random}, which is the reason for the similar results of the apparent moduli of the two samples (Table 4.1).

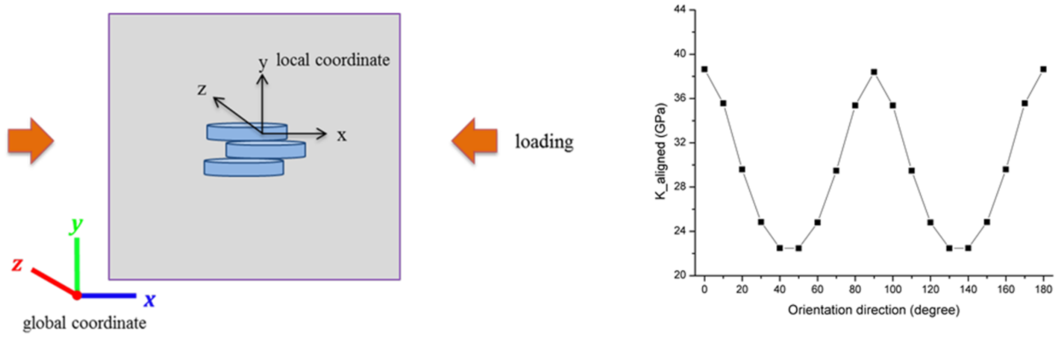

(a) (b)

Fig. 4.6 Preferential alignment effect on the apparent modulus of HAp crystallites in human dentine. (a) A simplified example of the alignment of HAp crystallites. The beam direction is along the global *Z*-axis and the alignment here represents the angle between the local *x*-axis and global *X*-axis (initially aligned angle $\varphi = 0^o$, i.e. the local *x*-axis of a penny is initially along global *X*-axis). (b) By changing the alignment angle (0°-180°), the average strain of the crystals along loading direction can be obtained by the multi-scale Eshelby model, which then indicates that $K_{aligned}$ varies with respect to the preferential alignment angle..

4.6. Conclusions

In this chapter, the relationship between the nano-scale crystal distribution and macroscopic mechanical elastic response of human dentine was investigated for the first time using a combined *in situ* synchrotron SAXS/WAXS technique. This provided access to the information on both the structural and mechanical aspects of the sample that thus allowed us to make further progress compared to previous studies that only used WAXS [131] to determine the HAp crystallites strain evolution in dentine but the main domain of SAXS pattern from two-phase system was not used to reveal the nano particles distribution, only to focus on the collagen diffraction. Moreover, an extended multi-scale Eshelby inclusion model was established to estimate and evaluate the elastic material properties of dentine as a two-level composite in terms of its constituents, showing good agreement with the experimental data both on lattice strain along loading direction and normal strain component in a general azimuthal plot, improving the Voigt composite model earlier proposed for bovine dentine [76]. The difference in the mechanical behaviour observed in the experimental results can be attributed to the second-level model effects, i.e. the degree of alignment and orientation angles.

Through this systematic experiment and modelling work, we are capable of observing the nano-scale structure, which is used to validate the model linking the nano-particle arrangement and deformation behaviour to the macroscopic loading response. In addition, the parameter refinement and validation in the model adopted in the present study offers a possibility in the identification of nano-scale parameters. The usual limitations of experimental characterization techniques such as nanoindentation or microscopy, e.g. confinement to the sample surface, make parameter identification difficult. We therefore argue that our approach enables the general characterization of the structure-property relationship in hierarchical biomaterials. An improved understanding of the multi-scale structural-mechanical properties within human dentine is important for developing better prosthetic materials and dental fillings. It may also shed light on the mechanical property evolution due to multi-scale structural changes within dentine because of disease and treatment.

Chapter 5

Hierarchical modelling of *in situ* elastic deformation of human enamel based on photoelastic and X-ray scattering analysis of stresses and strains

This chapter is based on the following published manuscripts:

- Tan Sui, Michael Sandholzer, et al, Hierarchical modelling of elastic behaviour of human enamel based on synchrotron diffraction characterization, Journal of Structural Biology, Vol. 184 (2), pp.136-146, 2013
- Tan Sui, Alexander M. Korsunsky, Hierarchical modelling of elastic behaviour of human dental tissue based on synchrotron diffraction characterization: Chapter **7** in *Advanced Healthcare Materials*, A. Tiwari, Ed., Advanced Materials Series, WILEY-Scrivener Publishing LLC, USA, 2013.
- Tan Sui, Michael Sandholzer, et al, Hierarchical modelling of in situ elastic deformation of human enamel based on photoelastic and diffraction analysis of stresses and strains, Acta Biomaterialia, Vol. 10 (1), pp. 343-354, 2014

5.1. Brief introduction

This Chapter focuses on the two-level hierarchical mineralised human enamel. Over half a century, research has been carried out on the mechanical properties of enamel, and on its macro- and micro-structure [35, 185]). To date, few studies have focused on how the mechanical behaviour of this tissue is affected by both the rod orientation at micro-scale and the preferred orientation of mineral crystallites at the nano-scale. Investigations at the nano-scale require the use of advanced techniques and systematic models to establish a firm basis for understanding the hierarchical structure–property relationships.

Synchrotron SAXS/WAXS techniques have been applied only recently to the study of mineralized biological composites, such as bones and bovine teeth [186]. Very few studies devoted to human enamel have been published [135], and early studies did not take into account the nanoparticle shape, size and orientation distribution [136]. Therefore, a deep understanding of the relationship between the nano-scale structure and the macroscopic mechanical behaviour of human enamel is still lacking.

A number of different models of composite deformation have been previously used to describe the elastic response of mineralized biological tissues that arises through the interaction between different constituent phases [136]. This approach also allowed the unknown properties of the component phases to be determined [187]. However, these models mainly focused on the analysis of deformation only in one direction (loading direction) and therefore were not able to provide adequate consideration of the elastic anisotropy. The multiscale Eshelby modelling approach was shown to capture the micromechanical response reasonably well using the two-level hierarchical description of the structure of dentine and enamel, with each level consisting of an isotropic matrix and a group of anisotropic inclusions.

In this study, two complementary synchrotron X-ray diffraction techniques, wide and small angle X-ray scattering (WAXS/SAXS) were used preliminarily to obtain multi-scale quantitative information about the structure and deformation response of human enamel under longitudinal compressive loading. Initial test experiments were carried out in which compressive load was applied directly to the small ($\sim 2\times 2\times 2$ mm^3)

enamel samples. It appeared that the attempt to apply compressive load of sufficient magnitude to cause measurable straining of HAp crystallites led to crushing and splitting of the sample in lateral directions, i.e. transversely to the axis of load application. Therefore, a novel experimental setup needed to be proposed and developed to enable quantitative stress distribution evaluation. The sample was embedded in birefringent mounting epoxy that provided moderate additional lateral constraint and prevented sample splitting. It is worth noting that this set up brought about the need to evaluate the transmission of the applied load through the epoxy mount to the sample embedded at its centre. This challenge was addressed by employing photoelastic stress evaluation techniques in parallel with diffraction strain analysis. Since the epoxy mount had the shape of a short cylinder (thick disc), it was possible to examine the influence of different relative orientations of the rod directions with respect to *in situ* uniaxial compressive loading. Data analysis allowed the apparent modulus to be determined linking the external load and the internal lattice strain in hydroxyapatite (HAp) crystallites. Two sets of experimental data were collected, with the compressive load applied along and transversely to the rod direction. The data were analysed using an advanced multi-scale Eshelby inclusion model that takes into account the two-level hierarchical structure of human enamel, and captures the differing rod directions and orientation distributions of HAp crystallites. The achieved satisfactory agreement between the model and the experimental data, in terms of the values of multi-directional strain components under the action of differently orientated loads, suggests that the multi-scale approach reasonably captures the structure-property relationship between the hierarchical architecture of human enamel and its response to the applied forces. This novel and systematic approach can be used to improve the interpretation of the mechanical properties of enamel, as well as of the textured hierarchical biomaterials in general.

5.2. Materials and methods

5.2.1. Sample preparation

Freshly extracted human third molar with no apparent damage, caries or other dental treatments were used for this study (ethical approval obtained from the National Research Ethics Committee; NHS-REC reference 09.H0405.33/ Consortium R&D No. 1465). Two millimetres thick enamel disks were cut from the same tooth using a low speed diamond saw (Isomet Buehler Ltd., Lake Bluff, Illinois, USA) and were further prepared into smaller bars. A series of polishing papers were used to refine the final $2\times2\times2$ mm^3 cube of enamel. Regarding the rod direction of the enamel sample, the cut in the prepared sample was close to the region perpendicular to the occlusion surface. Therefore, the predominant rod direction was the longitudinal direction in the sample. To determine the measuring positions and loading cross-section for the SAXS/WAXS experiments, a micro-CT scan was carried out as illustrated in Figure 5.1 a.

In the improved experimental configuration, rather than loading the enamel cubes directly, they were first embedded in a photoelastic epoxy disk that was then compressed diametrally. In previous attempts to carry out the measurements it was found that without the protection of the epoxy disk, early in the loading samples developed microcracks that reduced the accuracy of measurement and later on led to sample splitting. Due to its birefringent properties, epoxy offers the possibility of deducing information about the internal stress distribution using photoelastic techniques. The enamel cubes were placed in the centre of a 12 mm diameter cylindrical mould and embedded in epoxy resin (Buehler Epokwick, ITW Test & Measurement GmbH, Dusseldorf, Germany). The disks' surfaces were subsequently polished to expose the enamel surfaces.

In total, one cubic enamel sample was prepared for the direct loading test (Figure 5.1 b) and another three cubic enamel samples were prepared (designated #6, #7 and #3) with different rod directions with respect to the loading direction (*x*-axis in Figure 5.1 c). The predominant direction of rods in sample #6 was parallel to the loading direction with rods lying in the *x*-*y* plane, in sample #7 it was perpendicular to the loading direction with rods lying in the *x*-*y* plane, and in sample #3 it was perpendicular to the loading direction with rods lying in the *y*-*z* plane.

5.2.2. *In situ* X-ray diffraction measurements

5.2.2.1. Mechanical loading setup

A schematic diagram of the experimental set-up is shown in Figure 5.1 b and c, where Figure 5.1 b is for the preliminary experiment and Figure 5.2 c is for the improved experiment. For the preliminary experiment, the sample of human enamel was slowly deformed in compression along the *x*-axis in the laboratory coordinates (Figure 5.1 b) at the displacement rate of 0.2 mm/min until failure, using a remotely operated and monitored compression rig (Deben, Suffolk, UK), with a 5 kN calibrated load cell. The rig was equipped with custom-made jaws, allowing a high-energy transmission X-ray setup to be used.

As for the improved experiment, the epoxy disk which contains the cubic sample of human enamel was also slowly deformed along *x*-axis in laboratory coordinates

(Figure 5.1 c). Compressive loading was applied along the *x*-axis at the load levels from 0N to 400N using the same remotely operated and monitored compression rig with the same load cell with the preliminary experiment. The load was incrementally increased (in 25 N steps and a loading rate of 3.8 Ns^{-1}) and held constant while the WAXS and photoelastic patterns were collected.

5.2.2.2. Beamline diffraction setup

Both the experiments were performed on the B16 test beamline at Diamond Light Source (DLS, Oxford, UK). A monochromatic X-ray beam of 20 keV photon energy (wavelength: λ=0.062 nm) was collimated by slits to a spot size of 0.5×0.5 mm^2.

In the preliminary experimental set-up, two separate WAXS and SAXS detectors were alternately set up to collect the patterns at consecutive loading increments downstream of the beam. WAXS diffraction patterns were recorded using a Photonic Science Image Star 9000 detector (Photonic Science Ltd., UK) placed at a sample-to-camera distance of 128.72 mm. Further downstream, a Pilatus 300K detector (Dectris, Baden, Switzerland) was positioned at a distance of 4358.47 mm to collect the SAXS patterns. In order to record both the WAXS and SAXS patterns at each scanning location, the WAXS detector was translated laterally to expose the SAXS detector after each WAXS exposure. A lightly compacted disk of NIST standard silicon powder was used for precise WAXS calibration of the sample to detector distance using diffraction pattern analysis [188]. A dry chicken collagen sample inserted close to the sample position were used as calibration for SAXS data analysis and to determine the sample-to-detector distance with the required precision [177].

In the improved experimental set-up, radiographic images of the samples were initially used to align the samples and determine the position of interest. The incident beam on the sample was perpendicular to the loading direction. Space restrictions of the beamline meant that the sample had to be translated laterally from the WAXS configuration into the photoelastic set-up at each consecutive loading increment. WAXS diffraction patterns were recorded using a Photonic Science Image Star 9000 detector (Photonic Science Ltd., UK) which was placed 177.33 mm downstream of the sample.

5.2.2.3. Photoelasticity setup

A Sharples S-12 demonstration polariscope was used to collect the *in situ* photoelastic images in the improved experiment. The setup consisted of light source, polarizers, quarter-wave plates and digital SLR camera as shown in Figure 5.1 c. The quarter-wave plates remained crossed and polarizers were aligned crossed to establish the dark field. A green-light filter (λ=550 nm) was also placed between the light source and the camera lens in order to obtain monochromatic fringes to simplify the analysis. A solid epoxy disk (without the sample in the centre) produced from the same batch of epoxy resin was used as a common calibration specimen.

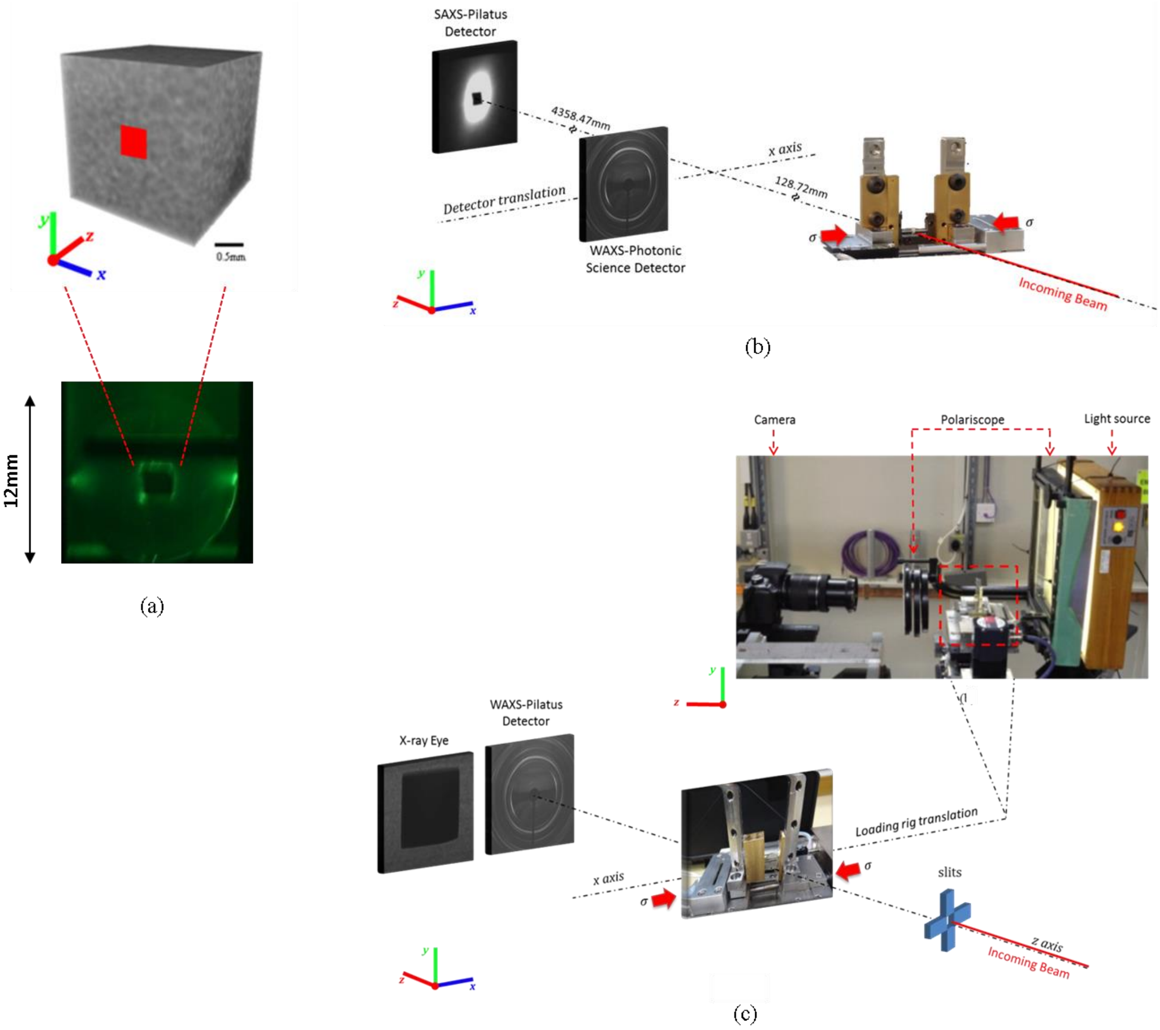

(a)

(b)

(c)

Fig. 5.1 Schematic diagram of *in situ* uniaxial loading experimental setup and cubic enamel sample; (a) The $2\times2\times2$ mm^3 cubes of enamel sample and the sample embedded in the epoxy; (b) The sample was under uniaxial compressive loading on the compression stage. The monochromatic X-ray beam was directed perpendicular to the sample surface and the loading direction. WAXS and SAXS diffraction patterns were recorded at each loading step at three locations on the sample. The WAXS detector was translated laterally out of the beam to expose the SAXS detector after each collection of WAXS. (c) The improved experimental setup composed of synchrotron beam set-up and photoelastic set-up. An X-ray Eye detector was used to ensure that the point of interaction between the beam and sample was in the central position of the enamel specimen. At each detection point, following centring, the X-ray Eye detector was translated laterally out of the beam to expose the WAXS detector. WAXS diffraction patterns were recorded at each loading step in three locations on the sample. After each WAXS pattern collection, the compression stage was laterally translated to the photoelastic set-up to collect the photoelastic patterns.

5.2.3. Data interpretation

5.2.3.1. SAXS/WAXS data analysis of pure enamel sample

A typical WAXS pattern of HAp crystallites in the pure enamel sample is shown in Figure 5.2 a (only the (002) peak is selected for interpretation). At each compressive load step, the beam was scanned between the loading platens, and only the results from the middle were selected for WAXS interpretation to guarantee that the same location was studied during compressive deformation. The (002) peak of interest from each pattern was "caked" within the range of 20^{o} around the loading direction (Figure 5.2 a). Furthermore, each pattern was "caked" with the same width of 20° in the direction of -15 °, 0 °, 15 °, 30 ° and 45 ° with respect to the (002) peak (see Figure 5.2 a). Due to the much larger azimuthal range of the WAXS rings in dentine (see Chapter 4) than that in enamel, more directional normal strains can be chosen from the rings in dentine. In order to cover the whole available azimuthal range, different selection procedures with respect to dentine and enamel were used. The normal strain component along the centre direction of each "cake slice" represents the strain component in the corresponding orientation. Subsequently the 1-D radial plot of each individual (002) peak within each sector was fitted with a Gaussian function to obtain the peak centre position. The sample under strain-free condition (without any load) was characterised by WAXS and used as the reference state for strain measurement. As the load increased, the shift of the peak centre position with respect to the strain-free reference point allowed the calculation of the elastic lattice strain of the HAp crystallites. In addition, the structural orientation angle was determined from the strain-free sample by azimuthal-radial "caking" of the (002) peak over the range of available peak (-30^{o} ~ 60^{o}), and fitting the azimuthal centre position of the pronounced peaks of $I_{WAXS}(\varphi) \sim \varphi_{\_WAXS}$ plot (Figure 5.2 c) [139].

For SAXS data analysis, the pattern from the strain-free enamel sample was taken as a reference. To quantify the degree of alignment in enamel, the 2-D SAXS patterns were processed by integrating over the entire relevant range of scattering vector *q*, resulting in a function $I_{SAXS}(\varphi)$ of the azimuthal angle $\varphi_{\_SAXS}$ (Figure 5.2 d) [153, 154]. The predominant orientation φ_{0_SAXS} of the mineral crystals is determined by the position of the two peaks in the plot of $I_{SAXS}(\varphi)$ (e.g. φ_{0_SAXS} in Figure 5.2 d), which corresponds to the short axis of SAXS pattern. Further, the degree of alignment ρ with respect to the predominant orientation of HAp crystallites can be calculated by Eq. 3.11.

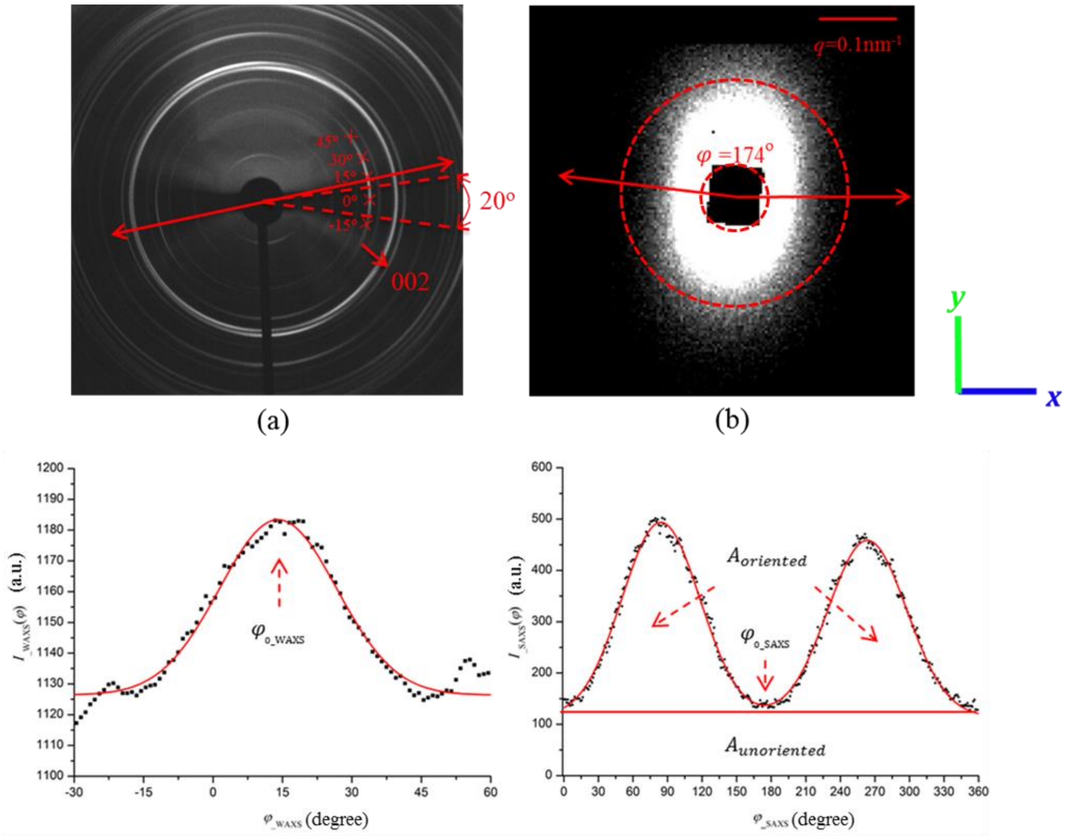

(a) (b)

(c) (d)

Fig. 5.2 (a) A representative enamel WAXS pattern of Debye-Scherrer rings with different intensities. The dark region in the centre is the beamstop. The (002) peak is marked with a small red arrow. Peak shifts at different positions on the (002) ring represent the average strains of (002) along different directions. Multiple angles with respect to the *x*-axis were “caked” (i.e. binned azimuthally within a 20^o range) in order to examine the strain variation (five angles are shown as examples -15^o, 0^o, 15^o, 30^o, 45^o). The direction with the double-arrow line indicates the preferred orientation interpreted from WAXS. (b) A representative enamel SAXS pattern. The direction of the short axis of the ellipse pattern indicates the predominant orientation of the HAp crystallites. The integration over *q* was performed from the beamstop radius to the outer radius of the pattern as marked with red dash. (c) A plot of $I_{WAXS}(\varphi) \sim \varphi_{\_WAXS}$ without any external load (black dots, Gaussian fit indicated in red). The predominant orientation φ_{0_WAXS} =14^o is given by the position of the pronounced peak centre. (d) A plot of $I_{SAXS}(\varphi) \sim \varphi_{\_SAXS}$ without any external load (black dots, Gaussian fit shown in red). The predominant orientation φ_{0_SAXS} =174^o is the average position of the two peaks. The ratio $A_{oriented} / (A_{oriented} + A_{unoriented})$ gives the degree of alignment.

5.2.3.2. WAXS data analysis of embedded enamel sample

For the improved experiment, only the WAXS technique was used because the preliminary experiment has shown that the nano-particle distribution determined by SAXS and WAXS is similar. In addition, such information obtained by WAXS is more reliable since it is more sensitive to the texture distribution of crystallites. Typical WAXS patterns of HAp crystallites of the three embedded enamel samples are shown in Figure 5.3 a-c and only the peaks of interest were selected for interpretation (#6 (002) peak, #7 (002) peak and #3 (210) peak). For samples #6 and #7, the (002) lattice plane reflection ring from HAp crystallites contains the information on the orientation of the *c*-axis of the crystals as well as the fibril orientation. This is due to the fact that the enamel structure has a characteristic strong and distinct parallel orientation of needle-shape crystals [76]. For sample #3 the *c*-axes of the crystals lie perpendicular to the measurement plane, so that the (002) peak is absent or weak. Therefore, another peak (210) needed to be selected. At each compressive loading step, the X-ray Eye detector (Photonic Science X-ray MiniFDI) was used to verify the central position. The Deben compression rig applied the load by displacing the two platens towards each other in a balanced way (i.e. at the same speed in an opposite direction), so as to preserve the centre position approximately stationary. This ensured that a consistent sample position in the centre of the sample was interrogated throughout the WAXS data collection. The elastic lattice strain of HAp crystallites was calculated as stated in section 3.1.4.1.

Initially the peak of interest on each pattern was "caked" around a particular azimuthal angle over the within a range of 20^o. The azimuthal angle is defined as the angle with respect to the *x*-axis in the x-y plane (perpendicular to the incident beam). For each specimen, a different azimuthal range was selected due to the preferred orientation of crystallites in the sample (for sample #6 between 0^o-45^o, for sample #7 between 45^o-90^o, and for sample #3 the available range was between 0^o-90^o). This is indicated by the red crosses in Figure 5.3 a-c. The lattice spacing value deduced for the centre direction of each caked sector gives rise to the normal strain value for the corresponding orientation (see Figure 5.3 a-c). To determine the lattice spacing, the experimental diffraction pattern was converted to the integrated 1-D plots of intensity vs. scattering angle. These plots for the three samples with peaks of interest are shown in Figure 5.3 d-f. The peaks of interest were fitted with a Gaussian function in order to obtain the peak centre. With increasing load, the peak centre position moved with respect to the strain-free reference value. Finally, the calculation of the HAp crystallites elastic lattice strain was performed using Eq. 3.6.

The orientation of the HAp crystallites was also carried out using a similar “caking” approach. In this case, the 1-D intensity was plotted as a function of azimuthal angle $I_{WAXS}(\varphi) \sim \varphi_{\_WAXS}$ (Figure 5.3 m-n). Gaussian fitting of the azimuthal centre position of these peaks of plots can then be used to define an associated orientation [139].

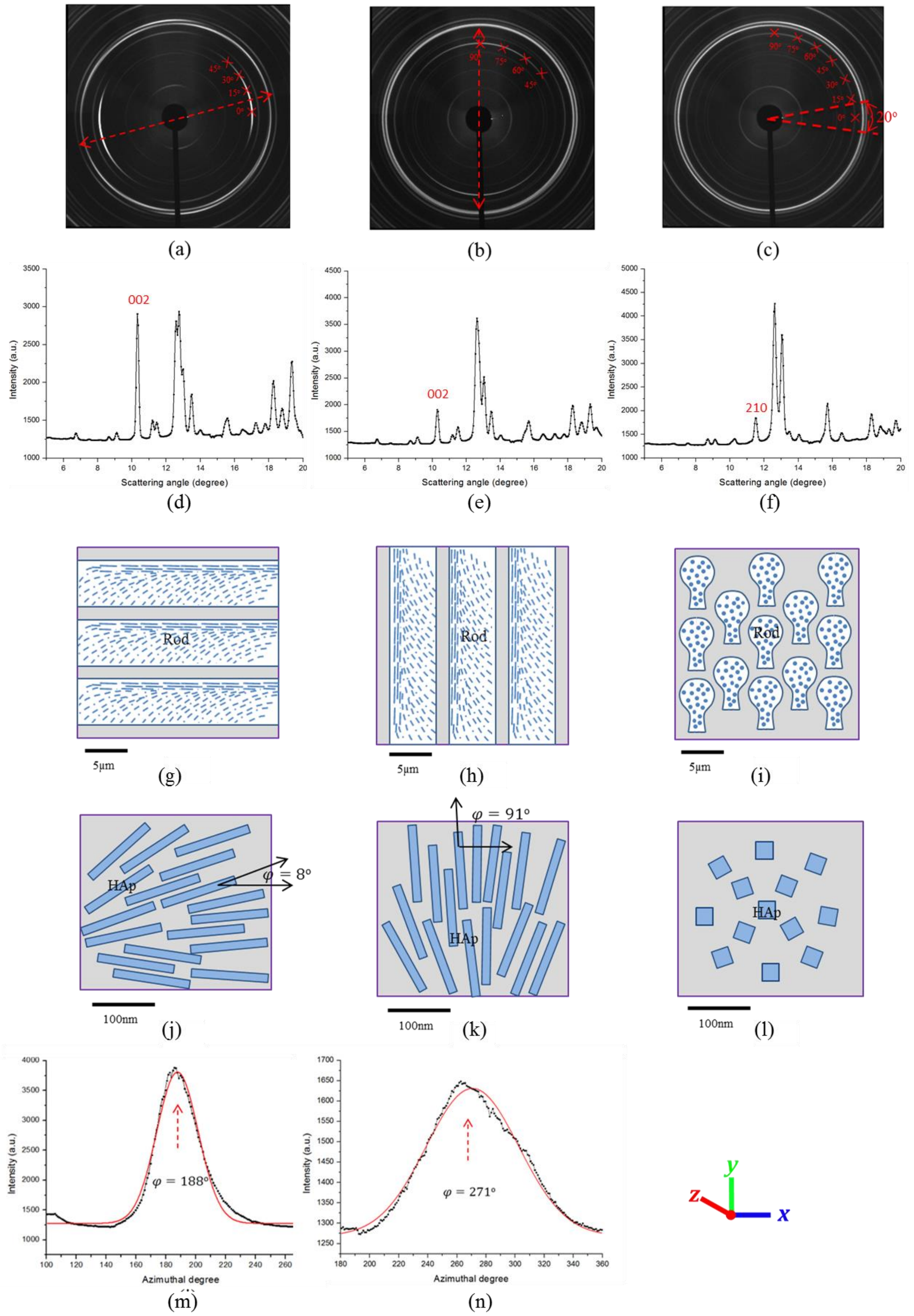

Fig. 5.3 Geometrical assumptions of three distinct orientation enamel sample. (a)-(c) Representative WAXS patterns of Debye-Scherrer rings with differing intensities corresponding to each of the three samples (#6, #7 and #3 respectively). The dark region in the centre of the pattern is the beamstop. The direction with the red dashed double-arrow lines in (b) and (c) indicate the preferred orientation of HAp crystallites. Multiple angles with respect to the x-axis were caked (within a 20° range) in order to examine the normal strain

variation (red crosses). (d)-(f) The experimental diffraction pattern of integrated intensity vs. scattering angle 2θ of the three samples (#6, #7 and #3 respectively), and the peaks of interested are marked in red (g)-(i) Schematic illustration of the first-level geometric model of aligned rods with embedded HAp crystallites in the three samples with respect to the laboratory coordinate system, the loading direction is into the page. (j-l) Schematic illustration of the second-level geometric model of HAp crystallites with different crystalline distributions viewed in the *x*-*y* plane (#6: with the preferred orientation at 8^{o}, #7: with the preferred orientation at 91^{o} and #3: random); (m)-(n) The intensity variation with the Gaussian fit (red curve) corresponding to the orientation distribution of samples #6 and #7.

5.2.3.3. Photoelasticity data analysis

For the calibration of the epoxy property to be used in finite element analysis, the solid epoxy disk without samples was preliminarily deformed. A series of loads (10 N, 100 N, 200 N, 300 N and 400 N) were applied to an empty epoxy disk and the corresponding fringe numbers were recorded as shown in the first row of Figure 5.5. As illustrated in section 3.3.2, an average value for photoelastic properties was determined as *f*=21.22 (N/mm•fringe). The patterns on the second row of epoxy with enamel samples in Figure 5.5 were then collected at the same series of loads. The numbers and distribution of fringes were recorded and then the difference between the principal stresses calculated by Eq. 3.34 was obtained and then compared with finite element modelling to determine the epoxy property. Since the loading was applied along the *x*-axis, with the epoxy disk lying in the *x*-*y* plane, the principal stresses were $\sigma_1 < 0$, $\sigma_2 > 0$ and $\sigma_3 = 0$.

5.3. Modelling

5.3.1. Geometrical assumptions

An outline of the geometrical assumption used in the enamel hierarchical model is given here. At the first structural level, the geometric model of human enamel involves aligned rods with a keyhole-shaped cross-section. The second-level structure consists of bundles of HAp needle-shaped crystallites found within each rod. These bundles are roughly aligned with the longitudinal direction of the rods with some minor misorientation. Figure 5.4 a illustrates the structure of enamel, modified from Habelitz [38] and the distribution of the HAp crystallites within the rod in 3D. For the simple way to demonstrate the misorientation distribution by considering the partial alignment of the crystallites, Figure 5.4 b-d provide schematic illustration of the geometric model derived from the enamel structure, where the first level regards the whole enamel sample as composed of aligned rods within a protein matrix phase (Figure 5.4 b), and the second level considers the rod as a composite in detail, consisting of partially aligned HAp crystallites and a protein matrix. This partially aligned distribution of HAp crystallites is based on the observation using scanning transmission electron microscopy (STEM), where a high percentage of HAp crystallites have a perfect alignment while the other crystals are more randomly distributed [49].

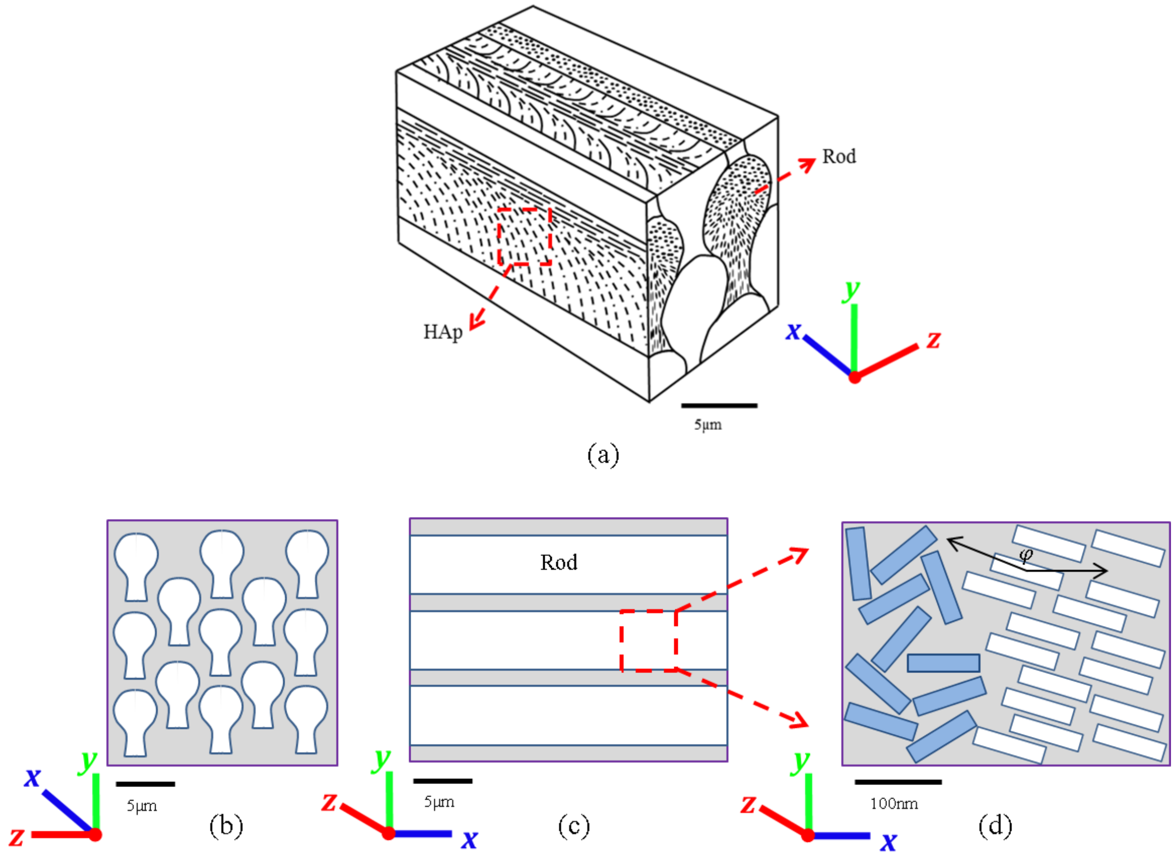

Fig. 5.4 Schematic diagram of two-level structure of human enamel. (a) A schematic 3D structure of enamel, showing keyhole-like rods aligned in parallel (modified from Habelitz (2001). The rods contain organized and bundled HAp crystallites; (b) Rods viewed along their longitudinal direction; (c) Rods viewed along their transverse direction; (d) The structure of partial aligned needle-like HAp crystallites viewed from the cross-section parallel to the rods direction. The alignment angle φ with respect to the global *x*-axis is also shown.

In order to achieve the orientation distribution of the rods in the enamel samples, improved illustration is shown in Figure 5.3 g-i. The degree of misorientation can be determined from careful WAXS data interpretation. This analysis assumes that the peak intensity at a given azimuthal angle is proportional to the number of HAp crystallites of this orientation [49]. Furthermore, the predicted distributions of needle-shaped HAp crystallites (in the measured cross-section, perpendicular to the beam direction) are shown in Figure 5.3 j-l in which the misorientation distribution is based on the intensity plots in Figure 5.3 m-n. The principal orientation of sample #3 is aligned so that orientation component is observed perpendicular to the beam, and therefore no equivalent plot is produced. Both levels are non-dilute systems consisting of a number of inhomogeneous inclusions. For simplicity, both rod and HAp crystallites are assumed to be of needle shape.

5.3.2. Two-level Eshelby model of enamel

5.3.2.1. First-level model: multiple aligned rod inclusions within enamel

The purpose of the first-level model for human enamel, which describes multiple aligned rod inclusions within enamel, is to establish the elastic relationship between the externally applied stress σ^A and the stress in the rod-like inclusions $\sigma^{inclusion} = \sigma^{rod}$, which has been shown in Eq. 3.28 (the orientation effect of rods by the orientation matrix T is included here, giving the orientation of an individual rod with respect to the laboratory coordinate system)

$$\sigma^{rod} = \left\{ T - (1 - f_1) C_{M1} (S_{rod} - I) \left\{ (C_{M1} - C_{rod}) \left[S_{rod} - f_1 (S_{rod} - I) \right] - C_{M1} \right\}^{-1} (C_{M1} - C_{rod}) T^{-T} C_{M1}{}^{-1} \right\} \sigma^A$$

or written more simply, $\sigma^{rod} = H\sigma^A$ (Eq. 5.1)

In the above expression, f_1 is the volume fraction of rods in the enamel, S_{rod} is the Eshelby tensor for a cylinder that approximates the rod shape and C_{M1}, C_{rod} are the stiffness tensors of the protein matrix and rod respectively. In the present model, the laboratory coordinate is fixed, and it is assumed that the rods are all aligned along the loading direction, thus T is constant. The rod stiffness remains to be determined from the second-level model.

5.3.2.2. Second-level model: partially aligned HAp inclusions within each individual rod

The purpose of the second-level model of enamel, which describes partially aligned HAp inclusions within one rod, is to establish the relationship between the rod inclusion stress and the average strain in the HAp crystallites within rod $\langle \varepsilon \rangle^{HAp}$ (σ^{rod}=$K_1 \langle \varepsilon \rangle^{HAp}$). The measured lattice strain corresponds to the mean strain value for all the crystallites within the considered gauge volume [179]. Due to the partial alignment of HAp crystallites within the rod, the real apparent stiffness K_1 is to be given by the values bounded by the two extreme cases, namely that of fully random distribution and that of perfect alignment.

a). Multiple perfectly aligned HAp crystallites

Supposing all the crystals are perfectly aligned and the alignment direction is described by the orientation matrix *T*, the relationship between the average HAp crystallites strain and the rod inclusion stress obtained from the first-level model has been established by Eq. 3.31:

$$\langle \varepsilon \rangle_{aligned}^{HAp} = T^T \left\{ \left\{ \left(I - C_{m2}{}^{-1} \langle C \rangle_{HAp} \right)^{-1} \left[\langle S \rangle_{HAp} - f_2(\langle S \rangle_{HAp} - I) \right]^{-1} - I \right\}^{-1} T^{-T} + T^{-T} \right\} C_{M2}{}^{-1} \sigma^{rod}$$

or expressed more simply $\sigma^{rod} = K_{aligned} \langle \varepsilon \rangle_{aligned}^{HAp}$ (Eq. 5.2)

where $\langle C \rangle_{HAp}$ and $\langle S \rangle_{HAp}$ are the average stiffness and Eshelby tensor. Since all the crystallites are perfectly aligned, $\langle C \rangle_{HAp}$=C_{HAp}, $\langle S_{HAp} \rangle$=S_{HAp}. Note that a single HAp crystallite in the second level can be regarded as a single inhomogeneity with needle-like shape, thus the Eshelby tensor for a single HAp crystallite should be the same as the rod inclusion ($S_{HAp} = S_{rod}$) and the stiffness of a single HAp crystallite has been reported to be transversely isotropic [189]. In Eq. 5.2, different orientation angles (different matrices *T*) would lead to different values of $\langle \varepsilon \rangle_{aligned}^{HAp}$.

b). Multiple randomly distributed HAp crystallites

Supposing all the crystals are randomly distributed, the relationship between the average strain in HAp crystallites and rod stress is independent of the orientation matrix in Eq. 5.2. Thus the relationship becomes

$$\langle \varepsilon \rangle_{random}^{HAp} = \left\{ \left\{ \left(I - C_{M2}{}^{-1} \langle C \rangle_{HAp} \right)^{-1} \left[\langle S \rangle_{HAp} - f_2 (\langle S \rangle_{HAp} - I) \right]^{-1} - I \right\}^{-1} + I \right\} C_{M2}{}^{-1} \sigma^{rod}$$

or expressed more simply $\sigma^{rod} = K_{random} \langle \varepsilon \rangle_{random}^{HAp}$ (Eq. 5.3)

Different from perfectly aligned crystallites, the average value of $\langle S \rangle_{HAp}$ can no longer be the value of a single crystallite, but should be obtained by the volume average value of all the crystallites. However, as an alternative, the averaging effect can be captured by using the single crystallite relationship as Eq. 5.2 and averaging over all the values with different Euler angles (see Eq. 3.32, averaging the results obtained from each single crystal relationship as Eq. 5.2 over all possible orientations).

c). Multiple HAp inclusions with partially aligned distribution

In order to model the observed preferred orientation of HAp inclusions (Figure 5.3 d), we represent it as a superposition of a random distribution with a volume fraction $f_{aligned}$ of perfectly aligned particles. In this case the overall apparent stiffness for the partially aligned HAp crystallites $K_{partial\_aligned}^{HAp}$ is given by the rule of mixture between K_{random} and $K_{aligned}$:

$$K_{partial\_aligned}^{HAp} = (1 - f_{aligned})K_{random} + f_{aligned}K_{aligned} \qquad \text{(Eq. 5.4)}$$

where $(1 - f_{aligned})$ now represents the volume fraction of the randomly distributed crystallites, and $f_{aligned}$ corresponds to the degree of alignment of crystallites revealed by SAXS measurement. Thus, the relationship between the rod inclusion stress and the average internal HAp crystallites lattice strain becomes

$$\sigma^{rod} = K_{partial\_aligned}^{HAp} \langle \varepsilon \rangle^{HAp} \qquad \text{(Eq. 5.5)}$$

d). Simplified model of partially aligned HAp inclusions

In order to evaluate the multi-directional normal strain components, a simplified second-level model of enamel is presented here. Considering Eq. 5.2, in this case, each azimuthal angle shown in Figure 5.3 a-c was considered to correspond to a group of perfectly aligned HAp crystallites with a certain volume fraction f_{2k} and orientation T_k, where f_{2k} can be determined from the WAXS intensity plot (Figure 5.3 m-n). In another word, the bundled HAp crystallites consist of a distribution of multiple groups with different orientations and different volume fractions. Meanwhile, in each group, all the crystallites are perfectly aligned, thus $\langle C \rangle_{HAp}$ and $\langle S \rangle_{HAp}$ can be represented by the single crystallite value $\langle C \rangle_{HAp} = C_{HAp}$, $\langle S \rangle_{HAp} = S_{HAp}$. Note that $S_{HAp} = S_{rod}$.

5.3.2.3. Determination of the rod stiffness

In Eq. 5.1, the stiffness of the rod C_{rod} still remains to be determined. Since the rod is regarded as a composite consisting of protein matrix and mineral HAp crystallites, C_{rod} can also be determined using the Eshelby inclusion model, taking into account the volume fraction (f_2), average Eshelby tensor ($\langle S \rangle_{HAp}$) and average stiffness ($\langle C \rangle_{HAp}$) of HAp crystallites in the second level. To simplify the determination, it is assumed that all HAp crystallites in the rods are aligned with an angle with respect to the longitudinal direction of rod (thus $\langle C \rangle_{HAp}$=C_{HAp} , $\langle S \rangle_{HAp}$=S_{HAp}). Such orientation is the preferred orientation revealed by SAXS/WAXS and is reflected in the model by a unique orientation matrix T_{HAp}. The expression of the stiffness of rod is given here without detailed derivation

$$C_{rod} = \left\{ {C_{M2}}^{-1} - f_2 \left\{ \left(\tilde{C}_{HAp} - C_{M2} \right) \left[\tilde{S}_{HAp} - f_2 \left(\tilde{S}_{HAp} - I \right) \right] + C_{M2} \right\}^{-1} \left(\tilde{C}_{HAp} - C_{M2} \right) {C_{M2}}^{-1} \right\}^{-1}$$

(Eq. 5.6)

where $\tilde{S}_{HAp} = T_{HAp}^{T} S_{HAp} T_{HAp}^{-T}$ is the transformed Eshelby tensor and $\tilde{C}_{HAp} = T_{HAp}^{-1} C_{HAp} T_{HAp}^{-T}$ is the transformed stiffness of aligned transversely isotropic HAp crystallites. Further, the overall relationship between the average HAp crystallites strain and the externally applied stress can be established by combining Eq.5.1 and Eq.5.5.

$$\sigma^{A} = H^{-1} \sigma^{rod} = H^{-1} K_{partial\_aligned}^{HAp} \langle \varepsilon \rangle^{HAp} = K \langle \varepsilon \rangle^{HAp} \qquad \text{(Eq. 5.7)}$$

5.3.3. Finite element analysis

The finite element package ABAQUS® v.6.9 was used in connection with the photoelastic technique to simulate the stress distribution and the associated photoelastic patterns around the enamel samples. Direct comparison of photoelastic patterns between model and experiment provides a way of simultaneously verifying the correctness of the macroscopic properties (of epoxy and enamel) and of the mechanical model of the stress distribution within the epoxy disk around the enamel samples. In order to visualise the photoelastic fringe patterns, the "Tresca equivalent stress" σ_{Tresca} was selected as the output parameter. Initially a simulation of the solid photoelastic epoxy disk (the calibration specimen) was carried out using a plate model with 12 mm diameter and 2 mm thickness. The elastic constants of the epoxy were identified by comparing σ_{Tresca} contour plot with the fringe patterns observed at different loads.

In order to model the enamel sample ($2 \times 2 \times 2$ mm^3), a cubic inclusion was introduced and embedded in the centre of the epoxy disk with the isotropic elastic constants obtained from the calibration. The experimentally applied loads were introduced on the edge of the epoxy model and the stress distribution around the sample (in the *x*-*y* plane in global coordinates) was recorded. The tractions present at the boundary of the enamel inclusion obtained from this model were then used as the externally applied stress values in the Eshelby model.

5.4. Experimental results and model evaluation

5.4.1. Finite element modelling of photoelastic patterns

The photoelastic fringe patterns of solid epoxy disks and epoxy with enamel embedded at the disk centre are shown in Figure 5.5 a. The results for Tresca stress distribution simulated in ABAQUS are shown in Figure 5.5 b. The stress variation along the edge of the samples simulated in ABAQUS was not a constant, but was concentrated especially at the two corners. Direct comparison and matching of the model to the photoelastic patterns for solid epoxy disks lead to the isotropic elastic constants of epoxy disk, estimated to be E_{epoxy} =1.2±0.015 GPa, υ_{epoxy} =0.35 [190]. These parameters were used for the samples with embedded enamel to calculate the predicted normal stress distribution around the enamel inclusion that are illustrated in Figure 5.6 a corresponding to the maximum external load of 400N. At this applied load the average stress values on all the nodes of each sample edge were calculated in order to eliminate the effect of the singular points or oscillation at the corner, with the result of -54.1 MPa in the *x*-axis and 0.27 MPa in the *y*-axis. Therefore the sample loading condition was found to be close to uniaxial. As expected, the average stress value applied to the sample was also found to be linearly proportional to the value of the externally applied load, as shown in Figure 5.6 b. Such average stress evolution was used as the external force in the next section for the embedded enamel sample.

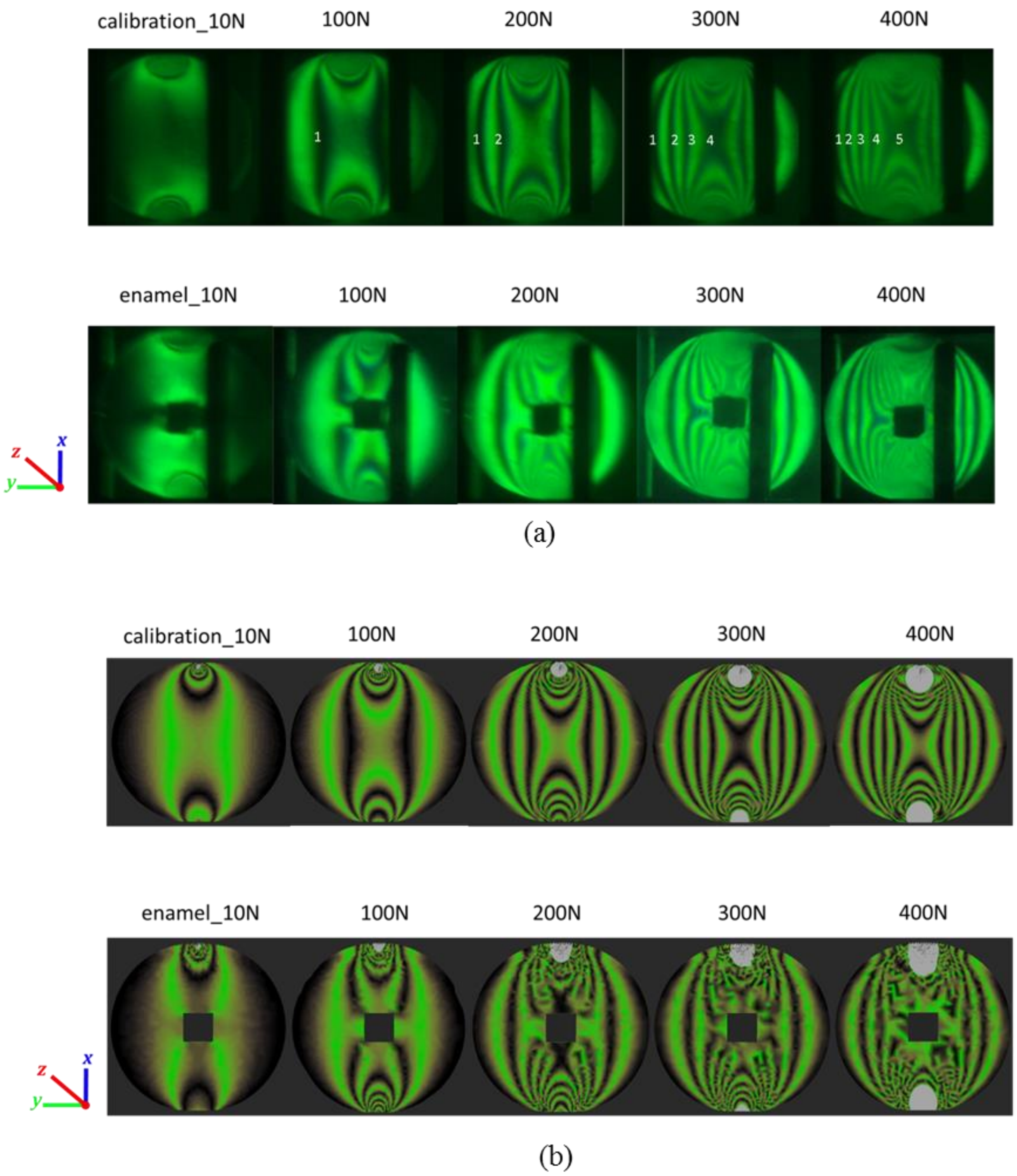

Fig. 5.5 (a) Photoelastic images and (b) ABAQUS simulation images of Tresca stress distribution of the epoxy disks without (first row) and with embedded enamel (second row) under series of loading conditions.

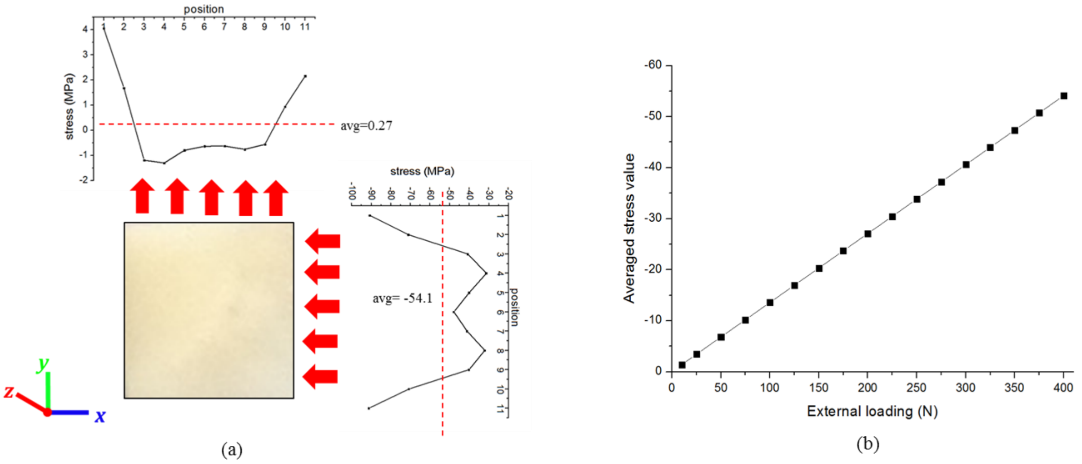

(a)

(b)

Fig. 5.6 (a) Normal stress distribution around the cubic enamel samples in *x*- and *y*- axis (*x*-*y* plane is the measurement plane) at the maximum external loading of 400N. The averaged value of the stress distribution was extracted as -54.1 MPa along *x*-axis (loading direction) and 0.27 MPa in *y*-axis (transverse direction). (b) The external load vs. the averaged stress value applied to the sample in the *y*-axis.

5.4.2. Nano-scale HAp crystallite distribution and the mechanical response of enamel

5.4.2.1. Pure enamel sample

For the pure enamel sample, the loading areas were accurately determined by micro-CT measurement, which was 3.55 mm^2. Figure 5.2 a shows a WAXS pattern of an enamel consisting of a system of Debye-Scherrer rings (peaks). Since enamel is textured, only limited range of diffraction rings can be captured. The radial shifts of the (002) peak in the WAXS pattern were measured under uniaxial compressive loading applied in longitudinal direction with respect to the rod direction. The preferential orientation of HAp crystallites obtained by WAXS pattern is shown to be roughly perpendicular to the arc of (002) peak and the detailed value is determined from the stress-free plot of $I_{WAXS}(\varphi) \sim \varphi$ (Figure 5.2 c) with the Gaussian fit (red line).

The SAXS pattern as shown in Figure 5.2 b contains the information of orientation and degree of alignment of the gaps between the HAp crystallites. As mentioned above, the information about HAp crystallites orientation distribution can be deduced by gap scattering. The preferential orientation shown in Figure 5.2 b is roughly along the short axis of the elliptical pattern and the detailed value is also determined from the stress-free plot of $I_{SAXS}(\varphi) \sim \varphi$ (Figure 5.2 d) with the Gaussian fit (red line). The detailed values of the orientation and degree of alignment obtained by WAXS and SAXS patterns are listed in Table 5.1, from which these parameters were used in the Eshelby model evaluation.

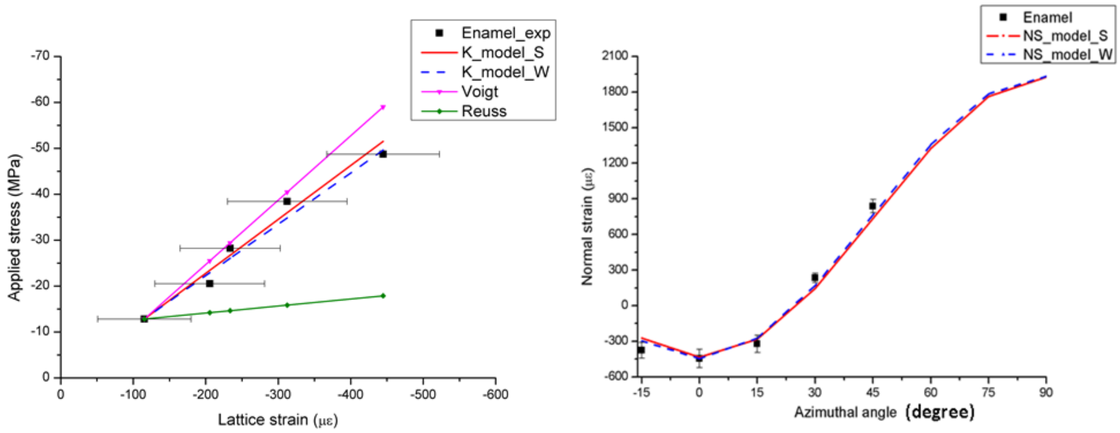

(a) (b)

Fig. 5.7 Comparison of experimental data and modelling results of pure enamel sample. (a) For the applied compressive stress vs. elastic lattice strain for HAp crystallites. (b) For the variation of normal strain (NS) with orientation (azimuthal angle).

The shifts of (002) peak from WAXS along *x*-direction were used to obtain the elastic lattice strain values. Figure 5.7 a shows the experimental results of the applied stress vs. HAp crystallites lattice strain of sample along the loading direction, indicating a linear increase as expected. Two results are given respectively using the preferred orientation angles obtained by SAXS and WAXS but keeping other parameters the same. The ratio of the uniaxial stress and the average lattice strain of

HAp crystallites gives the apparent modulus [50], which is listed in Table 5.1. Meanwhile, the residual (initial) strain was found to be quite small and can therefore be neglected. The shifts of (002) peak along other directions were also measured, e.g. by caking each pattern with the width of 20° along the directions of -15 °, 0 °, 15 °, 30 ° and 45° to determine the azimuthal variation of the normal strain component. The result is shown as an azimuthal plot in Figure 5.7 b, where 0° represents the loading direction. Note that the normal strain component undergoes a transition from negative to positive at around 25 °.

5.4.2.2. Embedded enamel sample

For the embedded enamel samples #6, #7 and #3, Figure 5.3 a-c respectively represent the typical WAXS patterns that consist of series of Debye-Scherrer rings (peaks). The textured nature of enamel means that only limited azimuthal ranges within the rings could be captured in samples #6 and #7. In contrast to that, in sample #3 the crystallites were approximately randomly distributed in the *x*-*y* plane, so that complete rings were observed. Figure 5.3 m-n respectively show the azimuthal intensity variation within the available azimuthal ranges in the measurement plane (*x*-*y* plane) in samples #6 and #7. This provides information about the crystallites orientation distribution. The preferred orientation direction of the basal plane in HAp crystallites in samples #6 and #7 is approximately perpendicular to the central bisector of the arc of the interested peak (see Figure 5.3 b-c). The precise values were determined from the Gaussian fit in Figure 5.3 m-n (red line). Since the deformation considered was elastic, the crystal orientation was examined to be unchanged, i.e. the peak centres found from the plots shown in Figure 5.3 m-n remain the same at all applied loads.

In order to obtain the variation of the average normal elastic lattice strain component of HAp crystallites with applied load, the peak shifts at different azimuthal angles were obtained from the WAXS data through caking each pattern into 20 ° sectors. The available range for each sample was different, as shown by the red marks in Figure 5.3 a-c: in sample #6 between 0 °-45 ° and in sample #7 between 45 °-90 °, while in sample #3 the range was 0 °-90 °. For each sample, the elastic lattice strain, as a function of applied stress calculated in section 5.4.1, is plotted as the argument against the applied stress for different azimuthal angles in Figure 5.8 (in which 0° represents the loading direction). The experimental results indicate that, as expected, there is an approximately linear relationship along each direction and that each azimuthal angle corresponds to a different slope. This ratio between the applied uniaxial external stress and the average HAp crystallites lattice strain gives the apparent modulus along different directions [50]. At this stage it is also relevant to mention that the initial residual strain in the samples was found to be negligible.

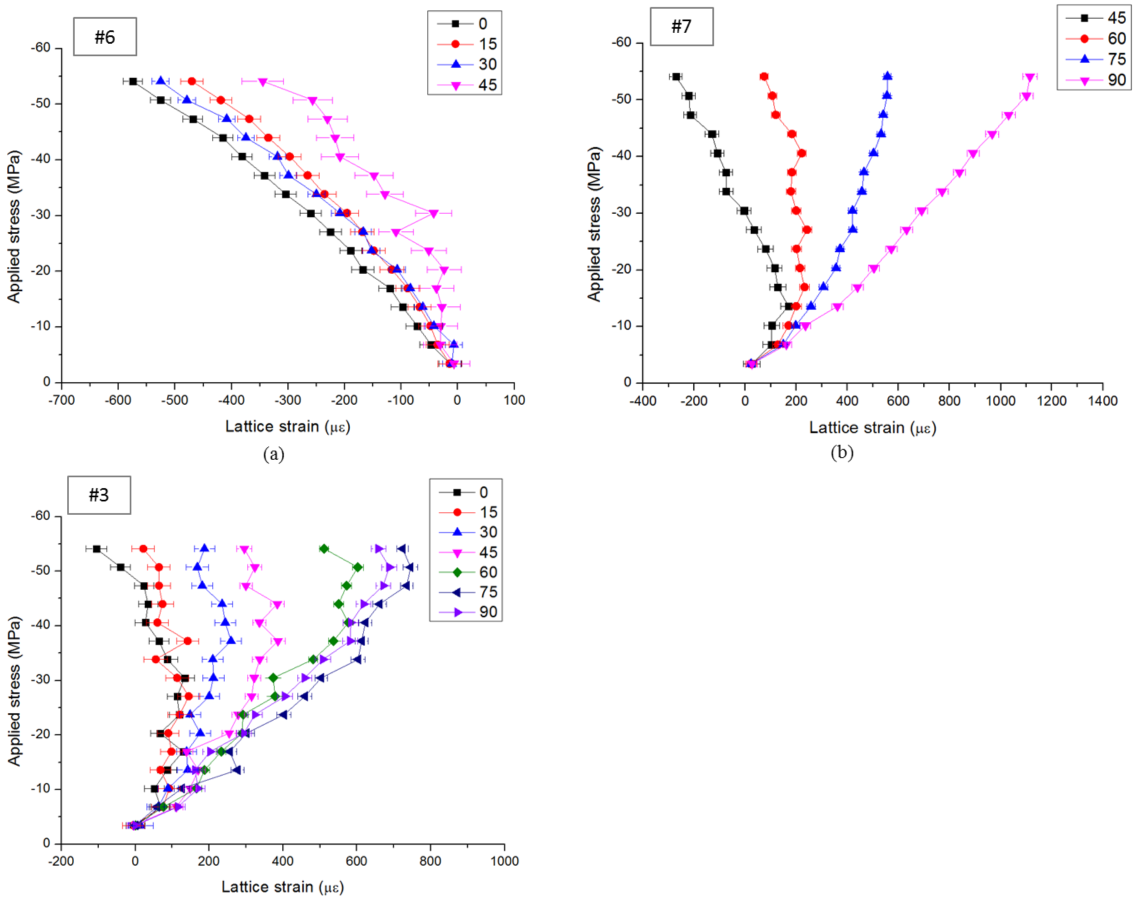

(a) (b)

(c)

Fig. 5.8 The experimental results of applied compressive stress vs. elastic lattice strain of HAp crystallites for the three samples at different azimuthal angles (every 15^{o} degree) with respect to the loading direction. (a) sample #6; Due to the symmetry, only the available angles from the (002) ring from 0^{o} to 45^{o} are selected. (b) sample #7; Due to the symmetry, only the available angles from the (002) ring from 45^{o} to 90^{o} are selected. (c) sample #3; Due to the symmetry, only the available angles from the (210) ring from 0^{o} to 90^{o} are selected.

5.4.3. Evaluation of the multi-scale Eshelby model

5.4.3.1. Pure enamel sample

In the model for pure enamel sample, the material properties and other parameters used were taken from literature [82, 83, 136, 189], and refined by fitting with the experimental data of HAp crystallites lattice strain. The initial volume fraction of HAp crystallites was taken from the previous analysis of the self-similar hierarchical two-level model of enamel, i.e. approximately 95% at both the micro-scale and nano-scale levels [136]. In detail, at the first level, 95% represents the volume fraction of rods within the protein matrix, while at the second level, 95% represents the volume fraction of mineral within each rod. This means that the overall volume fraction of mineral in the enamel is ~90%. In general, Young's modulus of 1GPa for protein is found in literature, without taking into account the viscoelasticity or viscoplasticity [82, 83]. The needle-like HAp crystallites in the enamel were also assumed to have a transversely isotropic stiffness with five independent elastic constants [189]. To represent the shape of the rod and of the HAp crystallites for each level, the cylinder Eshelby tensor (prolate spheroid) was used. The elliptical semi-axes a_1 and a_2 within the transverse cross-section were assumed to be the same, ($a_1/a_2=1$), but different from a_3. The apparent modulus K was calculated based on the different preferred orientation angles of the HAp crystallites obtained by both SAXS and WAXS. All the parameters refined to obtain the best fit are listed in Table 5.1, as well as the reference values from literature. A comparison of the stress/strain curve along the loading direction between the model prediction and the experiment is plotted in Figure 5.7 a, where the Voigt and Reuss bounds are also provided. As expected, it is found that the modified Eshelby model prediction lies between the two bounds and gives a satisfactory agreement with the experimental data. Meanwhile, the comparison of normal strain variation with the azimuthal angle is presented in Figure 5.7 b. It gives the model prediction results using different preferred orientation angles of HAp crystallites obtained by both SAXS and WAXS.

Tab. 5.1 Experimental results from SAXS/WAXS, and the refined structural parameters of the enamel used in the multi-scale Eshelby model (values reported in literature are also presented)

Parameter	**Enamel**	**Reference values**
Orientation (from SAXS)	174 °	N/A
Orientation (from WAXS)	14 °	N/A
Degree of alignment	0.6	N/A
K_exp.	124.3 GPa	N/A
$f_1 = f_2$	95%	95% [136]
C_{M1}	E_m=1GPa, v_m=0.3	$E_{protein}$=1GPa, $v_{protein}$=0.3 [82]
C_{M2}	E_m=1GPa, v_m=0.3	$E_{protein}$ =1GPa, $v_{protein}$=0.3 [82]
C_{HAp}	E_{xx}=148.42GPa, G_{xy}= G_{xz}=39.6GPa v_{xy}= v_{xz} =0.34, v_{yz}=0.21 E_{yy}= E_{zz}=114.26GPa	E_{xx}=140GPa, G_{xy}= G_{xz}=39.6GPa v_{xy}= v_{xz} =0.3, v_{yz}=0.2 E_{yy}= E_{zz}=114.26GPa [189]
$S_{cylinder\_1} = S_{cylinder\_2}$	$a_1 / a_2 = 1$	[35]
K_model (from SAXS)	122.9 GPa	N/A
K_model (from WAXS)	120.4 GPa	N/A

5.4.3.2. Embedded enamel sample

Following the same way of doing parameter refinement as stated in section 5.4.3.1, the final refined parameters and reference values for the embedded enamel sample are summarized in Table 5.2. In Figure 5.9, the comparison between the model prediction and experimental data of the normal strain variation in the three samples under the maximum external load of 400N (derived from the ABAQUS model) is shown as a plot against the azimuthal angle.

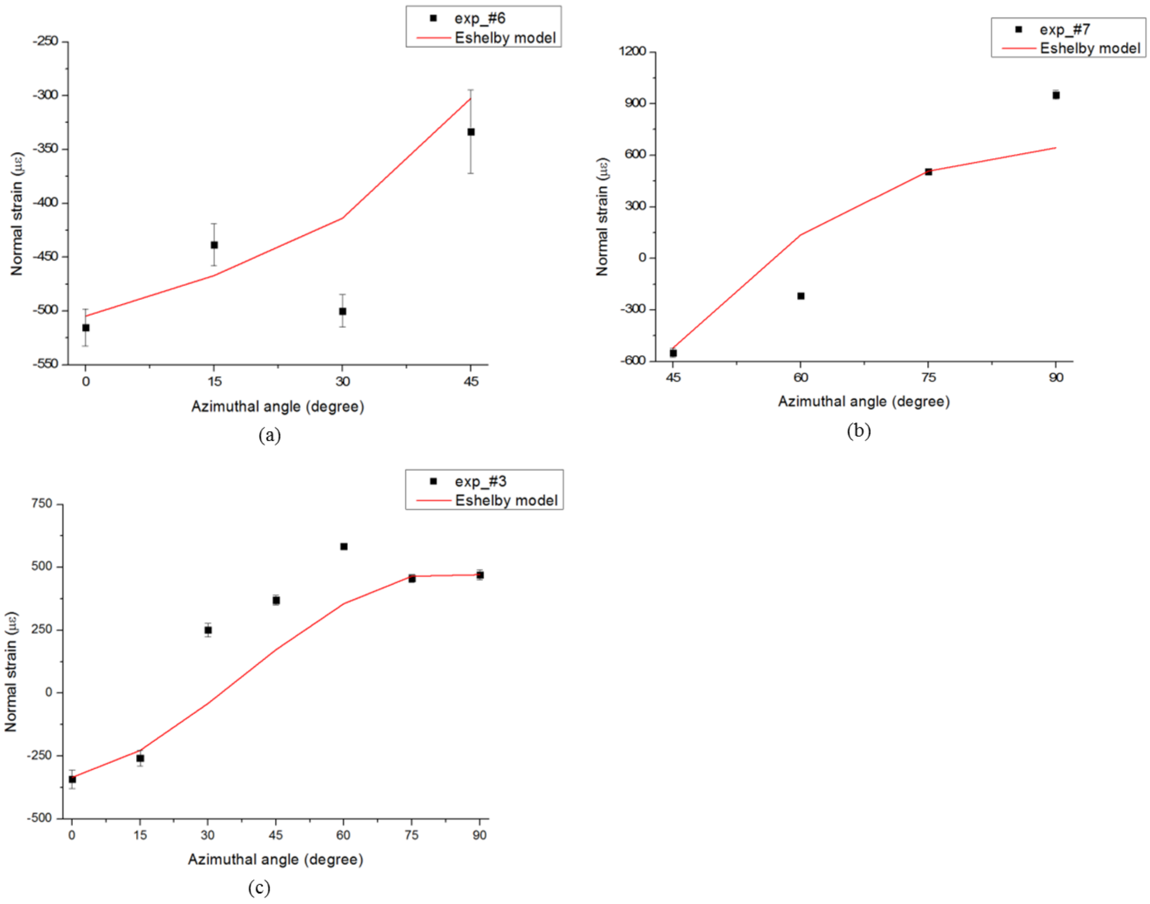

(a)

(b)

(c)

Fig. 5.9 Comparison of experimental data (black markers) and modelling results (solid black lines) for the variation of normal strain component with orientation distribution (azimuthal angle) at the maximum externally applied load of 400N. (a) sample #6, from 0-45°; (b) sample #7, from 45-90°; (c) sample #3, from 0-90°.

Tab. 5.2 Preferred orientation and refined structural parameters of the enamel embedded in the epoxy used in the two-level Eshelby model (values reported in literature are also presented)

Parameter	**#6**	**#7**	**#3**	**Reference values**
Preferred orientation	8 °	91 °	-	
$f_1 = f_2$	93%	90%	95%	95% [35]
$C_{M1} = C_{M2}$	E_m=1GPa, v_m=0.3			$E_{collagen}$=1GPa, $v_{collagen}$=0.3 [191]
C_{HAp}	E_{xx} = 132.1 ±9GPa, G_{xy} = G_{xz} = 39.6GPa v_{xy} =v_{xz} = 0.33 ±0.07, v_{yz} = 0.31 ±0.08 E_{yy} =E_{zz} = 114.3 ±6.5GPa			E_{xx} = 138.42GPa, G_{xy} =G_{xz} = 39.6GPa v_{xy} =v_{xz} = 0.30, v_{yz} =0.2 E_{yy} =E_{zz} =114.26GPa [82]
$S_{cylinder\_1} = S_{cylinder\_2}$	$a_1 / a_2 = 1$			[31]

5.5. Discussion

The hierarchical nano-structure of human enamel may vary significantly between patients due to personal history, diet, ethnic origin, etc. However, due to the ethical legislation in the UK, it was not possible to obtain or publish any further information on the medical history of the patients.

This study was conducted using the penetrating power of synchrotron X-rays to provide a bulk probe for structure and strain analysis. Unlike the vast majority of studies that rely on the surface characterization (SEM, AFM, nanoindentation, Raman, etc., and also the reflection mode of X-ray diffraction), this WAXS study requires less preparation effort in terms of cutting and storage and surface conditioning. The use of much thicker samples and gauge volumes (~2 mm) than those for other methods

(~0.05 mm) ensured that the bulk response investigated was not affected by minor surface changes. The combination of the data obtained using penetrating radiation (synchrotron X-ray) with model refinement offers the possibility of identifying the nano-scale parameters of the bulk enamel. The parameter refinement and validation strategy employed in the model adopted in the present study is particularly helpful in the identification of nano-scale parameters that may be hard to determine in other experiments. The relationship between the nano-scale structure and the macroscopic mechanical behaviour established in our study improves the understanding of the nano-particle distribution effects that was lacking in the earlier studies [132, 135, 139].

5.5.1. Refined parameters of the two-level Eshelby model

The inputs from reference data on material parameters (HAp crystallites stiffness, etc.) were only used as the starting guess for the optimization of the elastic constants in order to obtain the best fit to our experimental data. The improved setup in the experiment involving photoelastic epoxy mounting, the three samples studied were cut from the same tooth. On the one hand, this limits the applicability and generality of the results to a particular tooth of a particular patient, reflecting corresponding biological and behavioural specificity. Therefore, it is important to draw any conclusions or generalisations with appropriate degree of caution. On the other hand, it is important to note that within the sample set considered here, their properties such as the degree of mineralisation, size of particles etc. were similar and consistent, with the exception of the single aspect, namely, the orientation distribution of the nano-HAp crystallites that is known to vary with location within the tooth. The single crystal elastic constants of HAp crystallites were assumed to be the same. The final parameters used in the multi-scale Eshelby model, outlined in Table 5.1 and Table 5.2, were refined iteratively, staring from the values reported in the literature. In order to estimate the error in our evaluation of parameters, we carried out a careful study of error propagation in our model fitting procedure following the error analysis methods in [192]. The 95% confidence interval in the fitting results was propagated back into elastic modulus uncertainty. Note that since the results of our test were not sensitive to the shear modulus, the uncertainty of the shear modulus was not assessed.

Of the refinable parameters, the key ones are the volume fraction of constituents at each level and the elastic constants of a single HAp crystallite. Among these parameters, the elastic constants, and the modulus in particular, exert the most profound influence on the result. In the model matching (optimization) process, within each specimen, the volume fraction of the rods in enamel and the HAp crystallites in rod were assumed to be the same. After the refinement of the elastic constants (within the range reported in the literature) the volume fraction was further refined. At this stage, further adjustments of other parameters were also attempted and it was found that this only had a minor effect. Note that for the improved experiment, the model fitting was carried out so as to find the parameters that gave the best agreement for all the three samples.

Furthermore, environmental and developmental factors may influence the mechanical behaviour of enamel [193]. Following tooth eruption, the interaction of the enamel surface with ions in saliva leads to enamel maturation. This post-eruptive maturation may affect the mechanical behaviour of enamel surface. For example, the incorporation of fluoride into enamel and the formation of fluoroapatite may exert an influence on the superficial layer of dental enamel. However, the transmission X-ray setup we employed ensured that the bulk rather than the surface was characterised for the samples obtained from freshly extracted teeth with no apparent damage, caries or evidence of dental treatments.

5.5.2. Residual strain

During the preparation process, a low speed diamond saw and polishing papers were used to minimise the effect of induced residual strain. The other origin of residual strain may be the natural growth of teeth. For the embedded enamel samples, at low load values, there is a transition region in the transversely loading samples (#7 and #3), which might result from the residual tensile strain in the transverse direction. However, as also shown in Figure 5.8 b-c, the residual strain in the samples was found to be small in magnitude and was relieved subsequently at higher load values. In addition, the pre-existing residual strain is also small as illustrated in Figure 5.7 a. The choice of the unstrained reference lattice parameter affects the results and may introduce errors in determining the elastic strain. It is important to note, however, that the principal aim of the present study was to consider the changes in elastic strains that occur with loading, that remain *unaffected* by the choice of unstrained reference. It is also worth noting that the lattice parameters reported in the literature are mostly obtained from the powdered samples. Large volume averaging of lattice parameters may over- or under- estimate the value found at a particular location in the structured sample. Note that in the experiments the X-ray beam illuminates the same area of the sample. In summary, the measured lattice parameter changes reflect correctly the lattice parameters evolution under varying external loading. Since the elastic response has been experimentally observed to be dominating after the transition (reflected in the linearity of the experimental stress-strain curve), the presence of this initial residual strain only amounts to an initial offset. This means that there has been no impact from residual strain on the prediction of the elastic properties and that this offset can be neglected in the present analysis.

5.5.3. Gap scattering (SAXS)

For the pure enamel sample, the good agreement between the apparent modulus K results calculated using different HAp preferential orientations determined by SAXS and WAXS provides strong evidence and validates the argument that the SAXS pattern arising from gap scattering [152] can be used to deduce the HAp crystallite orientation distribution, i.e. the gaps are almost parallel to HAp crystallites inside the rod. Therefore, we report confirmation that SAXS data provides beneficial complimentary information for determining the crystal orientation distribution in enamel and other mineralised tissues. However, since WAXS is more sensitive to crystals while SAXS is only sensitive to the nano-particle distribution of crystals or non-crystals, WAXS is more reliable in determining crystal orientation.

5.5.4. The effects of preferred orientation of HAp crystallites

The effect of the nano-scale structure (the HAp crystallite distribution) on the macroscopic mechanical response was further investigated by changing the preferential crystal orientations (changing the orientation matrix in Eq. 5.3). A 3D model of perfectly aligned crystals inside a rod is established (Figure 5.10 a) with the angle φ describing the rotation of the alignment direction around the global Z-axis. When all HAp crystallites are aligned along the global X-axis, φ equals to 0°. By changing the relative alignment direction, the variation of $K_{aligned}$ with respect to the loading direction can be calculated (Figure 5.10 b). From Figure 5.10 b, the corresponding results using the real orientation angles found in the experiment (174° from SAXS and 14° from WAXS) are found to be $K_{aligned\_SAXS}$ =138.1 GPa and $K_{aligned\_WAXS}$ =131.8 GPa, i.e. closely similar values. Meanwhile, due to the high degree of alignment of HAp crystallites in the enamel, the value of the overall apparent modulus $K^{HAp}_{partial\_aligned}$ lies closer to $K_{aligned}$ rather than K_{random}. The enamel displays strong microscopic elastic anisotropy. It is interesting to note that the orientation with the largest stiffness is found, as expected, around 0° with respect to the loading direction. However, the most compliant orientation observed is not at 90° (perpendicular to the loading direction), but rather around 50° or 130°. This is due to the transversely isotropic stiffness of HAp crystallites.

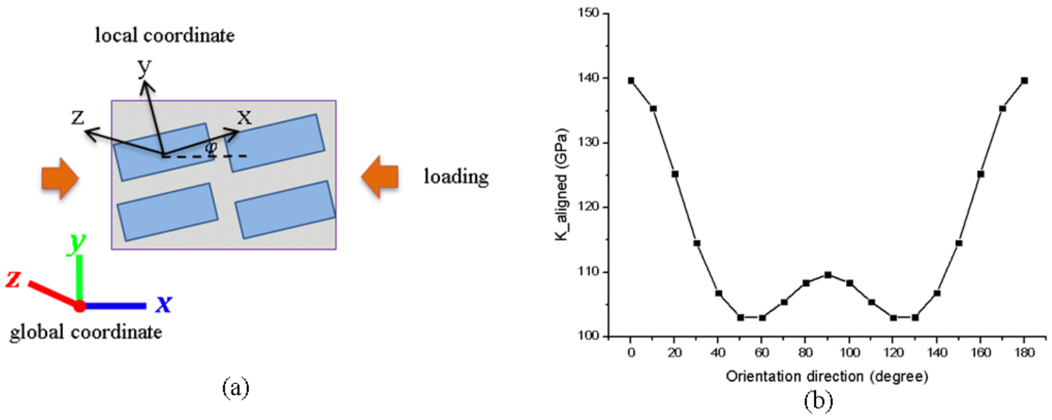

(a)

(b)

Fig. 5.10 Preferential alignment effect on the apparent modulus of HAp crystallites in human enamel. (a) A simplified visualization of the alignment of HAp crystallites. The beam direction is along the global *Z*-axis and the alignment here represents the angle between the local *x*-axis and global *X*-axis (initially aligned angle $\varphi = 0^o$, i.e. the local *x*-axis of a needle is initially along the global *X*-axis). (b) By changing the alignment angle (0°-180°), the average strain of the crystals along the loading direction can be obtained by the multi-scale

Eshelby model, which then indicates that $K_{aligned}$ varies with respect to the preferential alignment angle.

5.5.5. Finite element simulation

The high level of correlation seen between the finite element analysis result (illustrated in Figure 5.5 b) and the photoelastic patterns (shown in Figure 5.5 a) suggests that the stress values extracted from the finite element model are a good representation of the tractions applied to the enamel sample embedded in the epoxy. In Figure 5.5 b the stress concentration region has been shaded grey. As this region is far enough away from the enamel inclusion, it can be neglected. Only the patterns and stress distribution close to the enamel need to be considered. The plot of the normal stress distribution in Figure 5.5 b is likely to originate from the frictional contact condition set between the enamel sample and epoxy in ABAQUS. However, the use of the averaged value of the stress distribution is able to minimize the effect of this oscillation. In short, the finite element results suggest an accurate estimation of the input stress for the two-level Eshelby model.

5.5.6. Normal strain component variation

The main difference between the three different samples was the orientation of the rods with respect to the external loading direction. For sample #6 in Figure 5.9 b, in which the load was applied along the longitudinal direction of the rod, the crystal lattice strain at a given stress was larger at 0^o (i.e. along the loading direction) than at any other angles (which is a direct result of the Poisson effect). However, for the other two samples (#3 and #7), in which the rod orientation was perpendicular to the loading direction and the lattice strain was found to be larger at 90^o than at other angles. These plots also demonstrate that loading along the transverse direction of the rod induces higher levels of stress or strain in the HAp crystallites. In addition, the deviation from linearity was found in the three samples (45^o for samples #6 and #7, and all the orientation angles for sample #3). Such relatively large experimental errors may result from the relatively weak intensity at the edge of the rings for samples #6 and #7, while for sample #3, the whole ring demonstrates a relatively weak intensity.

The plots of applied stress against lattice strain also have a common trend, in that the linear relationship starts only after a certain applied stress has been reached, especially in samples #3 and #7 (shown in Figure 5.9 a and c). Since the initial evolution of normal strains along different directions is identical, it indicates that the sample is subjected to hydrostatic stress condition. In any case, this effect appears to have only minor influence on the further response.

5.5.7. The elastic anisotropy of the HAp crystallites

The different mechanical responses of HAp crystallites with respect to the loading direction shown in Figure 5.8 and 5.9 originate not only from the different rod directions, but also in the strong anisotropic stiffness of HAp crystallites. The three-dimensional directional modulus of a single HAp crystallite was calculated by transforming the transversely isotropic stiffness matrix of a single crystal with different rotation matrices. The result is shown in Figure 5.11. The non-spherical shape corresponds to the elastic anisotropy of the HAp crystallite. In Figure 5.11 a, the *x*-axis represents the longitudinal direction of the needle-shape HAp crystallite. Figure 5.11 b demonstrates the projections of the resulting modulus on the *x*-*y* plane and *y*-*z* plane. The projection on the *x*-*y* plane is similar to the cases of samples #6 and #7, and the circular projection on the *y*-*z* plane is similar to the case of sample #3 in which an isotropic modulus is observed. The orientation with the largest stiffness is found to be along the *x*-axis, as expected (longitudinal direction of the HAp crystallite). However, the most compliant orientation observed in Figure 5.11 b is not at 90°, but rather around 60° due to the transverse isotropic stiffness of HAp crystallites.

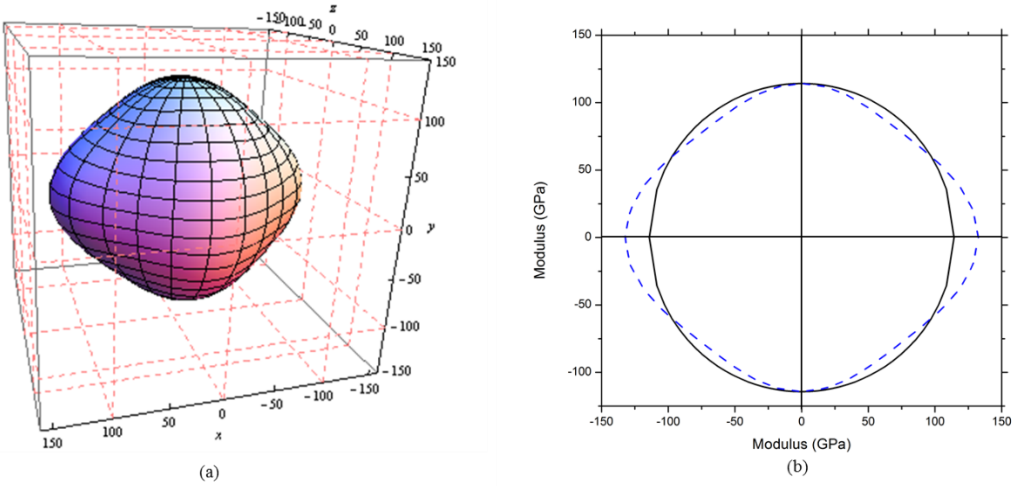

Fig. 5.11 3-D transversely isotropic elastic modulus of HAp crystallite. (a) 3-D representation of directional dependency of HAp crystallite elastic modulus (unit: GPa); (b) the projections of directionally dependent modulus on the *x*-*y* plane (blue dashed line) and *y*-*z* plane (solid black line).

5.6. Conclusions

In this study, the lattice strain variation related to the nano-scale HAp crystallites distribution of human enamel was measured during *in situ* elastic compression by the combination of synchrotron SAXS/WAXS and photoelasticity techniques. The coherent results obtained for both WAXS and SAXS indicate that the SAXS pattern arising from the inter-mineral gaps can be used to reflect the HAp crystallites orientation. In addition, as an improvement of the earlier proposed composite model [77, 78], a multi-scale Eshelby inclusion model was established to estimate the elastic properties of enamel, considering it as a two-level composite. Such second-level effect cannot be ignored since the mechanical behaviour shows strong dependence on the nano-scale crystallite orientation distribution. This model was validated in both cases (pure enamel sample and embedded enamel samples) with good agreement observed between the measured and calculated normal lattice strain component variation in different azimuthal directions.

This is the first study with combined SAXS/WAXS on the nano-scale structure and its influence on the macroscopic and microscopic mechanical behaviour of human enamel. It provides access to the information on both the structural and mechanical aspects of the sample and allows us to make further progress compared with the previous studies which only used WAXS [134, 135] to determine the HAp crystallites strain evolution but the main domain of SAXS pattern from two phase system was not used to reveal the nano particles distribution, only to focus on the collagen diffraction . This systematic experimental and modelling approach is able to capture the complete picture of the multi-scale structure, material elastic properties and its evolution under loading. The parameter refinement and validation approach adopted in the present study offers an important alternative route to the identification of nano-scale parameters to other techniques. Other established experimental characterization techniques, such as nanoindentation and microscopy, are confined to the sample surface, making overall bulk parameter identification difficult. Combining the present results on enamel with previously published data on human dentine in Chapter 4, an improved understanding of the multi-scale structural-mechanical properties within human dental tissues can be given. Besides the implications for the characterization of the structure-property relationship of other hierarchical biomaterials, this knowledge is essential for developing better prosthetic materials and dental fillings, and could also shed light on the mechanical property evolution associated with the multi-scale structural changes within human teeth due to disease and treatment. Finally, this approach also enables the characterization of the structure-property relationship of other hard hierarchical biomaterials.

Chapter 6

Structural-property characterization of the dentine-enamel junction (DEJ)

6.1. Brief introduction

For many decades now, the continued demand for improved dental treatment and prosthetics has driven the advancement of understanding of the micro-architecture of human teeth. The dentine-enamel junction (DEJ) is an important internal interface between the highly mineralized hard outer layer (enamel) and the softer tooth core (dentine). Unless diseased, this interface never fails by fracture or collapse, despite the extreme thermo-mechanical loading it experiences in the oral cavity. This stands in stark contrast to the interfaces between artificial dental restorative materials (fillings) and dentine [194]. The DEJ thus constitutes a superb lesson from nature on how to achieve strong, durable bonding between significantly dissimilar materials: the hard, brittle outer layer of enamel and the softer, but tougher dentine. It is the desire to learn from nature's architecture of mineral-organic composite, hierarchically structured, property gradient materials that provided the motivation for the studies described in the present Chapter.

In this study a range of experimental techniques was employed for the purpose of structure-property analysis of this naturally engineered interface. The microstructure of the DEJ was firstly investigated by Micro-Computed Tomography (Micro-CT). Two modern high-resolution X-ray synchrotron scattering analysis techniques (SAXS/WAXS) were then applied in the undisturbed state to visualize the spatial distribution of HAp crystallites across the DEJ. *In situ* WAXS successfully captures the structure-property relationship between the architecture of DEJ and its response to the applied force. The insight obtained into the thermal response of DEJ is briefly discussed in the end. The systematic experimental work reported here can be used to improve the understanding of the DEJ function in terms of its complex microstructure. The knowledge of the architecture and properties of the natural DEJ will benefit the biomimetic engineering of superior dental restorations and prosthetics, and the development of novel materials to emulate the DEJ.

6.2. Structure characterization

6.2.1. Micro-CT reconstruction

The microstructure of the DEJ was firstly investigated by Micro-Computed Tomography (Micro-CT) and Environmental Scanning Electron Microscopy (ESEM) (see Figure 6.1 a). The micro-CT system (SkyScan 1172 scanner, Kontich, Belgium) was used to obtain 3-D information about the tooth sample (including dentine, enamel and the DEJ). The high resolution scan was carried out at 0.6 μm resolution using 40kV voltage, 120uA current and a 0.5mm aluminium filter. The resulting 3-D slices were reconstructed with SkyScan NRECON package and were shown in Figure 6.1 b. the DEJ appears to form a complex shaped interface at the micrometer scale as observed in the 3-D reconstruction and also the 2-D topography contrast image (Figure 6.1 c). The contrast between dentine and enamel from Figure 6.1 c indicates that the interface is not sharp [195]. The 3-D scalloped structure is visualized in Figure 6.1 d that provides further confirmation of this micro- structural feature of the DEJ by showing with a series of 25–100 μm diameter scallops [196]. The observation from micro-CT is important in establishing the basic structural understanding of the scallop-like structure of the DEJ, which contributes to its remarkable mechanical behaviour. Scalloping is assumed to improve the bonding strength between enamel and dentine by increasing the interfacial area and it may lead to less stress concentration [39]. This motivates the examining of the mechanical property across the DEJ, which will be discussed later.

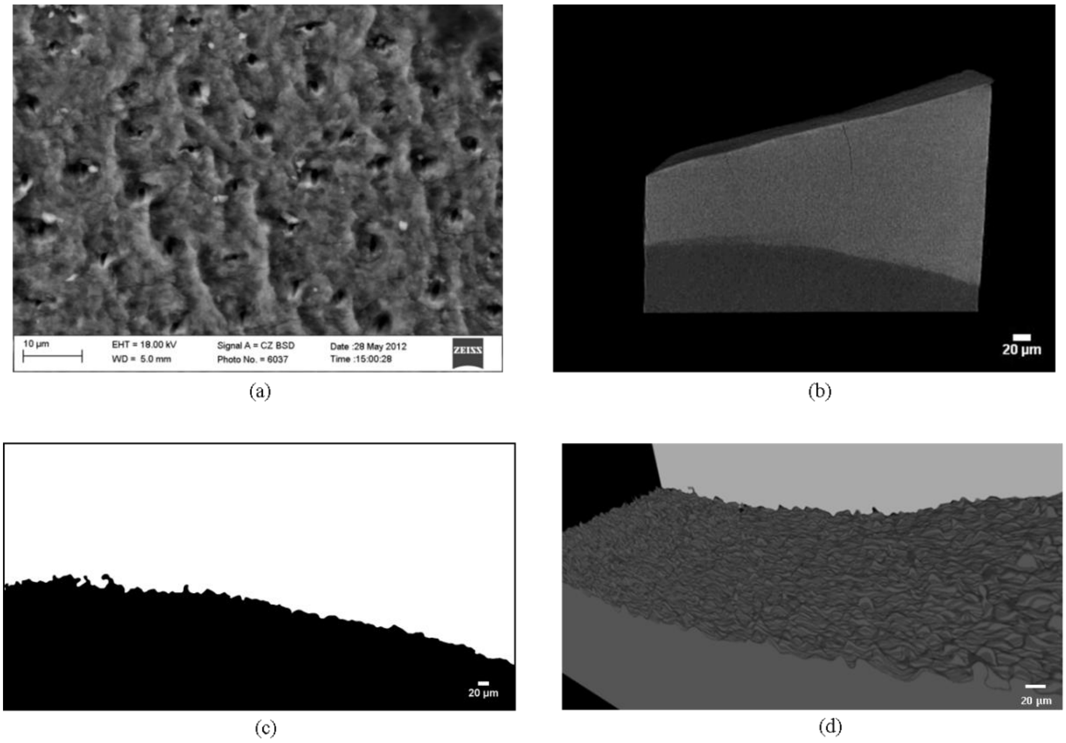

(a) (b)

(c) (d)

Fig. 6.1 Microstructural characterization of the dentine-enamel-junction (DEJ) (a) ESEM observation of scalloped structure; (b) 3-D reconstruction of DEJ sample; (c) 2-D projection of binary image of the DEJ; (d) scallop-like cross-section of the DEJ.

6.2.2. Synchrotron X-ray scattering methods

6.2.2.1. Micro-beam WAXS mapping

The micro-beam X-ray diffraction experiments were performed on B16 beamline at Diamond Light Source (DLS, Oxford, UK) using monochromatic X-rays at18 KeV.

X-ray Eye detector (Photonic Science X-ray MiniFDI) was initially used by opening the slits to take the pictures of samples by radiography technique. It was used on the selection of the region of interest of samples with sharp interface across the DEJ with sample thickness ~ 300 μm in Figure 6.2 a in order to guarantee that the thin DEJ plane of the selected area was almost parallel to the X-ray beam (to within ~1-2°). Then the slits were closed and WAXS detector was exposed to collect WAXS pattern. The KB mirrors were used to focus the incident X-ray beam down to $2.7\times3.8\ \mu m^2$, and thus, with such small beam size, the high resolution X-ray diffraction could be achieved to capture the structural variation across the DEJ and the results is shown in Figure 6.2 b.

The quantitative analysis of 2θ (scattering angle) of (002) peaks variation across the DEJ reveals the lattice parameter (*c*-axis) changes. The steep gradient over the DEJ thickness was collected based on the lattice parameters variation and was clearly visible in a range of 20 μm, which agrees with the observation in the Micro-CT scanning in Figure 6.1 c. Furthermore, a bump was observed as shown in Figure 6.2 b. The amount and depth of the scallops were found to vary between species, types of teeth and even between locations within a single tooth. In this case, the combination provides a consistent description of the DEJ spanning the range of length scales from the micro-scale down to sub-nano scale.

2-D mapping of structural transition of the DEJ (shown in Figure 6.2 c) was then detected by medium resolution X-ray diffraction mapping with beam size focused down to $0.3\times0.3\ mm^2$ from the region of interest in the dental slice (marked in a rectangular in Figure 6.2 a). Figure 6.2 d presents the phase mapping by interpreting (002) peaks in dentine and enamel separately. There is a debate of whether the lattice parameter change of HAp crystallites during the growth of human dental tissue is attributed to chemical or mechanical processes (e.g. residual stress). Most of the effort has been put on the chemical change [139]. However, the residual stress may also be associated with the natural growth process of each tooth, but no such quantification is currently available. Further examination by FIB-assistant DIC methods is needed in the future work.

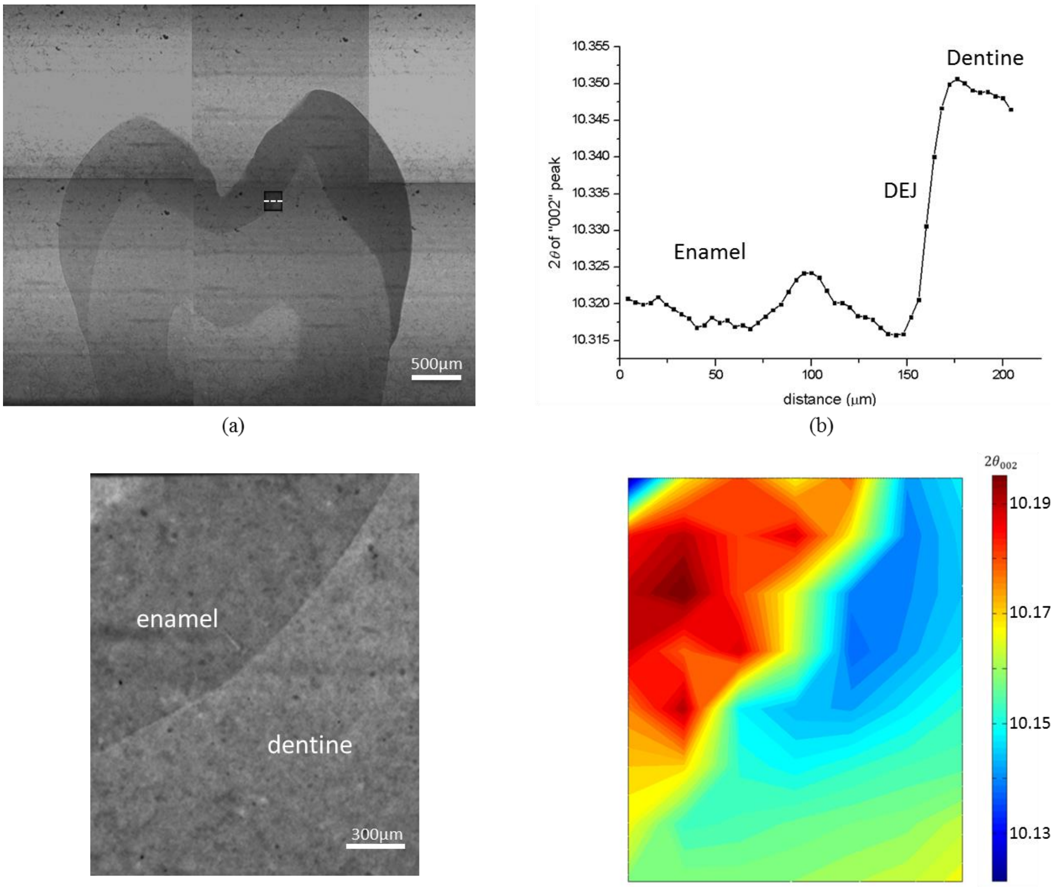

(a) (b)

(c) (d)

Fig. 6.2 Micro-beam X-ray diffraction mapping of dental slice; (a) radiographic image of dental slice; (b) high resolution line scan across the DEJ; the transition feature of the DEJ is clearly shown; (c) radiographic image of the region of interest (ROI); (d) phase mapping of dentine and enamel by interpreting (002) peak

6.2.2.2. Micro-beam SAXS mapping

Micro-focus SAXS experiments were carried out on I22 beamline at Diamond Light Source (DLS, Oxford, UK) using monochromatic 18KeV X-rays. The SAXS patterns were collected on the 2-D detector (Pilatus 2M, Dectris Ltd., Baden, Switzerland) positioned downstream of the sample with distance about 1040 mm. Compound lens were used to focus the incident X-ray beam down to the spot size of 14.5×19 μm^2. The dental slice illustrated in Figure 6.3 a was repeatedly shifted in the sample plane perpendicular to the X-ray incident beam to collect a map of SAXS patterns.

The data analysis was applied following the procedure as described in section 3.1.4. The mean thickness and degree of alignment with orientation marked by black lines of HAp crystallites in the region of interest (see Figure 6.3 a) including dentine, enamel and the DEJ are shown in Figure 6.3 b-c as colour coded 2-D plot. This provides an opportunity to map the structural variation in the plane of the dental slice. The gradient spatial distribution of the mean thickness is shown in Figure 6.3 b. Decreased value of the mean thickness was observed from enamel to the DEJ and further through the deep dentine. The 2-D spatial distribution of the degree of alignment and preferred orientation of the HAp crystalline nano-particles were visualized by SAXS as shown in Figure 6.3 c. The enamel and dentine are readily distinguishable by their clearly different degrees of alignment. In detail, enamel has higher degree of alignment in the range of red colour (0.4-0.5), whereas dentine mostly locates at (0.1-0.3) from the colour bar. A region of increased alignment is found to lie just below the high gradient transition band close to the DEJ. The preferred orientation of HAp crystallites is shown by the black bars superimposed on the colour map. In enamel, the particles are almost orthogonal to the DEJ plane. The same feature can be observed for the particles in dentine, but the particles gradually become parallel to the DEJ plane through the region near the DEJ. The variation of the structural properties of the DEJ suggests that a change in the internal nano- and micro-structure built into the structure optimizes the mechanical performance of dentine in the vicinity of the interface with the much harder, highly mineralized enamel [21].

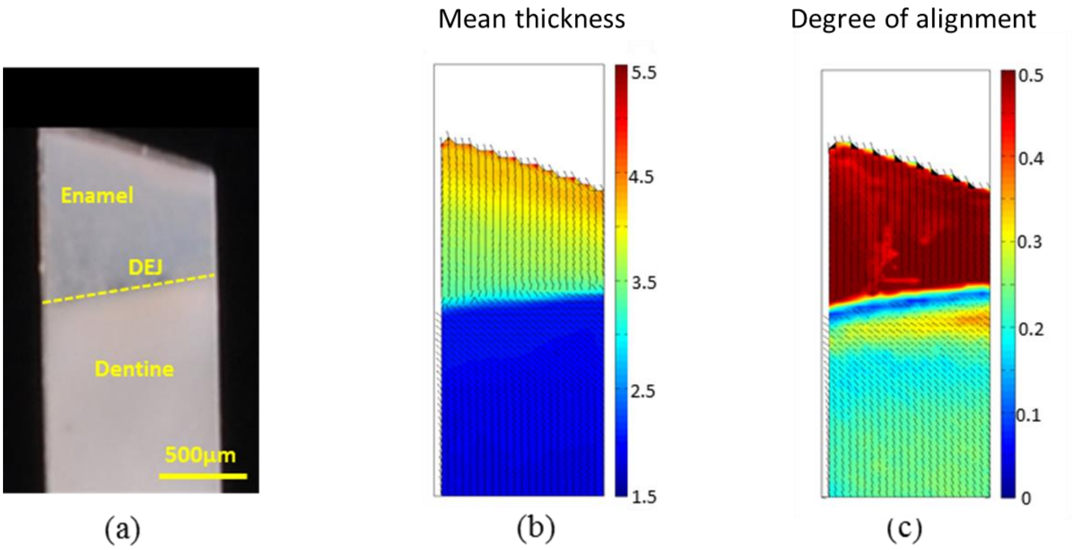

Fig. 6.3 Micro-focus SAXS mapping of dental slice. (a) human dental slice of region of interest (ROI); (b) mean thickness and (c) degree of alignment mapping obtained by SAXS data analysis

6.3. Mechanical behaviour of the DEJ

6.3.1. Nanoindentation mapping of the DEJ

Nanoindentation mapping on the dental slice was carried out by a nanohardness tester (NHT) with a Berkovich diamond probe from CSM (Neuchatel, Switzerland). A load function composed of 30s loading, followed by 30s holding and 30s unloading was used under the force control feedback mode to a peak force of 2 mN. Mapping was performed on the region of interest (see Figure 6.4 a) with scanning space about 60 µm apart both in the *x*- and *y*-axis.

Figure 6.4 b and c demonstrate the results of the spatial distribution of reduced modulus and hardness respectively in the colour- coded 2-D maps of the region of interest. In general, contrast values were reflected in the colour ranges between dentine and enamel. In dentine, most regions have the reduced modulus below 40 GPa and hardness below 1 GPa, whereas in enamel, most regions have the reduced modulus in a range of 80-120 GPa and hardness in a range of 3-5 GPa. The DEJ is in the transition region with values gradually increased from dentine to enamel. However, it is found that the averaged reduced modulus of dentine was 20±6 GPa and that of enamel was 70±17 GPa. In addition, the averaged hardness in dentine was 0.7±0.1 GPa, and 3.0±1.3 GPa in enamel. The hardness and reduced modulus of the control sample were consistent with the earlier nanoindentation studies on dental tissues [154, 160].

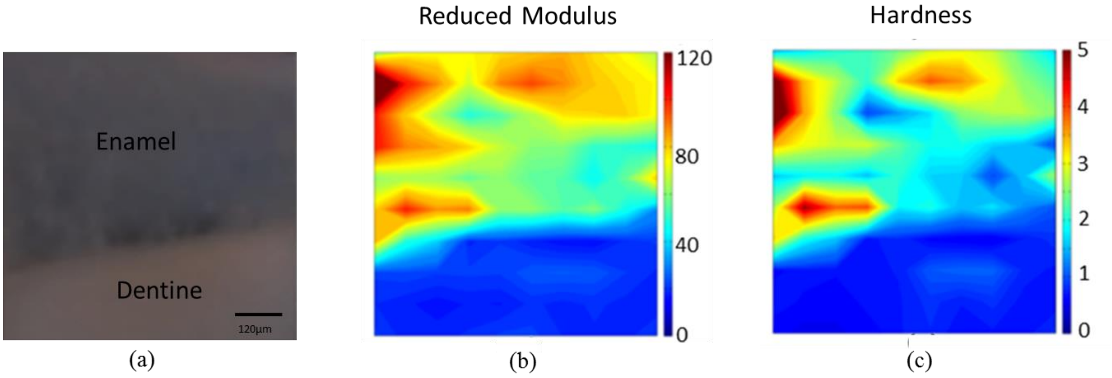

Fig. 6.4 Nanoindentation mapping of dental slice. (a) region of interest (ROI) in the human dental slice; (b) reduced modulus and (c) hardness obtained by nanoindentation data analysis

6.3.2. High resolution elastic modulus mapping of the DEJ by CR-FM

The structure variation of the DEJ has been determined in last sections by X-ray imaging and scattering techniques. In order to study the local variation of the elastic properties in the region of the DEJ gradient (20 μm), contact resonance force microscopy (CR-FM) was used for the high resolution elasticity mapping of the scanned surface. Followed by the basic sample preparation procedure as described in section 3.3.3., the DEJ samples were polished and stored under ambient conditions for further examination. Three scanning areas were selected as 30×15 µm^2, 10×5 µm^2 and 3×1.5 µm^2. To quantify the elastic modulus of the DEJ, a reference sample with the average value of elastic modulus of dentine and enamel (around 40 GPa) was selected (in this work, it is Mg) and needed to be examined as well. The sample surface vibration response to the excitation of the AFM tip is picked up by the AFM probe and recorded. The tip-sample contact resonance frequency reveals the sample stiffness information. The use of a reference sample avoids the need for precise calibration of the tip contact shape and radius that is required for the calculation of elastic modulus.

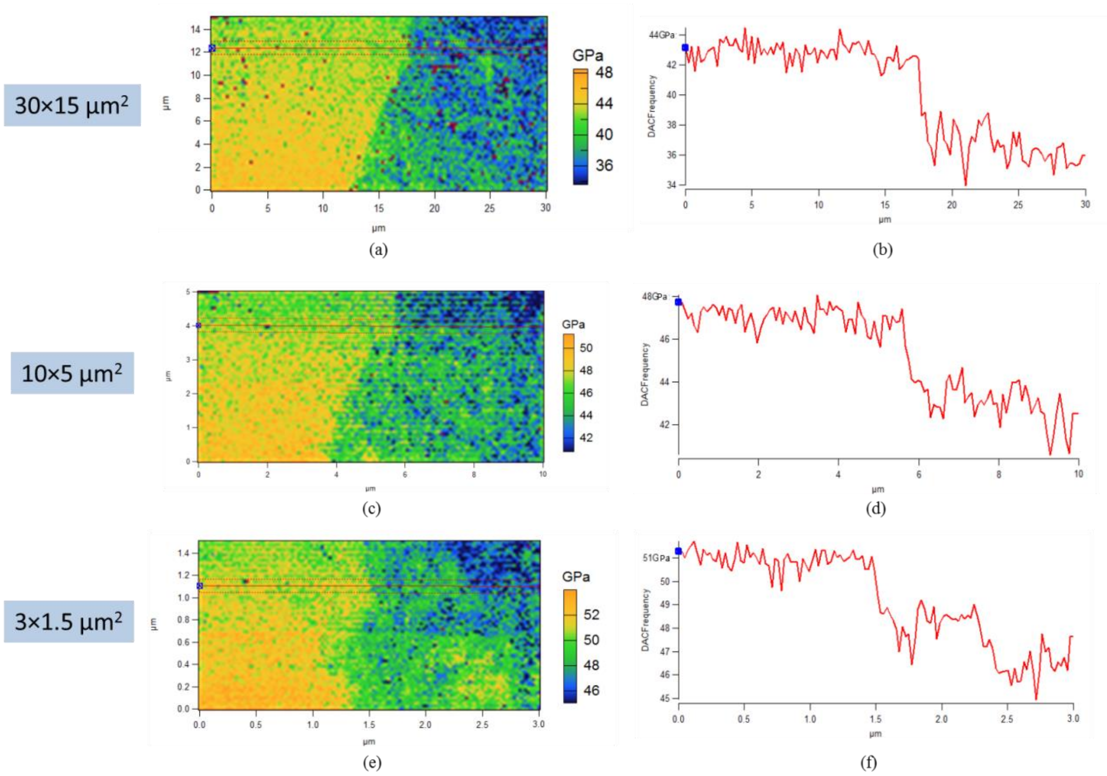

(a) (b)

(c) (d)

(e) (f)

Fig. 6.5 Elasticity mapping of the DEJ in the area of 30×15 µm^2, 10×5 µm^2, and 3×1.5 µm^2. (a), (c) and (e) are higher resolution elastic modulus mapping of the DEJ by band excitation CR-FM; (b), (d) and (f) are line profile (red line in (a), (c) and (e)) of the elastic modulus of the DEJ.

Figure 6.5 coincides with the previous observation, where enamel (yellow coloured region) generally has higher elastic modulus than dentine (depicted in blue and green region), which is softer compared to enamel. This is also consistent with the results illustrated in Table 2.1 and Table 2.2 as well as that obtained by nanoindentation (Figure 6.4). Furthermore, it is found that, with the reduction of the scanning area, the mechanical property transition region becomes blurrier and smaller, despite the slight difference still visible between dentine and enamel. Such observation supports that the DEJ is a region with varied properties from enamel to dentine. In addition, most importantly, the DEJ should be seen as a graded band rather than a discrete interfacial line since gradual change in mechanical properties is the most important feature of the DEJ. Such graded transition from enamel to dentine may sustain higher loads than a direct bond between two distinct adhesive layers.

The observed values of the elastic moduli may have errors from the true values for the region of interest. The potential error source includes the surface roughness of the sample as well as the selection of the reference sample. However, the examination region is small and it is expected that the elastic modulus variation across the small region would not be significant. Much higher resolution on the measurement of surface layer by CR-FM mapping provides valuable insights into the stiffness variation and arrangement of this remarkable interface.

6.3.3. *In situ* X-ray diffraction measurements of elastic deformation of the DEJ

This experiment was aimed at obtaining functional micro-probe maps of the DEJ at high resolution and providing critical insight into the microstructure and load-bearing characteristic of the DEJ under uniaxial loading with *in situ* WAXS measurement. The previous studies as presented in Chapter 4 and Chapter 5 have been carried out using synchrotron X-ray beamlines on the dentine and enamel separately by applying *in situ* uniaxial loading measurement. The Eshelby model proposed was used to evaluate the experimental data for the elastic lattice strain evolution within HAp crystallites. Meanwhile, the changes of *d*-spacing across the DEJ by high resolution X-ray diffraction has shown the gradient *d*-spacing spanning (see Figure 6.2 b) between the two contrast materials (enamel and dentine), which is essential for understanding the remarkable load-bearing function of the DEJ. Therefore, *in situ* WAXS mapping can be further developed, focusing on the response to loading of the regions adjacent to the DEJ. The understanding of how the DEJ accommodates this large modulus difference and distributes strain when stress rises is important in biology and in materials science of coatings.

Sample is selected and prepared so that the DEJ plane is almost parallel to the X-ray beam. The aim of this experiment is to have medium resolution scanning to obtain the strain gradient across the DEJ. Sub-micron beam with different setup would be needed to characterize the micro-scalloped structure on the DEJ with high resolution. However, although this approach would be able to reveal the fine structure of DEJ, the possibility of revealing the structural variation over a larger region would be lost.

The experiment was carried out on the B16 beamline at Diamond Light Source (DLS, Oxford, UK) using monochromatic 20KeV X-rays. X-ray Eye detector (Photonic Science X-ray MiniFDI) was firstly used to characterize the DEJ morphologies precisely, and to locate the DEJ region. Next, *in situ* loading was applied to specimen using a small compression loading rig especially designed for this purpose. Micro-beam was focused down to 2.1×1.4 μm^2 with KB mirrors. Then a line scan across dentine and enamel through the DEJ was carried out and the strain evolution of HAp crystallites could be obtained by the quantitative analysis of WAXS patterns collected by Photonic Science Image Star 9000 detector in the downstream of the X-ray source. Transmitted intensities were used to identify the DEJ position at each load and to detect any specimen movement during loading as shown in Figure 6.6. Then, the diffraction pattern analysis followed the previous studies as described in section 3.2 as well as in Chapter 4 and Chapter 5. (002) peak was selected for the peak fitting and the resulting peak centre movement was used to quantify the strain evolution of HAp crystallites during *in situ* compressive loading.

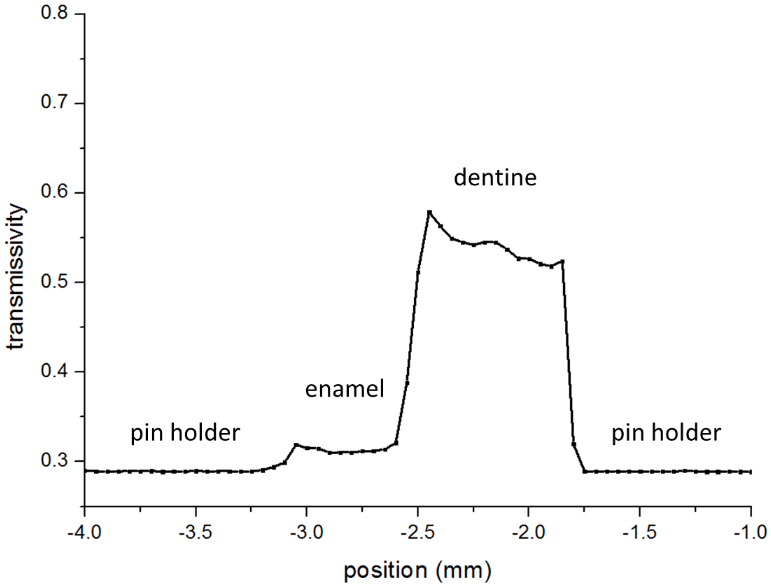

Fig. 6.6 Identification of the DEJ position. Plot of transmission vs. position for the DEJ scanning.

Figure 6.7 shows the region of interest (black line) which identifies the DEJ position by looking at the transmitted energy, of which dentine has higher transmission. The normalised apparent modulus within the same region from enamel to dentine across the DEJ was plotted in Figure 6.7 (red line). The apparent modulus was determined by the ratio of the uniaxial compressive stress and the average lattices strain of HAp crystallites. It is interesting to observe that $K_{enamel} > K_{dentine} > K_{DEJ}$. A strain gradient was also observed across the DEJ, which is consistent with the observation in bovine tooth specimens [132]. This reveals the complexity of the mechanical coupling but it is not contradictory to the mapping results of graded property obtained by indentation or other methods, from which the composite (composed of mineral inclusion with organic matrix) modulus was measured. The *in situ* WAXS measurement directly links the mineral response to the external loading thus the distribution of apparent modulus shown in Figure 6.7 could be reasonable.

This result supports the hypothesis that the DEJ has an effect of structural adaptation for transferring and minimizing stress. The DEJ also has been observed to display a remarkable ability to transfer loads between enamel and dentine such that cracks or fracture planes that are formed within enamel rarely propagate across the DEJ into the underlying dentine [197].

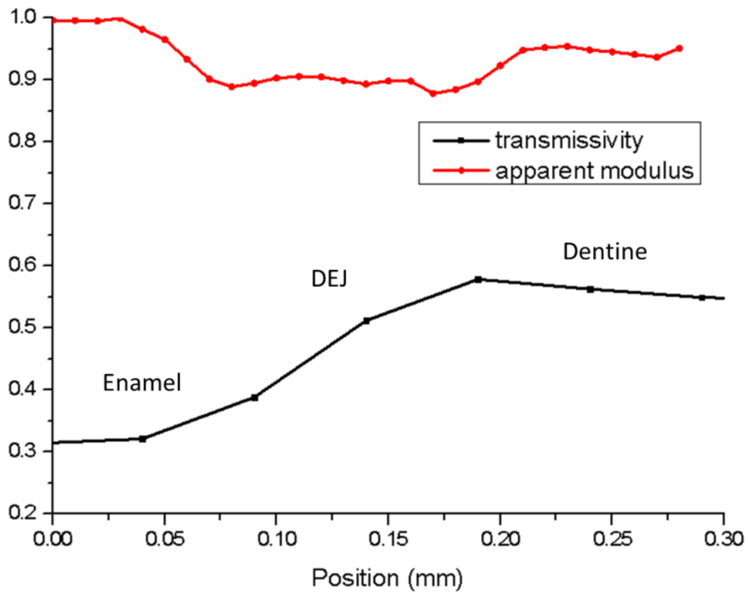

Fig. 6.7 Apparent modulus variation (red line) across the transmission identified region of interest (black line).

6.4. Thermal behaviour of the DEJ

Though considerable efforts have been directed at the study of structural and mechanical properties of the DEJ, improved understanding of the DEJ interface structure response to thermal treatment is still lacking. The effect of exposure of human skeletal tissues to elevated temperature is an important study topic in the context of forensic investigations, accident analysis, archaeology and paleontology [94]. However, an in-depth study of the heat-induced alterations of dental tissue remains lacking. Moreover, advanced high-energy techniques used in dentistry (e.g., dental lasers and light polymerizing units) may induce high temperature within teeth [198]. This provides additional need for detailed study of the effect of thermal exposure on the ultrastructural response of dental tissues. In particular, the DEJ is an important internal interface between the highly mineralized hard outer layer (enamel) and the softer tooth core (dentine), showing a gradient [56]. Due to heat, a sudden detachment of the enamel can be seen around 500^{o}C (see Figure 6.8 a). However, the detailed mechanisms are still unclear [90]. By examining the morphology of the DEJ exposed to different temperatures as shown in Figure 6.8 b-f, it was found that the crack initiated at 400^{o}C, and further propagated from 500^{o}C to 700^{o}C. The detachment occurred between dentine and enamel at 800^{o}C. The crack may be due to different thermal expansion coefficients, mechanical properties alteration during the thermal treatment or the structural changes around the DEJ (e.g. organic components in the dental tissue burnt off, resulting in no fibril connection any more between dentine and enamel). The different behaviours in terms of temperature observed in Figure 6.8 for the entire dental slice and uniform shaped sample are attributed to the thermal distribution being more uniform in the regular sample when it is compared to the complex geometrical sample.

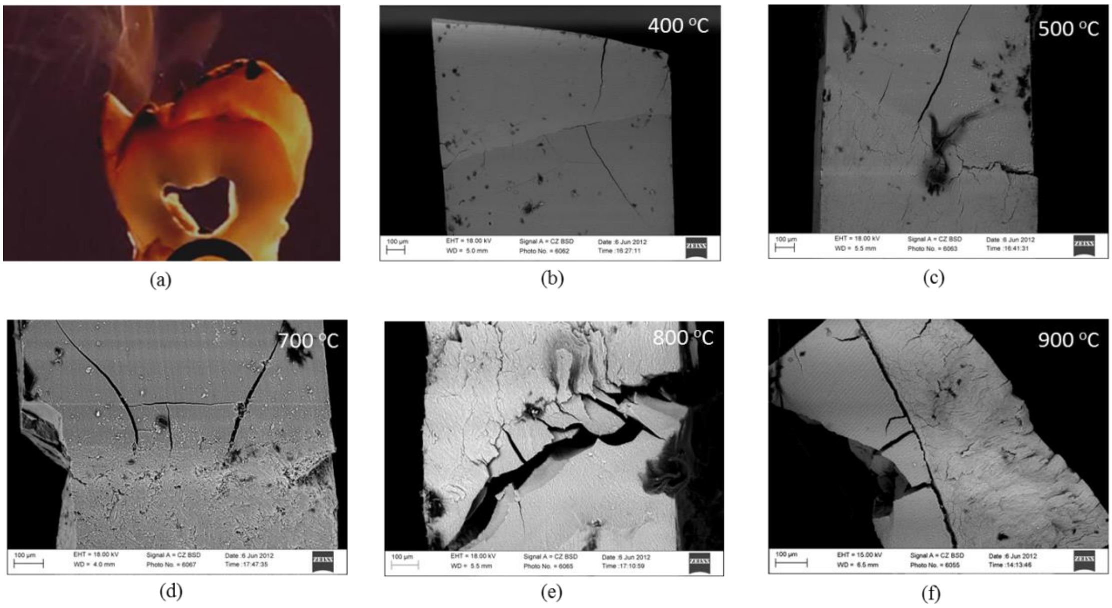

(a) (b) (c)

(d) (e) (f)

Fig. 6.8 (a) Sudden detachment in enamel near the DEJ at around 500^{o}C; (b)-(f) Crack initiation and propagation around the DEJ observed at different temperatures.

6.5. Conclusions

The microstructure of the DEJ was firstly investigated by X-ray imaging method (Micro-CT) and synchrotron X-ray scattering (SAXS/WAXS) techniques. The complex and scalloped structure at micro-scale was fully observed by 3-D reconstruction techniques. Furthermore, the high resolution probing of the lattice parameter variation at sub-nano scale reveals the structural variation at the same range (~20 μm) as has done by imaging. The 2-D spatial distribution of HAp crystalline nano-particles in terms of lattice parameters, mean thickness, degree of alignment and preferred orientation were also visualized.

In order to further examine the mechanical function region within the region of the DEJ, high resolution elastic modulus mapping was applied by band excitation CR-FM mapping. The results indicate that the DEJ is a band with a graded mechanical property rather than a discrete interface. Furthermore, X-ray diffraction measurements of the DEJ subjected to the *in situ* uniaxial loading was then carried out and successfully captured the structure-property relationship between the architecture of the DEJ and its response to the applied force. The knowledge of the architecture and properties of the natural DEJ will help in biomimetic engineering of superior dental restorations and prosthetics, and the development of novel materials to emulate DEJ.

Interesting detachment of enamel phenomenon was captured in dental tissues during thermal treatment, and crack initiation and prorogation around DEJ further approved the significant structural alteration occurred during heating. In order to understand its thermal behaviour, further investigation of the ultrastructural alteration of dental tissues at nano- and sub-nano scale upon thermal treatment as well as the corresponding mechanical properties alteration is essential, which will be described in Chapter 7 and Chapter 8.

Chapter 7

Nano-scale structure-mechanical property relations as a function of temperature of thermal exposure

This chapter is based on the following published manuscript:

- Tan Sui, Michael Sandholzer, et al, Structure-mechanical function relations at nano-scale in heat-affected human dental tissue, Journal of the Mechanical Behavior of Biomedical Materials, Vol. 32, pp.113-124, 2014

7.1. Brief introduction

Over many decades, the demand for dental treatment and prosthetics has driven improvements in the understanding of the micro-architecture of human teeth. The knowledge of the mechanical properties of dental materials related to their hierarchical structure is essential for understanding and predicting the effect of microstructural alterations on the performance of dental tissues. The effect of exposure of human skeletal tissues to elevated temperature is an important study topic in the context of forensic investigations, accident analysis, archaeology and paleontology [90, 91]. Moreover, advanced high-energy techniques used in dentistry (e.g., dental laser-assisted caries protection treatment) may induce high temperature within teeth that leads to increase mineralization locally [88]. So far, an in-depth study of the heat-induced alterations of dental tissue remains lacking and few studies have focused on the nano-scale structure-mechanical function relationship of human teeth altered by chemical or thermal treatment. The response of dental tissues to thermal treatment is thought to be strongly affected by the mineral crystallite size, their spatial arrangement and preferred orientation.

Multiple techniques (e.g. Fourier transform infrared spectroscopy, FTIR and lab-based X-ray powder diffraction, XRD) have been used to study the heat-induced ultrastructural alterations of skeletal hard tissues. However, most of those methods involve grinding the samples. In order to understand and quantify more precisely the mechanism of such ultrastructural alterations, the application of advanced non-destructive techniques offers an appropriate route. Synchrotron based X-ray diffraction, small- and wide angle X-ray scattering (SAXS and WAXS, respectively), are advanced non-destructive techniques that enable characterising the mineralized tissue ultrastructure [76, 139].

The aim of this study was to obtain a medium resolution mapping using synchrotron-based small and wide angle X-ray scattering (SAXS/WAXS) techniques to investigate the micro-structural alterations (mean crystalline thickness, crystal perfection and degree of alignment) of heat-affected dentine and enamel, as well as in the region near the DEJ of human teeth samples.. Additionally, nanoindentation mapping was applied to detect the spatial and temperature-dependent nano-mechanical properties variation. The analysis of the correlation between the ultrastructure and mechanical properties coupled with the effect of temperature demonstrate the effect of mean thickness and orientation on the local variation of mechanical properties.

7.2. Materials and methods

7.2.1. Sample preparation

Four freshly extracted intact human molars (ethical approval obtained from the National Research Ethics Committee; NHS-REC reference 09.H0405.33/ Consortium R&D No. 1446) were disinfected in 15mM sodium azide solution and washed under running water for 5-6 hours before being mechanically cleaned to eliminate residues. Teeth were chosen from the study to be free of damage (e.g. broken roots), endodontic treatment, dental restorations or caries. Details such as age, sex and patients ethnic background remained anonymous as part of patient confidentiality regulations. In total, twelve teeth sections ($3\times1\times0.5$ mm^3) were prepared and kept in a hydrated state in Phosphate Buffer Solution (PBS) at 4 ℃ before the experiment [21]. Of these, ten sections were allocated into five temperature groups for 30 min constant exposure at 400 ℃-800 ℃ (in steps of 100 ℃), and two additional unheated sections were used as controls. An ashing furnace (Carbolite AAF 11/3, Sheffield, United Kingdom) was used to generate the thermal treatment. Each tooth sample was then subjected to a thermal history that heated the sample to the final (maximum) temperature (constant exposure) and were then removed from the furnace after the desired duration of exposure was reached, and subsequently cooled down in the crucibles to room temperature and stored in padded containers.

For the purpose of planning the measuring positions and Region of Interests (ROIs) of the SAXS/WAXS mapping, micro-CT scans of the samples were performed as shown in Figure 7.2 a-c. In addition, it should be noted that the micro-CT scan was also used on the selection of samples in order to largely guarantee that the DEJ plane of the selected samples was parallel within experimental error to the X-ray beam.

The nanoindentation measurements were performed on the same teeth sections after embedding in epoxy resin (Buehler Epo-Kwick, Buehler Ltd., Lake Bluff, IL) to preserve their integrity and were analysed in the dry condition. The maximum peak temperatures of the epoxy during curing the manufacturer was 145 ℃ with a short period of time (less than a minute during the hardening), of which the influence on the sample was thought to be limited. Furthermore, the sections were carefully ground with a series of grinding papers (P800-P4000) to expose the surface and finally polished with 3 μm diamond polishing compound. This way, it was made sure that properties of the tissue were measured, but not properties of the epoxy resin.

In summary, six samples (RT, 400 ℃, 500 ℃, 600 ℃, 700 ℃ and 800 ℃) were used for the SAXS/WAXS mapping measurements and three out of those six samples including RT, 500 ℃ and 700 ℃ were further selected for the nano-indentation mapping, since these temperatures were representatives of major compositional changes and weight loss [199].

7.2.2. Micro-focus small angle X-ray scattering experiment

Micro-focus SAXS experiments were performed on the I22 beamline at Diamond Light Source (DLS, Oxford, UK) using monochromatic 18 keV X-rays. The distance between detector and sample was 1040 mm, guaranteeing that clear and complete SAXS patterns and a partial WAXS pattern could be captured on the 2-D detector (Pilatus 2M, Dectris Ltd., Baden, Switzerland) positioned downstream of the sample. The incident X-ray beam was focused down to the spot size of $14.5 \times 19\ \mu m^2$ to achieve the required spatial resolution. Each sample was mounted upright in air and scattering patterns were collected in transmission mode while the sample was repeatedly shifted in the plane perpendicular to the X-ray incident beam (travelling in the *z*-axis) to collect the map of SAXS patterns. The mapping area of region of interest (ROI) for the control sample and samples from 400 ℃-800 ℃ was 0.6×0.6 mm^2. The spacing between each two measurement points of the mapping scans was 40 μm both along longitudinal (*y*-axis) and transverse (*x*-axis) directions, resulting in a total of 225 scattering patterns per sample (see Figure 7.1 a).

The experiment allows us to consider the DEJ as a functionally and structurally gradient layer - a common approximation that is used with considerable success in the study of inhomogeneous materials, interfaces, surface treated systems, etc. Since the main interest is in-plane variation, all possible efforts have been made to ensure that the X-ray beam travelling through the sample is almost parallel to the DEJ and the beam size (14.5×19 μm^2) is able to provide a result averaged over the gauge volume that crosses the DEJ. Samples of the thickness ~500 μm represent the practical limit in terms of survival of thermal exposure. As for the SAXS measurements conducted in transmission mode in these experiments, sample thinner than that is likely to result in low intensity of the SAXS signal.

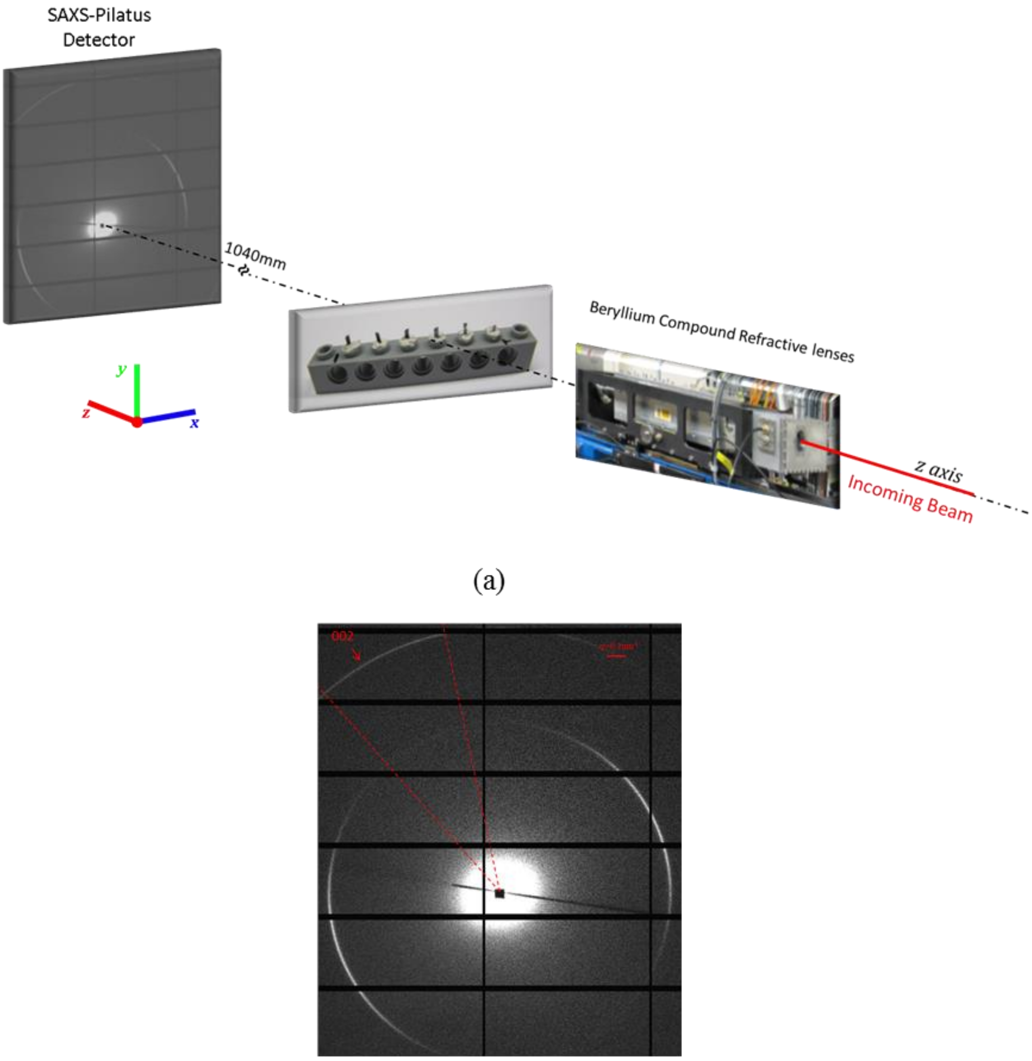

(a)

(b)

Fig. 7.1 Schematic diagram of the micro-focus SAXS experimental setup. (a) micro-focus SAXS setup; (b) WAXS patterns can also be partly obtained on the SAXS-Pilatus detector

7.2.3. Data interpretation

The typical SAXS/WAXS pattern collected in a single detector is shown in Figure 7.1 b. The quantitative interpretation of partial WAXS patterns has been described in section 3.1. Of those shown in Figure 7.1, the (002) peak of interest from each pattern was selected for the interpretation. Subsequently the 1-D radial plot of each individual (002) peak within each sector was collected and compared with respect to the temperature variation. Then the crystal perfection alteration was tracked.

To quantify the mean crystalline thickness, orientation and degree of alignment, the complete 2-D SAXS patterns in the central region in the detector in Figure 7.1 b were processed by separately integrating over the entire relevant range azimuthally and radially. The resulting 1-D plots were used to calculate the structure and distribution of HAp crystallites as described in detail in section 3.2.

7.2.4. Nanoindentation experiment

Nanoindentation tests are widely used to determine material properties such as hardness and reduced modulus. Each nano-indent operation involves a loading and unloading process, while the indentation load-depth data is recorded for each operation [162]. A nanohardness tester (NHT) with a Berkovich diamond probe from CSM (CSM, Neuchatel, Switzerland) was utilised to perform nanoindentation on the thermally treated samples. The calibration was done by fused silica and the procedure suggested by Oliver and Pharr [163] was used to correct the load-frame compliance of the apparatus and the imperfect shape of the indenter tip. The tests were performed at room temperature under force control feedback mode to a peak force of 2 mN. A load function composed of 30s loading, followed by 30s holding and 30s unloading was used [200, 201]. The hold period at maximum load (30s) is used to constrain creep upon unloading, and thereby allow for a more reliable extraction of mechanical properties from the unloading curve [202]. The contact depth was between 100 and 400 nm, much lower than the tooth sample thickness (0.5 mm), so that the properties obtained can be confidently assigned to the bulk. Maps of indents were performed along the same ROI used for the scattering experiment. The indents were spaced approximately 60 μm apart both in the *x*- and *y*-axis and performed using automation.

A schematic diagram of the nanoindentation process is shown in Figure 3.11, where the hardness H of the sample was obtained by dividing the load by the projected area of indentation. Using the compliance method as described in section 3.3.1, the reduced modulus E_r was determined directly from the analysis of load-displacement data [157].

7.2.5. Statistical Analysis

The calculated mean crystalline thickness values were statistically analysed with two-tailed paired sample t-tests using SPSS version 19 (IBM SPSS Inc., Chicago, USA). Probability levels of $p<0.05$ (95% confidence interval) were considered statistically significant.

7.3. Results

Progressive, temperature-dependent shifts in colour from a yellowish/white (control) to dark brown (400 ℃), brown (500-600 ℃), dark grey (700 ℃), light greyish-blue (800 ℃) and chalky-white (900 ℃) in dentine were observed. In all burned samples the micro-CT models showed small cracks in the slices, while in groups treated at ≥700°C additional multiple larger longitudinal and numerous transversal cracks were also visible in dentine. The enamel was well preserved in all samples ≤800°C in this study. Colour coded 2-D mapping provides a general qualitative understanding of the spatial distribution of the ultrastructural and mechanical properties and their variations with temperature. It also offers a validation on extracting the line measurements or 1-D plot with the detailed quantitative information of the changes and correlation of the results. For reasons of consistency, the central line values were chosen in all samples and no dependency of the measurement results on the line position was found. In this section, both the 2-D mapping results and the line plot were presented.

7.3.1. Ultrastructural observations

7.3.1.1. Mean crystalline thickness

The spatial mean thickness variations of HAp crystallites in the control sample (RT, room temperature), samples heat treated at 500 ℃ and 700 ℃ were visualized in Figure 7.2 d-f as colour coded 2-D plots. Similar features from the three samples were observed, of which the mean crystalline thickness decreased from enamel to the DEJ, and further down through deeper dentine. From Figure 7.2 d-f, it was found that the mean thickness of HAp crystallites increases with temperature, which was reflected through the 2-D colour changes (enamel from blue in Figure 7.2 d to red in Figure 7.2 f, while dentine from dark blue to red). In addition, the spatial difference of the crystalline thickness between enamel and dentine was found to gradually decrease with temperature since in Figure 7.2 f, enamel and dentine almost share the same colour.

In order to trace the average crystalline thickness alteration with increasing temperature, the thickness values along the central line of dentine and enamel in the mapping area were extracted from the 2-D mapping results, which are shown in Figure 7.4. The variation of the averaged mean crystalline thickness of the central line of dentine and enamel with increasing temperature are illustrated in Figure 7.5 a-b, from which the crystallites in dentine were nearly tripled from 1.94 ± 0.06 nm at room temperature (RT) to 5.16 ± 0.06 nm at 800 ℃, while that of crystallites in enamel increased from 3.81±0.28 nm at RT to 4.90±0.04 nm at 800 ℃ (for additional values see Table 7.1).

7.3.1.2. Orientation and degree of alignment

The 2-D maps of the degree of alignment variation of the same three samples (RT, 500 ℃ and 700 ℃) within the region of interest are shown respectively in Figure 7.2 g-i. The enamel and dentine show distinctive results visualized by the colour coding. Similar gradient features as the mean thickness results were observed. Generally, enamel has higher degree of alignment than dentine. However, it was found that the degree of alignment of both enamel and dentine decreased with temperature as the colour changed mostly from red to yellow in enamel and yellow to blue in dentine.

The angular orientation of the mineral particles in the 2-D teeth slices is depicted by the small black lines superimposed on the degree of alignment mapping (shown in Figure 7.2 g-i). In enamel, all the particles are almost orthogonal to the DEJ plane. Same features can be observed for the particles in dentine but only for the region far beneath the transition area of the DEJ. It appears that mineral particles gradually become parallel to the DEJ plane through the region near the DEJ.

The same central line of dentine and enamel as presented in the mean thickness visualization were selected from 2-D mapping results. Only the line variation of the result in dentine is of the most interest and is shown in Figure 7.4 b. It was found that in the specific area in dentine just beneath the DEJ, the degree of alignment was relatively higher than the area far away from the DEJ, shown as a bump in Figure 7.4 b. However, the overall degree of alignment of crystallites in dentine decreased (also see Figure 7.4 c and d) and the bump gradually disappeared with temperature. This indicates a tendency towards more random distribution of crystallites as the temperature increased (see Table 7.1).

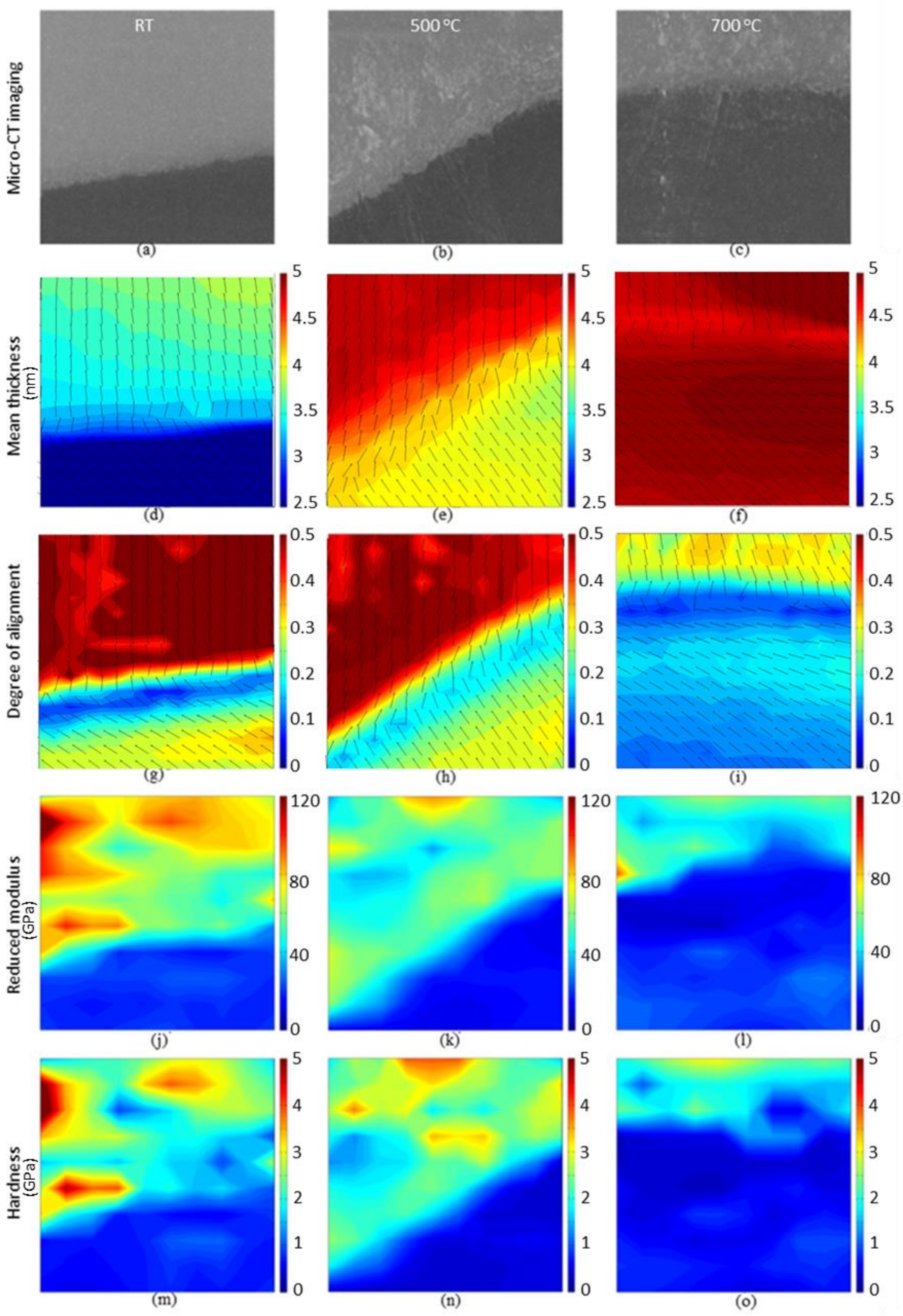

Fig. 7.2 Region of interest (0.6×0.6 mm^2) of dental slice mapped with SAXS and nanoindentation techniques. Each column represents the results within the same area under a

certain temperature as labelled. (a-c) ROI of RT (room temperature), 500°C and 700°C samples revealed by Micro-CT; 2-D colour coded of SAXS results: (d-f) mean thickness (nm) and (g-i) degree of alignment of HAp crystallites, with the crystal orientation marked by the black lines. The mean thickness of the crystallites in both dentine and enamel increases as the temperature increases (from light blue to red for enamel and from dark blue to red for dentine). However, the spatial difference between dentine and enamel decreases with temperature. The degree of alignment drops as the temperature increases (from red to yellow for enamel and from yellow to blue for dentine); 2-D colour coded of nanoindentation results: (j-l) reduced modulus (GPa) and (m-o) hardness (GPa); The reduced modulus and hardness of enamel is observed to decrease significantly with the increasing temperature (from yellow-red mixture to light blue)

7.3.2. Mechanical properties characterization

7.3.2.1. Reduced modulus

Figure 7.2 j-k demonstrate the results of the spatial distribution of reduced modulus within the 2-D interested area of the three samples (RT, 500 ℃ and 700 ℃). The DEJ is clearly visible whereas the distribution inside the enamel and dentine is limited. It was found that only enamel has a pronounced colour change (from yellow-red in Figure 7.2 j to light blue in Figure 7.2 l), indicating a significant decrease of reduced modulus in enamel with temperature.

The variations of the averaged reduced modulus of the central line of dentine and enamel with respect to all the tested temperatures are illustrated in Figure 7.4 a and c. From the figure, it was found that the averaged reduced modulus of dentine decreased from 20±6 GPa at RT to 15±2 GPa at 500 ℃ and then increased to 29±10 GPa at 800 ℃, while in enamel it decreased from 70±17 GPa at RT to 56±17 GPa at 500 ℃, and then further down to 47±18 GPa at 800 ℃ (see Table 7.1).

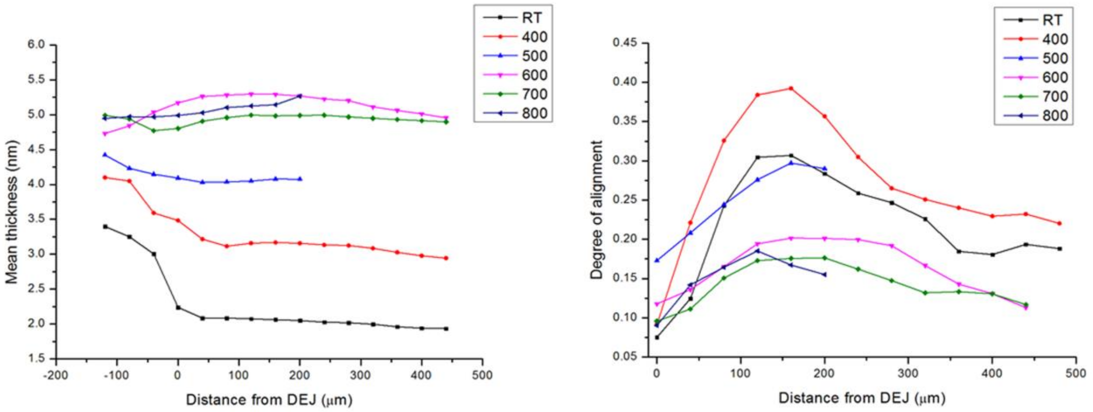

(a) (b)

Fig. 7.3 Ultrastructural variations along the central line from the 2-D mapping result of ROI as a function of temperature and distance from the DEJ. (a) results of the mean thickness of HAp crystallites. The first three measurement points (with minus distances from the DEJ) represent the results in enamel; (b) results of the degree of alignment of HAp crystallites. Only the results of crystals in dentine are shown due to the complex variations from the DEJ to the deep dentine.

7.3.2.2. Hardness

The overall spatial distribution of hardness of the three samples (RT, 500 ℃ and 700 ℃) in the ROI can be observed in Figure 7.2 m-o. The DEJ is still recognisable, but the spatial changes are not as clearly shown as in the structural mapping of thickness and degree of alignment. Similar tendencies to the reduced modulus were found in that the hardness of enamel dropped significantly with temperature, which is reflected from the pronounced colour change.

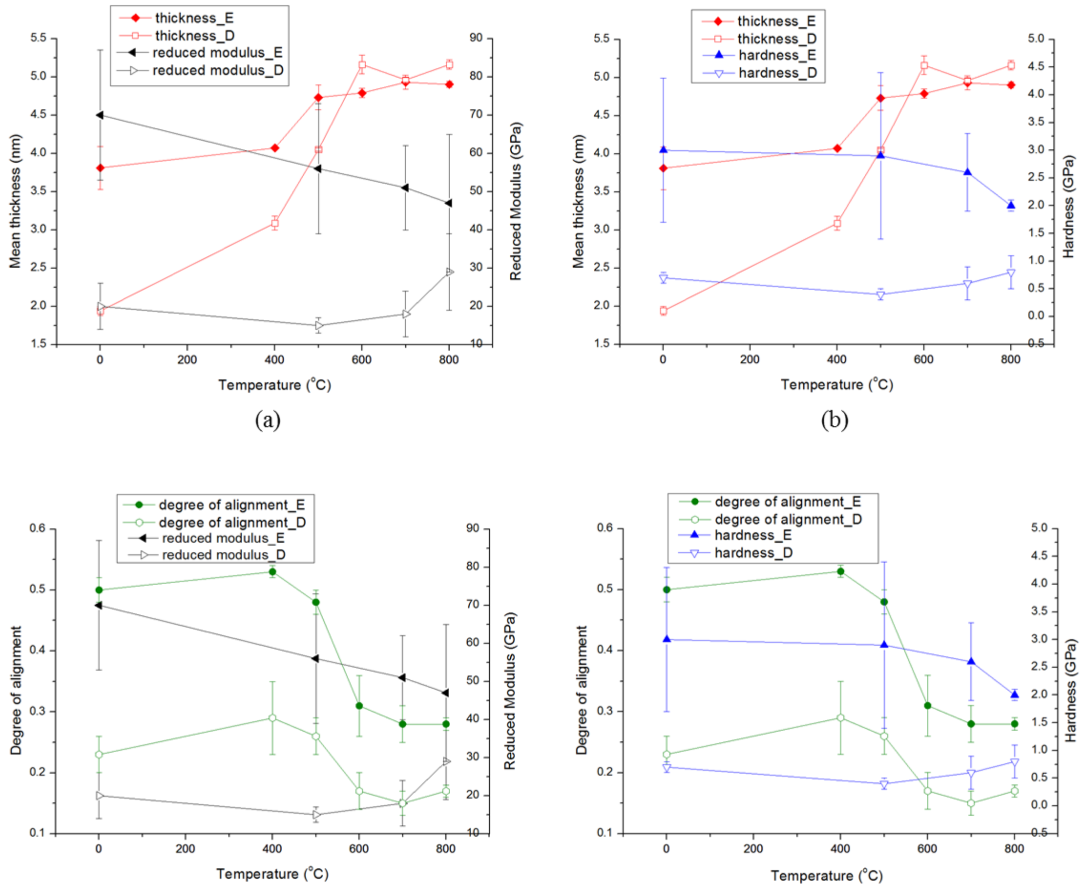

(a) (b) (c) (d)

Fig. 7.4 Correlation analysis between structural-mechanical parameters coupled with increasing temperature ("E" means enamel while "D" means dentine). All the results are the averaged values of different regions along the selected central line in ROI. (a) mean thickness vs. reduced modulus; (b) mean thickness vs. hardness; (c) degree of alignment vs. reduced modulus; (d) degree of alignment vs. hardness. Error bars ± 1SD.

The detailed alteration of the hardness with increasing temperature can be further visualized from the selected central line of dentine and enamel (Figure 7.4 b and d). It was found that the averaged hardness variation has the similar tendency of variation as that of the averaged reduced modulus both in dentine and enamel. The averaged hardness in dentine decreased from 0.7±0.1 GPa at RT down to 0.4±0.1 GPa at 500 ℃ and then increased to 0.8±0.3 GPa at 800 ℃, while in enamel the averaged hardness decreased from 3.0±1.3 GPa at RT to 2.9±1.5 GPa at 500 ℃ and then to 2.0±0.1 GPa at 800 ℃ (see Table 7.1).

Tab. 7.1 Overview of SAXS and nanoindentation measurement results collected from central line from 2-D mapping results. Statistical significance was evaluated using two-tailed paired sample t-tests with a 95% confidence interval for the mean thickness results (*p<0.05, **p<0.005, ***p<0.0005).

Temperature (℃)		**Mean crystalline thickness (nm)**	**Degree of alignment**	**Crystalline shape**	**Hardness (GPa)**	**Reduced modulus (GPa)**
RT	Enamel	3.81(SD: 0.28)	0.50(SD: 0.02)	1.40(SD: 0.04)	3.0(SD: 1.3)	70(SD:17)
400		4.07(0.02)	0.53(0.01)	2.03(0.05)		
500		4.73(0.16)*	0.48(0.02)	2.20(0.01)	2.9(1.5)	56(17)
600		4.79(0.06)	0.31(0.05)	3.53(0.08		
700		4.93(0.09)	0.28(0.03)	3.50(0.06)	2.6(0.7)	51(11)
800		4.90(0.04)	0.28(0.01)	3.29(0.04)	2.0(0.1)	47(18)
RT	Dentine	1.94(0.06)	0.23(0.03)	2.77(0.07)	0.7(0.1)	20(6)
400		3.09(0.09)***	0.29(0.06)	2.84(0.03)		
500		4.05(0.02)***	0.26(0.03)	3.28(0.01)	0.4(0.1)	15(2)
600		5.16(0.12)***	0.17(0.03)	3.16(0.02)		
700		4.96(0.03)***	0.15(0.02)	3.14(0.07)	0.6(0.3)	18(6)
800		5.16(0.06)	0.17(0.01)	3.09(0.05)	0.8(0.3)	29(10)

7.3.3. Crystal perfection

The WAXS patterns collected from HAp crystallites in both the enamel and dentine provide information about the crystalline perfection in different regions. Due to the limited size of the 2-D detector, i.e., limited observed WAXS rings, it is hard to do the quantitive analysis on all the peaks. Only the (002) peak could be partially captured and analysed to present the intensity variation. As a result, the orientation and potential HAp crystallite size information from WAXS could not be fully extracted. Figure 7.5 shows the diffraction intensity variation of the (002) peak for a selected region of scattering angles (11.2°-11.5°) with the temperature change. A sharpening of the peak at higher temperatures was observed, compared to the broad one of the control sample at lower temperature due to the influence from amorphous HAp crystallites. This represents an increased diffraction contribution from HAp crystallites within this scattering angle range as the temperature increased, which indicates that the crystal perfection increased remarkably during the heating. Note that the peak sharpening in dentine is more obvious than that in enamel.

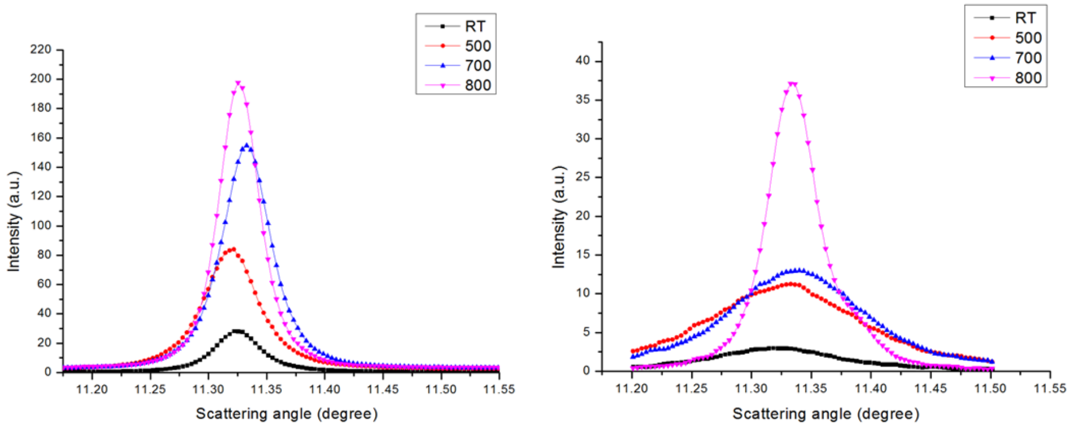

(a) (b)

Fig. 7.5 Intensity variation of the (002) reflection in the WAXS patterns of different regions at different temperatures: (a) enamel; (b) dentine. The observed peak sharpening and higher intensity at higher temperatures compared with the control sample indicates an increased diffraction contribution from HAp crystallites.

7.4. Discussion

Walker et al. (2008) [101] have proposed that a combination of multiple conditions in the cremation environment (e.g. duration, temperature and oxygen availability) determines the extent of the macro- and microscopic alterations observed in mineralized remains. Furthermore, Piga et al. (2009) [90] noted the limitation of lab-based research and that heating of skeletal tissue in cultural cremations is likely to be non-uniform. To ensure the comparability of our results, the selected temperature range (400°C-800°C) and duration were matched to previous studies to include possible archaeological and forensic scenarios [90, 110]. Additional factors in those studies, such as the presence of soft tissues, fast increase or fluctuation of temperature or the presence of contaminants, have generally not been taken into account in lab-based research but they might also have some effects on skeletal hard tissues. As the sample was subjected to the thermal treatment at high temperature and had to embedded into epoxy resin for nanoindentation, it was reasonable to assume that the influence of water could be ignored, i.e. the samples were analyzed dry. The main focus of this study was to evaluate the ultrastructural and mechanical heat-induced changes, which are of importance for forensic dentistry. In contrast to observations made on the entire teeth [90], where the enamel lifted off at the dentine-enamel junction (DEJ) at ~700°C, the enamel was preserved in all our samples treated at ≤800°C, enabling the combined analysis of enamel and dentine. Although the exact mechanisms of the enamel shattering in teeth are unclear, the preservation in our samples can be ascribed to the small slice dimensions which might minimize heat-induced stress around the DEJ.

7.4.1. Ultrastructural observations

7.4.1.1. Mean crystalline thickness

Overall the mean crystalline thickness distribution in dentine was more uniform compared with that in enamel. The mean crystalline thickness was observed to obviously decrease in enamel and slightly increase in dentine towards the DEJ at low temperatures, which may be ascribed to the gradient properties of human dental slice [198] as illustrated in Figure 7.3 a. However, also clearly seen in Figure 7.3 a is that, as temperature increases, this gradient becomes smaller. Besides the visible gradient features, the major drop visible near the transition area around the DEJ indicates the spatial structural variation in the human dental slice.

The mean crystalline thickness of the control sample (3.81 ±0.28 nm in dentine and 1.94 ±0.06 nm in enamel) is consistent with the earlier transmission electron microscopy (TEM) studies and XRD data [21, 203]. The increase of mean crystalline thickness happened after 400^{o}C implies the onset of sintering of the HAp crystallites, which leads to crystallite growth. This process becomes dramatic after 600^{o}C, as can be confirmed by tracking the WAXS peak variation as illustrated in the Figure 7.5 [199]. In addition, the small increase in crystallite size for enamel with increasing temperature is likely to be related to the denser arrangement of HAp crystallites compared with dentine.

7.4.1.2. Orientation and degree of alignment

The local structural variation of the degree of alignment in dentine with distance from the DEJ (Figure 7.3 b) represents the micro-structural adaptation at different position of the human tooth. The higher degree of alignment of HAp crystallites near the DEJ is expected to stiffen the dentine. Thus the higher mineral particle co-alignments beneath the chewing surface cusps may be important for the transfer or the redistribution of mastication loads from the much harder, highly mineralised enamel deep into bulk dentine [173].

The degree of alignment in dentine (0.23±0.03) from the control sample (room temperature, Figure 7.4 c-d) indicates an almost random orientation of HAp crystallites, while in enamel is more strongly textured (0.50±0.02). This is consistent with earlier SAXS results for dental tissue [173, 204], where the internal architecture in dentine was observed to be net-like fibrils wound around tubules with decorated HAp crystallites. If it is observed along tubule direction, the fibrils will display an almost random distribution [178]. Therefore, when the beam illuminates perpendicular to the dental slice, i.e. perpendicular to the cross section of tubule, the HAp crystallites will have a much lower degree of alignment than that of well-packed HAp crystallites in enamel, where the crystallites partially align along the prisms (or rods) [31]. It was noted that in both dentine and enamel, there was a reduction in the degree of alignment as the temperature increased. The reduction of the overall degree of alignment as well as the bump gradient of the central line observed in Figure 7.3 b with increasing temperature may be explained by the burning-off or gradual disappearance of the organic phase, most of which is collagen. Since the organic phase serves as the support of the structure, such disappearance may lead to the rearrangement of crystallites associated with rotation or anisotropic sintering. In addition, the rearrangement of crystallites may increase the crystal perfection, especially in dentine (Figure 7.5), due to its larger amount of organic phase than in enamel.

7.4.1.3. Crystal perfection

The (002) peak variation measured from WAXS resulted from the diffraction by HAp crystallites. Increasing temperature leads to the disappearance of the organic components in between the mineral phase and a higher degree of perfection of the HAp crystallite can be observed, accompanied by further crystallization of the amorphous part [94]. Finally, at high temperatures sintering of HAp crystallites leads to grain growth and improved crystal quality, resulting in significant growth and sharpening of the diffraction peaks [118].

7.4.2. Mechanical properties characterization

Both hardness and reduced modulus mapping showed the obvious contrast of properties between dentine and enamel. The boundary between dentine and enamel is clearly shown in Figure 7.2 j-o and regions with large reduced modulus and hardness match very well as expected. However, it was found that the transition feature of mechanical properties in dentine was not as clear as the ultrastructural visualization, which was partly due to the low resolution of nanoindentation compared with SAXS/WAXS and the mechanical-response dispersion of both enamel and dentine. In addition, the existing cracks or surface defects in all the samples may affect the indentation results, and increase the relatively large error bounds in Figure 7.4.

The different behaviours of dentine and enamel might result from their different mineral contents. The initial reduction of the mechanical properties in dentine might be due to the gradual disappearance of collagen and the subsequent increase at higher temperatures might be explained by the occurrence of sintering and significantly increased crystal perfection, which was partly reflected in the sharp peak variation in dentine in Figure 7.5.

7.4.3. Ultrastructure and mechanical properties correlation

The relationship between the variations of the ultrastructure and mechanical properties with respect to different temperatures are reflected in Figure 7.4 a-d. As illustrated in Figure 7.4 a-b, in the enamel the reduced modulus (solid black symbols) and hardness (solid blue symbols) decrease as the mean thickness (solid red symbols) goes up. In contrast, the opposite trend is observed in dentine as illustrated in the empty symbols. One such possibility may be the formation of oxidation layer at the elevated temperatures which could affect the hardness values, particularly for dentine.Thus, the mean thickness is found to be a good predictor of the reduced modulus and hardness.

No obvious correlation between the degree of alignment and the mechanical properties can be observed in Figure 7.4 c-d except that the region with higher modulus as shown in Figure 7.2 almost matches the region with higher degree of alignment of the HAp crystallites, which indicates that the local structural variation may result in the local change of modulus in the same area. Furthermore, the orientation distribution of HAp crystallites may indicate a correlation between the orientation effect or texture effect and the mechanical property variation, as discussed in our previous work [205].

Similar variation tendency of reduced modulus and hardness [206] is observed in Figure 7.4. , The crack is visible in micro-CT observation (see Figure 7.6 a-c), Thermal strain or misfit strain facilitates the initiation and propagation of crack. In addition, the burnt-off collagen also results in the missing link in between dentine and enamel. This could be used to explain the mechanisms that a sudden detachment of the enamel that was captured by the high-speed camera observation after 500°C (see Figure 6.8 a).

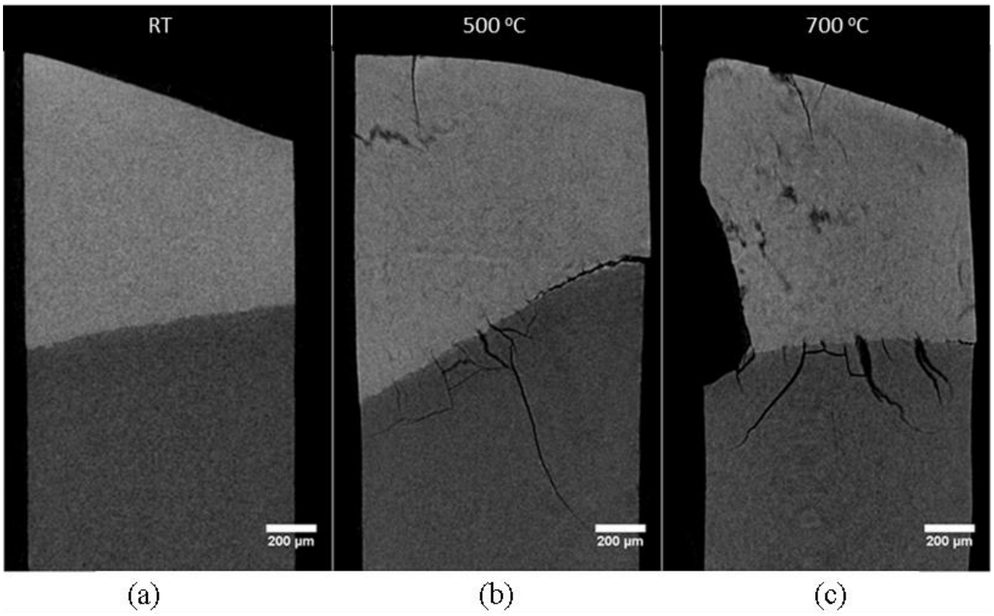

Fig. 7.6 Crack development revealed by micro-CT cross-sectional images. The control sample (a) shows no cracks around the DEJ; whilst an increase in number of cracks and lifting of the enamel can be seen at 500°C (b) and 700°C (c);

7.5. Conclusions

The ultrastructural alteration of skeletal hard tissues exposed to the thermal treatment process developed in the present study by synchrotron X-ray techniques provides a better and more reliable basis for deducing the heating history, compared with the conventional methods based on monitoring the macro- and microstructural colour [90-92] in the forensic and archaeological investigation. In the clinical application like caries prevention, the present study offers an opportunity to characterize the microstructural features affected by laser therapies.

The previous analysis of the entire powdered tooth obscures the sharpness of ultrastructural variations in dentine and enamel [90, 119]. The present study clearly illustrates how the observed evolution of the ultrastructure reflects the differences between dentine and enamel, suggesting that enamel and dentine must be investigated separately in order to evaluate the exposure temperature precisely in the forensic cases as well as to optimize laser-assistant treatment in clinical application.

The structural-mechanical properties correlation to the temperature provides an additional guidance to track the heating history in the forensic study. In addition, for caries prevention, it provides the evidence that the alteration of mechanical properties should also be taken into account during the sintering process.

The effects of heat treatment on human dental tissues were successfully elucidated by a systematic study of the combined SAXS/WAXS mapping and nanoindentation mapping techniques. Quantitative analysis of SAXS patterns of human teeth samples revealed a temperature-dependent variation of the mean crystalline thickness and the degree of alignment of nano-scale mineral phase (HAp crystallites) both in dentine and enamel. Furthermore, nanoindentation mapping captured the decrease of the hardness and modulus as the temperature increased. The relationship between the ultrastructural changes and mechanical behaviour changes with increasing temperature indicates that the structure has a strong effect on the mechanical properties.

The SAXS/WAXS results revealed that the mean crystalline thickness distribution in dentine was more uniform compared with that in enamel. Although in general the mean crystalline thickness increased both in dentine and enamel as the temperature increased, the local structural variations gradually reduced. Meanwhile, the hardness and reduced modulus in enamel decreased as the temperature increased, while for dentine, the tendency reversed at high temperature. This structural-mechanical property alteration is likely to be due to changes of HAp crystallites, thus dentine and enamel exhibit different responses at different temperatures.

In conclusion, the combination of synchrotron-based SAXS/WAXS and nanoindentation mapping methods has been shown to be a powerful method for the determination of the variation of the structural-mechanical property relationship in human dental tissues induced by thermal treatment. Our results enable an improved understanding of the mechanical properties correlation in hierarchical biological materials, and human dental tissue in particular. Ultimately, the SAXS mapping approach developed in the present study might allow further design and optimization of laser treatment strategies for clinical applications, and will possibly provide an effective approach to deduce the heating history for teeth samples in the forensic and archaeological context.

Chapter 8

X-ray scattering evaluation of ultrastructural changes of natural and synthetic hydroxyapatite under *in situ* thermal treatment

This chapter is based on the following published manuscript:

- Tan Sui, Michael Sandholzer, et al, *In situ* X-ray scattering evaluation of heat-induced ultrastructural changes in dental tissues and synthetic hydroxyapatite, *Journal of The Royal Society - Interface*, Vol. 11, 2014

8.1. Brief introduction

Human dental tissues consist of inorganic constituents (mainly crystallites of hydroxyapatite, HAp) and organic matrix. In addition, synthetic HAp powders are frequently used in medical and chemical applications. Insight into the ultrastructural alterations of skeletal hard tissues exposed to thermal treatment is crucial for the estimation of temperature of exposure in forensic and archaeological studies. However, at present only limited data exist on the heat-induced structural alterations of human dental tissues. The experiments described in Chapter 7 were conducted *ex situ*, where it was possible to consider only a limited number of samples after exposure to temperatures in the 400–800 ℃ range. In addition, by necessity, different samples were used for each measurement, and thus the sample-to-sample ultrastructure variation could not be excluded. This aspect may weaken the reliability of the conclusions drawn regarding the mechanism of local ultrastructural changes.

Furthermore, the *ex situ* mode of sample characterization is applied only after heating and cooling the samples to/from different temperatures. Obviously, no information is available on the structure evolution during heating or cooling. To the best of our knowledge, no results have been reported on monitoring heat-induced ultrastructural changes of HAp crystallites using an *in situ* experimental protocol spanning the entire relevant range of heating and cooling nor has the comparison been made between the naturally occurring HAp crystallites within human dental tissues and synthetic HAp powders. Thus, *in situ* thermal measurement will help to understand the internal architecture of complex natural materials (highly mineralized human tissues), and its evolution during thermal exposure.

In this Chapter, advanced non-destructive Small- and Wide Angle X-ray Scattering (SAXS/WAXS) synchrotron techniques were used to investigate the in situ ultrastructural alterations in thermally treated human dental tissues and synthetic HAp powders. The crystallographic properties were probed by WAXS, whilst HAp grain size distribution changes were evaluated by SAXS. The results were analysed in order to understand how the internal ultrastructure within the human dental tissues and the synthetic HAp powders evolves during the heating and cooling schedule.

8.2. Materials and methods

8.2.1. Sample preparation

Freshly extracted intact human third molars (ethical approval obtained from the National Research Ethics Committee; NHS-REC reference 09.H0405.33/ Consortium R&D No. 1465) were washed and cleaned in distilled water to eliminate residues so that the possibility of contamination or other chemical effects was excluded. The samples were cut into 1mm-thick cross-sectional slices in the bucco-lingual orientation including dentine and enamel (see Figure 1a) using a low speed diamond saw (Isomet Buehler Ltd., Lake Bluff, Illinois, USA) and polished using a sequence of grit papers to minimise the induced residual strain. In total, four cross-sections were prepared and were kept in distilled water in a commercial fridge at 4°C until the experiment was performed. Low temperature storage conditions ensured relatively low diffusion rates so as to impede or exclude any possibility of superficial demineralization effect of water.

HAp powder has been widely used as coating materials in the implantology for dental application due to its similar chemical composition to the natural dental tissues. A mould was filled with 100mg of commercially available HAp powder which is manufactured by wet chemical precipitation method (Hydroxyapatite HTP powder, Bio-Rad, Hercules, CA, USA) and compacted with using an Instron 5544 machine (Instron Ltd., Bucks, United Kingdom) at 1.8kN force. The resulting disk was 1.2mm thick and 8 mm in diameter, with an approximate density of 1150 mg/cm^3 to obtain powder disk with a similar density to the dentine. The compression was done in dry state, and storage was at RT (room temperature) in the padded containers, so the humidity is as normal.

The weight-loss over time was additionally evaluated using Thermogravimetry (TGA) at a rate of 12˚C/min using three cube-shaped dental samples (3×3×3mm) extracted from two molars. The weight fraction of the organic component was determined with TGA using one cubic dentine sample that was placed in a rotating 10% formic acid bath for 14 days to eliminate the mineral content, thus producing a purely organic sample.

8.2.2. *In situ* scattering measurements

8.2.2.1. Thermal treatment setup

In situ thermal treatment of the samples was performed using a remotely operated and monitored furnace that allows collection of SAXS/WAXS data at temperatures up to 1000˚C. This furnace is a modification of the design used at Daresbury laboratory [207]. The samples were fixed in specially designed ceramic sample holders. A Kapton window in the furnace allowed a high-energy X-ray transmission setup to be used, as illustrated in Figure 8.1 a. The heating and cooling protocols were controlled using a Eurotherm controller. The protocols incorporated ramps at 12^{o}C/min, and constant temperature holds of 200 seconds for each temperature level within dental slice samples studied (enamel and dentine in Figure 8.1 d). The protocol for synthetic HAp powders is also shown in Figure 8.1 e. Slightly different thermal protocols were used for natural and synthetic materials due to the limitations of the experimental set-up (furnace heating rates accessible for different samples). However, preliminary measurements carried out showed that, within the range of heating rates considered, the resulting differences were negligible. The temperature output by the furnace controller and thermocouple was of high accuracy (one decimal point, approximately 0.1 ° nominal precision). This could be achieved since the thermocouple is passed through the wall of the refractory sample holder and put in contact with the sample itself. Overall, the measurements were conducted at three different points in dentine, one measurement point in enamel and one point in the synthetic HAp sample. Larger number of data sets would improve the quality of data and provide better statistical information on data quality. However, although the collection of additional datasets was not possible due to the limited availability of synchrotron beamtime, such first trial demonstrates the feasibility of applying the X-ray techniques on the *in situ* measurement and also it is important to provide better insights into further investigation. The statistical error analysis of dentine has been included in the results, and is reported below.

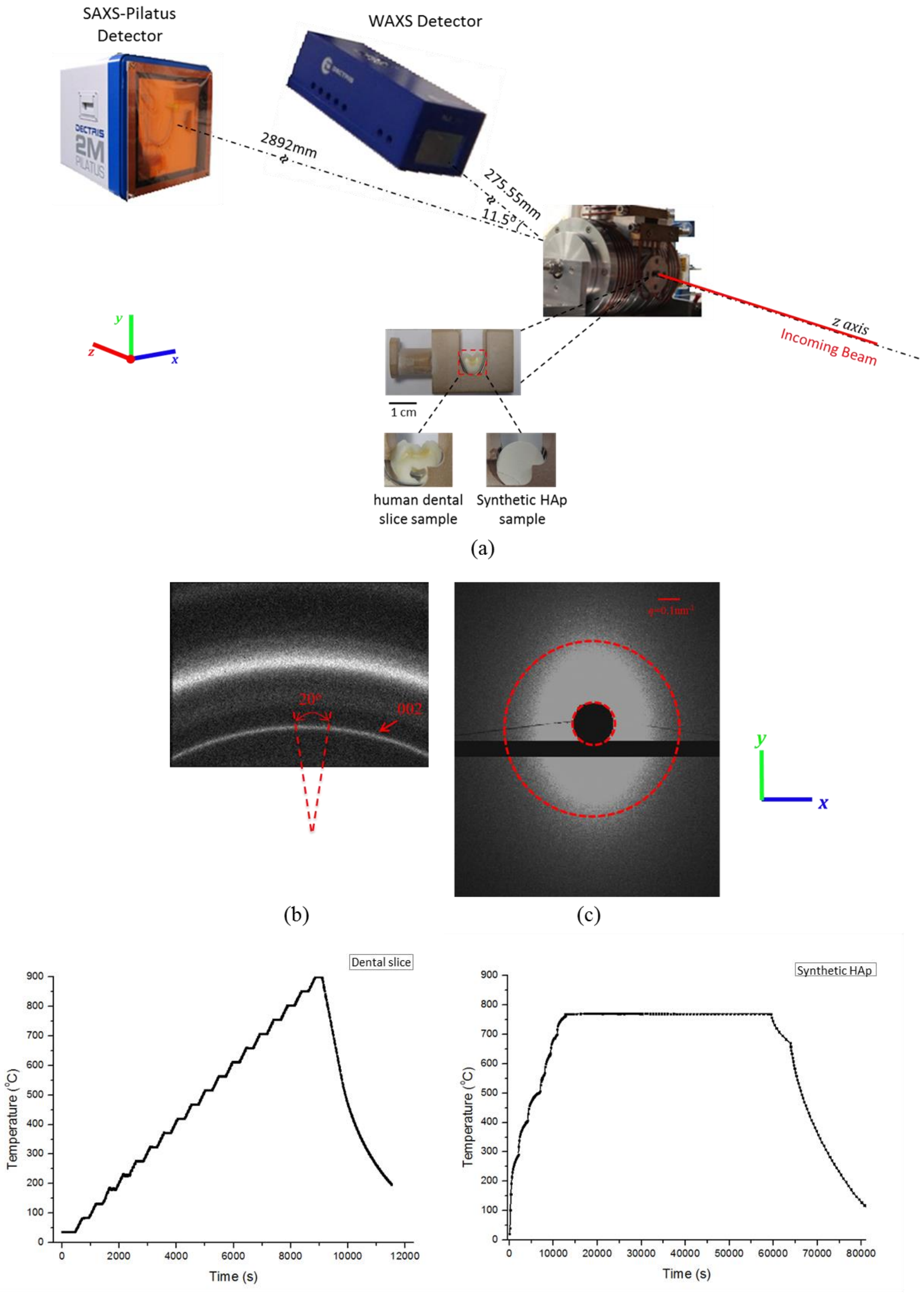

(a)

(b) (c)

(d) (e)

Fig. 8.1 (a) Schematic illustration of the *in situ* SAXS/WAXS experimental set-up ensuring that the WAXS and SAXS patterns were collected simultaneously. (b) A representative WAXS pattern showing the Debye-Sherrer ring corresponding to the (002) peak indicated by the red arrow. On the ring, the section along the y-axis in (a) was "caked" (see text) with a 20^o range in order to capture the peak shift upon heating and cooling process. (c) A representative SAXS pattern. The dark region in the middle is the beamstop. The ellipsoidal shape of the pattern indicates a partial alignment of HAp crystallites. The pattern for randomly distributed crystals is a round disc with the outline marked with red dashed circle. (d) and (e) illustrate the different heating and cooling protocols used for the human dental slice samples and the synthetic HAp powders sample.

8.2.2.2. Beamline scattering setup

The experiment was carried out on the I22 experimental beamline at Diamond Light Source, Oxford Harwell Campus, Didcot, UK. A monochromatic X-ray beam (photon energy of 18keV) was used to illuminate the samples with the beam size of $65\times120\,\mu m^2$ as illustrated schematically in Figure 8.1 a. At each heating or cooling step, WAXS and SAXS patterns were simultaneously collected at consecutive heating and cooling increments at enamel and dentine or synthetic HAp crystallite across the specimens. A lightly compacted disk of NIST standard silicon powder was used for the WAXS data calibration and a disk of Silver Behenate (AgBe) powder was used for the SAXS data calibration [177].

WAXS diffraction patterns (Figure 8.1 b) were recorded using a Pilatus 100K detector (Dectris, Baden, Switzerland) placed at a sample-to-camera distance of 275.55mm (Figure 8.1 a). Further downstream of the beam a Pilatus 2M detector (Dectris, Baden, Switzerland) was positioned at a distance of 2892mm to collect the SAXS patterns (Figure 8.1 c). In order to record simultaneously the WAXS and SAXS patterns at each scanning location, the WAXS detector was titled and offset at 11.5^o to the incident beam.

8.2.3. Data interpretation

8.2.3.1. WAXS data analysis

As stated in section 3.1.2., each WAXS peak corresponds to a certain family of lattice planes within a certain crystallographic phase. The changes of *d*-spacing could be utilized to examine the residual lattice strain and trace the phase transformation. Therefore, diffraction pattern analysis can be used to identify and quantify the crystallographic phases and structure parameters. The typical WAXS pattern is shown in Figure 8.1 b and the whole peaks in the region can be used to show and compare the crystallographic properties (e.g. crystal perfection) [118].

In Figure 8.1 b, the ring with the strongest intensity represents the diffraction from the (002) family of lattice planes. For this study, only the (002) peak was selected for interpretation. The variation of interplanar spacing (*d*-spacing) with respect to the temperature between the (002) lattice planes was captured using WAXS. In detail, each 2-D diffraction image was firstly pre-processed into 1-D plots. The (002) peak of interest from each pattern was “caked” (i.e. binned in the radial-azimuthal coordinates) within the range of 20^{o} in the *y*-axis (Figure 8.1 b). Subsequently the (002) peak was fitted with the Gaussian curve to obtain the peak centre position of $d_{spacing}^{002}$.

The (002) peak width is associates with the crystallite length and thus *L* deduced from the Eq. 3.7 of (002) peak could be used to estimate the average length of HAp crystallites. Thus *L* deduced from Eq. 3.7 reveals the average length of HAp crystallites [76]. Therefore, by monitoring the variation of full width at half maximum (FWHM) during different heating-cooling procedures, the normalized length of the HAp crystallites was deduced.

8.2.3.2. SAXS data analysis

Quantitative interpretation of SAXS patterns provides insight into the mean thickness and degree of alignment of HAp crystallites as described in section 3.1.4. The typical 2-D SAXS pattern were integrated over all the possible scattering vectors q (0.13-7.07 nm^{-1}) with the range selected from the outline of the beamstop to the outline of the pattern in the main scattering effect as shown in Figure 8.1 c, and the resulting 1-D plots were used to calculate the structure and distribution of HAp crystallites. The scattering subjects was also analysed following the method described in section 3.1.3.

8.3. Results

8.3.1. WAXS data

8.3.1.1. *d*-spacing variation

The thermally induced variation of *d*-spacing of HAp crystallites in human dentine and enamel samples is illustrated in Figure 8.2 a-b. This is observed to be almost reversible during heating and cooling, although a visible drop at ~200^{o}C is seen in the plot for dentine. In contrast, the synthetic HAp polycrystals displays a distinct irreversible change of *d*-spacing (see Figure 8.2 c).

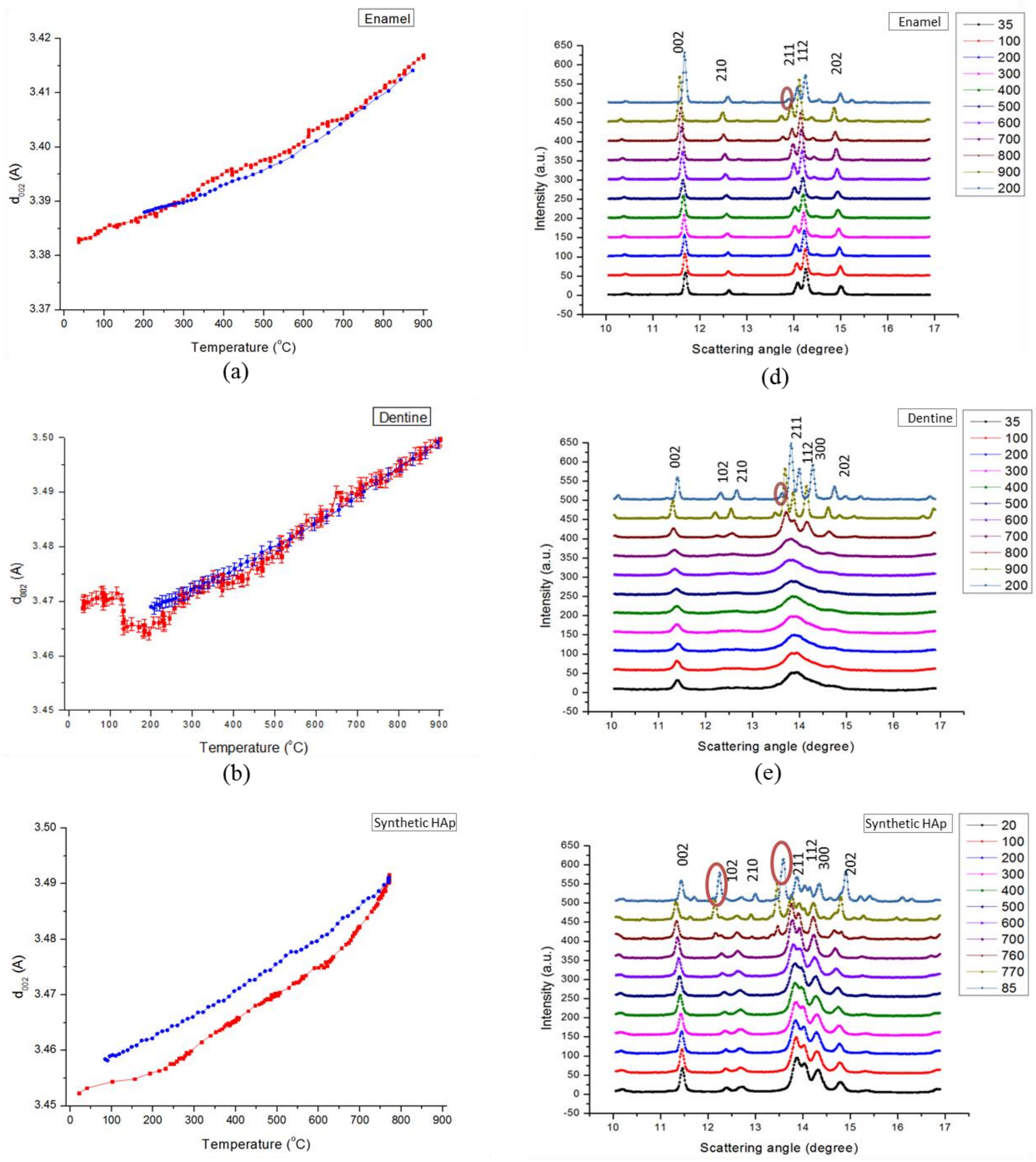

(a) (d)

(b) (e)

(c) (f)

Fig. 8.2 (a)-(c) The changes in the d_{002}-spacing of HAp crystallites in enamel, dentine and synthetic HAp powders samples, respectively, during heating and cooling stages (heating: red points; cooling: blue points). Intensity variation upon heating and cooling, caused by (d) HAp crystallites in enamel; (e) HAp crystallites in dentine and (f) synthetic HAp powders. The red marks in (f) indicate the occurrence of two new peaks.

8.3.1.2. Crystal perfection

The sharp diffraction peaks of the natural enamel and the synthetic HAp polycrystals show very small changes during the heating process (Figure 8.2 d-f). In contrast, the diffraction peaks of natural HAp crystallites in dentine are initially broad as shown in Figure 8.2 e. Furthermore, it is obvious that the peaks started to split and sharpen as temperature increased, which indicates that the perfection increased remarkably during the heating, similar to the behaviour found in human bone [115, 118]. During cooling the degree of crystal perfection remained unchanged for all three materials. The peaks were indexed by reference to standard HAp patterns (JCPDS 9-432) [208].

8.3.1.3. Crystallite length

The interpretation of the (002) peak width provides information on the evolution of the crystallite length. Figure 8.3 a-c demonstrate the variation of the normalized crystallite length of HAp crystallites in dentine and enamel and in synthetic HAp polycrystals, with the value at the initial temperature serving as the reference (unity). Overall, not much change was observed in the HAp crystallite length in the enamel, although some oscillation was seen at medium temperatures (from ~300^{o}C to ~600^{o}C). In dentine, the HAp crystallite length remained almost constant until above ~600^{o}C. Upon further heating, a significant length increase occurred, followed by the size remaining almost constant during cooling. In synthetic HAp crystallites, however, an apparent change of crystallite length occurred above ~500^{o}C. The thermal history was different from that in dentine, with the crystallite length continuing to grow even during the cooling process (see Figure 8.3 c).

8.3.2. SAXS data

8.3.2.1. Scattering intensity and volume fraction variation

In the context of the Babinet principle, initially the scattering objects in the dentine and synthetic HAp polycrystalline samples are the HAp crystallites. In contrast, in the enamel, initially the scattering objects are the gaps between HAp crystallites filled with organic matter. However, due to the gradual denaturing and disappearance of the organic matrix as well as the accompanying process of crystal growth, the scattering objects in the dentine and HAp polycrystalline samples may also change to gaps. In order to verify the hypothesis that such change in the nature of the scattering objects in human dentine and synthetic HAp polycrystalline samples indeed takes place, the overall intensity variations from the SAXS patterns of the human dentine, enamel and synthetic HAp polycrystalline samples are plotted in Figure 8.8 a-c using open markers. The overall low intensity for the enamel sample indicates that the volume fraction of the scattering objects (gaps between crystallites) remains low. As for dentine and synthetic HAp crystallites, the observed large increase in the intensity coincides with the stage at which the HAp crystallites undergo fast growth, as reflected in the crystalline mean thickness plots in Figure 8. 3 e&f.

Meanwhile, the scattering intensity also increased until the transition temperature (~745^{o}C for dentine and ~612^{o}C for synthetic HAp polycrystals in Figure. 8.8 b&c), which reflects the volume fraction of the scattering objects (HAp crystallites) evolution. At this point the increased volume fraction of particles (and the reduced volume fraction of gaps) leads to the gaps between particles becoming the principal scattering objects, resulting in the dramatic decrease of scattering intensity.

8.3.2.2. Crystalline mean thickness with constant volume fraction

The normalized crystallite mean thickness results for samples were calculated by SAXS interpretation using constant volume fraction of constituent phases (Figure 8.3 d-f). During the heating process, a hump is observed in Figure 8.3 e for dentine at ~300^{o}C. Upon further heating, the mean thickness started to increase in the range from ~500^{o}C to ~700^{o}C. This was followed by a slight decrease up to ~900^{o}C. The mean thickness remained almost constant during cooling. The variation for the synthetic HAp polycrystals (Figure 8.3 f) is similar, but appears smoother compared with that of HAp crystallites in dentine (Figure 8.3 e). Crystal growth in dentine appears to be faster than that in the synthetic polycrystals. In addition, no obvious hump is observed at low temperature in the graph of the synthetic HAp polycrystals (Figure 8.3 f). As for the mean thickness variation of HAp crystallites in enamel, a drop is visible at low temperature (Figure 8.3 d). Beyond this drop, the overall variation is much smaller compared to the results for dentine and synthetic HAp crystallites.

8.3.2.3. Crystalline mean thickness with varied volume fraction

Based on the above analysis of the scattering objects, we postulated the variation of the volume fraction during heating and cooling as shown in Figure 8.8, starting with the initial volume fraction obtained by TGA analysis. The volume fraction was assumed to remain constant during cooling. Note that the dramatic changes of intensity observed are associated with the change of the principal scattering objects that occurred when the volume fraction passed 50%. By taking the volume fraction variation of HAp crystallites in dentine, enamel and the synthetic HAp polycrystalline sample into account, the updated results of the crystalline mean thickness based on Eq. 3.10 are shown in Figure 8.3 g-i.

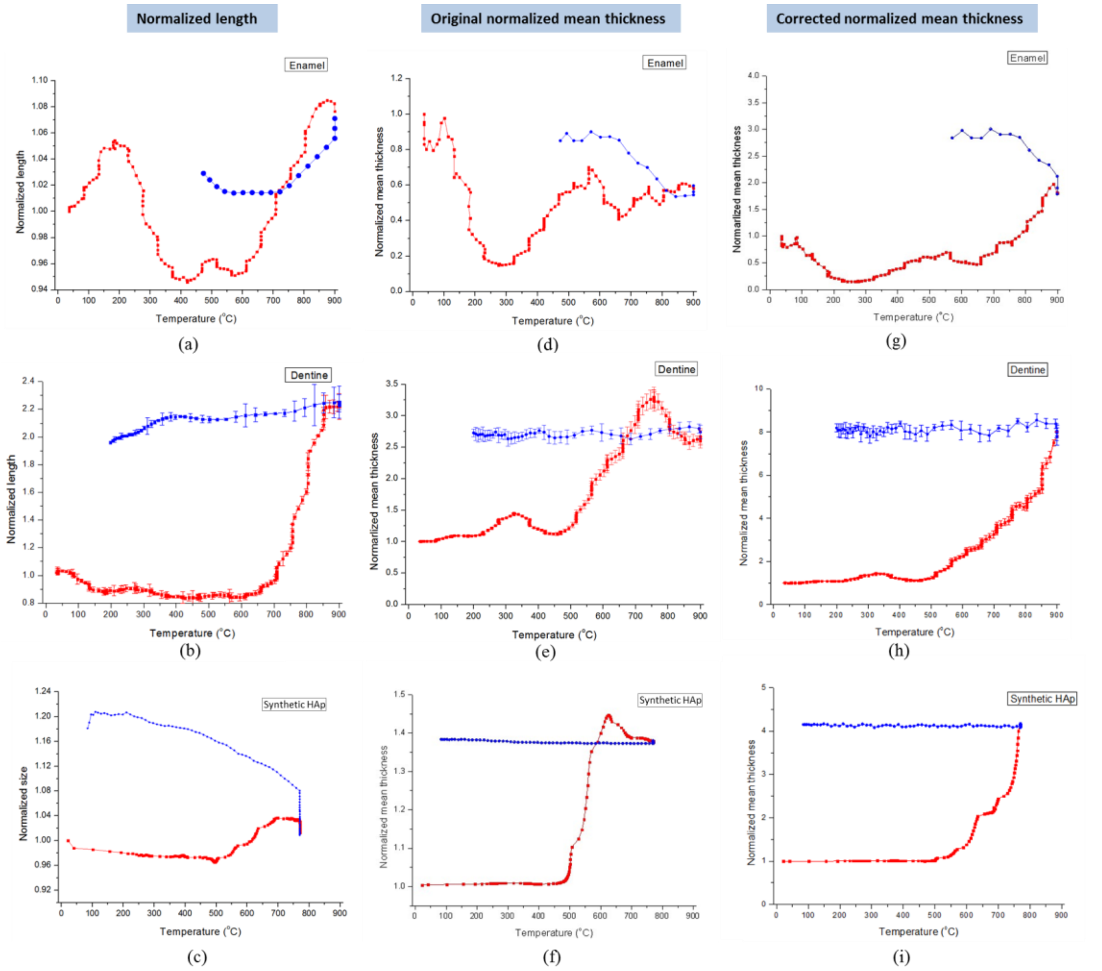

Fig. 8.3 (a)-(c) The variation of the normalized length of HAp crystallites in human enamel, dentine and synthetic HAp powders (red points for heating and blue points for cooling). (d)-(f) The normalized mean thickness (with constant volume fraction) of HAp crystallites in enamel, dentine and synthetic HAp powders. (g)-(i) The normalized mean thickness accounting for the mineral volume fraction variation of HAp crystallites in enamel, dentine and synthetic HAp powders.

8.3.2.4. Degree of alignment

Since the synthetic HAp polycrystals were produced from powdered HAp crystallites, they show an orientation distribution that is close to random at all temperatures. Thus, only the evolution of the degree of alignment of HAp crystallites in dentine and enamel is presented (Figure 8.7). During heating, the overall degree of alignment of HAp crystallites decreased from 0.75 to 0.29 in the enamel, and from 0.17 to 0.05 in dentine. In more detail, in the enamel the degree of alignment remained almost constant at very low (~0-100^{o}C) and very high temperatures (~800-900^{o}C), while a decrease occurred above ~300-400^{o}C, followed by the slight increase up to ~800^{o}C. Contrary to the result for enamel, dentine exhibited a longer low temperature range (~0-300^{o}C) with constant degree of alignment. Afterwards, the evolution followed a similar trend to that in enamel, with a decrease from ~300-400^{o}C and an increase from ~400-800^{o}C. However, a more dramatic decrease occurred at ~800-900^{o}C compared with that in the enamel at the same temperature range. The degree of alignment remained unchanged during cooling.

8.3.3. TGA analysis

Figure 8.6 a shows the weight loss of dentine, enamel and the organic tooth sample (with most mineral content was removed chemically) with increasing temperature. Two dramatic drops were visible in the pure organic tissue, at ~300^{o}C and ~650^{o}C respectively. Around 750^{o}C the organic phase in the tooth almost completely disappeared. As for dentine and enamel, the weight loss was observed to be less significant than in the pure organic tooth tissue. A dramatic drop was still apparent at

~350°C, and the rate of weight loss continued to decrease slowly at high temperature after ~750°C. The initial weight fraction of HAp crystallites in dentine and enamel can be calculated by monitoring the weight remaining at 750°C in dentine (70.3%) and enamel (95.8%), since the weight loss up to this temperature corresponds to that of water and the organic phase. Using the reported HAp density of 3.16 g/cm^3 and the methods described in the literature [76], the initial volume fractions of HAp crystallites were calculated to be 45% (dentine) and 90% (enamel).

8.3.4. AFM observations

The morphology alteration of HAp crystallites in human dental tissues are illustrated in Figure 8.4 (dentine) and Figure 8.5 (enamel) respectively by high resolution *ex situ* measurements. In dentine, the shape initially was platelet-like, almost monodisperse. As the temperature increased, an obvious change of the crystalline size was observed at around 200°C, where the platelet enlarged compared with the original size at room temperature. However, it then shrank relatively at around 400°C. Further, sintering process became apparent at 500°C, accompanied by the growth of the crystallites. Later at 800°C the crystalline shape became largely polydisperse. Such shape evolution also occurred in enamel, where the initial shape of crystallites was needle-like but the variation between 100°C-200°C was not distinct and the HAp crystallites even had smaller thickness than that at room temperature. The evident variation in the morphology occurred after 300°C, while significant sintering occurred after 600°C, leading to the final polydisperse state.

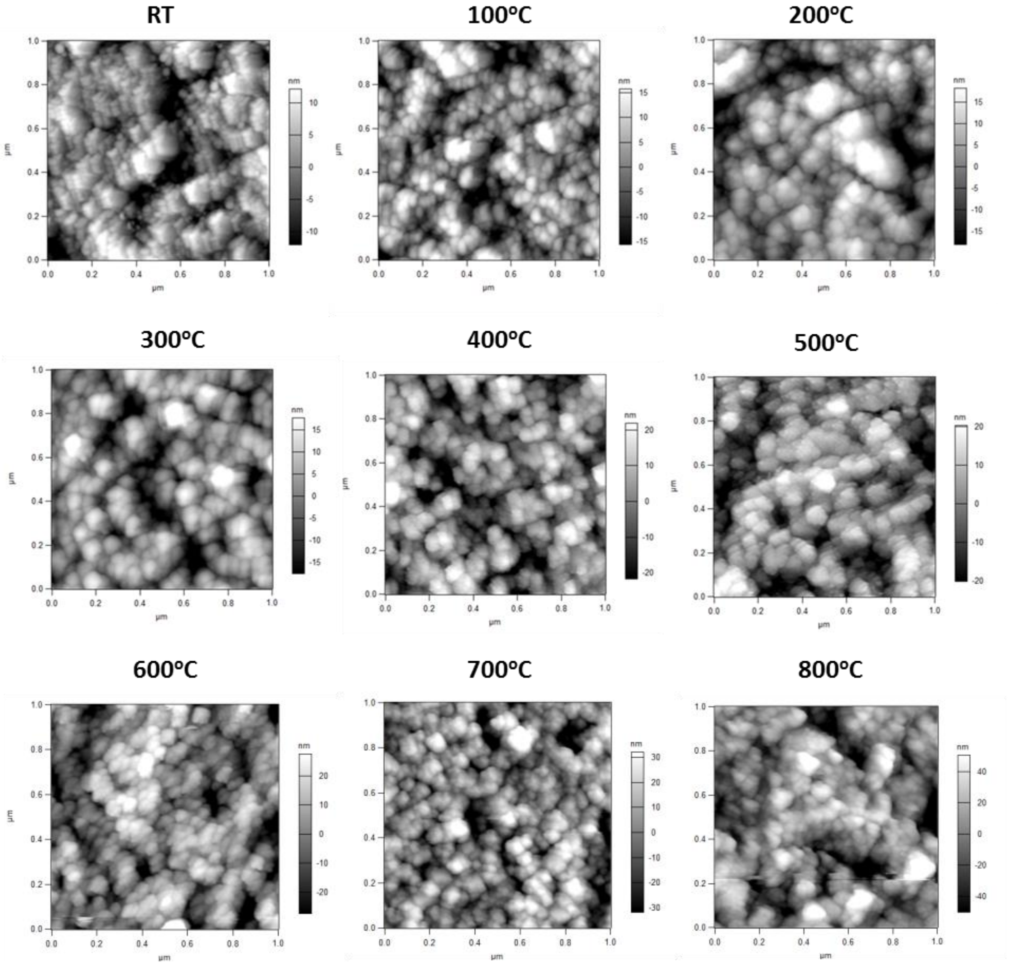

Fig. 8.4 AFM observation of HAp crystallites sintering in dentine

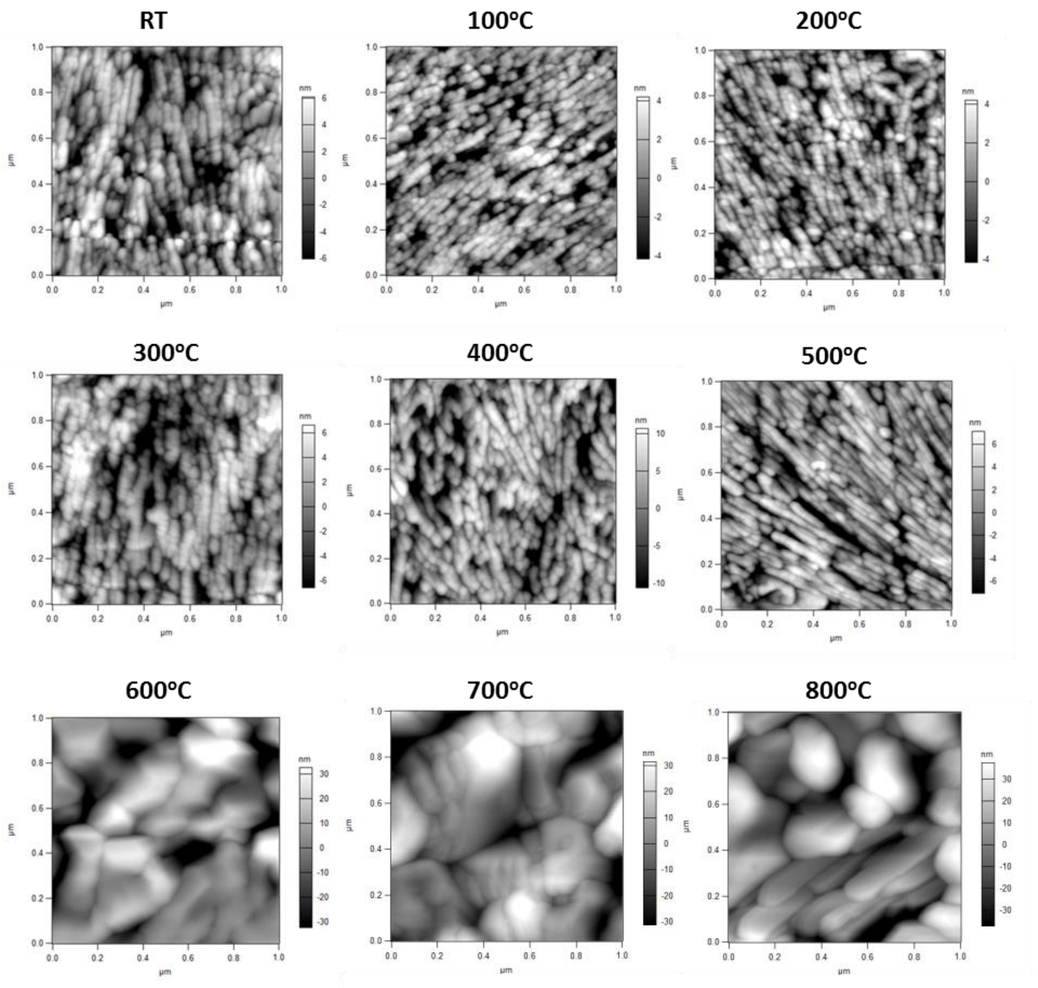

Fig. 8.5 AFM observation of HAp crystallites sintering in enamel

8.4. Discussion

The *in situ* thermal treatment in the current study revealed the complete history of the evolution of the ultrastructure of bio-apatite samples during a continuous heating-cooling schedule. In a previous *ex situ* study [95], only point-wise (in terms of temperature) and post-treatment data could be collected. This led to a fragmented and incomplete picture of the process. In comparison, the present study provides reliable information on the sample heating history and ultrastructural response, with the consistency between samples assured by a degree of cross-comparison, full coverage of the entire temperature range, and complete observation of the cooling procedure.

SAXS patterns are sensitive to the nano-scale structure, allowing the determination of the mean thickness of the crystallites by considering the scattering from two-phase systems [120]. The precise nature of the particles involved (e.g. amorphous vs. crystalline) is not important in this instance. In contrast, WAXS peaks arise as a consequence of scattering from the short range atomic arrangement, so that the information derived from WAXS data interpretation reveals crystal lattice properties, such as prevailing interatomic distances, the degree of (dis)order and lattice (im)perfection within the crystallites.

The principal outcome of quantitative analysis of SAXS and WAXS patterns was to reveal the temperature-dependent variation of the nano-structure (thickness, orientation and degree of alignment) of HAp crystallites, as well as the crystallographic properties (*d*-spacing, crystal perfection and length) variation during the heating and cooling processes. It is interesting to note how the observed evolution reflects the differences between dentine and enamel, and also the differences between the natural HAp crystallites embedded within organic matrix in human dental tissues, on the one hand, and synthetic HAp powders on the other. The role played by the organic matrix during heating is particularly important, as it turns out to govern the evolution of size and strain of HAp crystallites. It is also important to draw the conclusion that in order to evaluate the exposure temperature precisely (e.g. in forensic cases), enamel and dentine must be investigated separately: the analysis of the entire powdered tooth obscures the sharpness of ultrastructural variations in dentine and enamel [90, 119].

8.4.1. *d*-spacing variation

In the case of unconsolidated and unconstrained thermal expansion and contraction during heating and cooling, the *d*-spacing variation curves shown in Figure 8.2 a-c would be fully reversible. The observed difference between the heating-cooling curves in Figure 8.2 may arise due to the existence and relaxation or development of residual mico-stresses, and in conjunction with structural and compositional (e.g. phase) changes. The reduction in the lattice spacing that occurred in dentine at low temperature (see the curves in Figure 8.2 a-b), is likely to be related to the changes that take place in the organic matrix in dentine. The changes that occurred in this matrix during heating are proposed and illustrated by the schematic diagram in Figure 8.6 b. At low temperatures the organic matrix expands (swells) more than the HAp crystallites due to its higher thermal expansion coefficient [209]. As a result, the HAp crystallites seemed to experience a compression (as marked by the red arrow in Figure 8.6 b) which reached a maximum when the protein matrix began to denature at ~200^{o}C. Above that temperature the protein matrix began to burn off and gradually disappeared with increasing temperature, which is consistent with the TGA plot in Figure 8.6 a. In parallel with that the compression in the HAp crystallites became relieved and the crystallites experienced additional expansion over and above the purely thermal strain.

Furthermore, it appears that the synthetic HAp polycrystals experienced a larger initial residual stress than HAp polycrystals found in human dental tissue (see Figure 8.2 a-c). Such difference may be the consequence of two phenomena. Firstly, during sample preparation, a significant compressive stress was applied to the HAp powder to obtain powder disks with a similar density to the dental tissue. In contrast, in the human dental tissue samples some residual stresses may have been relaxed during the cutting of slices. Secondly, in the synthetic HAp crystallites the appearance of a new phase was observed above 760°C (β-TCP, tricalcium phosphate). Such decomposition of HAp crystallites to β-TCP has been reported [210]. The phase change leads to the irreversible changes of the lattice parameters, providing an explanation of the considerable difference in the *d*-spacing traces during heating and cooling. It is noted that although the β-TCP has also been observed in dentine (900°C) and enamel (800°C) as shown in Figure 8.2 d & e, its concentration is very low, and its effect on *d*-spacing variation can be ignored within the bounds of experimental accuracy, so that the curves appear reversible. The different transformation temperatures indicate an intrinsic difference in the characteristics between the bio-apatites (like the HAp crystallites in dentine and enamel) and the pure synthetic hydroxyapatites.

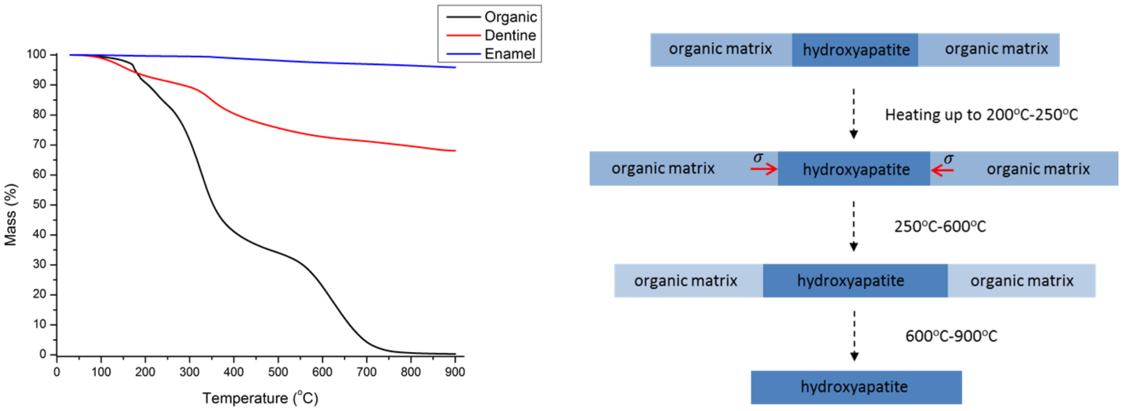

(a) (b)

Fig. 8.6 (a) TGA plot of weight loss of dental tissues: pure organic tooth with the inorganic content removed (black line), dentine (red line) and enamel (blue line). (b) A schematic diagram of the ultrastructural alteration of organic matrix and HAp crystallites in human dentine upon heating. The process begins with the superior thermal expansion of the organic matrix compared with the HAp crystallites, resulting in compression of HAp during heating (red arrow). The compression will relaxes gradually as the organic matrix begins to denature and burn off, leading to the additional expansion in the HAp crystallites in excess of the pure thermal strain.

8.4.2. Crystal perfection

A high degree of crystal perfection was observed in enamel and synthetic HAp crystallites compared to dentine, as shown in Figure 8.2 d-f. The difference arises from the different micro-morphology of HAp crystallites among the three materials studied. The improved perfection (sharper and stronger peaks) in dentine with increasing temperature (see Figure 8.2 e) is due to the sintering of HAp crystallites that takes place at high temperatures (above ~700^{o}C). During the heating process, as the organic matrix was gradually burnt off, the interlayers of adjacent HAp crystallites disappeared. Further heating leads to crystal growth and annealing of crystal defects, resulting in the significant peak sharpening. The increasing size of the HAp crystallites contributes to the narrowing of the peak width according to *Scherrer equation*. Although the contribution from the non-uniform microstrain must usually be taken into account in terms of its effect on peak broadening, it could be excluded from the present consideration, since published literature states that in dental tissues this effect is insignificant [149]. Further crystallization of the amorphous part observed in bone alteration [115, 118] may also contribute to this effect. The integrated intensity of the (002) peak has been examined and shown to increase in enamel but slightly decreases in dentine. The obvious sintering phenomenon observed in enamel, as shown in Figure 8.5, indicates that the amorphous particles gradually change into regular crystallites thus more diffraction intensity could be achieved. In contrast, not dramatic sintering in dentine, as shown in Figure 8.4, indicates only trivial change of the intergrade intensity. However, since the HAp crystallites become more compact due to the burning-off of the organic phase, the volume fraction of the crystallites increases, leading to more absorption and slight decrease of the integrated intensity.

8.4.3. Degree of alignment

The overall reduction of the degree of alignment in enamel and dentine during heating may be associated with the polydisperse distribution of the particles associated with the changes of crystalline size or shape at high temperature [118]. The initial stage of constant degree of alignment observed both in enamel (RT-100^{o}C) and dentine (RT-300^{o}C) in Figure 8.7 b may correspond to the absence of crystallite rotation or growth. Once the organic matrix began to denature, a slight increase in the degree of alignment was noted at ~300-400^{o}C for both dentine and enamel. Such increase corresponds to the gradual disappearance of the organic matrix accompanied by the relaxation of the residual strain. The greater reduction in the degree of alignment observed in dentine compared to enamel in the ~800-900^{o}C range reflects the difference in the composite structures. At very high temperatures the degree of alignment in enamel remained high, due to the highly directional structure of long prismatic HAp crystallites that remained aligned even after the organic matrix had been fully burnt off. In contrast, in dentine the disappearance of the large amount (~45% by volume) of organic matrix is likely to correspond to the loss of the supporting structure, causing the collapse and rearrangement of HAp crystallites that is associated with large rotation and anisotropic sintering.

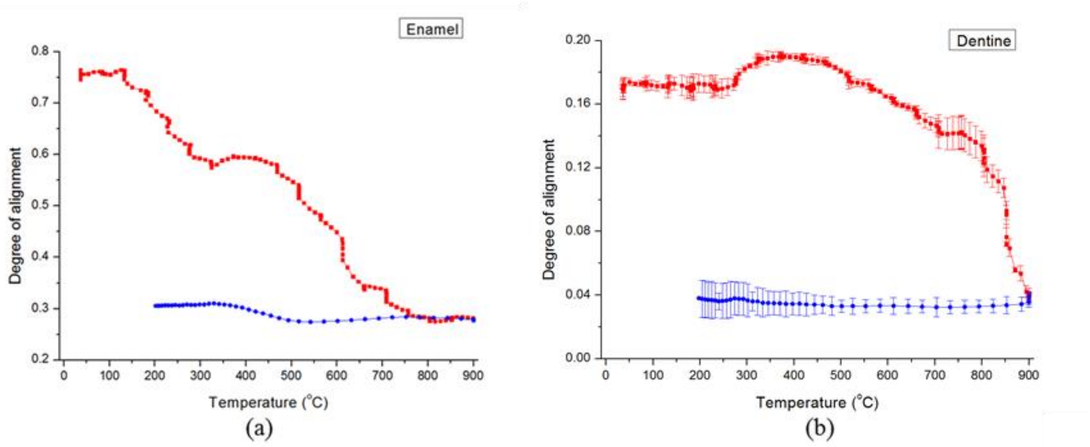

Fig. 8.7 The variation of the degree of alignment of HAp crystallites upon heating/cooling in (a) human enamel and (b) human dentine (red points for heating and blue points for cooling).

8.4.4. Intensity variation

In the analysis of synchrotron-based SAXS data that has so far been reported in the literature, the volume fraction of HAp crystallites was always assumed to remain constant during heating [118]. However, the volume fraction in fact varies due to the burning off of the protein matrix, and the sintering of crystallites during heating (that influences the calculation of the mean crystallite thickness). Therefore, the volume fraction variation associated with intensity variation is taken into account in this calculation. The overall low intensity change indicates a small ultrastructural alteration, which may reflect the limited space for crystal expansion and growth within the enamel sample. The difference between the dentine sample and synthetic HAp powders is also reflected in the scattering behavior, where the comparatively lower value of intensity for dentine at low temperatures is likely to be associated with the presence of the protein matrix in dentine. Given the similar volume fractions of HAp crystallites in the two materials and close initial density values, the difference in the intensity is ascribed to the electron density contrast between the protein matrix and the crystals, which is smaller than that between gaps and the crystals (see Eq.3.12).

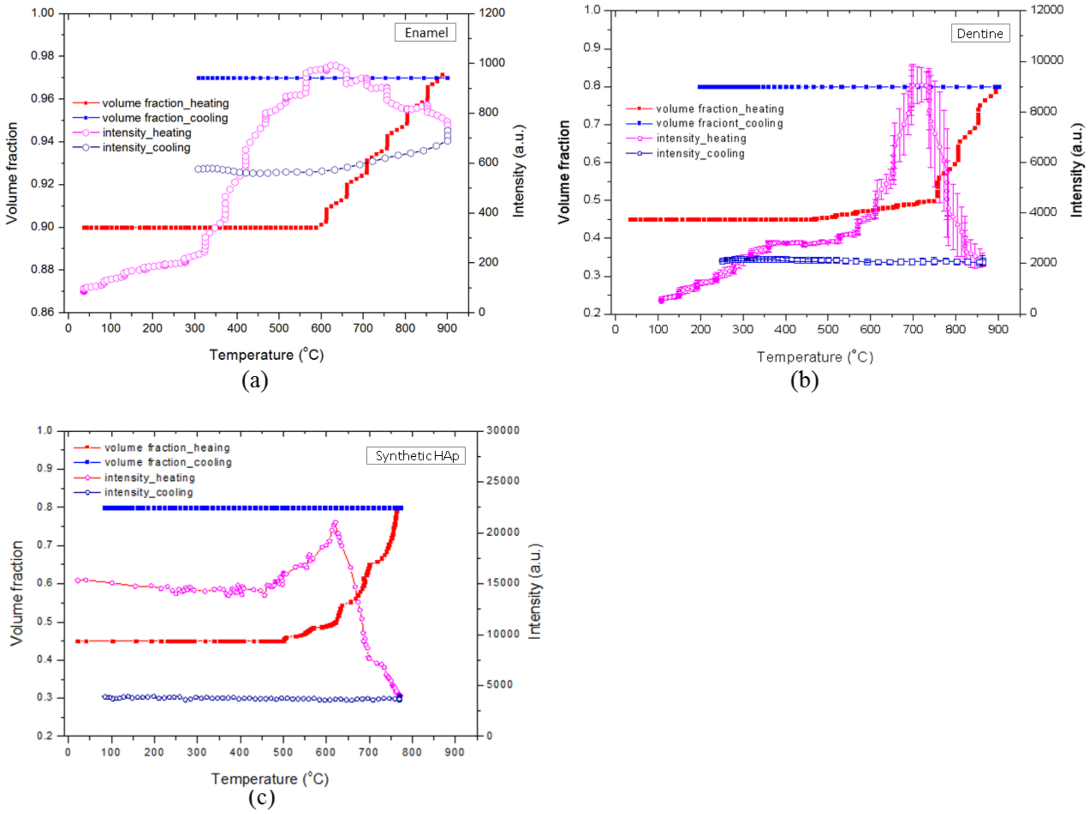
(a) (b) (c)

Fig. 8.8 The correlation of the peak intensity variation from SAXS patterns with the mineral volume fraction for (a) human enamel (b) human dentine and (c) synthetic HAp powders. Open purple markers (heating) and open blue markers (cooling) in (a)-(c) represent the results obtained from constant mineral volume fraction, while the red points (heating) and blue points (cooling) in (a)-(c) correspond to the results obtained with the variation of mineral volume fraction taken into account.

8.4.5. Crystallite size determined by SAXS/WAXS

Combined with the WAXS characterization on the length calculation of HAp crystallites, a schematic illustration of how the crystallite dimensions change in dentine and enamel during heating is depicted in Figure 8.9. Two temperature ranges are identified based on the processes taking place in the organic matrix (the separation temperature is around 500°C). As the organic phase gradually disappeared in "temperature range II", crystal growth became unconstrained. Unlike the crystals in enamel, it was also observed that the crystallites in dentine gradually became misaligned, as indicated by the drop in the degree of alignment. Similar phenomena have been observed in *ex situ* bone characterization [199].

It was interesting to observe that in the synthetic HAp polycrystals, continued sintering took place during a high temperature hold and even continued during cooling. This is probably due to the fact that sintering is driven by the overall change in the free energy of the system [211].

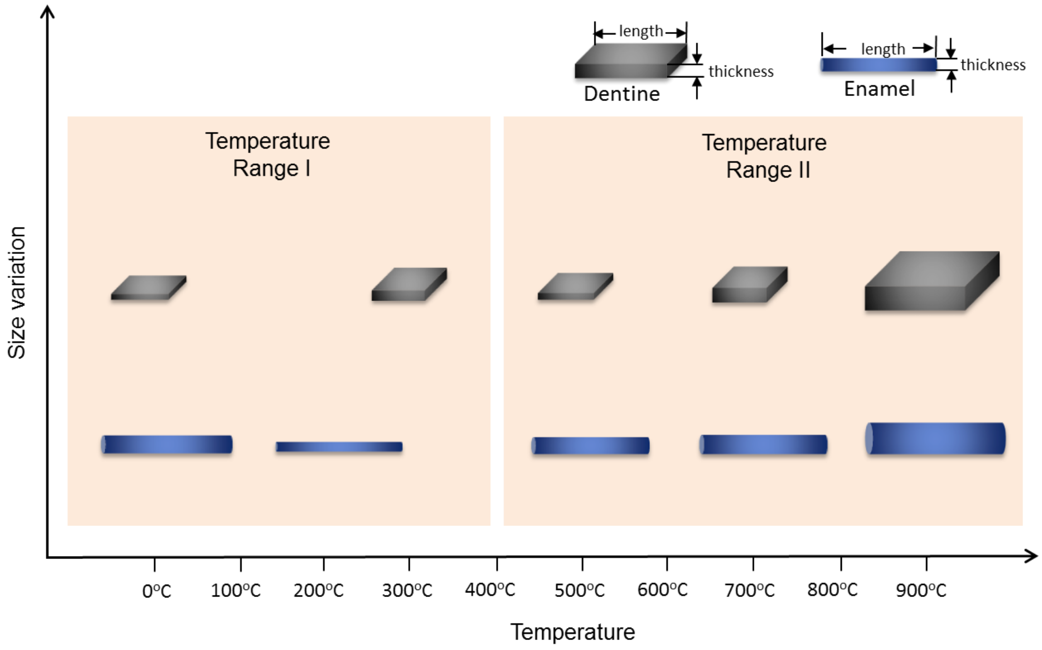

Fig. 8.9 A schematic illustration of the size variation of HAp crystals within human enamel and dentine upon heating. The crystals in enamel are needle-shaped while those in dentine are platelet-shaped. In temperature range I, the interaction between crystals and the protein matrix occurs, while in temperature range II, the protein matrix gradually disappears and the interaction is weakened.

8.4.6. Comparison of scattering interpretation and AFM observation

According to the result, initially, the crystallites in dentine were almost platelet-like while those in enamel were needle-shaped. As the temperature increased, the comparatively obvious sintering for crystallites in both tissues occurred after 500 ^{o}C. For both dentine and enamel, the trend of the variation nearly coincides with the illustration with the X-ray scattering data interpretation as illustrated in Figure 8.9. This, on one hand, verifies the result obtained by scattering; on the other hand, it indicates that the scattering is a feasible approach to capture the morphology of crystallites. In addition, since the AFM mapping is likely to be on non-identical regions under such thermal treatment (may result in different observations from Figure 8.9), it further strengthens the advantage of X-ray scattering of doing *in situ* measurement and illuminating the same gauge volume, which can guarantee the structural consistency. Interpretation of the integrated intensity evolution as described in section 8.4.2.in dentine and enamel requires looking at AFM images to make sense. This also indicates the capability of using X-ray scattering methods to capture the ultrastructural alteration in the real space.

8.5. Conclusions

The effects of *in situ* heat treatment on the hydroxyapatite (HAp) crystallites (human dental tissues) and synthetic HAp crystallites were explored using combined synchrotron based small/wide angle X-ray scattering (SAXS/WAXS) techniques. From the quantitative analysis of SAXS and WAXS patterns, multi-scale characterization of the hierarchical structure of enamel and dentine allows establishing the temperature-dependent variation of the nano-structural parameters (thickness, orientation and the degree of alignment) of HAp crystallites from SAXS and crystallographic properties (*d*-spacing, crystal perfection and length) from WAXS during the heating and cooling processes. The results generally reflect the difference between dentine and enamel, natural and synthetic HAp crystallites. In the analysis presented, the emphasis is placed on understanding the role of the organic matrix during heating. An important conclusion is made that the scattering object that contributes to the creation of the SAXS pattern undergoes change during heating. Therefore, to obtain correct mean thickness calculation, the effect of volume fraction variation of HAp crystallites on the scattering object should be taken into account.

In conclusion, the synchrotron-based combined SAXS/WAXS analysis has been shown to be a powerful method for the determination of nano-structure variation induced by thermal treatment in human enamel and dentine, as well as in synthetic HAp crystallites. The *in situ* thermal treatment conducted in the present study covered the entire relevant temperature range and revealed the complete continuous history of ultrastructure evolution within a single sample during a continuous heating-cooling schedule. It was clearly demonstrated that insignificant structural changes occur during cooling, indicating that relevant conclusions can be drawn when dental remains samples are analysed as part of archaeological or forensic studies. The approach to the study of ultrastructural alteration in skeletal hard tissues exposed to *in situ* thermal treatment developed in the present study provides a better, more reliable basis for deducing the heating history compared with conventional methods based on the monitoring the macro- and microstructural colour [90, 91, 102]. Furthermore, it allows the interaction between the mineral crystallites and the organic phase during heating to be captured. These advantages show the superior utility of *in situ* thermal treatment analysis over previous *ex situ* tests. The standard error of multiple measurement points in dentine as shown in Figure 8.2, 8.3, 8.7 and 8.8 confirmed the reliability of the conclusions drawn. The results of this work will also be beneficial to the optimization of the laser fluence used in dental practice, and in the future design of biomimetic materials.

Chapter 9

Conclusions and Future work

9.1. Conclusions

A substantially large body of experimental data related to the ultrastructural changes of dentine, enamel and the DEJ during thermo-mechanical loading has been collected. Analytical and finite element models have been elaborated to support the interpretation of the synchrotron small- and wide angle X-ray scattering (SAXS/WAXS) observations. Together with other advanced characterization methods, this allowed hierarchical multi-scale information about the internal structure of dental tissues to be collected. The primary aims of the research project were:

- Demonstrate the possibility of applying synchrotron X-ray techniques to explore the internal architecture of human dental tissues (dentine, enamel and the DEJ) and its relationship to the main structural features, where the crystalline size and orientation of HAp crystalline nano-particles are obtained by SAXS and the lattice strain is deduced by WAXS analysis.
- Conduct experimental and theoretical research into the correlation between the hierarchical two-level structure and the remarkable mechanical performance of human dental tissues.
- Study the thermo-mechanical structure-property relationships in human dental tissues in order to understand the mechanical property correlations in hierarchical biomaterials in the context of forensic and archaeological investigations as well as high energy dental treatment used in the clinical

practice.

- Develop a systematic approach to analyzing the thermal history of heat-affected dental tissues and improve the understanding of laser assisted caries prevention by tracking the ultrastructural alteration of natural and synthetic HAp crystallites via an improved analytical SAXS/WAXS approach.

Firstly, a review on the human dental tissues in terms of their structure and thermo-mechanical properties was introduced in detail, followed by a summary of two distinct representative X-ray diffraction techniques (SAXS/WAXS) and their application to the study of natural mineralised tissues, particularly the human dental tissues. Next, a modelling approach was proposed and complementary characterization methods were briefly described.

The following principal conclusions can be drawn from the work reported in this thesis:

- When two synchrotron X-ray diffraction techniques, small and wide angle X-ray scattering (SAXS/WAXS) are used together, it is possible to obtain multi-scale information about the response of human enamel and dentine subjected to *in situ* uniaxial compressive loading. An improved multi-scale Eshelby inclusion model was proposed taking into account the two-level hierarchical structure, and was validated against the experimental strain evaluation data. Complementary photoelastic methods with finite element modeling helped further validation of the multi-scale model. The achieved agreement indicates that the multi-scale model accurately reflects the microstructural arrangement of human dental tissues and their responses to externally applied forces. These results provide the basis for the improved understanding of the mechanical properties of the hierarchical biomaterials.

- An quantitative analytical approach based on synchrotron radiation combined with the small and wide angle X-ray scattering (SAXS/WAXS) techniques was used to investigate the heat-induced ultrastructural alterations of human dentine and enamel, providing relevant additional information to estimate the cremation temperature of isolated intact or fragmented dental hard tissues recovered from archaeological excavations. A subsequent study by nanoindentation was introduced to map the nano-mechanical properties variation in thermally treated dental tissues. The results are likely to be also broadly useful in understanding the mechanical property correlations in the hierarchical biomaterials in the context of laser assisted caries prevention.

9.2. Future work

The future work is aimed at applying the methods developed in the thesis and extending the scope of the current research. In particular, further studies could be directed at the following specific areas:

- In the present research, the principal interest was placed on healthy human dental tissues. It would be interesting to also study the diseased dental tissues (e.g. affected by genetic abnormalities, or dental pigmentation) with benefits for further possible application in the clinical practice. This could enable experimental and theoretical work to be extended to include clinically relevant aspects such as understanding and predicting the effects of structural alterations that may occur due to disease or treatment on the performance of dental tissues and their artificial replacements.
- The evolution of lattice strain subjected to *in situ* loading described in Chapters 4-6 and the ultrastructural and mechanical property alteration due to thermal

exposure presented in Chapters 7 and 8 concentrate on the lateral variations in the plane normal to the incident beam. Methods capable of 3D characterization of the mechanical state are of significant further interest. Procedures for data analysis of diffraction tomography data need to be further developed, improved and validated. Further theoretical and numerical analysis of 3D studies with respect to the thermo-mechanical properties will benefit the improved understanding of the hierarchical dental tissues and the development of bio-composite materials. This information feeds into the evolving multi-scale model of the structure and mechanical properties of hierarchical mineralized tissues.

- Further studies should expand the range of characterization scales accessible for replacement dental materials. Among these are all-porcelain crown materials, of which, due to the aesthetic appearance, biocompatibility and favorable mechanical properties, the yttrium-stabilized polycrystalline zirconia is one of the most promising restorative structural materials that offers an important alternative to metallic alloys. However, veneering porcelain chipping remain a major concern in the clinical environment. Thus, improving the durability and mechanical properties of all-ceramic dental restorations remains an outstanding challenge to be addressed.
- Preliminary results pertaining to the structural-thermo-mechanical properties of the DEJ have been obtained by a range of techniques described in Chapters 6-8. Further significant studies of the DEJ should be carried out to find the details of the intricate deformation and load transfer mechanisms operating in the the DEJ. Micro-samples must be prepared from different locations of the DEJ by focused ion beam (FIB) milling. The focused ion beam (FIB) instrument has

revolutionized the way in which biological samples can be investigated by providing access to high quality TEM sample preparation. The medium resolution imaging of TEM offers the direct comparison and validation of the structural differences between dentine, enamel and the DEJ (e.g. HAp crystallite distribution), while high resolution TEM imaging provides information related to the atomic properties, e.g. dislocation and defects within crystallites. Apart from the necessity of using TEM with the help of FIB, FIB milling and digital image correlation (DIC) also opens new avenues for the determination of the residual stress at micro-level. The general procedure is described in Figure 9.1.

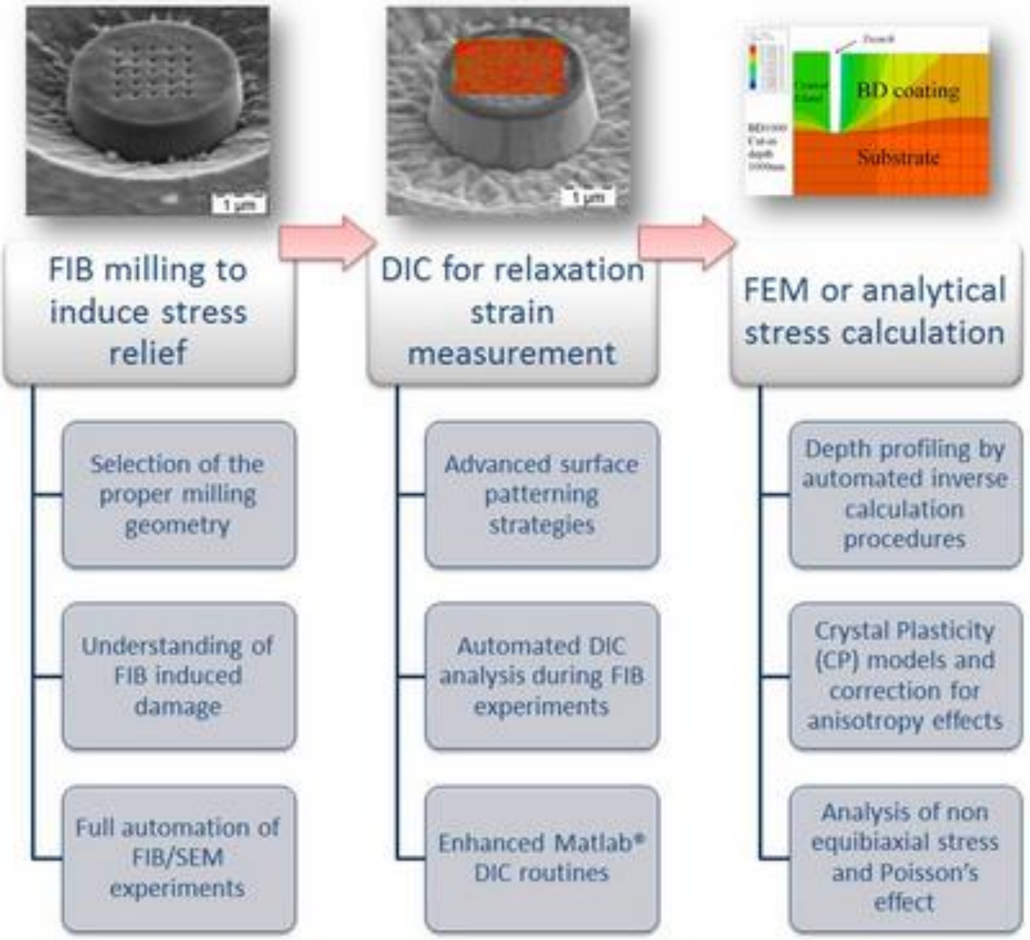

Fig. 9.1 Main experimental and calculation steps of the FIB-DIC procedure for residual stress analysis [212]

Particularly in the study of dental tissues, FIB offers the possibility to elucidate the underlying reasons for lattice parameter changes. This can be achieved by examining the strain relief across the junction during the FIB milling (Figure 9.2), which could be used to verify the controversy regarding whether the lattice parameter variation at the DEJ is associated with strain or lattice structure changes. Multi-modal microscopy (micro-scale ESEM to sub-micron AFM and FIB-STEM, to atomic lattice scale HR-TEM) will underpin multi-scale modeling of hierarchical scalloped structure with the help of self-consistent models or finite element models. Understanding the internal architecture of the complex, hierarchically structured tissue will benefit biomimetic design and understanding of how the residual stress can contribute to the remarkable durability of dental materials, both natural and artificial.

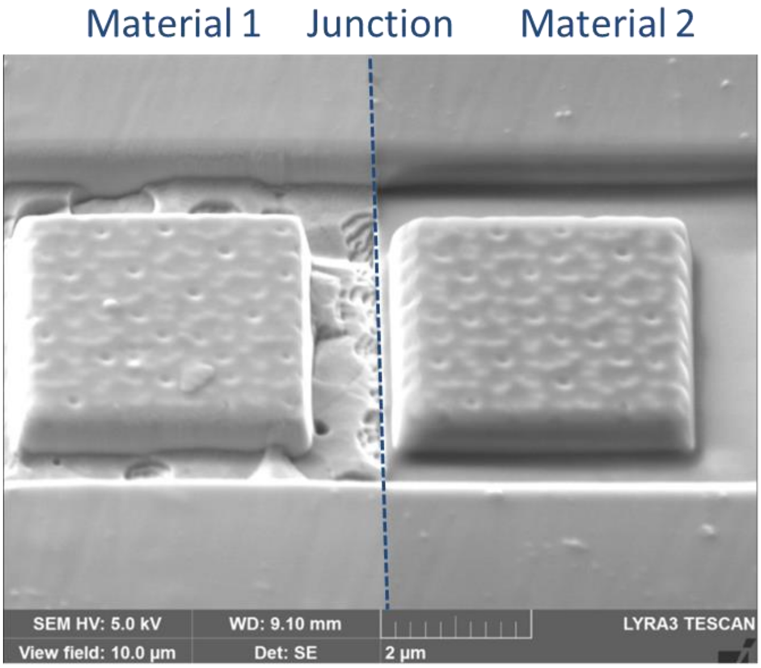

Fig. 9.2 Residual stress analysis of the DEJ by a new FIB-DIC method

References

[1] Graham T, Sarikaya M. Growth dynamics of red abalone shell: a biomimetic model. Mat Sci Eng C-Bio S 2000;11:145-53.

[2] Calvert P, Mann S. Synthetic and Biological Composites Formed by Insitu Precipitation. J Mater Sci 1988;23:3801-15.

[3] Aksay IA, Materials Research Society. Hierarchically structured materials : symposium held December 2-6, 1991, Boston, Massachusetts. Pittsburgh, Pa.: Materials Research Society; 1992.

[4] Mann S. Biomimetic materials chemistry. New York ; Cambridge: VCH; 1996.

[5] Sarikaya M, Aksay IA. Biomimetics : design and processing of materials. Woodbury, N.Y.: AIP Press; 1995.

[6] Rieke PC, Calvert P, Alper M. Materials synthesis utilizing biological processes : symposium held November 28-November 30, 1989, Boston, Massachusetts, U.S.A. Pittsburgh, Pa.: Materials Research Society; 1990.

[7] Heuer AH, Fink DJ, Laraia VJ, Arias JL, Calvert PD, Kendall K, et al. Innovative Materials Processing Strategies - a Biomimetic Approach. Science 1992;255:1098-105.

[8] Espinosa HD, Rim JE, Barthelat F, Buehler MJ. Merger of structure and material in nacre and bone - Perspectives on de novo biomimetic materials. Prog Mater Sci 2009;54:1059-100.

[9] Nair AK, Gautieri A, Chang SW, Buehler MJ. Molecular mechanics of mineralized collagen fibrils in bone. Nat Commun 2013;4:1724.

[10] Kruzic JJ, Ritchie RO. Fatigue of mineralized tissues: Cortical bone and dentin. J Mech Behav Biomed 2008;1:3-17.

[11] Su XW, Belcher AM, Zaremba CM, Morse DE, Stucky GD, Heuer AH. Structural and microstructural characterization of the growth lines and prismatic microarchitecture in red abalone shell and the microstructures of abalone "flat pearls". Chem Mater 2002;14:3106-17.

[12] Crick RE. Origin, evolution, and modern aspects of biomineralization in plants and animals. New York ; London: Plenum; 1989.

[13] DiMasi E, Sarikaya M. Synchrotron x-ray microbeam diffraction from abalone shell. J Mater Res 2004;19:1471-6.

[14] Li XD, Chang WC, Chao YJ, Wang RZ, Chang M. Nanoscale structural and mechanical characterization of a natural nanocomposite material: The shell of red abalone. Nano Lett 2004;4:613-7.

[15] Jackson AP, Vincent JFV, Turner RM. The Mechanical Design of Nacre. Proc R Soc Ser B-Bio 1988;234:415-+.

[16] Liu R, Xu XR, Cai YR, Cai AH, Pan HH, Tang RK, et al. Preparation of Calcite and Aragonite Complex Layer Materials Inspired from Biomineralization. Cryst Growth Des 2009;9:3095-9.

[17] Sui T, Hofmann F, Li T, Zeng KY, Eve S, Korsunsky AM. Local orientation analysis of abalone nacre by micro-beam laue diffraction. Mechanics of Nano, Micro and Macro Composite Structures 2012;Politecnico di Torino, .

[18] Ma YR, Aichmayer B, Paris O, Fratzl P, Meibom A, Metzler RA, et al. The grinding tip of the sea urchin tooth exhibits exquisite control over calcite crystal orientation and Mg distribution. P Natl Acad Sci USA 2009;106:6048-53.

[19] Juliev ENЖ, E.H.). Fixed prosthetics (Несъемные протезы) / НГМА – Nijnegorodskoi Gosudarstveni Medisinskoi Akademi /Н. Новгород – Novogorad. 2000;ISBN 5-7032-0330-9, P151.

[20] Bath-Balogh M, Fehrenbach MJ, Thomas P. Illustrated dental embryology, histology, and anatomy. Philadelphia, Pa. ; London: Saunders; 1997.

[21] Marten A, Fratzl P, Paris O, Zaslansky P. On the mineral in collagen of human crown dentine. Biomaterials 2010;31:5479-90.

[22] De Sant'anna GR, Dos Santos EAP, Soares LES, Santo AMD, Martin AA, Duarte DA, et al. Dental Enamel Irradiated with Infrared Diode Laser and Photoabsorbing Cream: Part 1-FT-Raman Study. Photomed Laser Surg 2009;27:499-507.

[23] Ten Cate AR, Dale AC. Oral histology : development, structure, and function. St. Louis: Mosby; 1980.

[24] Petrovic LM, Spasic DT, Atanackovic TM. On a mathematical model of a human root dentin. Dent Mater 2005;21:125-8.

[25] Pashley DH, Ciucchi B, Sano H, Carvalho RM, Russell CM. Bond strength versus dentine structure: A modelling approach. Arch Oral Biol 1995;40:1109-18.

[26] Johansen E, Parks HF. Electron Microscopic Observations on the 3-Dimensional Morphology of Apatite Crystallites of Human Dentine and Bone. J Biophys Biochem Cy 1960;7:743-&.

[27] Voegel JC, Frank RM. Ultrastructural-Study of Apatite Crystal Dissolution in Human Dentin and Bone. J Biol Buccale 1977;5:181-94.

[28] Stock SR, Veis A, Telser A, Cai Z. Near tubule and intertubular bovine dentin mapped at the 250 nm level. J Struct Biol 2011;176:203-11.

[29] Wenk HR, Heidelbach F. Crystal alignment of carbonated apatite in bone and calcified tendon: Results from quantitative texture analysis. Bone 1999;24:361-9.

[30] Vennat E, Bogicevic C, Fleureau JM, Degrange M. Demineralized dentin 3D porosity and pore size distribution using mercury porosimetry. Dent Mater 2009;25:729-35.

[31] Macho GA, Jiang Y, Spears IR. Enamel microstructure--a truly three-dimensional structure. J Hum Evol 2003;45:81-90.

[32] Gao HJ, Ji BH, Jager IL, Arzt E, Fratzl P. Materials become insensitive to flaws at nanoscale: Lessons from nature. P Natl Acad Sci USA 2003;100:5597-600.

[33] Siang BY, Varatharajoo R. Optimal control for combined energy storage and attitude control system (CEACS) in small satellites. Appl Mech Mater 2012;110-116:3587-92.

[34] Kerebel B, Daculsi G, Kerebel LM. Ultrastructural Studies of Enamel Crystallites. Journal of Dental Research 1979;58:844-51.

[35] He LH. Mechanical behavior of human enamel and the relationship to its structural and compositional characteristics. PhD thesis 2008.

[36] Shimizu D, Macho GA. Functional significance of the microstructural detail of the primate dentino-enamel junction: a possible example of exaptation. J Hum Evol 2007;52:103-11.

[37] Shane N. White, Michael L. Paine, Wen Luo, Mehmet Sarikaya, Hanson Fong, Zhaokun Yu, et al. The Dentino-enamel Junction is a Broad Transitional Zone Uniting Dissimilar Bioceramic Composites. J Am Ceram Soc 2000;83:238-40.

[38] Habelitz S, Marshall SJ, Marshall GW, Balooch M. Mechanical properties of human dental enamel on the nanometre scale. Archives of Oral Biology 2001;46:173-83.

[39] Bodier-Houlle P, Steuer P, Meyer JM, Bigeard L, Cuisinier FJ. High-resolution electron-microscopic study of the relationship between human enamel and dentin crystals at the dentinoenamel junction. Cell Tissue Res 2000;301:389-95.

[40] Sela J, Sela M, Lustmann J, Ulmansky M. Dentinoenamel junction area of a resorbing permanent incisor studied by means of scanning electron microscopy. J Dent Res 1975;54:110-3.

[41] Lingg B, Marshall GW, Watanabe LG, Habelitz S, Ho SP, Marshall SJ. Incisor and molar DEJ scallop size as a function of intratooth location. Journal of Dental Research 2002;82(spec. Issue AADR).

[42] Lin CP, Douglas WH, Erlandsen SL. Scanning Electron-Microscopy of Type-I Collagen at the Dentin Enamel Junction of Human Teeth. J Histochem Cytochem 1993;41:381-8.

[43] Palamara J, Phakey PP, Rachinger WA, Orams HJ. Electron-Microscope Study of the Dentine-Enamel Junction of Kangaroo (Macropus-Giganteus) Teeth Using Selected-Area Argon-Ion-Beam Thinning. Cell and Tissue Research 1981;221:405-19.

[44] Lawn BR, Lee JJW, Chai H. Teeth: Among Nature's Most Durable Biocomposites. Annu Rev Mater Res 2010;40:55-75.

[45] Young RA, Mackie PE. Crystallography of Human Tooth Enamel - Initial Structure Refinement. Mater Res Bull 1980;15:17-29.

[46] Wilson RM, Elliott JC, Dowker SEP. Rietveld refinement of the crystallographic structure of human dental enamel apatites. Am Mineral 1999;84:1406-14.

[47] Wilson RM, Elliott JC, Dowker SEP, Smith RI. Rietveld structure refinement of precipitated carbonate apatite using neutron diffraction data. Biomaterials 2004;25:2205-13.

[48] Klionsky DJ, Abdalla FC, Abeliovich H, Abraham RT, Acevedo-Arozena A, Adeli K, et al. Guidelines for the use and interpretation of assays for monitoring autophagy. Autophagy 2012;8:445-544.

[49] Huang Z, Newcomb CJ, Bringas P, Stupp SI, Snead ML. Biological synthesis of tooth enamel instructed by an artificial matrix. Biomaterials 2010;31:9202-11.

[50] Powers JM, Farah JW. Apparent Modulus of Elasticity of Dental Amalgams. Journal of Dental Research 1975;54:902-.

[51] Stanford JW, Weigel KV, Paffenbarger GC, Sweeney WT. Compressive properties of hard tooth tissues and some restorative materials. J Am Dent Assoc 1960;60:746-56.

[52] Bowen RL, Rodriguez MS. Tensile Strength and Modulus of Elasticity of Tooth Structure and Several Restorative Materials. J Am Dent Assoc 1962;64:378-&.

[53] Mahoney EK, Rohanizadeh R, Ismail FSM, Kilpatrick NM, Swain MV. Mechanical properties and microstructure of hypomineralised enamel of permanent teeth. Biomaterials 2004;25:5091-100.

[54] Kishen A, Ramamurty U, Asundi A. Experimental studies on the nature of property gradients in the human dentine. J Biomed Mater Res 2000;51:650-9.

[55] Angker L, Swain MV, Kilpatrick N. Micro-mechanical characterisation of the properties of primary tooth dentine. J Dent 2003;31:261-7.

[56] Marshall GW, Balooch M, Gallagher RR, Gansky SA, Marshall SJ. Mechanical properties of the dentinoenamel junction: AFM studies of nanohardness, elastic modulus, and fracture. J Biomed Mater Res 2001;54:87-95.

[57] Hosoya Y, Marshall GW. The nano-hardness and elastic modulus of sound deciduous canine dentin and young premolar dentin - Preliminary study. J Mater Sci-Mater M 2005;16:1-8.

[58] Ziskind D, Hasday M, Cohen SR, Wagner HD. Young's modulus of peritubular and intertubular human dentin by nano-indentation tests. J Struct Biol 2011;174:23-30.

[59] Habelitz S, Marshall SJ, Marshall GW, Jr., Balooch M. Mechanical properties of human dental enamel on the nanometre scale. Arch Oral Biol 2001;46:173-83.

[60] Hassan R, Caputo AA, Bunshah RF. Fracture-Toughness of Human-Enamel. Journal of Dental Research 1981;60:820-7.

[61] Yoshida T, Hayashi N, Nishimura S, Itoh T, Kawahara K, Okita K, et al. Mechanism of Action of Ethanolamine Oleate Used in Injection Sclerotherapy with Special Emphasis on the Bronze Varices. J Gastroen Hepatol 1989;4:173-5.

[62] Craig RG, Johnson DW, Peyton FA. Compressive Properties of Enamel, Dental Cements, and Gold. Journal of Dental Research 1961;40:936-&.

[63] Tyldeslsy WR. The mechanical properties of hunman dental enamel and dentin. Br Dent J 1959;106:269-78.

[64] Xu HHK, Smith DT, Jahanmir S, Romberg E, Kelly JR, Thompson VP, et al. Indentation damage and mechanical properties of human enamel and dentin. Journal of Dental Research 1998;77:472-80.

[65] Braly A, Darnell LA, Mann AB, Teaford MF, Weihs TP. The effect of prism orientation on the indentation testing of human molar enamel. Archives of Oral Biology 2007;52:856-60.

[66] Willems G, Celis JP, Lambrechts P, Braem M, Vanherle G. Hardness and Young Modulus Determined by Nanoindentation Technique of Filler Particles of Dental Restorative Materials Compared with Human Enamel. J Biomed Mater Res 1993;27:747-55.

[67] Wang RZ, Weiner S. Strain-structure relations in human teeth using Moire fringes. J Biomech 1998;31:135-41.

[68] Urabe I, Nakajima S, Sano H, Tagami J. Physical properties of the dentin-enamel junction region. Am J Dent 2000;13:129-35.

[69] Dieulesaint E, Royer D. Elastic waves in solids : applications to signal processing. Chichester: Wiley; 1980.

[70] Katz JL, Ukraincik K. On the anisotropic elastic properties of hydroxyapatite. J Biomech 1971;4:221-7.

[71] Tofail SAM, Haverty D, Cox F, Erhart J, Hana P, Ryzhenko V. Direct and ultrasonic measurements of macroscopic piezoelectricity in sintered hydroxyapatite. J Appl Phys 2009;105.

[72] Menendez-Proupin E, Cervantes-Rodriguez S, Osorio-Pulgar R, Franco-Cisterna M, Camacho-Montes H, Fuentes ME. Computer simulation of elastic constants of hydroxyapatite and fluorapatite. J Mech Behav Biomed 2011;4:1011-20.

[73] Ching WY, Rulis P, Misra A. Ab initio elastic properties and tensile strength of crystalline hydroxyapatite. Acta Biomater 2009;5:3067-75.

[74] Snyders R, Music D, Sigumonrong D, Schelnberger B, Jensen J, Schneider JM. Experimental and ab initio study of the mechanical properties of hydroxyapatite. Appl Phys Lett 2007;90.

[75] de Leeuw NH, Bowe JR, Rabone JAL. A computational investigation of stoichiometric and calcium-deficient oxy- and hydroxy-apatites. Faraday Discuss 2007;134:195-214.

[76] Deymier-Black AC, Almer JD, Stock SR, Haeffner DR, Dunand DC. Synchrotron X-ray diffraction study of load partitioning during elastic deformation of bovine dentin. Acta Biomater 2010;6:2172-80.

[77] Jones RM. Mechanics of composite materials. 2nd ed. Philadelphia, Pa. ; London: Taylor & Francis; 1999.

[78] Bar-On B, Wagner HD. Elastic modulus of hard tissues. Journal of Biomechanics 2012;45:672-8.
[79] Ji BH, Gao HJ. Mechanical properties of nanostructure of biological materials. J Mech Phys Solids 2004;52:1963-90.
[80] Withers PJ, Stobbs WM, Pedersen OB. The Application of the Eshelby Method of Internal-Stress Determination to Short Fiber Metal Matrix Composites. Acta Metall Mater 1989;37:3061-84.
[81] Takao Y, Taya M. The Effect of Variable Fiber Aspect Ratio on the Stiffness and Thermal-Expansion Coefficients of a Short Fiber Composite. J Compos Mater 1987;21:140-56.
[82] Qin Q-H, Swain MV. A micro-mechanics model of dentin mechanical properties. Biomaterials 2004;25:5081-90.
[83] Huo B. An inhomogeneous and anisotropic constitutive model of human dentin. J Biomech 2005;38:587-94.
[84] Wang YN, Qin QH. A generalized self consistent model for effective elastic moduli of human dentine. Compos Sci Technol 2007;67:1553-60.
[85] Huo B, Zheng QS. Effect of dentin tubules on the mechanical properties of dentin. Part I: Stress-strain relations and strength criterion. Acta Mech Sinica 1999;15:355-65.
[86] Palmer LC, Newcomb CJ, Kaltz SR, Spoerke ED, Stupp SI. Biomimetic Systems for Hydroxyapatite Mineralization Inspired By Bone and Enamel. Chem Rev 2008;108:4754-83.
[87] Kantola S. Laser-Induced Effects on Tooth Structure .8. X-Ray-Diffraction Study of Dentin Exposed to a Co2-Laser. Acta Odontol Scand 1973;31:381-6.
[88] Fried D, Zuerlein MJ, Le CQ, Featherstone JDB. Thermal and chemical modification of dentin by 9-11-mu m CO2 laser pulses of 5-100-mu s duration. Laser Surg Med 2002;31:275-82.
[89] Zuerlein MJ, Fried D, Featherstone JDB. Modeling the modification depth of carbon dioxide laser-treated dental enamel. Laser Surg Med 1999;25:335-47.
[90] Piga G, Thompson TJU, Malgosa A, Enzo S. The Potential of X-Ray Diffraction in the Analysis of Burned Remains from Forensic Contexts. J Forensic Sci 2009;54:534-9.
[91] Thompson TJU. Heat-induced dimensional changes in bone and their consequences for forensic anthropology. J Forensic Sci 2005;50:1008-15.
[92] Thompson TJU, Islam M, Piduru K, Marcel A. An investigation into the internal and external variables acting on crystallinity index using Fourier Transform Infrared Spectroscopy on unaltered and burned bone. Palaeogeogr Palaeocl 2011;299:168-74.
[93] Goncalves D, Thompson TJU, Cunha E. Implications of heat-induced changes in bone on the interpretation of funerary behaviour and practice. J Archaeol Sci 2011;38:1308-13.
[94] Shipman P, Foster G, Schoeninger M. Burnt Bones and Teeth - an Experimental-Study of Color, Morphology, Crystal-Structure and Shrinkage. J Archaeol Sci 1984;11:307-25.
[95] Sandholzer MA, Sui T, Korsunsky AM, Walmsley AD, Lumley PJ, Landini G. X-ray scattering evaluation of ultrastructural changes of human dental tissues with thermal treatment. 2014.
[96] Enzo S, Bazzoni M, Mazzarello V, Piga G, Bandiera P, Melis P. A study by thermal treatment and X-ray powder diffraction on burnt fragmented bones from tombs II, IV and IX belonging to the hypogeic necropolis of "Sa Figu" near Ittiri, Sassari (Sardinia, Italy). J Archaeol Sci 2007;34:1731-7.

[97] Rogers KD, Daniels P. An X-ray diffraction study of the effects of heat treatment on bone mineral microstructure. Biomaterials 2002;23:2577-85.

[98] Beckett S, Rogers KD, Clement JG. Inter-Species Variation in Bone Mineral Behavior upon Heating. J Forensic Sci 2011;56:571-9.

[99] Reyes-Gasga J, Garcia-Garcia R, Arellano-Jimenez MJ, Sanchez-Pastenes E, Tiznado-Orozco GE, Gil-Chavarria IM, et al. Structural and thermal behaviour of human tooth and three synthetic hydroxyapatites from 20 to 600 degrees C. J Phys D Appl Phys 2008;41.

[100] Etok SE, Valsami-Jones E, Wess TJ, Hiller JC, Maxwell CA, Rogers KD, et al. Structural and chemical changes of thermally treated bone apatite. J Mater Sci 2007;42:9807-16.

[101] Walker PL, Miller KWP, Richman R. Time, Temperature, and Oxygen Availability: An Experimental Study of the Effects of Environmental Conditions on the Color and Organic Content of Cremated Bone. Analysis of Burned Human Remains 2008:129-35.

[102] Thompson TJU, Islam M, Bonniere M. A new statistical approach for determining the crystallinity of heat-altered bone mineral from FTIR spectra. J Archaeol Sci 2013;40:416-22.

[103] Devlin JB, Herrmann NP. Bone Color as an Interpretive Tool of the Depositional History of Archaeological Cremains. Analysis of Burned Human Remains 2008:109-28.

[104] Merlati G, Savio C, Danesino P, Fassina G, Menghini P. Further study of restored and un-restored teeth subjected to high temperatures. Journal of Forensic Odonto-Stomatology 2004;22:34-9.

[105] Moreno S, Merlati G, Marin L, Savio C, Moreno F. Effects of high temperatures on different dental restorative systems: Experimental study to aid identification processes. Journal of Forensic Dental Sciences 2009;1:17-23.

[106] Muller M, Berytrand MF, Quatrehomme G, Bolla M, Rocca JP. Macroscopic and microscopic aspects of incinerated teeth. J Forensic Odontostomatol 1998;16:1-7.

[107] Schmidt CW. The Recovery and Study of Burned Human Teeth. Analysis of Burned Human Remains 2008:55-74.

[108] Bachmann L, Sena ET, Stolf SF, Zezell DM. Dental discolouration after thermal treatment. Archives of Oral Biology 2004;49:233-8.

[109] Beach JJ, Passalacqua NV, Chapman EN. Heat-Related Changes in Tooth Color: Temperature Versus Duration of Exposure. Analysis of Burned Human Remains 2008:137-44.

[110] Myers SL, Williams JM, Hodges JS. Effects of extreme heat on teeth with implications for histologic processing. J Forensic Sci 1999;44:805-9.

[111] Schmidt C, Reinhardt G, Nawrocki RS, Hill M. Analysis of burned dental remains. Am J Phys Anthropol 2005:183-.

[112] Fereira JL, de Fereira AE, Ortega AI. Methods for the analysis of hard dental tissues exposed to high temperatures. Forensic Sci Int 2008;178:119-24.

[113] Hughes CE, White CA. Crack Propagation in Teeth: A Comparison of Perimortem and Postmortem Behavior of Dental Materials and Cracks. J Forensic Sci 2009;54:263-6.

[114] Hollund HI, Ariese F, Fernandes R, Jans MME, Kars H. Testing an Alternative High-Throughput Tool for Investigating Bone Diagenesis: Ftir in Attenuated Total Reflection (Atr) Mode. Archaeometry 2013;55:507-32.

[115] Rogers K, Beckett S, Kuhn S, Chamberlain A, Clement J. Contrasting the crystallinity indicators of heated and diagenetically altered bone mineral. Palaeogeogr Palaeocl 2010;296:125-9.

[116] Squires KE, Thompson TJU, Islam M, Chamberlain A. The application of histomorphometry and Fourier Transform Infrared Spectroscopy to the analysis of early Anglo-Saxon burned bone. J Archaeol Sci 2011;38:2399-409.

[117] Piga G, Malgosa A, Thompson TJU, Enzo S. A new calibration of the XRD technique for the study of archaeological burned human remains. J Archaeol Sci 2008;35:2171-8.

[118] Hiller JC, Thompson TJ, Evison MP, Chamberlain AT, Wess TJ. Bone mineral change during experimental heating: an X-ray scattering investigation. Biomaterials 2003;24:5091-7.

[119] Kugler M. X-ray diffraction analysis in forensic science: the last resort in many criminal cases. Advances in X-ray Analysis 2003;46.

[120] Hiller JC, Wess TJ. The use of small-angle X-ray scattering to study archaeological and experimentally altered bone. J Archaeol Sci 2006;33:560-72.

[121] Kwiatek WM. Biomedical Applications of Synchrotron X-Ray-Fluorescence. Acta Phys Pol A 1994;86:695-703.

[122] Synchrotron facility. http://wwwdiamondacuk/Home/Media/imageshtml.

[123] Synchrotron Techniques. http://wwwsynchrotronrsnzorg/science/techniquesphp.

[124] Glatter O, Kratky O. Small angle x-ray scattering. London ; New York: Academic Press; 1982.

[125] Svergun DI, Fe**gin LA, Taylor GW. Structure analysis by small-angle x-ray and neutron scattering. New York ; London: Plenum; 1987.

[126] Beaucage G, Kammler HK, Pratsinis SE. Particle size distributions from small-angle scattering using global scattering functions. J Appl Crystallogr 2004;37:523-35.

[127] Fraser RDB, Macrae TP. Unit-Cell and Molecular Connectivity in Tendon Collagen. Int J Biol Macromol 1981;3:193-200.

[128] Rong LX. SAXS analysis on polymer, nano-oxide, and porous carbon. PhD thesis 2003;Beijing: Institute of High Energy Physics Chinese Academy of Science.

[129] Wide Angle X-ray Scattering. http://enwikipediaorg/wiki/Wide_angle_X-ray_scattering.

[130] Brumberger H, North Atlantic Treaty Organization. Scientific Affairs Division. Modern aspects of small-angle scattering. Dordrecht ; London: Kluwer Academic; 1995.

[131] Daniels JE, Pontoni D, Hoo RP, Honkimaki V. Simultaneous small- and wide-angle scattering at high X-ray energies. J Synchrotron Radiat 2010;17:473-8.

[132] Almer JD, Stock SR. High energy X-ray scattering quantification of in situ-loading-related strain gradients spanning the dentinoenamel junction (DEJ) in bovine tooth specimens. J Biomech 2010;43:2294-300.

[133] Singhal A, Almer JD, Dunand DC. Variability in the nanoscale deformation of hydroxyapatite during compressive loading in bovine bone. Acta Biomater 2012;8:2747-58.

[134] Almer JD, Stock SR. Internal strains and stresses measured in cortical bone via high-energy X-ray diffraction. J Struct Biol 2005;152:14-27.

[135] Fujisaki K, Todoh M, Niida A, Shibuya R, Kitami S, Tadano S. Orientation and deformation of mineral crystals in tooth surfaces. J Mech Behav Biomed 2012;10:176-82.

[136] Bechtle S, Ozcoban H, Lilleodden ET, Huber N, Schreyer A, Swain MV, et al. Hierarchical flexural strength of enamel: transition from brittle to damage-tolerant behaviour. J R Soc Interface 2012;9:1265-74.

[137] Nogueira BCL, Fernandes PM, Santana LNS, Lima RR. Ultrastructural Characterization of Bovine and Buffalo Enamel Through Scanning Electron Microscopy. XXIII Congress of the Brazilian Society of Microscopy and Microanalysis 2011.

[138] Lopes MB, Sinhoreti MA, Gonini Junior A, Consani S, McCabe JF. Comparative study of tubular diameter and quantity for human and bovine dentin at different depths. Braz Dent J 2009;20:279-83.

[139] Al-Jawad M, Steuwer A, Kilcoyne SH, Shore RC, Cywinski R, Wood DJ. 2D mapping of texture and lattice parameters of dental enamel. Biomaterials 2007;28:2908-14.

[140] Deymier-Black AC, Yuan F, Singhal A, Almer JD, Brinson LC, Dunand DC. Evolution of load transfer between hydroxyapatite and collagen during creep deformation of bone. Acta Biomater 2012;8:253-61.

[141] Almer JD, Stock SR. Micromechanical response of mineral and collagen phases in bone. J Struct Biol 2007;157:365-70.

[142] Deymier-Black AC, Almer JD, Stock SR, Dunand DC. Variability in the elastic properties of bovine dentin at multiple length scales. J Mech Behav Biomed Mater 2012;5:71-81.

[143] Fratzl P, Schreiber S, Klaushofer K. Bone mineralization as studied by small-angle x-ray scattering. Connect Tissue Res 1996;35:9-16.

[144] Hammersley AP. "FIT2D: An Introduction and Overview". ESRF Internal Report1997.

[145] Young ML, Almer JD, Daymond MR, Haeffner DR, Dunand DC. Load partitioning between ferrite and cementite during elasto-plastic deformation of an ultrahigh-carbon steel. Acta Mater 2007;55:1999-2011.

[146] Young ML, DeFouw J, Almer JD, Dunand DC. Load partitioning during compressive loading of a Mg/MgB2 composite. Acta Mater 2007;55:3467-78.

[147] Mueller R, Rossoll A, Weber L, Bourke MAM, Dunand DC, Mortensen A. Tensile flow stress of ceramic particle-reinforced metal in the presence of particle cracking. Acta Mater 2008;56:4402-16.

[148] Korsunsky AM, Baimpas N, Song X, Belnoue J, Hofmann F, Abbey B, et al. Strain tomography of polycrystalline zirconia dental prostheses by synchrotron X-ray diffraction. Acta Mater 2011;59:2501-13.

[149] Egan CK, Jacques SD, Di Michiel M, Cai B, Zandbergen MW, Lee PD, et al. Non-invasive imaging of the crystalline structure within a human tooth. Acta Biomater 2013;9:8337-45.

[150] Holden JL, Clement JG, Phakey PP. Age and Temperature-Related Changes to the Ultrastructure and Composition of Human Bone-Mineral. J Bone Miner Res 1995;10:1400-9.

[151] Fratzl P, Schreiber S, Boyde A. Characterization of bone mineral crystals in horse radius by small-angle X-ray scattering. Calcified Tissue Int 1996;58:341-6.

[152] Tanaka T, Yagi N, Ohta T, Matsuo Y, Terada H, Kamasaka K, et al. Evaluation of the Distribution and Orientation of Remineralized Enamel Crystallites in Subsurface Lesions by X-Ray Diffraction. Caries Res 2010;44:253-9.

[153] Tesch W, Vandenbos T, Roschgr P, Fratzl-Zelman N, Klaushofer K, Beertsen W, et al. Orientation of mineral crystallites and mineral density during skeletal development

in mice deficient in tissue nonspecific alkaline phosphatase. J Bone Miner Res 2003;18:117-25.

[154] Tesch W, Eidelman N, Roschger P, Goldenberg F, Klaushofer K, Fratzl P. Graded microstructure and mechanical properties of human crown dentin. Calcified Tissue Int 2001;69:147-57.

[155] Clyne TW, Withers PJ. An introduction to metal matrix composites. First paperback edition 1995. ed. Cambridge: Cambridge University Press; 1993.

[156] Mura T. Micromechanics of defects in solids. 2nd rev. ed. Dordrecht ; Boston, Higham, Mass.: M. Nijhoff ; Distributors the U.S. and Canada, Kluwer Boston; 1987.

[157] Ebenstein DM, Pruitt LA. Nanoindentation of biological materials. Nano Today 2006;1:26-33.

[158] Kinney JH, Marshall SJ, Marshall GW. The mechanical properties of human dentin: a critical review and re-evaluation of the dental literature. Crit Rev Oral Biol Med 2003;14:13-29.

[159] Haque F. Application of nanoindentation to development of biomedical materials. Surf Eng 2003;19:255-68.

[160] Roy S, Basu B. Mechanical and tribological characterization of human tooth. Mater Charact 2008;59:747-56.

[161] Fong H, Sarikaya M, White SN, Snead ML. Nano-mechanical properties profiles across dentin-enamel junction of human incisor teeth. Mat Sci Eng C-Bio S 2000;7:119-28.

[162] Hsu CM, Lin AD, Chien HL, Hung TP, Kuang JH. Using nanoindentation techniques to investigate the Young's moduli for human teeth of different ages.

[163] Oliver WC, Pharr GM. An Improved Technique for Determining Hardness and Elastic-Modulus Using Load and Displacement Sensing Indentation Experiments. J Mater Res 1992;7:1564-83.

[164] Le Bourhis E, Patriarche G. TEM-nanoindentation studies of semiconducting structures. Micron 2007;38:377-89.

[165] Lim CT, Hairul Nizam BR, Omar BHB, Chng HK, Yap AUJ. Probing the nanomechanical properties of teeth. ICF11 proceeding 2005.

[166] Dally JW, Riley WF. Experimental stress analysis. 3rd ed ed. New York ; London: McGraw-Hill; 1991.

[167] Environmental scanning electron microscope. http://enwikipediaorg/wiki/Environmental_scanning_electron_microscope.

[168] Transmission electron microscopy. http://enwikipediaorg/wiki/Transmission_electron_microscopy.

[169] Zapletalova Z, Kubinek R, Vujtek M, Novotny R. Examination of dentin surface using AFM (our experience). Acta Medica (Hradec Kralove) 2004;47:343-6.

[170] T L, Zeng KY. Nanoscale elasticity mappings of micro-constituents of abalone shell by band excitation-contact resonance force microscopy. Nanoscale 2014;6:2177-85.

[171] Buzug TM. Computed tomography : from photon statistics to modern cone-beam CT. Berlin: Springer; 2008.

[172] De Witte Y, Cnudde V, Pieters K, Masschaele B, Dierick M, Vlassenbroeck J, et al. X-ray micro-CT applied to natural building materials and art objects. X-Ray Spectrom 2008;37:383-7.

[173] Eliceiri KW, Berthold MR, Goldberg IG, Ibanez L, Manjunath BS, Martone ME, et al. Biological imaging software tools. Nat Methods 2012;9:697-710.

[174] Katz JL. Hard Tissue as a Composite Material .1. Bounds on Elastic Behavior. Journal of Biomechanics 1971;4:455-&.

[175] Hashin Z. Analysis of Composite-Materials - a Survey. J Appl Mech-T Asme 1983;50:481-505.
[176] Gottesman T, Hashin Z. Analysis of Viscoelastic Behavior of Bones on the Basis of Microstructure. J Biomech 1980;13:89-96.
[177] Calibration DLS. Diamond Light Source Calibration. 2013.
[178] Bozec L, de Groot J, Odlyha M, Nicholls B, Nesbitt S, Flanagan A, et al. Atomic force microscopy of collagen structure in bone and dentine revealed by osteoclastic resorption. Ultramicroscopy 2005;105:79-89.
[179] Chou TW, Sun, C.T, . Nanocomposites. In: Hyer M, W, editor.: DEStech Inc; 2012.
[180] Dourda AO, Moule AJ, Young WG. A morphometric analysis of the cross-sectional area of dentine occupied by dentinal tubules in human third molar teeth. Int Endod J 1994;27:184-9.
[181] Kinney JH, Habelitz S, Marshall SJ, Marshall GW. The importance of intrafibrillar mineralization of collagen on the mechanical properties of dentin. J Dent Res 2003;82:957-61.
[182] Kinney JH, Gladden JR, Marshall GW, Marshall SJ, So JH, Maynard JD. Resonant ultrasound spectroscopy measurements of the elastic constants of human dentin. Journal of Biomechanics 2004;37:437-41.
[183] Habelitz S, Marshall GW, Jr., Balooch M, Marshall SJ. Nanoindentation and storage of teeth. J Biomech 2002;35:995-8.
[184] Deymier-Back AC, Singhal A, Yuan F, Almer JD, Brinson LC, Dunand DC. Effect of high-energy X-ray irradiation on creep mechanisms in bone and dentin. J Mech Behav Biomed 2013;21:17-31.
[185] Nakamura T, Lu C, Korach CS. Mechanical Properties of Tooth Enamel: Microstructural Modeling and Characterization. Conference Proceedings of the Society for Experimental Mechanics Series 2011;9999:171-9.
[186] Sui T, Sandholzer MA, Baimpas N, Dolbnya IP, Landini G, Korsunsky AM. Hierarchical modelling of elastic behaviour of human enamel based on synchrotron diffraction characterization. J Struct Biol 2013;In press.
[187] Xie ZH, Swain MV, Swadener G, Munroe P, Hoffman M. Effect of microstructure upon elastic behaviour of human tooth enamel. Journal of Biomechanics 2009;42:1075-80.
[188] Beamline Calibration. 2013.
[189] Ochsner A, Ahmed W. Biomechanics of Hard Tissues. John Wiley & Sons 2011.
[190] McCrum NG, Buckley CP, Bucknall CB. Principles of polymer engineering. 2nd ed. Oxford: Oxford University Press; 1997.
[191] Sui T, Korsunsky AM. Hierarchical modelling of elastic behaviour of human dental tissue based on synchrotron diffraction characterization: Advanced Materials Series; 2013.
[192] Taylor JR. An introduction to error analysis : the study of uncertainties in physical measurements. 2nd ed. Sausalito, Calif.: University Science Books; 1997.
[193] Takagi S, Liao H, Chow LC. Effect of tooth-bound fluoride on enamel demineralization/remineralization in vitro. Caries Res 2000;34:281-8.
[194] White SN, Miklus VG, Chang PP, Caputo AA, Fong H, Sarikaya M, et al. Controlled failure mechanisms toughen the dentino-enamel junction zone. J Prosthet Dent 2005;94:330-5.
[195] Stock SR, Vieira AEM, Delbem ACB, Cannon ML, Xiao X, Carlo F. Synchrotron microComputed tomography of the mature bovine dentinoenamel junction. J Struct Biol 2008;161:162-71.

[196] Marshall SJ, Balooch M, Habelitz S, Balooch G, Gallagher R, Marshall GW. The dentin-enamel junction - a natural, multilevel interface. J Eur Ceram Soc 2003;23:2897-904.

[197] Keswani M, Raghavan S, Deymier P. Characterization of transient cavitation in gas sparged solutions exposed to megasonic field using cyclic voltammetry. Microelectron Eng 2013;102:91-7.

[198] Jacobs HR, Thompson RE, Brown WS. Heat-Transfer in Teeth. Journal of Dental Research 1973;52:248-52.

[199] Pramanik S, Hanif ASM, Pingguan-Murphy B, Abu Osman NA. Morphological Change of Heat Treated Bovine Bone: A Comparative Study. Materials 2013;6:65-75.

[200] Patriarche G, Le Bourhis E, Khayyat MMO, Chaudhri MM. Indentation-induced crystallization and phase transformation of amorphous germanium. J Appl Phys 2004;96:1464-8.

[201] Le Bourhis E, Patriarche G, Largeau L, Riviere JP. Polarity-induced changes in the nanoindentation response of GaAs. J Mater Res 2004;19:131-6.

[202] Angker L, Swain MV, Kilpatrick N. Characterising the micro-mechanical behaviour of the carious dentine of primary teeth using nano-indentation. Journal of Biomechanics 2005;38:1535-42.

[203] Reiche I, Vignaud C, Menu M. The crystallinity of ancient bone and dentine: New insights by transmission electron microscopy. Archaeometry 2002;44:447-59.

[204] Jiang HD, Liu XY, Lim CT, Hsu CY. Ordering of self-assembled nanobiominerals in correlation to mechanical properties of hard tissues. Appl Phys Lett 2005;86.

[205] Sui T, Sandholzer MA, Baimpas N, Dolbnya IP, Walmsley AD, Lumley PJ, et al. Multi-scale modelling and diffraction-based characterization of elastic behaviour of human dentine. Acta Biomater 2013;9:7937-47.

[206] Bao YW, Wang W, Zhou YC. Investigation of the relationship between elastic modulus and hardness based on depth-sensing indentation measurements. Acta Mater 2004;52:5397-404.

[207] Dent AJ, Greaves GN, Roberts MA, Sankar G, Wright PA, Jones RH, et al. A New Furnace Design for Use in Combined X-Ray-Absorption and Diffraction of Catalysis and Ceramics Studies - Formation from Carbonate Precursors of Cu, Co, Mn Spinels for the Oxidation of Co and the Formation of Plzt, a Piezoelectric Ceramic. Nucl Instrum Meth B 1995;97:20-2.

[208] Ooi CY, Hamdi M, Ramesh S. Properties of hydroxyapatite produced by annealing of bovine bone. Ceram Int 2007;33:1171-7.

[209] Lei HJ, Liu B, Fang DN. The coefficient of thermal expansion of biomimetic composite. Front Mater Sci China 2010;4:234-8.

[210] Elliott JC. Structure and chemistry of the apatites and other calcium orthophosphates. Amsterdam ; London: Elsevier; 1994.

[211] Kingery WD, Bowen HK, Uhlmann DR. Introduction to ceramics. 2nd ed. New York ; London: Wiley; 1976.

[212] Tan TCJ, Rahman R, Jaber-Hijazi F, Felix DA, Chen C, Louis EJ, et al. Telomere maintenance and telomerase activity are differentially regulated in asexual and sexual worms. P Natl Acad Sci USA 2012;109:4209-14.